Smart and Green Energy Systems

SmartGY

SUM

Smart and Green Energy Systems

Smart and Green Energy Systems

Compilation of selected
SMARTGYsum project scientific results

ISBN 978-84-09-81019-2
1st Edition 2025

SMARTGYsum consortium
www.smartgysum.eu
Edited by Enrique Romero-Cadaval. Project Coordinator

This book has received funding from the European Union's Horizon 2020 research and innovation programme under the Marie Skłodowska-Curie grant agreement No 955614.

Preface

This book has been a result of the project SMARTGYsum, funded by the European Union's Horizon 2020 research and innovation programme under the Marie Skłodowska-Curie grant agreement no. 955614, under Innovative Training Networks (ITN) call H2020-MSCA-ITN-2020).

The project has been run by a consortium coordinated by University of Extremadura (Spain) and conformed by Aalborg University (Denmark); Christian-Albrechts-Universitaet Zu Kiel (Germany); Tallinn University of Technology (Estonia); Universitá degli Studi di Salerno (Italy); CY Cergy Paris Université (France); Politechnika Gdanska; Politechnika Warszawska (Polan); Chernihiv National Technological University (Ukarine); Siemens Industry Software SAS France (France); Smart Energy Products and Services (Spain); Karlsruhe Institut für Technologie (Germany); Universitá Commerciale Luigi Bocconi (Italy); and Universidade Nova de Lisboa (Portugal).

Its general objective is to drive the evolution of European Electric Energy Systems by integrating the knowledge on Power Electronics, Electric Engineering and Information and Communication Technology as well as their socio-economical aspects with the creation of new Businesses Models to cover the green economy energy requirements (sustainability, efficiency, reliability and manageability). SMARTGYsum contributes to long-term structural challenges and also proposes an innovative program for training ESRs following a collaborative, transferable, inter and multidisciplinary approach, aimed at raising the employability and career opportunities of ESRs within the public and the private sectors, as well as their potential for conducting innovation, entrepreneurship and for impacting in European society at medium and long-term.

The overall objective of this ITN is to implement a multidisciplinary and innovative research and training programme, bringing together different scientific fields and industrial participation to enable a new generation of Early Stage Researchers (ESR) to foster a New Green Energy Economy in Europe. SMARTGYsum – Smart and Green Energy Systems and Business Models research and training programme will focus on providing the ESR with relevant knowledge, methods and skills across a wide range of disciplines around the Energy ecosystem and within the accelerating area of Renewable Electric Energy Systems (REES) to sustain the proliferation and consolidation of business models which will sustain the deployment of REES and technologies into the green energy system. Today, various barriers prevent an increased deployment of renewable electric energy systems including market and social barriers (as price distortion through externalities, low priority of energy issues, split incentive); financial barriers (investment, high up-front costs, lack of access to capital); Information failures (lack of awareness, knowledge and competence); and regulatory barriers (restrictive procurement rules). The business models in SMARTGYsum – will be developed as strategies to invest in renewable electric energy systems in which the financing and implementation of renewable electric energy systems contribute to overcome the deployment of REES. This goal will be achieved by a unique combination of direct research training, non-academic internships and courses and seminars/workshops on scientific and complementary so-called “transversal” or “soft” skills facilitated by a multidisciplinary, multisectoral and international consortium.

The objectives of the project are:

- The generation and storage of electric energy using Renewable Electric Energy Generation (REEG) sources and distributed energy resources (DER), and their integration in ESS. (Addressed in WP2)
- The distribution of electric energy from generator to consumers, ensuring the optimal efficiency of the system through collaborative models and radial networks.
- The analysis of the socioeconomic elements, among them the consumption patterns and behaviours, consumer engagement and other aspects that allow to understand and promote new business models to tackle with the customer prosumption concept, as well as the market uptake of energy and ICT innovation.
- Coordination of all sectors of Electric Energy Systems fusing smart grids, combining IoT, sensor networks, Big Data, AI and together with societal/social and behavioural aspects.
- To perform knowledge networks and platforms to promote the required changes in academia, industry, policy and society.

This book is a compilation of selected SMARTGYsum scientific results produced in the different individual research projects run during the project execution from September 2021 to September 2025.

Enrique Romero Cadaval
eromero@unex.es
SMARTGYsum Project Coordinator
Department of Electric, Electronic and Automation Engineering,
University of Extremadura. Badajoz, Spain

Contents

Cooperative Smart Inverters for Green Generation Plants
WP2 - Green and Renewable Distributed Electric Generation and Storing

Ayesha Wajiha Aslam[1] , Víctor Minambres-Marcos[1], Carlos Roncero-Clemente[2]

[1] Department of R&D and Innovation,
Senergy Products and Services. Badajoz, Spain

[2] Department of Electric, Electronic and Automation Engineering,
University of Extremadura. Badajoz, Spain

ayesha@senergyps.com, victor@senergyps.com, carlosrc@unex.es

Abstract. This chapter investigates advanced control and power quality enhancement for an AC nanogrid combining a two-level voltage source inverter (2L VSI) and a three-level T-type inverter (3L T-type). Discrete-time proportional-resonant (PR) controllers are designed and tuned using MATLAB's SISOTOOL and validated through PLECS simulations under various load conditions, including linear, nonlinear, and unbalanced loads. The control strategy integrates droop control, virtual impedance, and multiple second-order generalized integrators (MSOGI) to achieve precise voltage and current regulation while mitigating harmonics and voltage imbalances. Stability is confirmed via Bode and Nyquist analyses, and power quality is assessed through Fourier analysis focusing on total harmonic distortion (THD) and compliance with European grid standards. Results show significant improvements in voltage stability, harmonic reduction, and balanced power sharing between inverters. This work offers a practical framework for optimizing power quality and control in modern nanogrid systems, supporting the development of reliable and efficient distributed energy solutions.

Keywords: AC nanogrid, Power quality, Harmonic compensation, Total harmonic distortion, Three-level T-type inverter

1 Introduction

The rapid growth of renewable energy integration and the increasing demand for reliable power conversion have brought significant attention to advanced inverter technologies in modern power electronics. Modern power electronics face escalating demands for high-efficiency, scalable energy conversion systems, driven by renewable energy integration and industrial electrification. Inverter systems, which convert DC to AC power, are central to this transition. The inverter systems play a vital role in the conversion of direct current (DC) obtained from renewable energy sources and batteries to alternating current (AC) which is then suitable for grid usage as well as local consumption. As power requirements continue to rise, the need for scalable, efficient, and resilient inverter solutions has become more pronounced [1].

One promising approach to meet these power demands is the parallel, cascaded operation of multiple inverter systems. By connecting the different inverter systems in parallel it is possible to achieve an increase in power capacity enhancement, overall reliability and stability of the system along with higher flexibility in the system design. Parallel architecture allows for upgradation and variations in incremental power without any replacements in the existing infrastructure. This is also the main reason why the parallel system architecture is considered as the optimal choice for critical applications such as data centers and medical facilities in order to ensure stable and uninterrupted power supply during any component or system failures [1]. Among the different inverter system topologies, the two-level voltage source inverter (2L VSI) and the three-level T-type inverter (3L T-type) systems have gained significant importance owing to the distinct advantages that they present regarding efficiency, stability, control and implementation. Moreover, according to studies, the 3L T-type inverter systems provide an overall reduction in switching losses by upto 30% as compared to 2L VSIs, while on the other hand the 2L VSI systems provide optimal performance in case of low-voltage and high-frequency situations. The parallel interconnection of both inverter systems in turn combines their specific optimum capabilities enabling efficiency gains that are load specific [2].

However, there are also certain technical and operational challenges associated with the parallel operation of multiple inverter systems. These challenges are particularly related to coordination, power sharing as well as harmonic mitigation capabilities. The control system of the 2L VSI system is relatively simple but faces high level of harmonic distortion and switching losses at high frequency levels. Whereas, the 3L T-type inverter configuration provides a reduction in harmonics but also requires precise voltage balancing at the neutral point. Moreover, parallel configuration also leads to a mismatch in the modulation schemes and switching frequencies. This can in turn develop circulating currents in the system, leading to a destabilization of the system [3]. The synchronization of the pulse width modulation (PWM) signals of both the inverter systems is also important to avoid imbalances and voltage spikes. The additional switching states of the 3L T-type inverter system further complicates this parallel coordination. Misalignments in the PWM signals generation along with dead-time implementations in the switching signals can cause deviations in voltage and current, disrupting power sharing during varying load changes [1][3].

The motivation for the project is taken from the untapped potential of hybrid configuration of parallel systems combining the cost-effectiveness of 2L VSIs with the stable and efficient performance of 3L T-type inverters. The existing research has mainly focused on the homogenous parallel inverter systems, leaving a gap in research regarding control strategies associated with heterogenous toplogies [4]. This project addresses this gap through:

1. Development of decentralized control algorithms for the synchronization of 2L VSI and 3L T-type inverter systems while minimizing the circulating currents and harmonics.
2. Proposition of a dynamic load sharing framework that leverages the strengths and advantages of each inverter system.
3. Validation of the hybrid parallel system through simulation and experimental testing, focusing on overall efficiency and harmonic suppression.

This pairing of the 2L VSI and 3L T-type inverter systems was chosen in order to achieve a balance in stablity, cost, efficiency and scalability. While the 3L T-type inverter topology provides optimum operational performance in medium-voltage applications, the high component count leads to an increase in costs. This is in turn compensated by the 2L VSI inverter topology that offers a low-cost solution for high frequency applications [5]. Combining both these systems provides a parallel structure that is optimized in terms of cost which is also adaptable to variations in load conditions.

2 Background

The two-level voltage source inverter (2L VSI) is a fundamental topology in power electronics, characterized by its simplicity and cost-effectiveness. It employs six switching devices to generate a two-level output waveform, making it suitable for low-to-medium power applications such as motor drives and residential solar systems. However, its abrupt voltage transitions result in significant harmonic distortion, particularly at higher switching frequencies, necessitating bulky passive filters to meet grid standards. In contrast, the three-level T-type inverter (3L T-type) introduces a third voltage level through a bidirectional switch connected to the DC-link midpoint. This configuration reduces total harmonic distortion (THD) by 40–60% compared to 2L VSIs and minimizes switching losses in medium-voltage applications. Despite these advantages, the 3L T-type requires precise neutral-point voltage balancing and advanced gate-drive synchronization, complicating its integration into parallel systems [6], [7].

Recent advancements in grid-forming (GFM) converter systems have placed significant emphasis on the development of advanced control strategies to mitigate voltage unbalance and minimize total harmonic distortion (THD). Effectively managing harmonic imbalances is critical for achieving stable and optimal system operation, particularly in modern microgrids and distributed generation environments. One notable approach, as discussed in [8], involves a control strategy designed to maximize voltage support during voltage sags by safely injecting current and selectively boosting the lowest phase voltage. This method ensures that voltage stability is maintained even under adverse grid conditions. Another significant contribution, presented in [9], targets the elimination of negative sequence voltages and the regulation of positive sequence voltages, while also imposing limits on the magnitude of injected currents. This strategy is particularly relevant for implementation in static synchronous compensators (STATCOMs), where precise control of current injection is essential for grid support. In addition, a cooperative compensation strategy has been proposed in [10], which mitigates voltage unbalance by controlling distributed generators (DGs) to behave as negative sequence conductance elements. However, this approach can inadvertently introduce disturbances into the voltage control loop, particularly when the compensation signal is injected at the voltage regulation stage. To address this challenge, a solution presented in [11], involves directly modifying the voltage reference to resolve unbalance issues, thereby preventing the compensation from interfering with the main voltage control loop.

Achieving effective suppression of harmonic imbalances is essential for maintaining stable and reliable operation, especially in islanded microgrids where power quality directly influences system performance. One notable contribution in this area is the introduction of the Three-Level Zero Harmonic Distortion (ZHD) grid-forming converter [12], which has been proposed as an innovative solution to power quality challenges in isolated microgrid environments. This converter topology is particularly advantageous because it eliminates the necessity for bulky capacitive filtering components, which are traditionally used to attenuate harmonics but often lead to increased system costs, reduced efficiency, and larger physical footprints. By inherently minimizing harmonic content in its output, the ZHD converter streamlines the system design and enhances overall performance. In addition to advancements in converter topology, novel control techniques have been developed to address power sharing and voltage regulation issues in parallel-connected inverter systems. For example, adaptive virtual impedance control [13], has been explored as a means to compensate for voltage drop mismatches and improve power distribution among multiple converters. This method involves dynamically adjusting the virtual impedance of each inverter based on real-time measurements of reactive power deviation, thereby equalizing voltage drops across different lines and facilitating more accurate load sharing. Harmonic control in GFM converters has also seen progress through the implementation of unified harmonic voltage-current drop strategies. This approach enables each converter to proportionally share harmonic currents according to its rated capacity, while simultaneously reducing harmonic voltages at the point of common coupling (PCC) [14]. Such coordinated control not only enhances harmonic mitigation but also ensures that the burden of harmonic compensation is distributed fairly among all participating units. Further improvements in voltage quality have been achieved through the application of dead-time compensation techniques within pulse width modulation (PWM) schemes [15]. By integrating quasi-resonant controllers, these methods effectively address the adverse effects of PWM switching, such as waveform distortion and timing errors, leading to more precise voltage regulation. Additionally, enhancements in droop-based control strategies have been proposed for shunt-compensated GFM inverters, including the introduction of modified secondary control loops [16]. These advanced control frameworks are designed to maintain voltage and frequency stability under varying load conditions, while also preserving equitable power sharing among inverter-based resources. Collectively, these developments represent significant progress toward achieving robust, high-quality power delivery in modern microgrid and distributed generation systems.

Recent developments in T-type multilevel inverter (TMLI) design have focused on enhancing efficiency, minimizing the number of components, and effectively mitigating leakage currents. One notable advancement is the hybrid asymmetrical TMLI [17], which integrates a neutral-point clamped (NPC) converter with a cascaded H-bridge and a level-doubling network. In this configuration, the DC buses are merged through the NPC arrangement, which eliminates the need for multiple capacitors and allows the system to operate with a single DC source. This design inherently reduces leakage currents, thereby improving safety and ensuring better compliance with grid standards. An important feature of this topology is the asymmetric division of the DC voltage in a 1:5 ratio, which enables the inverter to generate a greater number of output voltage levels compared to traditional symmetric designs. This approach not only enhances the quality of the output waveform but also avoids increased switching losses, as the NPC stage is operated at the fundamental frequency rather than at higher switching frequencies. Additionally, voltage balancing is achieved cost-effectively by employing a low-rated buck-boost converter instead of a transformer, further reducing the overall system cost while maintaining reliable operation [17]. These advancements in TMLI design and control align with the parallel 2L VSI and 3L T-type inverter architecture explored in this work. The asymmetric voltage division and self-balancing mechanisms in TMLIs, for instance, report strategies for reducing harmonic distortion and enhancing voltage regulation in nanogrids. Similarly, the hybrid modulation approaches (e.g., carrier-based PWM) provide a foundation for discrete-time PR controller tuning, ensuring robust performance under nonlinear and unbalanced loads. By integrating these insights, the project advances power quality and reliability in renewable energy systems. Table 1 provides a comparative analysis of the performance parameters of the mostly used three-phase multilevel inverters which include neutral point clamped (NPC), flying capacitor (FC) and cascaded H-bridge (CHB) inverters.

Table 1. Comparison of Performance Parameters of 3-Phase Multilevel Inverter Topologies [17]

	NPC	**FC**	**CHB**
Voltage Stress	50%	50%	33
Leakage Current	600 mA	750 mA	450 mA
Efficiency	98%	97%	99%
Hardware cost	1.5x	1.7x	1.6-2x
THD	1.5-3%	1.5-3%	1-2.5%
Modulation complexity	High	Low	Lowest

While proportional-resonant (PR) controllers are widely recognized for their ability to suppress steady-state errors and harmonics in AC systems, most design and tuning methodologies for these controllers are rooted in the continuous (s-domain) framework. This traditional approach, although analytically mature, presents significant limitations when transitioning to practical digital implementations, which inherently operate in the discrete (z-domain) time domain. The discretization process introduces challenges such as computational delays, quantization effects, and altered dynamic behavior, all of which can compromise the intended performance of the controller if not properly addressed [18]. As a result, tuning algorithms developed for continuous systems often cannot be directly applied to digital platforms, necessitating specialized design techniques that account for the unique characteristics of discrete-time control.

Furthermore, most existing control strategies for islanded microgrids rely on separate compensation mechanisms to address voltage unbalance and harmonic distortion, which are typically treated as distinct problems. This fragmented approach can lead to suboptimal power quality, particularly under the influence of non-linear and unbalanced loads, which are increasingly prevalent in modern microgrid environments. Comprehensive power quality assessment methodologies have highlighted the importance of unified control schemes that can simultaneously manage multiple power quality indices, such as total harmonic distortion (THD), voltage stability, and current limits, to ensure compliance with established standards and to maintain reliable operation in case of diverse disturbances.

In response to these gaps, this project is dedicated to the development and implementation of a discrete-time PR control strategy specifically tailored for islanded AC nanogrids. The discussed approach not only addresses the intrinsic challenges of digital controller design but also integrates this discrete control with the continuous dynamics of the plant to achieve robust harmonic suppression and voltage balancing. Furthermore, the study adopts a unified control scheme capable of mitigating both voltage imbalances and harmonic distortion under non-linear and unbalanced load conditions. By systematically evaluating key power quality indicators, this research aims to demonstrate the effectiveness of the considered methodology in meeting power quality requirements and in advancing the state of the art for digital control in microgrid applications.

3 System Architecture

3.1 Power System

The AC nanogrid system considered in this work is designed to combine the strengths of both conventional and advanced inverter technologies by integrating a two-level voltage source inverter (2L VSI) in parallel with a three-level T-type inverter (3L T-type). The system architecture is illustrated in Fig. 1.

By connecting both inverters in parallel, the system leverages the economic advantages of the 2L VSI while simultaneously benefiting from the advanced features of the 3L T-type inverter. This parallel arrangement not only improves the overall reliability of the nanogrid, since either inverter can continue to operate if the other encounters a fault, but also facilitates effective sharing of load currents. This redundancy enhances system stability and ensures a more balanced and robust response to varying load conditions. Each inverter is powered by its own independent DC voltage source, providing flexibility in energy management and source integration. To further improve the output waveform and suppress high-frequency switching harmonics, both inverters are equipped with LCL filters at their AC output terminals. These filters play a crucial role in meeting grid interconnection standards and protecting sensitive loads.

The nanogrid is designed to supply a diverse range of loads, including linear, non-linear, and unbalanced types. All loads are connected at a common bus, known as the point of common coupling (PCC), where the outputs of both inverters converge. Voltage and current sensors are strategically placed at the PCC to enable continuous monitoring and assessment of power quality parameters such as total harmonic distortion (THD), voltage stability, and current sharing between the inverters. This architecture not only enables the study of individual inverter performance but also provides a comprehensive platform for evaluating how the combined system manages voltage imbalances, harmonic suppression, and dynamic load sharing under a variety of operating conditions. The flexibility and redundancy inherent in this design make it well-suited for modern nanogrid applications, where reliability and high power quality are of importance.

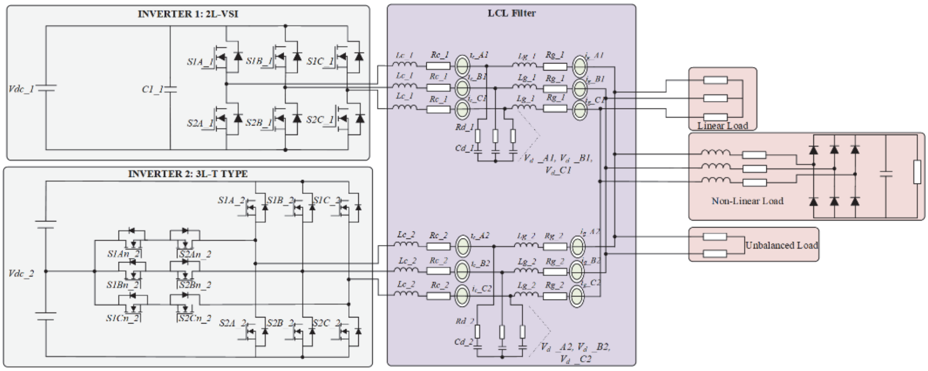

Fig. 1. Structure of the considered ac nanogrid.

3.2 Control System

The control architecture of the AC nanogrid, illustrated in Fig. 2, employs a decentralized strategy to regulate voltage, frequency, and power sharing between the parallel 2L VSI and 3L T-type inverters. The system relies on primary droop control without secondary control layers, simplifying implementation by using local measurements and eliminating communication dependencies.

3.2.1 Droop Control

The droop control method adjusts the inverter's output frequency ω and voltage magnitude V based on active P and reactive Q power measurements. This mimics the behavior of synchronous generators, enabling autonomous power sharing without inter-inverter communication [19]. The governing equations are:

$$\omega = \omega^* - m_p(P - P^*) \qquad \textbf{(1)}$$

$$V = V^* - m_q(Q - Q^*) \qquad \textbf{(2)}$$

Here, ω* and V* are the rated frequency and voltage, while P* and Q* are the reference active and reactive power values. The droop coefficients mp and mq are calculated as:

$$m_p = \frac{\Delta\omega}{P_{\max}} \qquad \textbf{(3)}$$

$$m_q = \frac{\Delta V}{Q_{\max}} \qquad \textbf{(4)}$$

where Pmax and Qmax represent the maximum deliverable power, and Δω and ΔV denote allowable deviations. Compliance with the EN 50160 standard ensures frequency deviations remain within ±2% and voltage deviations within ±10% of rated values [19].

3.2.2 Virtual Impedance Loop

A virtual impedance loop modifies the inverter's output impedance to improve power-sharing accuracy and mitigate circulating currents [20]. By introducing resistance Rv and inductance Lv, the loop decouples power dynamics from physical line impedances. The αβ frame voltage references are adjusted as:

$$\begin{aligned} v_\alpha &= R_v \cdot i_{g\alpha} - \omega L_v \cdot i_{g\beta} \\ v_\beta &= R_v \cdot i_{g\beta} + \omega L_v \cdot i_{g\alpha} \end{aligned} \quad \textbf{(5)}$$

Here, $v_{\alpha\beta}$, $i_{g\alpha\beta}$ are the voltage and output current in the stationary reference frame. This adjustment ensures proportional load sharing and stabilizes the system under identical line conditions.

3.2.3 Proportional-Resonant(PR) Controller

PR controllers regulate voltage and current by providing high gain at the fundamental frequency, effectively suppressing steady-state errors and harmonics [21]. The transfer function is:

$$G_c^{PR}(s) = K_p + K_r \frac{s}{s^2+\omega^2} \quad \textbf{(6)}$$

where Kp (proportional gain) ensures fast transient response, and Kr (resonant gain) eliminates steady-state errors at the target frequency. The resonant term $\frac{s}{s^2+\omega^2}$ creates an infinite gain at ω enhancing harmonic rejection.

3.2.4 Space Vector Pulse-Width Modulation

The SVPWM technique generates gate signals for the inverter switches using reference voltages from the PR controllers. This method optimizes switching sequences to minimize harmonic distortion and maximize DC-link utilization [22]. Each inverter operates under an independent SVPWM scheme, ensuring synchronized yet autonomous operation.

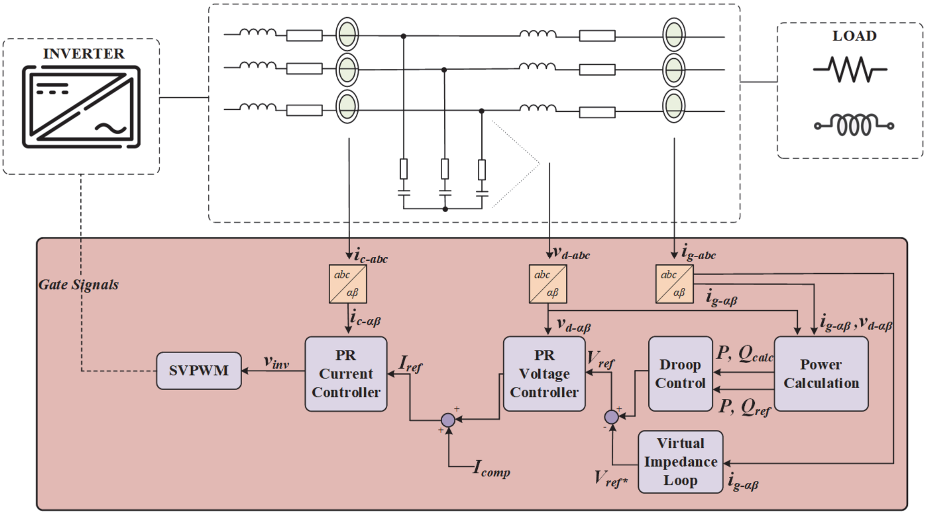

Fig. 2. Control scheme of the considered ac nanogrid.

4 Control Strategies

This section includes the different control strategies employed in order to assess the nanogrid system performance.

4.1 Control System Tuning

4.1.1 Model Description

Developing an accurate mathematical model of the inverter system is a foundational step for designing and tuning its control algorithms. Analytical modeling enables a deeper understanding of how various system parameters influence stability and dynamic performance, which is essential before any control strategy is implemented. In this work, the tuning of the proportional-resonant (PR) controllers for both voltage and current regulation is based on the methodology presented in [23]. The inverter system is equipped with an LCL filter, as shown in Fig. 1, which serves to attenuate high-frequency switching harmonics and improve the quality of the output waveform. To properly characterize the behavior of the system, Kirchhoff's laws are applied to the LCL filter circuit, resulting in a block diagram that captures the dynamic relationships among the inverter, filter components, and the grid interface. This block diagram, illustrated in Fig. 3, forms the basis for deriving the system's transfer functions.

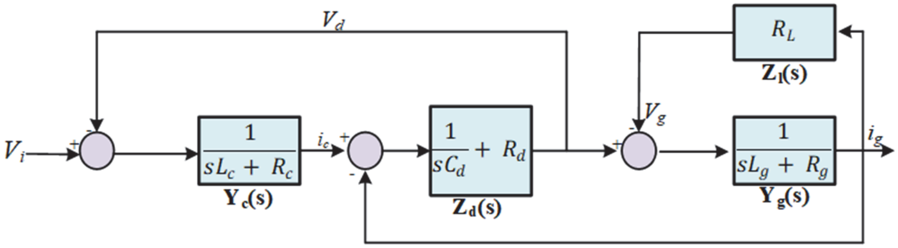

Fig. 3. Block diagram of LCL filter.

Using the principles of block diagram manipulation and Mason's Gain formula, the transfer functions that describe the cascaded control structure are systematically obtained. The first transfer function, $G_p^i(s)$, represents the relationship between the inverter's reference voltage input and the resulting filter current. The second, $G_p^v(s)$, relates the inverter's input to the output voltage across the filter. These transfer functions are mathematically expressed as follows:

$$G_p^i(s) = \frac{i_c(s)}{V_i(s)} \quad \textbf{(7)}$$

$$G_p^i(s) = \frac{Y_c(s)\left[1+Y_g(s)Z_d(s)+Y_g(s)Z_l(s)\right]}{1+Y_g(s)Z_d(s)+Y_g(s)Z_l(s)+Y_c(s)Z_d(s)\left[1+Y_g(s)Z_l(s)\right]} \textbf{(8)}$$

$$G_p^v(s) = \frac{Z_d(s)\left[1+Y_g(s)Z_l(s)\right]}{1+Y_g(s)Z_d(s)+Y_g(s)Z_l(s)+Y_c(s)Z_d(s)\left[1+Y_g(s)Z_l(s)\right]} \textbf{(9)}$$

Here, the terms $Y_c(s)$, $Y_g(s)$, $Z_d(s)$ and $Z_l(s)$ represent the admittances and impedances of the various branches within the LCL filter network. These transfer functions provide a detailed mathematical framework for analyzing the closed-loop performance of the cascaded voltage and current control loops.

To further assess the effectiveness of the controller design, a digital pre-filter, denoted as F(z), is incorporated into the simulation and implementation process. This pre-filter is designed to shape the system's response to a unit step input, effectively transforming it into a sinusoidal reference signal. Such a filter is essential for evaluating how well the controller can track sinusoidal commands, which is a critical requirement in AC power systems. The pre-filter is mathematically defined as:

$$F(z) = \left(\frac{(z-1)}{z}\right)\left(\frac{\sin(\omega_0 T_S)}{z^2-2\cos(\omega_0 T_S)z+1}\right) \quad \textbf{(10)}$$

In this expression, ω_0 denotes the fundamental angular frequency of the AC waveform, and T_s is the sampling interval used in the digital controller. The choice of sampling time T_s is a key design decision, as it must be short enough to ensure accurate digital representation and timely control action, while still being compatible with the computational capabilities of the controller hardware. Selecting an appropriate sampling period is thus vital for achieving both precise control and reliable real-time operation.

4.1.2 Controller Design

The process of designing and tuning the control system is centered around meeting specific dynamic performance targets, such as minimizing settling time and overshoot, while ensuring robust stability for the inverter system operating with a LCL filter and load. To achieve these objectives, the SISOTOOL environment in MATLAB was used for both the 2L VSI and 3L T-type inverter systems. SISOTOOL was chosen for its powerful visualization capabilities, which allow for real-time assessment of design criteria and comprehensive stability analysis throughout the controller development process.

A key focus of this work is the implementation and fine-tuning of the inner control loops in the discrete time domain, aligning with the requirements of modern embedded digital controllers. For this reason, the proportional-resonant (PR) controller transfer function has been discretized using the Tustin method with pre-warping [23]. This discretization technique was selected because it preserves the essential frequency response characteristics of the original continuous-time controller, making it particularly effective for digital implementations of resonant controllers where accurate frequency tracking and stability are paramount. The resulting discrete-time transfer function for the PR controller system shown in (7) is expressed as:

$$G_C^{PR}(z) = K_p + K_r \left(\frac{\sin(w_o T_s)}{2w_o}\right)\left(\frac{(z^2-z)}{(z^2-2\cos(w_o T_s)z+1)}\right) \quad \textbf{(11)}$$

The overall block diagram for the PR controller design, shown in Fig. 4, incorporates the transfer functions for both the controllers and the LCL filter, providing a comprehensive view of the control structure.

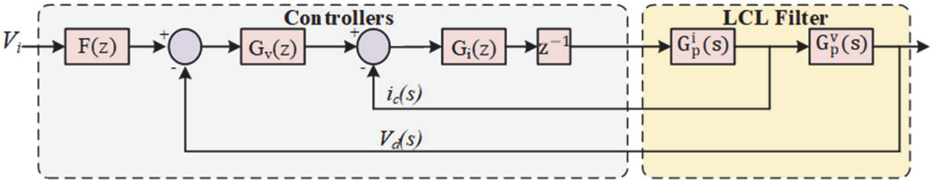

Fig. 4. PR controller + plant block diagram used for controller design.

To accurately represent the plant dynamics in the digital domain, the transfer functions for the current and voltage loops, as previously derived, were discretized using the First Order Hold (FOH) method. This ensures that the digital control system closely mirrors the behavior of the actual physical system.

4.1.3 Tuning of PR Current Controller

The tuning process for the PR current controller consists of defining target performance metrics, including settling time, rise time, and allowable overshoot. Within the SISOTOOL environment, the PR current controller was integrated into a single-loop control architecture. The discrete-time transfer function of the PR controller $G_C^{PR}(z)$ was paired with the discretized plant model and a pre-filter F(z) was included to facilitate sinusoidal step response testing.

The design and tuning algorithm implemented in SISOTOOL for the PR current controller is explained in detail:

1. The initial step involved defining the performance criteria for the inner current control loop, specifically targeting parameters such as settling time, rise time, and permissible overshoot.

2. Using SISOTOOL's control system designer, a single-loop control configuration was established. In this setup, the discrete-time transfer function of the PR current controller, $G_C^{PR}(z)$, was assigned as the controller, while the plant was represented by the discretized transfer function $G_p^i(z)$ of the LCL filter. The pre-filter, F(z), was also incorporated to enable testing with a sinusoidal step input.

3. The tuning process proceeded by first selecting the resonant gain, K_r, and then systematically adjusting the proportional gain, K_p, until the resulting sinusoidal response satisfied the specified dynamic performance requirements.

Tuning involved first selecting the resonant gain K_r and then incrementally adjusting the proportional gain K_p until the desired system response was achieved. The final controller gains were determined to be K_{pi}=20 and K_{ri}=15000, which satisfied the design criteria of a settling time under 0.1 seconds, a rise time below 0.05 seconds, and an overshoot less than 10%. The effectiveness of the current controller is demonstrated in Fig. 5, which shows a rapid and stable response to a step change in reference current.

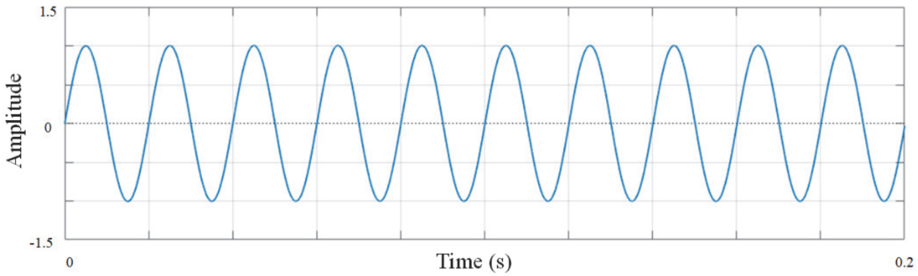

Fig. 5. PR current controller step response.

4.1.4 Tuning of PR Voltage Controller

The design and tuning algorithm implemented in SISOTOOL for the outer PR voltage control loop is explained in detail:

1. The initial step involved the establishment of the desired performance criteria for the voltage control loop, focusing on parameters such as settling time, rise time, and allowable overshoot.
2. In SISOTOOL's control system designer, a cascaded control structure was configured. This setup incorporated the discrete-time transfer functions of both the PR voltage controller, $G_V^{PR}(z)$, and the previously tuned PR current controller, alongside the plant models $G_p^i(z)$ and $G_p^v(z)$ representing the respective LCL filter dynamics. The pre-filter, F(z), was also included to facilitate sinusoidal step response testing.
3. The tuning procedure involved first selecting the resonant gain, K_r, and then incrementally adjusting the proportional gain, K_p, until the voltage controller produced a sinusoidal response that met the specified dynamic performance targets.

The tuning approach mirrored that of the current controller: the resonant gain K_r was fixed, and the proportional gain K_p was varied to achieve the optimal response. The finalized gains for the voltage controller were K_{pv}=0.025 and K_{rv}=50. These values reflect the need for the current loop to respond more rapidly than the voltage loop, as accurate current tracking is essential for maintaining overall system stability. Fig. 6 illustrates the step response of the voltage controller, confirming its ability to quickly stabilize the output voltage within the specified performance limits.

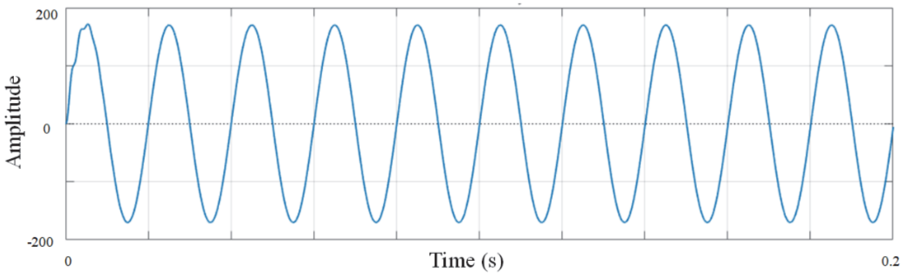

Fig. 6. PR voltage controller step response.

4.1.5 Stability Analysis

To ensure the designed controllers would provide stable operation under all expected conditions, both Bode and Nyquist plots were generated using the finalized controller parameters. The Bode plot, presented in Fig. 7, reveals a pronounced gain peak at the resonant frequency (50 Hz or 314 rad/s), indicating the controller's strong tracking capability at this frequency. The phase margin, which exceeds 45 degrees, confirms that the system maintains a buffer against instability.

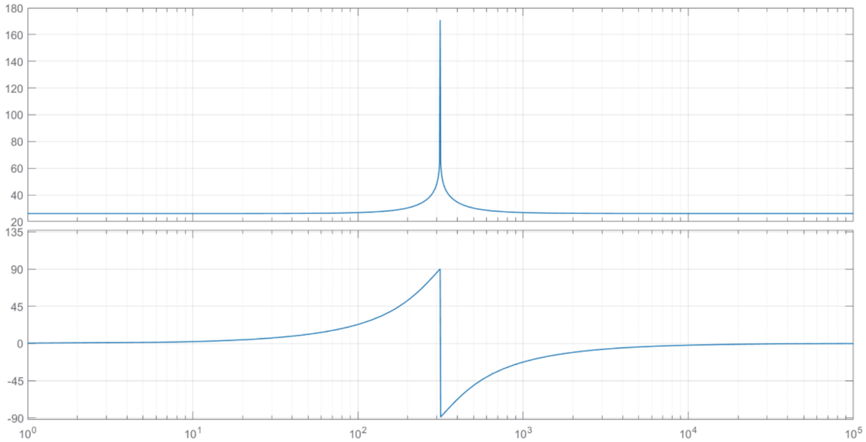

Fig. 7. Bode Plot for the cascaded control system.

The Nyquist plot, shown in Fig. 8, further validates stability by demonstrating that the system’s frequency response does not encircle the critical point (-1, 0), a key criterion for closed-loop stability. Together, this analysis confirmed that the controller design is robust and well-suited to the demands of the parallel inverter nanogrid system.

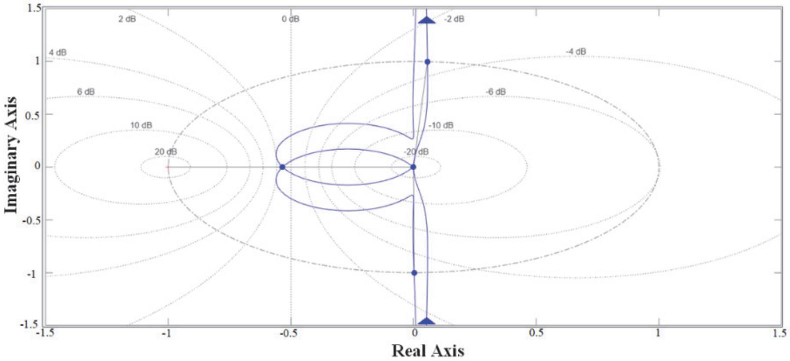

Fig. 8. Nyquist Diagram for the cascaded control system.

Tables 2 and 3 summarize the final tuning results for the PR current and voltage controllers respectively, providing a clear reference for implementation and further analysis.

Table 2. Tuning results for PR Current Controller

Proportional Gain	20
Resonant Gain	15000
Gain Margin	31.6 dB
Gain Margin frequency	1.57 x10^5 rad/s
Phase Margin	88.4 degrees
Phase Margin frequency	1.43 x10^5 rad/s

Table 3. Tuning results for PR Voltage Controller

Proportional Gain	0.025
Resonant Gain	50
Gain Margin	6.83 dB
Gain Margin frequency	2.11 x10^3 rad/s
Phase Margin	10.9 degrees
Phase Margin frequency	3.13 x10^3 rad/s

4.2 Power Quality Analysis

This section investigates how different types of loads affect the performance of the AC nanogrid, with a particular focus on enhancing power quality through targeted harmonic compensation a nd balanced power sharing. The analysis is based on a control strategy designed to dynamically adjust the inverter output [24], thereby reducing voltage harmonics and correcting imbalances that arise from non-linear and unbalanced loads. The objective is to maintain a stable and reliable voltage profile across the nanogrid, ensuring efficient operation even under challenging load conditions.

A key aspect of this approach is the selective compensation of voltage harmonics and negative sequence components. The control system is specifically configured to counteract voltage imbalances and suppress harmonics of the -5th, 7th, -11th, and 13th orders, which are commonly introduced by non-linear devices and asymmetrical loading. To achieve this, the system computes a compensation current, denoted as I_{comp} , which is injected to offset both the undesired harmonic content and the negative sequence components present in the voltage waveform. Fig. 9 presents a block diagram of the power quality control scheme, illustrating how the compensation current is generated. In this diagram, k_G represents the compensation gain, while G is the conductance used in the compensation process.

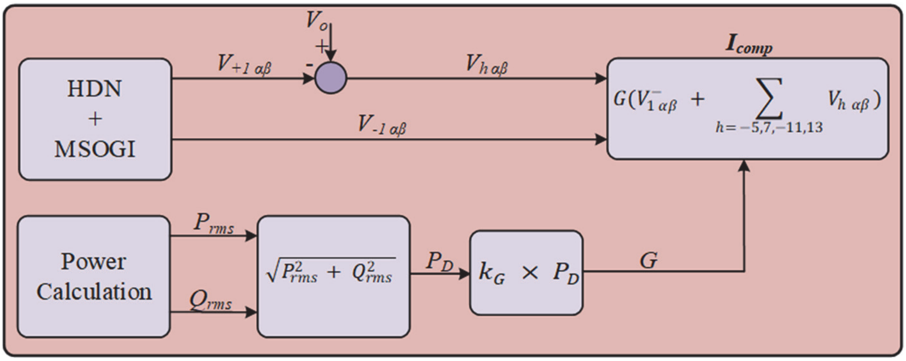

Fig. 9. Block diagram of power quality control scheme for generation of compensation current.

To effectively address voltage unbalance, the control algorithm first isolates the negative sequence component of the voltage. This process involves extracting both harmonic and negative sequence elements from the measured voltage and current signals. The extraction is accomplished using a Harmonic Decoupling Network (HDN) in combination with Multiple Second Order Generalized Integrators (MSOGI), as depicted in Fig. 10. The HDN and MSOGI modules work together in a feedback arrangement to separate the fundamental frequency component as well as the positive and negative sequence harmonics from the original waveform. Following this, a Positive and Negative Sequence Calculation (PNSC) step determines the respective sequence components from the filtered data.

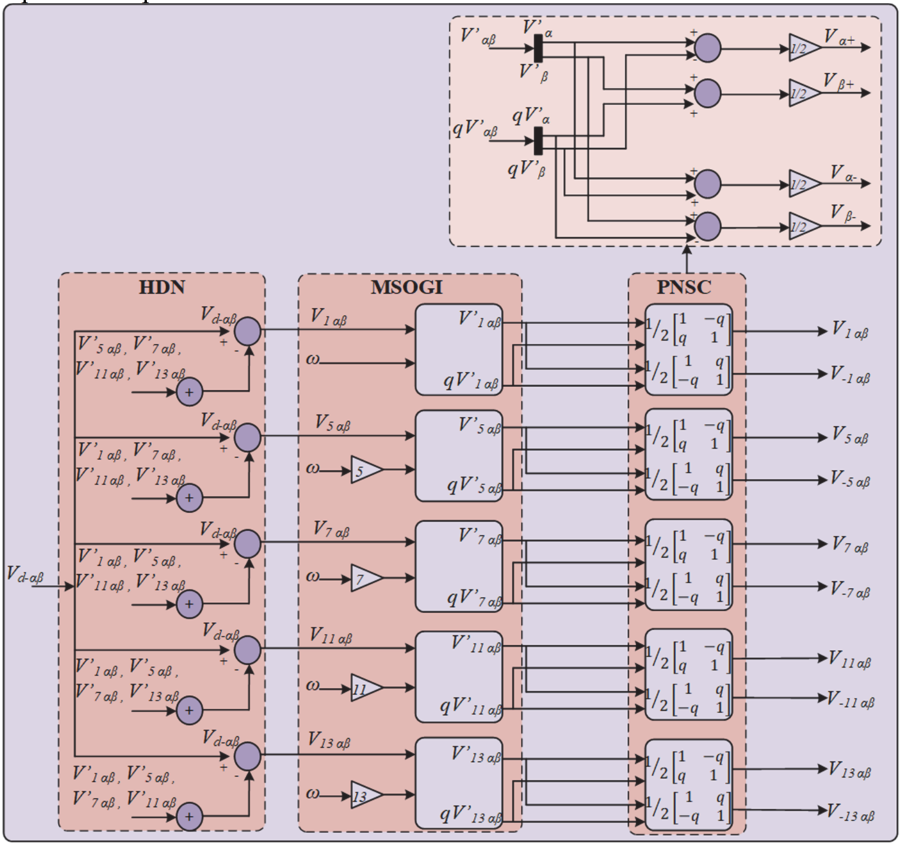

Fig. 10. HDN+MSOGI structure for fundamental and harmonic extraction.

The compensation process begins by calculating the root mean square (RMS) values of the active and reactive power. These are obtained by subtracting the calculated values from the instantaneous measurements:

$$P_{rms} = P_{inst} - P_{calc} \quad \textbf{(12)}$$

$$Q_{rms} = Q_{inst} - Q_{calc} \quad \textbf{(13)}$$

where P_{rms} and Q_{rms} are the RMS values of active and reactive power, P_{inst} and Q_{inst} are the instantaneous powers, and P_{calc} and Q_{calc} are the calculated reference values. Next, the total power distortion, P_D, is determined using the following relationship:

$$P_D = \sqrt{P_{rms}^2 + Q_{rms}^2} \quad \textbf{(14)}$$

This measure quantifies the combined effect of active and reactive power distortions due to harmonics and imbalances. The conductance G used in the compensation algorithm is then calculated as:

$$G = k_G \times P_D \quad \textbf{(15)}$$

Here, k_G is a tunable gain factor that dictates the strength of the compensation. Finally, the compensation current I_{comp} is computed to target both the negative sequence of the fundamental voltage and the specified harmonic orders:

$$I_{comp} = G\left(V_{(1\alpha\beta)}^{-} + \sum\nolimits_{h=-5,7,-11,13} V_{(h\alpha\beta)}\right) \quad \textbf{(16)}$$

In this equation, $V_{(1\alpha\beta)}^{-}$ denotes the negative sequence component of the fundamental voltage, and $V_{(h\alpha\beta)}$ represents the voltage harmonics for the specified orders h. The calculated compensation current is then compared with both the reference and actual output currents of the inverter. This comparison allows the control system to inject the appropriate current to correct the voltage waveform, thereby improving power quality by reducing both harmonics and voltage imbalance.

5 Simulation Results and Analysis

This section discusses the implementation of the control strategies previously mentioned and their simulation results in detail.

5.1 Performance of Discretized PR Voltage and Current Controllers

5.1.1 Simulation Results

In order to evaluate the effectiveness of the designed proportional-resonant (PR) controllers, a comprehensive simulation study was conducted using the PLECS platform. The modeled system consisted of a parallel configuration of a two-level voltage source inverter (2L VSI) and a three-level T-type inverter, both operating under identical system parameters and control gains. This setup ensured a fair comparison and allowed for a unified assessment of the controllers' performance across both inverter types. The PR controllers were implemented in the discrete domain to accurately reflect the behavior of digital controllers in practical embedded systems. All simulation parameters, including filter values, controller gains, and load characteristics, are detailed in Table 4.

Table 4. Nominal values of AC nanogrid components

Description	Symbol	Value
DC voltage	V_{dc}	725 V
System frequency	f	50 Hz
Switching frequency	f_s	50 kHz
LCL Filter inductance	L_c, L_g	1 mH
LCL Filter resistance	R_c, R_g	$0.4\,\Omega$
LCL Filter capacitance	C_d	$100\,\mu F$
Damping resistance	R_d	$3.3\,\Omega$
Resistive load (linear load)	R_{linear}	$20\,\Omega$
Resistive load (non-linear load)	$R_{non-linear}$	$349\,\Omega$
Rectifier output capacitor	$C_{non-linear}$	$1\,mF$
Resistive load (2-phase unbalanced load)	$R_{unbalanced}$	$175\,\Omega, 175\,\Omega$
PR voltage controller proportional gain	K_{pv}	0.025
PR voltage controller resonant gain	K_{rv}	50
PR current controller proportional gain	K_{pi}	20
PR current controller resonant gain	K_{ri}	15000
Reference active power rating	P_{ref}	5 kW
Reference reactive power rating	Q_{ref}	1.5 kVAR
Compensation Gain	k_G	0.00045

The dynamic response of the PR voltage controller is presented in Fig. 11. In all tested scenarios, the output voltage closely tracks the reference signal, with the error signal remaining negligible throughout the simulation. This precise tracking is maintained even as the system is subjected to varying load conditions and the introduction of compensation currents. The controller's ability to maintain such a minimal error demonstrates its effectiveness in regulating the output voltage, thereby ensuring stability and reliability in the nanogrid.

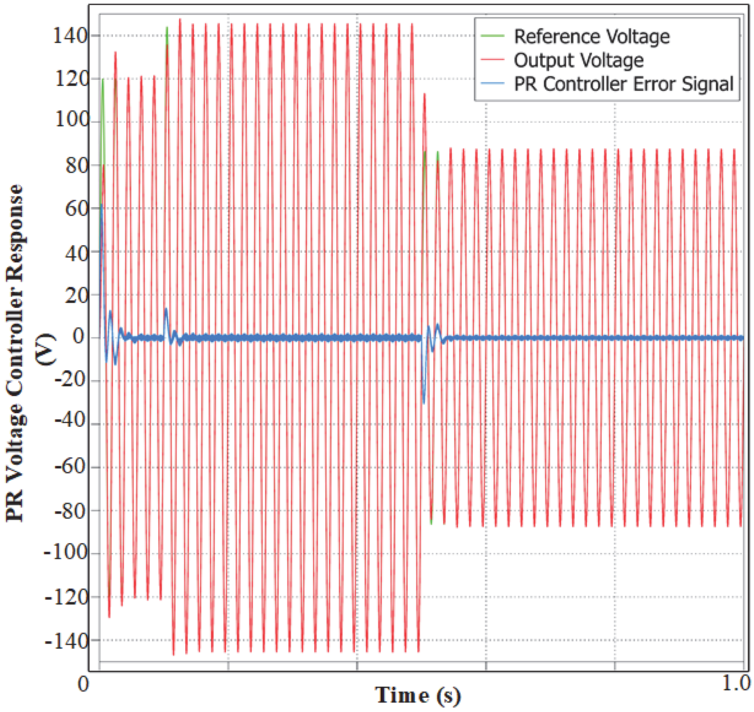

Fig. 11. PR voltage controller response of ac nanogrid.

Similarly, the performance of the PR current controller is illustrated in Fig. 12. The measured output current aligns almost perfectly with the reference current, as indicated by the near-zero error. This high degree of accuracy is preserved across different case studies, including sudden changes in load demand and the activation of compensation currents. The rapid and precise response of the current controller is crucial for minimizing current distortion and supporting the overall power quality of the system.

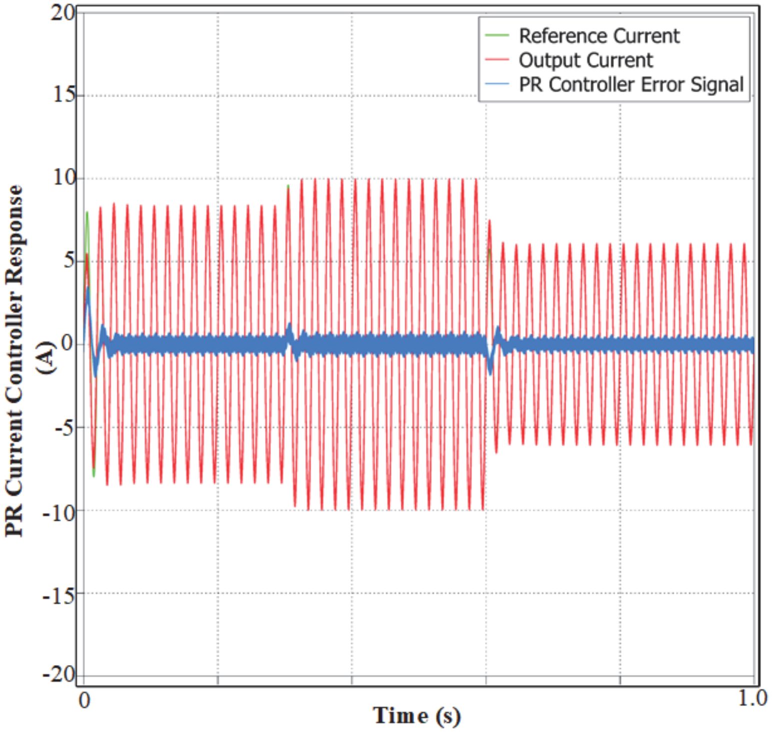

Fig. 12. PR current controller response of ac nanogrid.

5.1.2 Analysis

The simulation findings reveal that both the PR voltage and current controllers deliver robust and stable operation for the parallel inverter system. The voltage controller's ability to maintain a consistent output, regardless of fluctuations in load or the presence of compensation currents, signifies its robustness and adaptability. This stability is particularly important for applications where voltage quality directly impacts the performance of connected loads.

The current controller's swift response to changes in current demand ensures that the system can quickly adjust to dynamic conditions, minimizing the risk of overcurrent situations or excessive harmonic distortion. Its capacity to maintain a low steady-state error and effectively reject disturbances further highlights the controller's suitability for real-world nanogrid applications. Collectively, these results demonstrate that the discrete-domain PR controllers are highly effective in achieving the dual objectives of voltage regulation and current control, even in the presence of system disturbances and non-linearities.

5.2 Selective Harmonic Compensation and Power Sharing

5.2.1 Simulation Results

To further enhance power quality, a selective harmonic compensation strategy was integrated into the control system. This approach was designed to specifically target and mitigate voltage harmonics and negative sequence components, which are common in nanogrids with non-linear and unbalanced loads.

The power quality control scheme was implemented in the simulation, and the system was tested under a range of load conditions. At 0.75 seconds, a compensation current was activated with the goal of suppressing harmonics of the 5th, 7th, 11th, and 13th orders, as well as negative sequence voltage components. Fig. 13 and Fig. 14 show the extracted harmonic voltages for both inverters, represented in the αβ domain. Prior to compensation, significant harmonic content is evident at the targeted orders, indicating notable voltage distortion. Upon activation of the compensation current, these harmonic components are significantly reduced, resulting in a much cleaner and more sinusoidal voltage waveform.

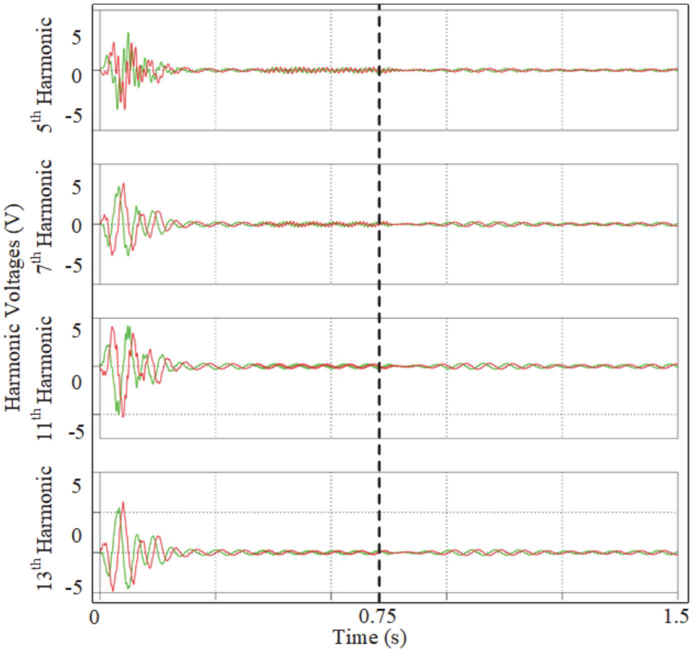

Fig. 13. Harmonic voltages - 2L VSI.

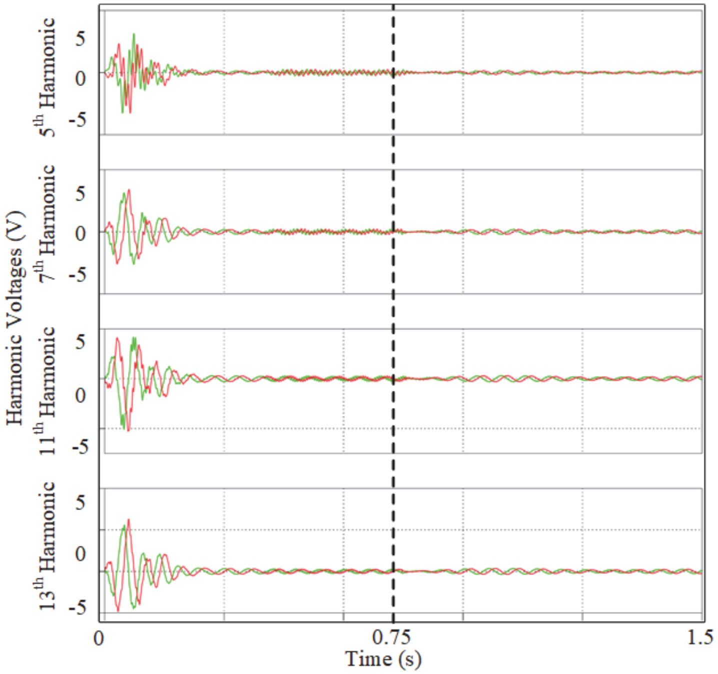

Fig. 14. Harmonic voltages - 3L T-type.

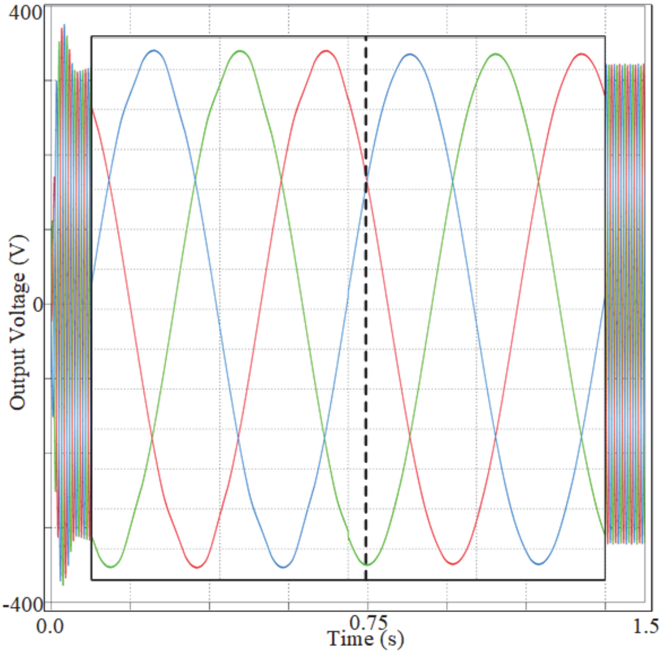

Fig. 15. Output voltage of ac nanogrid system.

Fig. 15 illustrates the voltage output at the filter terminals for both inverters, highlighting the improvement in waveform quality following compensation. The system demonstrates a stable and high-quality voltage profile, even as load conditions vary. The effectiveness of the control strategy in achieving balanced power sharing is demonstrated in Fig. 16. Here, both the 2L VSI and 3L T-type inverter contribute equally to meeting a combined load demand of approximately 5 kW. This balanced distribution of power is essential for preventing individual inverter overload and ensuring the efficient utilization of system resources.

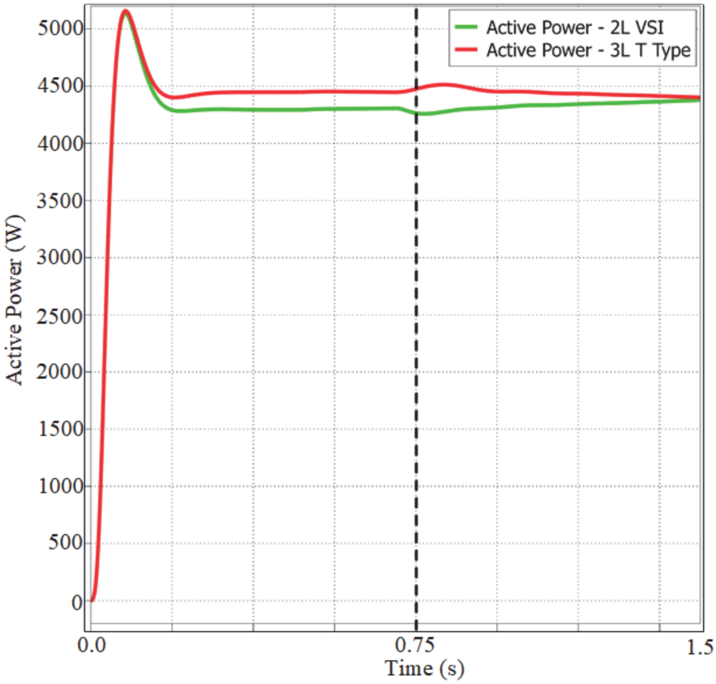

Fig. 16. Power sharing performance by both inverters in nanogrid.

A detailed harmonic analysis was also performed on the output voltage and current. Fig. 17 and Fig. 18 present the Fourier spectra before and after compensation, respectively. Initially, the output voltage spectrum reveals prominent harmonic peaks at integral multiples of the fundamental frequency, reflecting significant distortion. After compensation, these peaks are substantially diminished, confirming the efficacy of the harmonic mitigation scheme.

5.2.2 Analysis

The simulation results provide strong evidence for the effectiveness of the selective harmonic compensation strategy. The marked reduction in harmonic voltages after the introduction of compensation current is critical for maintaining a stable and sinusoidal output voltage, which is vital for the operation of sensitive electronic equipment and for compliance with power quality standards.

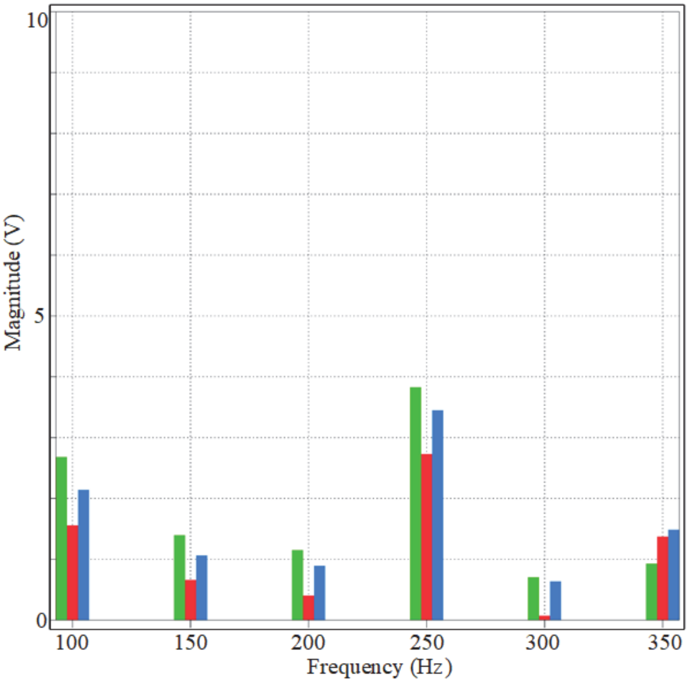

Fig. 17. Fourier spectrum of the output voltage before compensation.

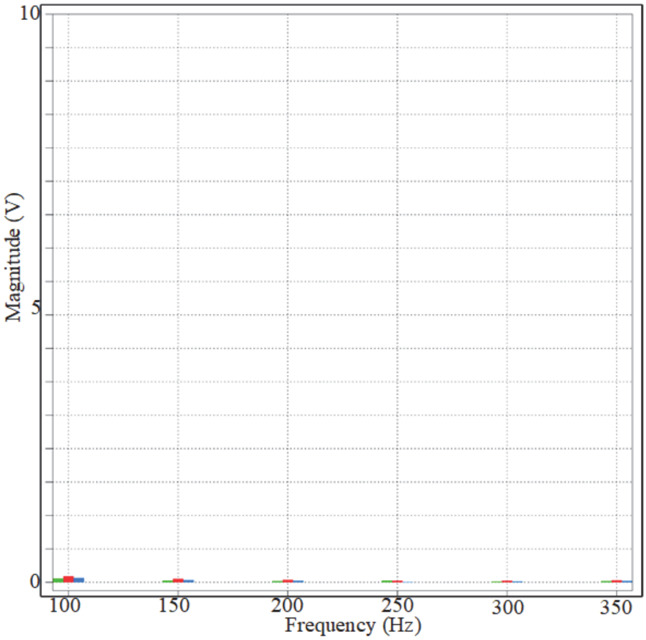

Fig. 18. Fourier spectrum of the output voltage after compensation.

The balanced sharing of load between the two inverter systems not only enhances overall system efficiency but also contributes to operational reliability, particularly during periods of fluctuating demand. This collaborative power-sharing capability is a direct result of the robust control scheme and the precise tuning of the PR controllers. The performance of the system was also benchmarked against major international standards for power quality, including IEEE 519, EN 50160, and IEC 61000-2-2/12. Table 5 summarizes the voltage distortion limits for Total Harmonic Distortion (THD) and odd harmonics in public Low Voltage (LV) and Medium Voltage (MV) networks, as specified by major international standards including IEEE 519, EN 50160, and IEC 61000-2-2/12 [25]. Tables 6 and 7 summarize the measured total harmonic distortion (THD) values for both voltage and current, as well as the individual harmonic components. To ensure the robustness of the control strategy under practical conditions, the simulation included a “worst-case" grid scenario with high line impedance, simulating weak or heavily loaded distribution networks. Despite these challenging conditions, the nanogrid maintained compliance with all relevant power quality standards, highlighting the resilience and adaptability of the proposed approach. Before compensation, the voltage THD was measured at 10.25%, exceeding the limits set by the standards for both low and medium voltage networks. After compensation, the THD was reduced to 7%, bringing the system into compliance with EN 50160 and IEC standards. Similarly, the current THD dropped from 10.8% to 3.6%, ensuring compliance with IEEE 519 requirements. The reduction in individual harmonic components, especially for the 3rd and 5th orders, further demonstrates the effectiveness of the compensation scheme.

Table 5. Voltage distortion limits for THD and odd harmonics in public LV and MV networks. [25]

h^1	**IEEE 519 LV**	**IEEE 519 MV**	**EN 50160 LV,MV**	**IEC 61000-2-2/12 LV,MV**
3	5	3	5	5
5	5	3	6	6
7	5	3	5	5
9	5	3	1.5	1.5
11	5	3	3.5	3.5
13	5	3	3	3
15	5	3	0.5	0.4
17	5	3	2	2
19	5	3	1.5	1.76
21	5	3	0.5	0.3
23	5	3	1.5	1.41
25	5	3	1.5	1.27
27—49	3	3	-	2.27(17/h)-0.27
THDv	8	5	8	8

Table 6. THD of output voltage and harmonic components in ac nanogrid system.

Harmonic Order	without I_{comp} (%)	with I_{comp} (%)
3	5	4.3
5	6	3.75
7	3.5	3.12
11	3	2.5
THDv	10.25	7

Table 7. THD of output current and harmonic components in ac nanogrid system.

Harmonic Order	without I_{comp} (%)	with I_{comp} (%)
3	9.3	3.33
5	5.3	1.33
7	1	0.26
11	0.53	0.06
THDi	10.8	3.6

5.2.3 Summary and Implications

In summary, the comprehensive simulation study demonstrates that the integrated control strategies, including discrete-time PR voltage and current controllers, combined with selective harmonic compensation substantially improve the performance of the AC nanogrid system. The controllers ensure precise voltage and current regulation, significantly reduce harmonic distortion, and enable efficient and balanced power sharing between parallel inverters.

The system's ability to maintain low THD and comply with international standards, even under adverse grid conditions, signifies the practical viability of the proposed approach for deployment in modern nanogrid and microgrid environments. The improvements in voltage and current quality, harmonic suppression, and load distribution collectively contribute to a more reliable, efficient, and resilient power system. These findings highlight the potential of advanced control and compensation strategies for optimizing power quality and operational stability in distributed energy systems, paving the way for their application in future smart grid and renewable energy networks.

6 Advancing Green Energy Transition: Practical Applications and Implications

The findings of this study hold significant potential to accelerate the global shift toward renewable energy by addressing critical challenges in grid stability, power quality, and decentralized energy management. Below are key applications of these control strategies and nanogrid architecture in real-world green energy systems:

6.1 Integration of Renewable Energy Sources

The discretized PR controllers and harmonic compensation schemes ensure stable voltage and current regulation, even when integrating intermittent renewable sources like solar and wind. By mitigating harmonic distortion and voltage imbalances, the system can accommodate higher shares of renewables without compromising grid reliability.

6.2 Localized Energy Generation

The parallel inverter architecture, with its robust power-sharing capabilities, allows for the deployment of hybrid systems combining cost-effective 2L VSI and high-efficiency 3L T-type inverters. This flexibility enables localized energy generation, storage, and consumption which are the key pillars of the green transition.

6.3 Reduction of Energy Waste

The harmonic suppression and voltage balancing achieved by the control scheme minimizes energy losses caused by distorted waveforms. In industrial settings, where non-linear loads like variable-speed drives are prevalent, this technology can reduce operational costs and carbon footprints by improving energy efficiency.

6.4 Enhancement of Grid Resilience

The system's ability to maintain stability under unbalanced and non-linear loads makes makes it integral for the provision of uninterrupted clean energy to critical infrastructure.

6.5 Compliance with Green Energy Standards

By adhering to international power quality standards (IEEE 519, EN 50160), the proposed system simplifies regulatory compliance for renewable energy projects in the future. This reduces barriers to grid interconnection for solar farms, wind parks, and community-owned energy systems, fostering faster adoption of green technologies.

6.6 Integration with Smart Grids and Electric Vehicles

The precise control of voltage and current harmonics ensures compatibility with smart grid technologies and EV charging stations, which are sensitive to power quality fluctuations. This paves the way for scalable EV adoption and bidirectional energy flow in vehicle-to-grid (V2G) systems, further decarbonizing transportation.

7 Conclusions

This work has presented a comprehensive control strategy for an AC nanogrid system featuring the parallel operation of a two-level voltage source inverter and a three-level T-type inverter. Through detailed simulation studies, the proposed approach centered on the discrete-time tuning of outer voltage and inner current proportional-resonant (PR) controllers has been validated for its ability to deliver stable voltage regulation, effective power sharing, and substantial reductions in harmonic distortion.

The results demonstrate that the PR controllers enable both inverters to closely track their reference signals, resulting in minimal steady-state error and robust dynamic performance under a variety of load conditions. The selective harmonic compensation scheme further enhances power quality by efficiently mitigating voltage and current harmonics, as well as addressing voltage unbalance. Notably, the system achieves significant improvements in total harmonic distortion and maintains compliance with international power quality standards, even when subjected to challenging grid scenarios. Furthermore, the ability of the two inverter systems to share power equitably while maintaining a stable output highlights the reliability and flexibility of the proposed control architecture. These findings collectively highlight the scheme's potential for advancing the performance, efficiency, and resilience of AC nanogrid systems, making it a strong choice for deployment in modern distributed energy environments.

Looking ahead, future work will focus on the experimental validation of the proposed control and power quality schemes. By implementing the tuned PR controllers and compensation strategies in a physical AC nanogrid system, further insights will be gained into their real-world effectiveness in mitigating voltage unbalance, suppressing harmonic distortions, and supporting reliable power sharing. This next phase will provide a comprehensive assessment of the approach's practicality and pave the way for its integration into future smart grid and microgrid applications.

Acknowledgments. This project has received funding from the European Union's Horizon 2020 research and innovation programme under the Marie Skłodowska-Curie grant agreement No 955614.

References

1. M. Stecca, L. R. Elizondo, T. B. Soeiro, P. Bauer, and P. Palensky, "A comprehensive review of the integration of battery energy storage systems into distribution networks," IEEE Open Journal of the Industrial Electronics Society, vol. 1. Institute of Electrical; Electronics Engineers Inc., pp. 46–65, 2020. doi: 10.1109/OJIES.2020.2981832.
2. R. Jain, "Efficiency comparison between two-level and t-type inverter for 800 v automotive application," 2022.
3. F. Sadeque, D. Sharma, and B. Mirafzal, "Multiple grid-forming inverters in black-start: The challenges," in 2021 IEEE 22nd workshop on control and modelling of power

electronics, COMPEL 2021, Institute of Electrical; Electronics Engineers Inc., 2021. doi: 10.1109/COMPEL52922.2021.9645936.

4. B. Wei, J. M. Guerrero, J. C. Vásquez, and X. Guo, "A circulating-current suppression method for parallel-connected voltage-source inverters with common DC and AC buses," IEEE Transactions on Industry Applications, vol. 53, pp. 3758–3769, July 2017, doi: 10.1109/TIA.2017.2681620.
5. T. Meng, W. Zhang, J. Yu, Y. Xu, and Z. Cai, "Distributed frequency control of heterogeneous resources-powered islanded microgrid with enhanced economic operation," doi: 10.17775/CSEEJPES.2021.04980.
6. R. Rosso, X. Wang, M. Liserre, X. Lu, and S. Engelken, "Grid-forming converters: Control approaches, grid-synchronization, and future trends - a review," IEEE Open Journal of Industry Applications, vol. 2. Institute of Electrical; Electronics Engineers Inc., pp. 93–109, 2021. doi: 10.1109/OJIA.2021.3074028.
7. S. Munawar, M. S. Iqbal, M. Adnan, M. A. Akbar, and A. Bermak, "Multilevel inverters design, topologies, and applications: Research issues, current, and future directions," IEEE Access, 2024, doi: 10.1109/ACCESS.2024.3472752.
8. A. Camacho, M. Castilla, J. Miret, L. G. de Vicuna, and G. L. M. Andres, "Control strategy for distribution generation inverters to maximize the voltage support in the lowest phase during voltage sags," IEEE Transactions on Industrial Electronics, vol. 65, pp. 2346–2355, Mar. 2018, doi: 10.1109/TIE.2017.2736486.
9. A. Camacho, M. Castilla, J. Miret, M. Velasco, and R. Guzman, "Positive-sequence voltage control, full negative-sequence cancellation, and current limitation for static compensators," IEEE Journal of Emerging and Selected Topics in Power Electronics, vol. 9, pp. 6613–6623, Dec. 2021, doi: 10.1109/JESTPE.2021.3066681.
10. P. T. Cheng, C. A. Chen, T. L. Lee, and S. Y. Kuo, "A cooperative imbalance compensation method for distributed-generation interface converters," IEEE Transactions on Industry Applications, vol. 45, pp. 805–815, 2009, doi: 10.1109/TIA.2009.2013601.
11. M. Savaghebi, A. Jalilian, J. C. Vasquez, and J. M. Guerrero, "Autonomous voltage unbalance compensation in an islanded droop-controlled microgrid," IEEE Transactions on Industrial Electronics, vol. 60, pp. 1390–1402, 2013, doi: 10.1109/TIE.2012.2185914.
12. G. V. Ramos, T. M. Parreiras, and B. J. C. Filho, "Control performance assessment of a zero harmonic distortion grid-forming converter for medium voltage islanded microgrids," Eletrônica de Potência, vol. 29, p. e202441, Oct. 2024, doi: 10.18618/REP.e202441.
13. J. Zhang, Y. Jia, Z. Li, X. Ye, C. Yang, and D. Jiang, "Adaptive virtual impedance control strategy for multiple grid-forming converters in islanded microgrid," in 2023 2nd asia power and electrical technology conference (APET), IEEE, Dec. 2023, pp. 599–604. doi: 10.1109/APET59977.2023.10489414.
14. Y. Li, J. Liu, and J. Liu, "Simultaneous voltage and current harmonic control of grid-forming converters based on unified harmonic voltage-current droop," in PEDG 2023 - 2023 IEEE 14th international symposium on power electronics for distributed generation systems, Institute of Electrical; Electronics Engineers Inc., 2023, pp. 684–690. doi: 10.1109/PEDG56097.2023.10215297.
15. H. Li, Y. Tao, G. Li, and Q. Li, "Enhancing the voltage quality of grid-forming converters by using improved dead time compensation strategy," in 2024 4th international conference on neural networks, information and communication (NNICE), IEEE, Jan. 2024, pp. 1380–1385. doi: 10.1109/NNICE61279.2024.10498296.
16. D. O. Williams, Z. S. Li, X. Luo, and T. F. Megahed, "Power quality improvement through a model predictive droop-based grid-forming inverter control," in 2024 IEEE international conference on prognostics and health management (ICPHM), IEEE, June 2024, pp. 212–216. doi: 10.1109/ICPHM61352.2024.10627662.
17. A. W. Aslam, J. Hassan, V. Minambres-Marcos, A. G. S. Al-salloomee, and C. Roncero-Clemente, "Traditional and hybrid topologies for single-/three-phase transformerless

multilevel inverters," Electronics, vol. 13, p. 4058, Oct. 2024, doi: 10.3390/electronics13204058.

18. O. Husev, C. Roncero-Clemente, E. Makovenko, S. P. Pimentel, D. Vinnikov, and J. Martins, "Optimization and implementation of the proportional-resonant controller for grid-connected inverter with significant computation delay," IEEE Transactions on Industrial Electronics, vol. 67, pp. 1201–1211, Feb. 2020, doi: 10.1109/TIE.2019.2898616.
19. I. Roasto, A. Blinov, D. Vinnikov, L. Mackay, and T. Jalakas, "DC droop control strategies and tuning principles," in 2023 IEEE 64th international scientific conference on power and electrical engineering of riga technical university (RTUCON), IEEE, Oct. 2023, pp. 1–6. doi: 10.1109/RTUCON60080.2023.10412947.
20. J. C. Vasquez, J. M. Guerrero, M. Savaghebi, and R. Teodorescu, "Modeling, analysis, and design of stationary reference frame droop controlled parallel three-phase voltage source inverters," in 8th international conference on power electronics - ECCE asia: "Green world with power electronics", ICPE 2011-ECCE asia, 2011, pp. 272–279. doi: 10.1109/ICPE.2011.5944601.
21. M. K. Mishra and V. N. Lal, "An improved proportional resonant controller for current harmonics reduction and power ripples mitigation of self-synchronized grid-tied PV system under distorted grid voltages," in 2021 IEEE energy conversion congress and exposition (ECCE), IEEE, Oct. 2021, pp. 939–944. doi: 10.1109/ECCE47101.2021.9595761.
22. NPEC : 2017 national power electronics conference : 18-20 december 2017, pune, india. Institute of Electrical; Electronics Engineers, 2018, p. 373.
23. J. D. Vasquez-Plaza, J. F. Patarroyo-Montenegro, D. D. Campo-Ossa, E. A. Sanabria-Torres, A. F. Lopez-Chavarro, and F. Andrade, "Formal design methodology for discrete proportional-resonant (PR) controllers based on sisotool/matlab tool," in IECON 2020 the 46th annual conference of the IEEE industrial electronics society, IEEE, Oct. 2020, pp. 3679–3684. doi: 10.1109/IECON43393.2020.9254717.
24. A. G. S. Al-Salloomee, E. Romero-Cadaval, C. Roncero-Clemente, and M. Swadi, "Efficient control scheme for compensating voltage unbalance and harmonics in islanded microgrid inverters," in 2024 IEEE 22nd mediterranean electrotechnical conference (MELECON), IEEE, June 2024, pp. 574–579. doi: 10.1109/MELECON56669.2024.10608793.
25. A. Arranz-Gimon, A. Zorita-Lamadrid, D. Morinigo-Sotelo, and O. Duque-Perez, "A review of total harmonic distortion factors for the measurement of harmonic and interharmonic pollution in modern power systems," Energies, vol. 14, p. 6467, Oct. 2021, doi: 10.3390/en14206467.

Development of Power Generators for Smart Buildings with Advanced Power Sharing Capabilities

Luis Martínez-Caballero[1], Radosław Kot[1], Adam Milczarek[1] and Mariusz Malinowski[1],

[1] Institute of Control and Industrial Elelctronics, Koszykowa 75,
00-662 Warsaw, Poland
{luis.martinez, radoslaw.kot, adam.milczarek, mariusz.malinowski,
}@pw.edu.pl

Abstract. The availability of photovoltaic (PV) sources has increased even at the residential level. In the grid-connected mode of operation, an energy storage device can be included in the system to support the inherent intermittency of the renewable energy source (RES). However, for the standalone mode of operation, this is almost a mandatory requirement in order to manage the power balance between load and generation in the system. The local controllers of the system are essential to provide the foundation that ensures stable and continuous operation during different scenarios. This work presents a PV and battery-based residential system, together with the control scheme used in the standalone mode of operation. Moreover, the experimental prototype used for this system is described thoroughly. Simulation and experimental results show the effectiveness of the proposed controllers for the operation of the system.

Keywords: photovoltaics, standalone, energy storage, power sharing, three-phase, four-leg inverter.

1 Introduction

The deployment of renewable energy technologies is accelerating in the upcoming years, especially wind-powered and photovoltaic (PV) systems, which are being developed due to their reduction in power generation costs at different scales [1]. However, renewable energy sources (RES) suffer from inherent intermittency, and energy storage systems (ESS) have emerged as a tool to provide support when the generation source is not available [2]. At the residential scale, the proliferation of rooftop PV installations and lithium-ion batteries enables consumers to become prosumers, providing more flexibility to the system. Moreover, in some cases, regulatory frameworks promote the participation of small-scale energy systems through economic incentives for residential prosumers [3]. With the increasing complexity of

---

[1] Please note that the LNCS Editorial assumes that all authors have used the western naming convention, with given names preceding surnames. This determines the structure of the names in the running heads and the author index.

these systems, effective coordination among components becomes essential. For instance, RESs must be controlled to extract the maximum available power, while ESSs must operate within safety constraints and provide high performance without compromising the useful lifetime.

The interactions between loads, generation units, storage devices, and the electrical grid demand the development of suitable control algorithms that provide continuous operation under different scenarios, for example, in grid-connected or standalone mode of operation. In general, such systems comprise three control layers, where the first one corresponds to the local controllers for power electronics converters (PECs) and the second and third layers allow for power sharing and energy management techniques. Typically, the energy management systems (EMSs), which are implemented as the third layer, are capable of real-time supervision and control of energy flows, ensuring secure operation, maintaining supply-demand balance, and achieving operational objectives such as economic optimization and resilience [4].

While many studies emphasize the optimization stage, several works address the operational requirements of the system by integrating the lower-level controllers that determine the dynamics in shorter time scales, typically within the order of milliseconds [5]. For example, an off-grid system comprising a wind turbine and PV array managed via a flowchart-based EMS is examined in [6]. In [7], forecasted load and generation data are employed to adjust the lower state-of-charge (SOC) threshold of the energy storage system, serving as a risk-mitigation strategy against uncertainty. The system in [8] integrates an electric vehicle to support peak demand. These implementations, while relying on relatively simple rule-based EMS frameworks, are necessary to ensure system resilience during critical events such as black-start conditions or grid outages. Moreover, in these studies, the local controllers are well described, and the experimental validation is conducted across various scenarios to demonstrate the performance of the system.

In a PV and battery-based residential system, the control scheme determines the power sharing in the system. Typically, in the grid-connected mode of operation, the ac converter is responsible for the power balance in the system by regulating the dc-link voltage. In contrast, in the standalone mode of operation, the most common approach is to use the ESS to regulate the dc bus voltage, which in turn regulates the power balance of the system. In this work, the control techniques for a PV and battery-based system operating in the standalone mode of operation for a residential system, are described.

2 System Description

The system under study comprises a photovoltaic array and a lithium-ion battery as the primary energy storage device, and is illustrated in **Fig. 1**. The PV array is interfaced with the dc bus using a boost converter. In contrast, the battery is connected through a bidirectional dc-dc converter. Both converters operate in interleaved mode, with this configuration having the ability to reduce the current stress on semiconductor devices. Compared to conventional single-phase converters, interleaving also enables a four times reduction in the filter size for the same input current ripple [9][10].

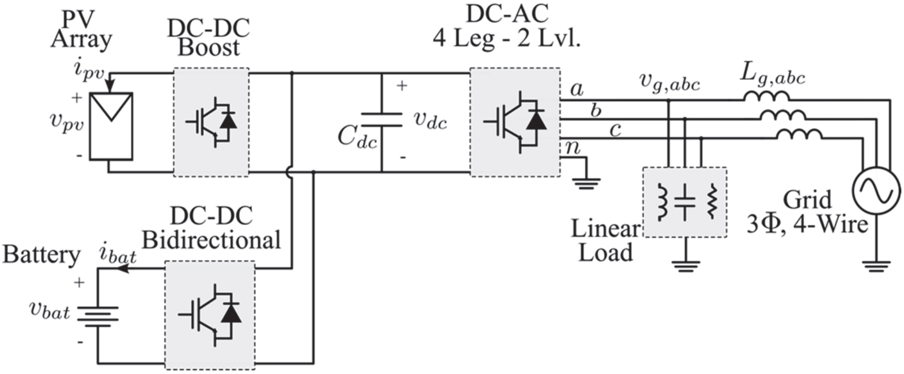

Fig. 1. PV and Battery-supported residential supply subsystem.

For the dc-ac converter, either three-leg or four-leg two-level inverters may be employed depending on the applications and the operation mode. In residential applications, where low-voltage distribution networks typically supply a set of single-phase and unbalanced three-phase loads, a four-leg inverter topology is preferred. This configuration allows for the regulation of zero-sequence components, which is essential for standalone operation, and enhances flexibility under unbalanced conditions. An LCL filter is connected to the output of the inverter to reduce the switching harmonics components and ensure compliance with the connection of the local loads, providing sinusoidal voltages at the point of common coupling [11]. The following section describes the detailed mathematical model of each element of the system and the corresponding controllers.

3 Modelling and Control

This section presents the modeling and control strategies for a PV and battery-based system interfaced through a three-phase four-wire inverter that supplies ac loads. The objective is to describe the mathematical models of the PV array, battery storage, and the corresponding power converters as a base to design the corresponding control loops. The control scheme regulates the power balance, maintains the voltage, and ensures the maximum energy extraction from the PV system. Each subsystem and its corresponding control scheme are described in the following.

3.1 PV System

The PV array is modeled using the single-diode Shockley equation and an irradiance-dependent current source. For this model, the inputs are the solar irradiance and the temperature, and the model accounts for the temperature drift of the open-circuit voltage as well as the short-circuit current. Additionally, the model is flexible because different power ratings can be achieved using the same model. The dc-dc converter used is an interleaved boost converter, that is connected to the dc bus capacitor that couples the dc sources with the ac converter.

The main task of the converter is to extract the maximum available power from the PV array, to either be used by the dc-ac converter or by the battery converter. To achieve this objective the controller structure has to account for a Maximum Power Point Tracking (MPPT) algorithm, which will produce a voltage reference that has to be controlled at the input terminals of the converter, to follow the voltage reference two cascaded proportional-integral (PI) regulators are chosen, the outer one provides a current reference to the inner loop. The latter produces the duty cycle that commands the converter switches. The topology of the PV converter is shown in **Fig. 2** (a), and the local controller is illustrated in **Fig. 2** (b).

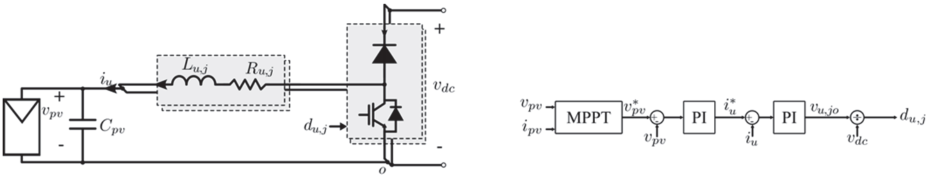

(a) (b)

Fig. 2. PV system. (a) Power stage. (b) Control diagram.

In this system, the measurements used for the control stage are the inductor currents $i_{u,j}$, the PV voltage v_{pv}, and the dc bus voltage v_{dc}. The MPPT algorithm is a simple perturb and observe (P&O). The mathematical model that describes the average inductor current $\bar{i}_{L,j}$ for each leg of the converter is given by,

$$\bar{i}_{L,j}(s) = \left(v_{pv} - \bar{v}_{conv,j}\right)\frac{1}{sL + R}$$

The control action corresponds to the average voltage $\bar{v}_{conv,j}$, at the IGBT terminals generated during one switching period T_s. It can be noted that in this transfer function the voltage $\bar{v}_{conv,j}$, and the relation between input and output is linear, allowing the use of a simple PI controller to track the current reference However, the power converter input is the duty cycle for each leg $d_{u,j}$. Therefore, the equation relating the duty cycle and the average voltage depends on the operating mode of the converter, which can be either continuous conduction mode (CCM) or discontinuous conduction mode (DCM). In [12], the process to obtain the corresponding duty cycle from the average voltage, regardless of the operating mode in a digital controller, is described and is the one implemented in this work. Assuming that the current through the inductors is equal, which is achieved through the use of independent PI controllers in the inner loop, the transfer function that relates the input voltage that has to be controlled for the PV to operate at the maximum power point, with the average inductor current as the control action, is given by:

$$\overline{v_{pv}}(s) = \frac{i_{pv} - 2\, i_{u,j}}{s \cdot C_{pv}}$$

It can be noted that the relation between input and output is again linear, allowing the implementation of a PI controller. Using a cascaded control structure and tuning with an order of magnitude difference between the controllers, the coupling between them is avoided.

3.2 ES System

For the development of the battery model, research of the different options available in the literature was conducted to determine which was the most suitable option for this application. After comparing the different characteristics, a run-time model was selected that allows for the inclusion of the capacity, dynamic behavior of the battery, and the non-linear relation between the State of Charge (SOC) and the battery voltage. The latter is one of the most important features, as the energy level of the battery has to be monitored and kept within allowable limits during operation to preserve the battery's lifetime. The ES system's power stage and local controller are shown in **Fig. 3**(a) and **Fig. 3**(b), respectively.

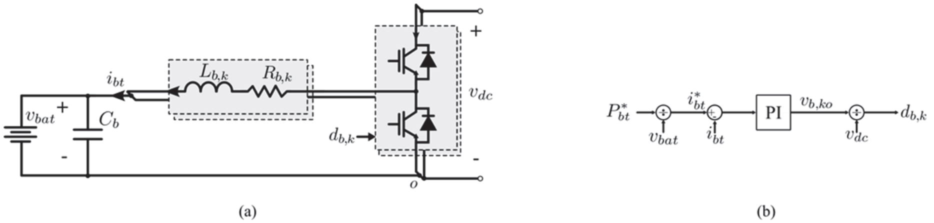

(a) (b)

Fig. 3. ES system. (a) Power stage. (b) Control diagram.

The PEC selected for this application is a bidirectional interleaved converter, which is in charge of controlling the charging and discharging of the battery. The lithium-ion battery can be operated in constant current mode in the range of 20% to 90%. Therefore, a current controller is used, and the power reference is converted to a current reference. Then, a PI controller is used to track the reference current to command the converter switches.

3.3 Grid Side dc-ac Converter

The dc-ac converter comprises four legs, this configuration provides better support to the unbalanced loads, to interface the converter to the grid it is necessary to reduce the harmonics produced at the switching frequency, therefore an LCL + L filter is used, compared to the L filter this configuration reduces the total inductance needed for the same attenuation. The converter and the local controller are presented in **Fig. 4**(a) and **Fig. 4**(b), respectively.

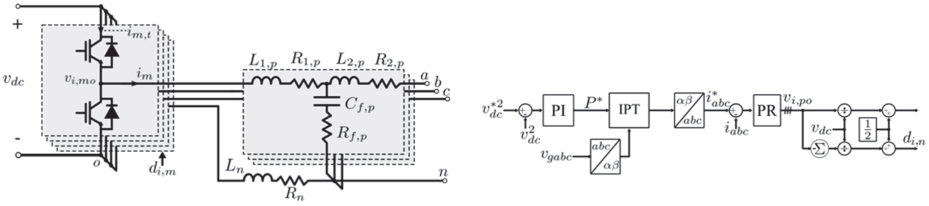

(a) (b)

Fig. 4. dc-ac stage. (a) Power stage. (b) Local controller.

The controller of this converter is in charge of regulating the power between the dc-dc converters (battery and PV) and the grid as needed, to provide energy from the PV and battery to the loads or to take power from the grid to charge the battery. As part of this task, the voltage on the capacitor that couples the dc and the ac stages has to be controlled. A cascaded control structure is used, in this case the dc bus voltage error is fed to a PI controller, its output and the grid voltage measurements are used to generate appropriate sinusoidal current references that are tracked using a proportional-resonant controller, to finally activate the switches of the converter accordingly.

4 Experimental Validation

This section comprises two parts, one is the description of the developed experimental prototype and its components, followed by the experimental tests conducted to demonstrate the effectiveness of the proposed control structure. The tests that were conducted corresponded to individual loops, and the complete control schemes for each converter.

4.1 Prototype Description

The prototype diagram is shown in **Fig. 5**. Each power electronic converter comprises a set of half-bridges, four for the grid side converter and two for each dc-dc converter. For each half-bridge, two MOSFETS and one gate driver per switching element are used. The grid side converter is a four-leg, three-phase converter connected to an LC filter in the three phases, and an L filter is used for the neutral leg. The filtering stage is followed by an additional breaker that enables the connection with a Chroma 6180. This device emulates the connection of a three-phase low-voltage network under safe operating conditions. Besides, a set of three Chroma 63804 programmable loads is used to emulate balanced or unbalanced loads. The coupling of the dc-ac converter and the dc-dc stage is made by means of a bank of electrolytic capacitors labeled as C_{dc}.

A bidirectional converter is used for the energy conversion stage of the battery system. At the input of this converter, one inductor per switching leg is used, and the inductors are connected to a small capacitor in parallel with an ITECH IT6018B bidirectional source. This device is utilized to emulate the behavior of a real battery, allowing the simulation of different technologies, power levels, and dynamic conditions. The PV converter has the same topology as the battery converter. However, it is important to note that this converter must be operated so that energy is sent from the source to the rest of the system and never in the opposite direction. Besides, the IT6018B DC source can be used to simulate the dynamic behavior of the PV modules, where different temperature and irradiance conditions can be programmed to emulate the dynamic scenarios under which the converter must operate.

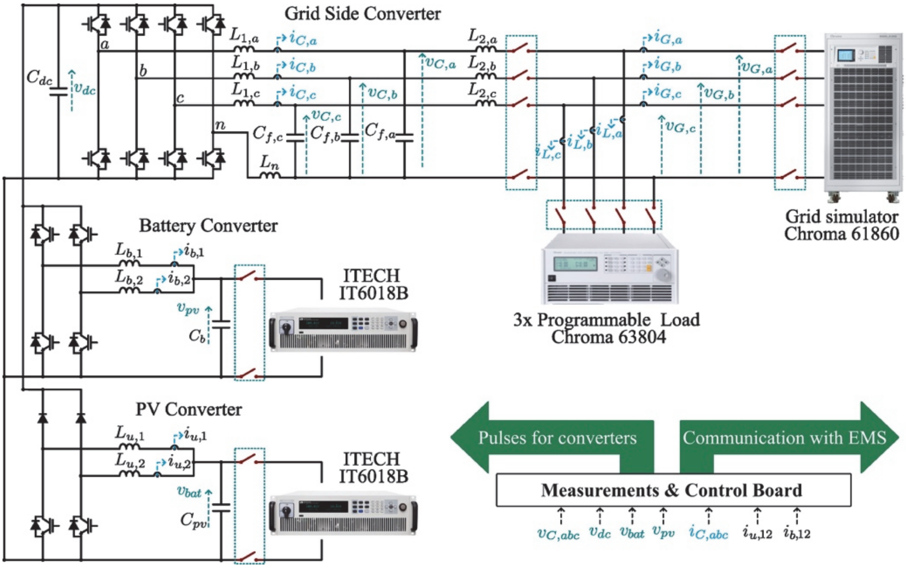

Fig. 5. Diagram of the experimental setup including power supplies.

The list of passive components, semiconductors, gate drivers, control devices, and measurements for the power converters is summarized in Table 1.

Table 1. Table of prototype components.

Component	Value/Description	Component	Value/Description
$L_{1,abcn}$	250 µH inductor	$L_{u,12}$	500 µH inductor
$C_{f,abc}$	10 µF capacitor	$L_{b,12}$	500 µH inductor
C_{pv}	10 µF capacitor	C_{bat}	10 µF capacitor
C_{dc}	990 µF capacitor	UCC21750-Q110-A	Isolated Gate Driver
AMC1306E05DWV	Single Channel ADC Delta-Sigma 20Msps Manchester Encoded	TMS320F28379D	Texas instruments microcontroller
MOSFET C3M0065090D	900 V / 24 A	ECP5U-LFE5U	Lattice FPGA

For every half-bridge of the converter, a pair of CMS62800 semiconductors is used. Each semiconductor is equipped with an isolated gate driver UCC21750-Q1, which can detect shoot-through events and faults that can be sent to the control board to disable the system's operation. The current measurements indicated in the schematic are taken using shunt resistors and single-channel Delta-Sigma analog-to-digital converters (ADC), which are isolated from the power stage. A voltage divider and the same ADC devices are used for the voltage measurements. These readings are sent to the FPGA, where filtering is performed, and the data is communicated to the microcontroller to carry out the necessary calculations and execution of the control routines.

The CAD of four switching legs, where each unit has a half-bridge arrangement of semiconductors, and the corresponding heat sink is shown in **Fig.6**(a). On the other hand, the partial assembly of the physical system is shown in **Fig.6**(b) for comparison with the CAD model. Besides, the assembly of the power stage of the prototype is presented in **Fig. 7**, which includes the passive components, measurements, and control board, and the switching devices.

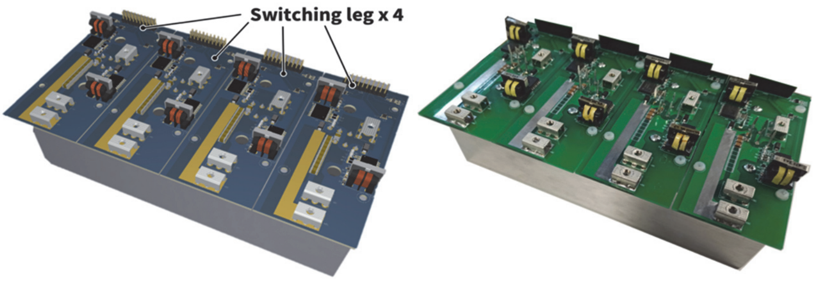

(a) (b)

Fig.6. Modular PCB for power stage including four switching legs and heatsink. (a) CAD design. (b) Physical prototype.

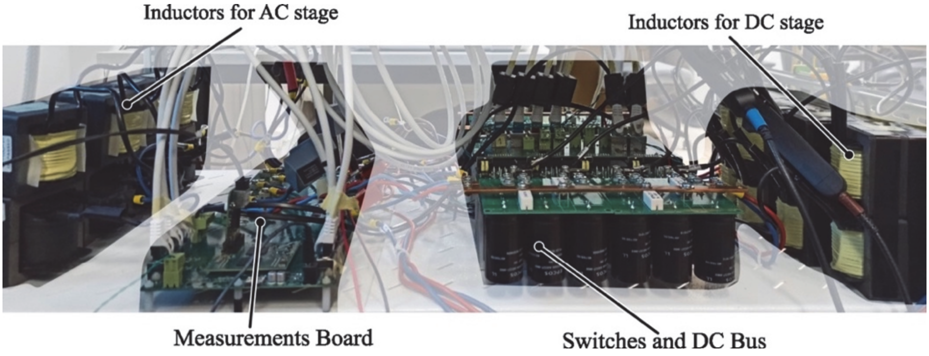

Fig. 7. Assembly of the power stage with dc link capacitors and filters.

4.2 ES System tests

The first test corresponds to the performance of the current control loop which is the inner-most loop in the control scheme of the ES system. In this scenario two voltage sources are connected one at the input side to emulate the battery, and another at the dc bus capacitor connection. The simulation and experimental results for a change in the reference current from 0.75 A to -1.0 at $t = 0.6$ ms, are illustrated in **Fig. 8**. In this case, the closed-loop response reaches 95% of the reference in 1.7 ms.

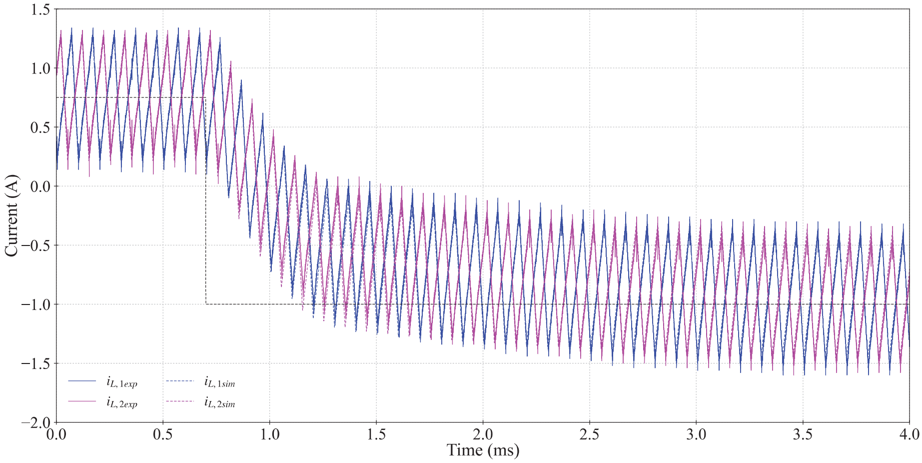

Fig. 8. Current control of ES system transition from discharging to charging.

In the standalone mode of operation, the ESS is in charge of balancing the power in the system by controlling the dc bus voltage. Once the current control loop has been validated, the following tests correspond to the regulation of the dc link voltage. During this test, a voltage source is connected at the input of the battery converter with a setting of 100 V, the controller is enabled at $t = 0.035$ s, and the reference voltage for the dc-link is set to 175 V. The dc bus voltage and the battery current are shown in **Fig. 9**(a)-(b). Regarding the step response of the voltage control, it corresponds to a second-order system, the reference is reached after 17 ms. However, the settling time is 85 ms. It can be noted that the battery current reaches a maximum value of 20 A, which corresponds to the saturation limit implemented in the voltage controller.

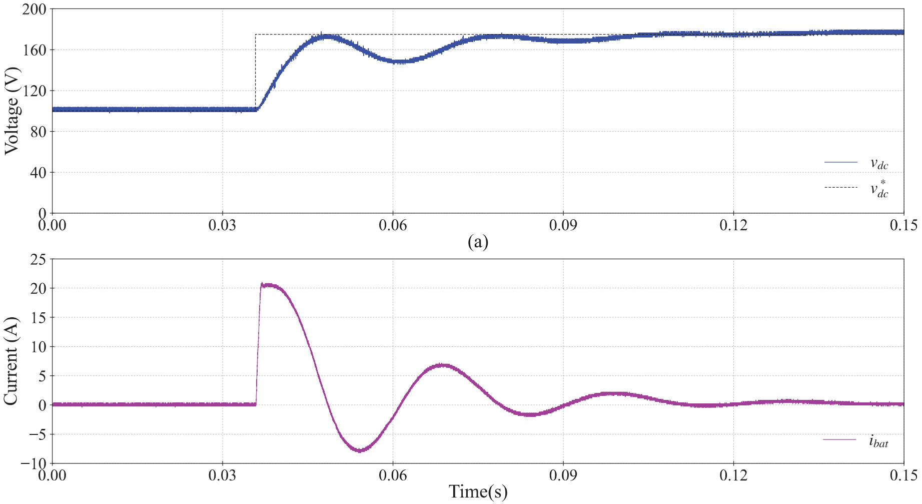

(a)

(b)

Fig. 9. Voltage control for the dc link from the battery converter.

4.3 PV System

The first test corresponds to the assessment of the performance of the current control loop, which is the innermost loop in the control scheme of the PV system. The controller must be tested in both the CCM and the DCM of operation, as well as the corresponding transitions between these modes. In this scenario a PV simulator is connected at the input of the converter and a bidirectional power supply is connected with a fixed dc bus voltage. The simulation and experimental results of the test from DCM to CCM are presented in **Fig. 10**. In this test, the reference for each leg is changed from 0.25 A to 2.25 A, at t =0.5 ms. The solid lines correspond to the inductor currents measured in the experimental setup, and the dashed lines correspond to the results obtained from the simulation model in the software PLECS. It can be noted that the time constant of the current control loop is of 1.1 ms.

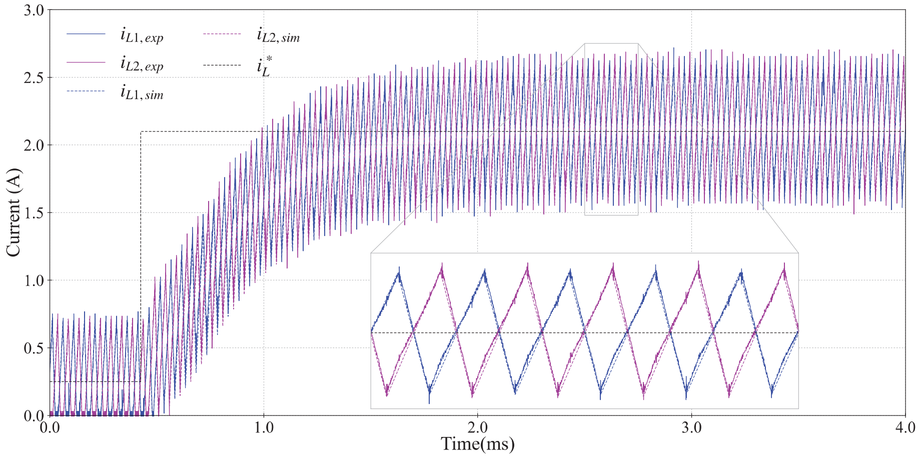

Fig. 10. Current control of PV system DCM to CCM transition.

On the other hand, a step change from the CCM to the DCM of operation is shown in **Fig. 11**, in this case, the change in reference current for both inductors is from 1.75 A to 0.25 A. The achieved time constant is 1.2 ms, which is only 9% different compared to the test in CCM, demonstrating that the current controller provides similar performance regardless of the operating mode.

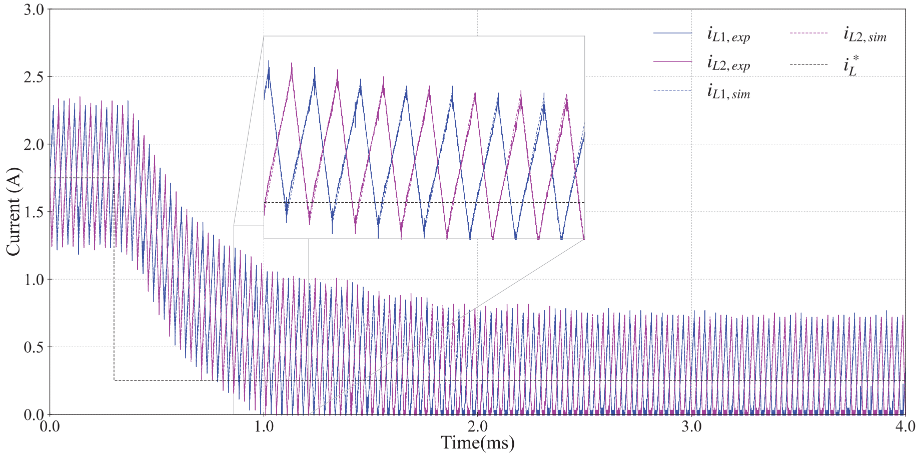

Fig. 11. Current control of PV system CCM to DCM transition.

After validating the current control loops, the MPPT and voltage control loops are tested. The setup is the same, using a PV simulator at the input of the converter and a power supply with constant voltage on the dc link capacitor. The results for the startup of the PV system are presented in **Fig. 12**. The voltage of the PV, and the corresponding reference set from the MPPT algorithm are presented in **Fig. 12**(a). The output current of the PV array, one of the inductor currents of the converter, and the reference current for one leg are shown in **Fig. 12**(b).

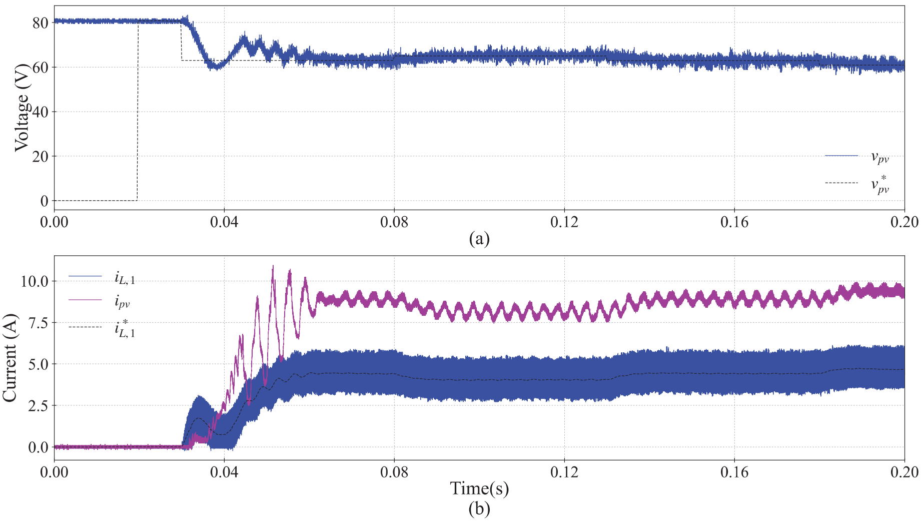

Fig. 12. Start-up of the PV system from open-circuit condition. (a) PV voltage. (b) PV, reference, and inductor current.

Similarly, the input voltage v_{pv}, and the corresponding reference algorithm during the MPPT mode are shown in **Fig. 13**(a). It can be observed that the PV system operates in the typical three-level operation of the P&O when the maximum power point has been reached. Moreover, the inductor, input, and reference currents are presented in **Fig. 13**(b).

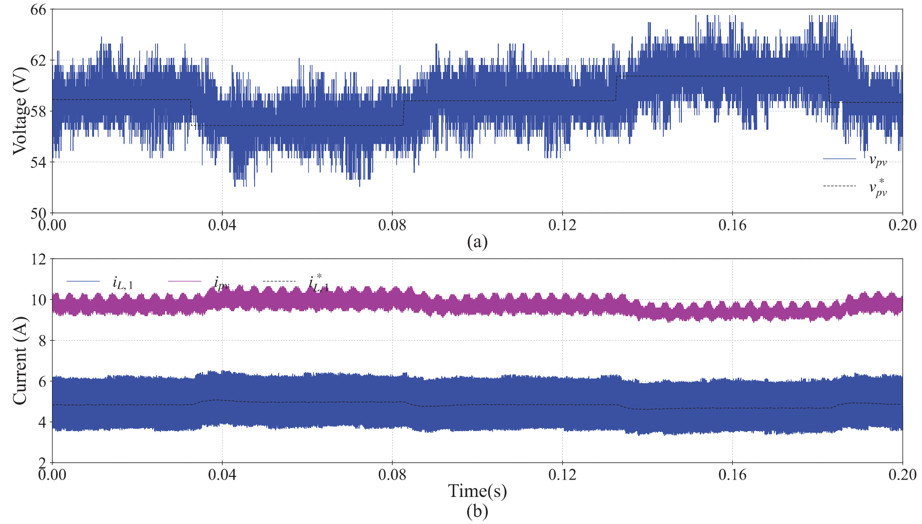

Fig. 13. PV system operation during MPPT mode. (a) PV voltage. (b) PV, reference, and inductor current.

4.4 GSC in Islanded Mode

The results to validate the voltage control of the ac converter are presented in **Fig. 14**. During this test, the dc-link voltage is regulated by the ES system, as can be observed in **Fig. 14**(a). In order to test the response of the system to unbalanced loads, three electronic loads are connected at the output of the LC filter of the converter. The load voltages $v_{g,abc}$ are presented in **Fig. 14**(b), corresponding to three sinusoidal waveforms, each phase-shifted by 120 degrees. Finally, the unbalanced load currents are shown in **Fig. 14**(c), demonstrating that the proposed control structure can supply unbalanced loads, which can appear due to the connection of single-phase loads to the system.

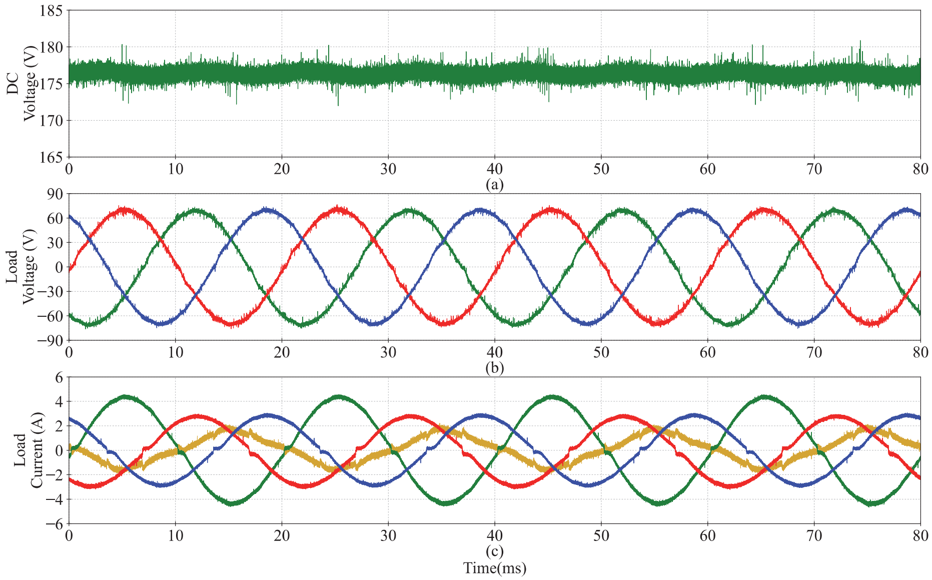

Fig. 14. Inverter operation in steady state. (a) DC Link voltage. (b) Load voltages. (c) Load currents.

5 Conclusions

This chapter presented the modeling, control design, and experimental validation of a standalone residential supply system that enables the power sharing between a photovoltaic (PV) generator and an energy storage system (ESS), which are interfaced to three-phase loads through a four-leg ac converter. Special attention is given to the mathematical model of the PV system, followed by the design of the corresponding controllers to ensure stable and efficient operation. The PV converter was controlled for maximum power point tracking (MPPT), the ESS converter ensured smooth power balance in the standalone mode of operation, and the grid-side converter enabled seamless operation for unbalanced load conditions.

Experimental results validated the effectiveness of each control strategy under realistic operating conditions using a custom-built prototype. Accurate MPPT and a stable start of the PV system have been demonstrated, as well as the ability of the ES System to control the dc-link voltage accurately. Moreover, the dc-ac can provide sinusoidal and balanced voltages even under unbalanced loading conditions. The proposed control lays the foundation for further developments such as power sharing in critical conditions and the implementation of energy management systems in the upper control layers.

Acknowledgments. This work has received funding from the European Union's Horizon 2020 research and innovation programme under the Marie Skłodowska-Curie grant agreement No 955614.

References

1. Fetting, C. The European Green Deal; Technical Report; ESDN Office: Vienna, Austria, 2020.
2. Stynski, S., Luo, W., Chub, A., Franquelo, L.G., Malinowski, M., Vinnikov, D. Utility-Scale Energy Storage Systems: Converters and Control. IEEE Industrial Electronics Magazine, 2020, 14, 32–52.
3. Martins, J.F.; Romero-Cadaval, E.; Vinnikov, D.; Malinowski, M. Transactive Energy: Power Electronics Challenges. IEEE Power Electronics Magazine, 2022, 9, 20–32.
4. Jafari, M.; Malekjamshidi, Z.; Zhu, J.; Khooban, M.H. A Novel Predictive Fuzzy Logic-Based Energy Management System for Grid-Connected and Off-Grid Operation of Residential Smart Microgrids. IEEE J. Emerg. Sel. Topics Power Electron. 2020.
5. J. M. Guerrero, J. C. Vasquez, J. Matas, L. G. de Vicuna, and M. Castilla, “1Hierarchical Control of Droop-Controlled AC and DC Microgrids—A General Approach Toward Standardization,” IEEE Transactions on Industrial Electronics, vol. 58, no. 1, pp. 158–172, Jan. 2011, doi: 10.1109/TIE.2010.2066534.
6. Merabet, A.; Tawfique Ahmed, K.; Ibrahim, H.; Beguenane, R.; Ghias, A.M.Y.M. Energy Management and Control System for Laboratory Scale Microgrid Based Wind-PV-Battery. IEEE Trans. Sustain. Energy 2017, 8, 145–154
7. Mahmud, K.; Sahoo, A.K.; Ravishankar, J.; Dong, Z.Y. Coordinated Multilayer Control for Energy Management of Grid-Connected AC Microgrids. IEEE Trans. Industry Appl. 2019.
8. E. González-Romera, E. Romero-Cadaval, C. Roncero-Clemente, M.-I. Milanés-Montero, F. Barrero-González, and A.-A. Alvi, “A Genetic Algorithm for Residential Virtual Power Plants with Electric Vehicle Management Providing Ancillary Services,” Electronics, vol. 12, no. 17, Art. no. 17, Jan. 2023.
9. Sakasegawa, E.; Chishiki, R.; Sedutsu, R.; Soeda, T.; Haga, H.; Kennel, R.M. Comparison of Interleaved Boost Converter and Two-Phase Boost Converter Characteristics for Three-Level Inverters. World Electr. Veh. J. 2023, 14, 7.
10. Kroicˇs, K.; Sta ,na, ,G. Bidirectional Interleaved DC–DC Converter for Supercapacitor Energy Storage Integration with Reduced Capacitance. Electronics 2023, 12, 126.
11. A. Naderipour, Z. Abdul-Malek, V. K. Ramachandaramurthy, A. Kalam, and M. R. Miveh, “Hierarchical control strategy for a three-phase 4-wire microgrid under unbalanced and nonlinear load conditions,” ISA Transactions, vol. 94, pp. 352–369, Nov. 2019.
12. L. Martínez-Caballero, R. Kot, A. Milczarek, and M. Malinowski, “A Current Control Method for an Interleaved Boost Converter Under CCM/DCM Operation in a PV System,” in 2024 IEEE 18th International Conference on Compatibility, Power Electronics and Power Engineering (CPE-POWERENG), Jun. 2024, pp. 1–6.

Virtual Power Plant for Operation, both Isolated and Connected

Anas Abdullah Alvi[1](✉) , Enrique Romero-Cadaval[1], Eva González-Romera[1]

[1]Electrical, Electronic and Control Engineering Department, University of Extremadura,
Badajoz 06006, Spain
alvi@unex.es

Abstract. To keep up with the rising demand for electricity, renewable energy sources (RES) including solar and wind power are being used on an increasing basis. However, grid stability is compromised by renewable energy resources' intermittent nature. Technologies for energy storage provide a solution by enhancing system flexibility. As prosumer-based electrical systems and distributed energy resources expand, energy management systems are becoming more essential for optimizing system functionality and efficiency by coordinating the operation of various devices. This paper deals with a genetic algorithm-based virtual power plant that consists of PV generation, household load, electric vehicle, and energy storage system in which the objective is to reduce electricity costs by defining the objective function and related constraints. The study also includes the definition of different parameters used in genetic algorithm and inclusion of technical constraints such as peak shaving for greater economic benefits. Finally, a business model is proposed to integrate the virtual power plants with industries and factories.

Keywords: cost minimization; energy management system; energy storage; genetic algorithm; optimization; electric vehicle

1 Introduction

The emergence of distributed energy systems has been promoted by the continuous increase in renewable energy sources like photovoltaic (PV) generation systems, supported by energy storage technologies such as Lithium batteries and electric vehicles (EV). Systems in this configuration provide additional flexibility and independence from the centralized electricity generation paradigm. In this sense, due to the increasing complexity, energy management systems (EMS) are necessary to coordinate each element of the system with a particular goal [1]. Typically, economic benefits and energy reduction are common goals for the EMS. In order to attain these objectives, an optimization algorithm is necessary in which the EV or the batteries are scheduled during the day [2].

Metaheuristic optimization algorithms are widely adopted due to their advantages, for example, these algorithms are easy to implement and are not limited to a particular type of objective function or constraints [3]. In contrast, other optimization algorithms, such as linear programming (LP), quadratic programming (QP), or mixed-integer linear programming (MILP), are only suitable for a particular problem formulation [4].

Several metaheuristic optimization algorithms have been compared when solving the energy management problem, such as particle swarm optimization (PSO), genetic algorithm (GA), gray wolf optimization (GWO), ant colony optimization (ACO), artificial bee colony (ABC) and bald eagle search (BES) [5-7]. Nonetheless, the performance of different algorithms may be statistically equivalent when compared to different problems, which is known as the no free lunch theorem [8]. Moreover, metaheuristic optimization algorithms need different parameters which are selected by the user. Among the most common are the number of iterations and the population size, that are directly related to an increase in the exploration space and performance of the algorithm. Despite the body of research devoted to comparison of metaheuristic algorithms, to the best of the authors knowledge, there is a research gap of the performance assessment based on the parameter selection for a given metaheuristic algorithm.

Genetic algorithm has demonstrated a good performance in solving the energy management problem [7,8,9]. Therefore, in this work, we perform an extensive study on the performance of the GA under different parameters to solve the energy management problem of a residential system with PV generation, battery supply, and EV availability during a given time frame. Different options for crossover and selection operators are tested together with different probabilities for each of them, to determine their impact on the optimization problem.

The EMS under study consists of a single household load, a PV power plant, a battery-based ESS and a EV as shown in Figure 1.

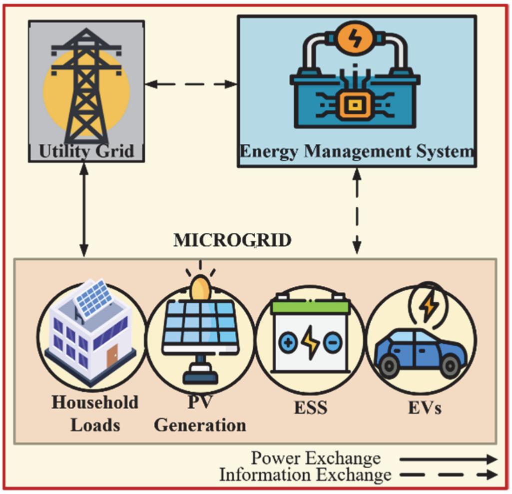

Figure 1. Elements of the MG under study

The main objective of this paper is to use different parameters considered in GA to optimize the EMS to reduce electricity bill by defining the objective functions and constraints to create new set-points of operation for the EV and the ESS and find out the best set of parameters which later can be used as a handbook for designing similar type of systems consisting of an EMS.

2 Relationship with Promoting the Transition to Green Electric Systems

In order to make interactive systems practical and beneficial, human-centered design applies human factors/ergonomics, usability knowledge and techniques, and focuses on the users, their needs, and requirements. This method counteracts the negative impacts of use on human health, safety, and performance while increasing effectiveness and efficiency, user satisfaction, accessibility, sustainability, and human well-being [10]. According to the definition of human centric systems as determined by ISO, it is clear that EMS can play a pivotal role in increasing the effectiveness of human well-being. EMS can be customized to match user requirements and preferences by utilizing human-centered design concepts. This leads to increased user satisfaction, better energy efficiency, and increased sustainability. EMS is a software-based system that is intended to track, regulate, and maximize the use of energy in different kinds of buildings. It is applied to minimize environmental effect, lower energy expenditures, and increase energy efficiency [11].

One of the key aspects of implementing an EMS is the ability to reduce electricity bills of residential households. With the addition of new types of consumer loads, such as EVs, electrical grids are subjected to more adverse and dynamic types of demand stress. This is why it is important to implement EMS with the electrical grids to manage and control these new types of severe demand profiles [12]. One possible solution of reducing electricity bill is to use the heavy loads during the off-peak period or valley hours during the day when the price of electricity is cheaper compared to the time of the day. However, it is difficult for the consumers to always control the heavy household loads or EVs manually to turn on only during the valley hours and hence an EMS can ease the use of this operation. An EMS can automatically control the adjustable loads to consume the electricity during the off-peak hours as well as supply electricity to the grid from the ESSs when the cost of electricity to sell is higher. These types of automatic control of energy flow eases the efficiency of human comfort where it is no longer necessary to control each load/EV manually.

3 State of the art

Genetic Algorithm (GA) is a technique that leverages the notion of genetic selection to optimize the search tool for complex situations. It is useful for research and development as well as machine learning in addition to optimization. With factors like selection, crossover, and mutation all constituting genetic operations that would initially be applied on a random population, it is comparable to biology in terms of chromosomal creation. The goal of GA is to produce answers for upcoming generations. The degree of success in individual production is directly correlated with the fitness of the solution that it represents, guaranteeing higher quality in subsequent generations. When a GA proves to be the most appropriate solution for the problems requiring optimization related to a computable system, the procedure is finished [13].

The Darwinian theory of evolution [14,15], which simulated the survival of fitter creatures and their genes, served as the model for GA. The GA algorithm is based on population. A chromosome is represented by each solution, and a gene is represented by each parameter. GA uses a fitness (objective) function to assess each member of the population's level of fitness. The best solutions are selected at random using a selection mechanism (such as a roulette wheel) in order to improve subpar alternatives. Given that the probability is correlated with the objective value of fitness, this operator has a higher likelihood of selecting the optimal solutions. Selecting subpar solutions also raises the likelihood of avoiding local optima. This implies that good solutions can be freed from a local solution if they are imprisoned there by other solutions.

Since the GA method is stochastic, one can wonder about its dependability. This algorithm's ability to keep the best solutions from each generation and use them to enhance subsequent solutions is what gives it its reliability and ability to estimate the global optimum for a particular problem. Individual crossing leads to the "area" between the two parent solutions being offered being exploited. Mutation also helps this method. The genes in the chromosomes are randomly altered by this operator, preserving the population's variety and enhancing GA's inquisitive behaviour. Like nature, the mutation operator may produce a solution that is noticeably superior to the original and guide more solutions in the direction of the global optimum.

As discussed in [16], an EMS can be economically optimized by using GA by following a series of procedures. Initially the objective functions to reduce the electricity bill must be defined accordingly. Some of the procedures are discussed in detail.

3.1 Initial Population

The GA algorithm operates by starting with a random population. To boost the diversity, this population can be created using a Gaussian random distribution. There are several solutions in this population, each of which represents a person's chromosome. A collection of variables on each chromosome replicates the genes. The primary goal of the initialization step is to distribute the solutions as evenly as possible throughout the search space in order to boost population diversity and improve the likelihood of locating promising areas [17]. In EMS, the solutions represent different strategies that can optimize the defined functions and constraints.

3.2 Selection

This part of the GA algorithm is mostly inspired by natural selection. In the natural world, there is a greater likelihood of food and mating for the most fit individuals. Because of this, the genes in them contribute more to the next generation of that species. Drawing inspiration from this straightforward concept, the GA algorithm uses a roulette wheel to allocate probability to individuals and choose which ones to include in the next generation based on their fitness (objective) values [18-23]. In EMS, a fitness function is constructed to assess each solution's performance in relation to the previously established objectives. This could involve calculating key metrics, such the cost of the electricity used in this instance and modelling the system's energy usage under each solution.

3.3 Crossover (Recombination)

To develop the next generation, the people who have been chosen via a selection operator must be employed. In the natural world, a new chromosome is created when the chromosomes from a male and a female gene join. In order to emulate this, the GA algorithm combines two solutions (parent solutions) chosen by the roulette wheel to create two new solutions (children solutions). In the literature, there are various methods for the crossover operator, of which two (single-point and double-point [24]). Crossover is a technique used in EMS to combine various schedules for energy consumption or configurations of energy-efficient devices to produce offspring solutions that may carry over positive traits from their parent solutions.

3.4 Mutation

The final evolutionary operator involves the alteration of one or more genes subsequent to the creation of offspring solutions. Because large mutation rates reduce GA to a rudimentary random search, the mutation rate is set at low in GA. Through the introduction of an additional degree of unpredictability, the mutation operator preserves the population's diversity. In actuality, this operator raises the likelihood that local solutions in the GA algorithm will not occur by preventing solutions from becoming identical. The three evolutionary operators—selection, crossover, and mutation—are combined by the majority of EAs. To raise the caliber of genes in the following generation, these operators are applied to each generation [25-32]. In EMS, mutation refers to the introduction of minor, arbitrary changes to energy schedules, energy-efficient device configurations, or renewable energy source settings which refers to the operation set-points of the EVs and ESSs in this case.

4 Genetic Algorithm in Virtual Power Plants

GA is widely used in performing the optimization of different objectives such as cost reduction, minimization of energy, minimization of environmental impacts etc. of

EMS. Here, some of the existing literatures are discussed and compared with this current paper to identify the novelty. Ref [33] proposes a smart-grid approach that uses energy storage and hybrid renewable energy generation to match HVAC loads with renewable energy generation based on GA. A hierarchical GA is used in ref [34] to synthesize a fuzzy inference system (rule-based) EMS using various techniques in an effort to optimize the profit from the energy exchange with the grid. In reference [35], GA is used to optimize the technical and economic problems with the MG, including the participation of different consumers in reserve schedules and demand response programs, which lowers the microgrid's operating costs. The objective of ref [36] is to create an advanced EMS model that can use GA to identify the best operating strategies for minimizing energy costs, reducing pollutant emissions, MG system constraints, and making better use of renewable energy sources like solar and wind power through daily load demand. In ref [37], the time of use (TOU) pricing system, together with GA and bat algorithm (BA) to schedule appliances to minimize electricity costs, the peak to average ratio, and appliance delay time, are used to optimize energy usage. Even though, all of references implement GA algorithms to optimize the energy interchange or to reduce electricity bills, none of them contain scheduling charging/discharging of EVs during the valley hours in the systems. Also, none of these references contain a proper explanation of the parameters used to design the GA algorithm. Ref [38],[39] contains the inclusion of charging/discharging of EVs in the MGs, but there is no guideline for the selection of proper values of the parameters considered in GA.

The chapter is organized in the following way. The first part consists of the performance evaluation of a three-phase PV power plant operating at both connected and isolated to the grid. This is an important part of the validation of the performance of a microgrid in VPP. The next part consists of the general algorithm development of VPP for cost optimization for different scenarios. A further study is also done for the validation of the proposed algorithm using PLECS simulation model in the next stage. Finally, a business model is proposed for the VPP.

4.1 Performance Evaluation of a Three-Phase PV Power Plant

The main aim of this study as discussed in [40] is to analyze the operation of a three-phase photovoltaic power plant (rated at 250 kW) supplying power to both three-phase and single-phase loads. The analysis covers both, connected and disconnected modes and also includes the performance of a basic islanding detection method and the effect on the whole system considering unbalanced situations.

Figure 2 represents the general block diagram of the overall system. It consists of a PV field composed by 616 solar panel modules (with parameters shown in Table I) connected in an array of 7 in series and 88 in parallel, totalling a power of 250kW. The rated frequency considered for the system is 50Hz. PV field is connected to three level with neutral point clamping (NPC) inverter that converts the DC power to AC and includes an LCL filter to effectively reduce the harmonics injected to an acceptable value achieving the desired power quality. The system is finally connected to the grid by means of a distribution transformer. A balanced three phase load rated at 250kW (at nominal voltage of 25kV$_{RMS}$) is placed in the high voltage side and, to perform the main analysis of this paper, a single-phase load is connected in the low voltage side.

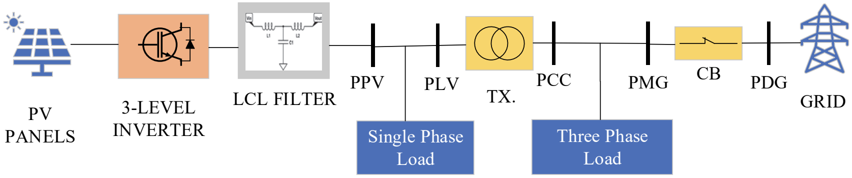

PPV- POINT OF PV
PLV- POINT OF LOW VOLTAGE
PCC- POINT OF COMMON COUPLING
PMG- POINT OF MICROGRID
PDG- POINT OF DISTRIBUTION GRID
TX.- TRANSFORMER
CB- CIRCUIT BREAKER

Figure 2. Power system under study

The general scheme of the inverter control algorithm three main parts:

- Algorithm for controlling the inverter in grid-connected mode.
- Algorithm for controlling the inverter in islanding mode.
- Islanding detection and selection of the right operation mode.

In the simulation results of the mentioned model is divided into two sections. In this section, the microgrid is operating as a balanced system whereas in next section, the system model will be analysed when operating in unbalanced situation. In the balanced situation, the microgrid is initially connected to the main grid and at 1s, it is disconnected after opening the corresponding breaker. Simulations results are shown in Figure 3 where it can be seen that the system operates properly in both modes. The reference voltages, both in LV and HV points of the inverter are 250 VRMS L-L and 25kVRMS L-L respectively.

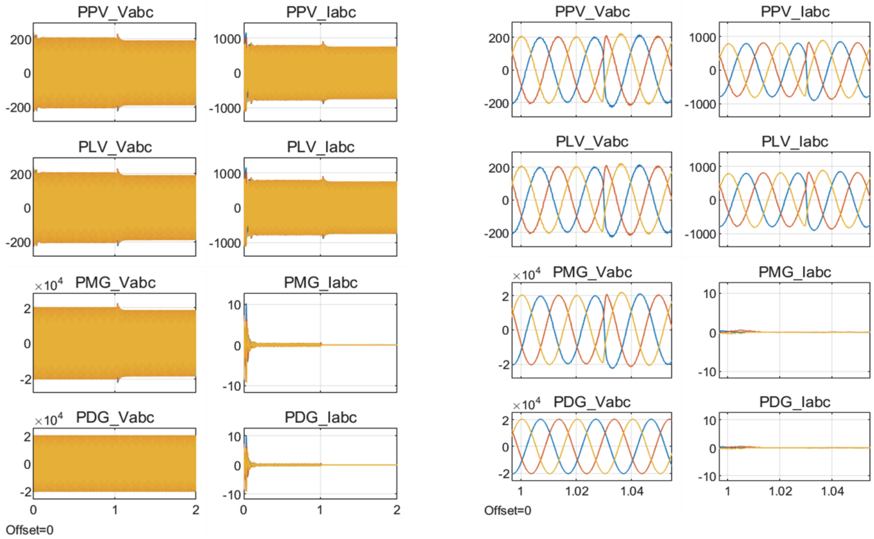

Figure 3. Voltage (in V) and current (in A) waveforms in different points of the microgrid, as indicated in Figure 1: (a) Simulated results, (b) Zoom at 1s (disconnection)

In this section the operation under unbalanced condition is analysed. This condition is created connecting a single-phase load in the low voltage feeder. To carry out the analysis, a case is proposed where the system is connected to the grid from 0s to 1s and then disconnected from 1s to 2s. Single-phase load is connected between 0.3s to 0.8s and 1.3s to 1.8s. This load is connected to phase a (blue waveform in figures)

Figure 4 shows the results for the proposed case when the irradiance level is 1000 W/m2. In this case, when the single-phase load is not connected the power generated by the PV is close to the power demanded by the local load in the microgrid. Figure 4 also shows the transient details when connecting and disconnecting the single-phase load in both grid-connected and isolated modes.

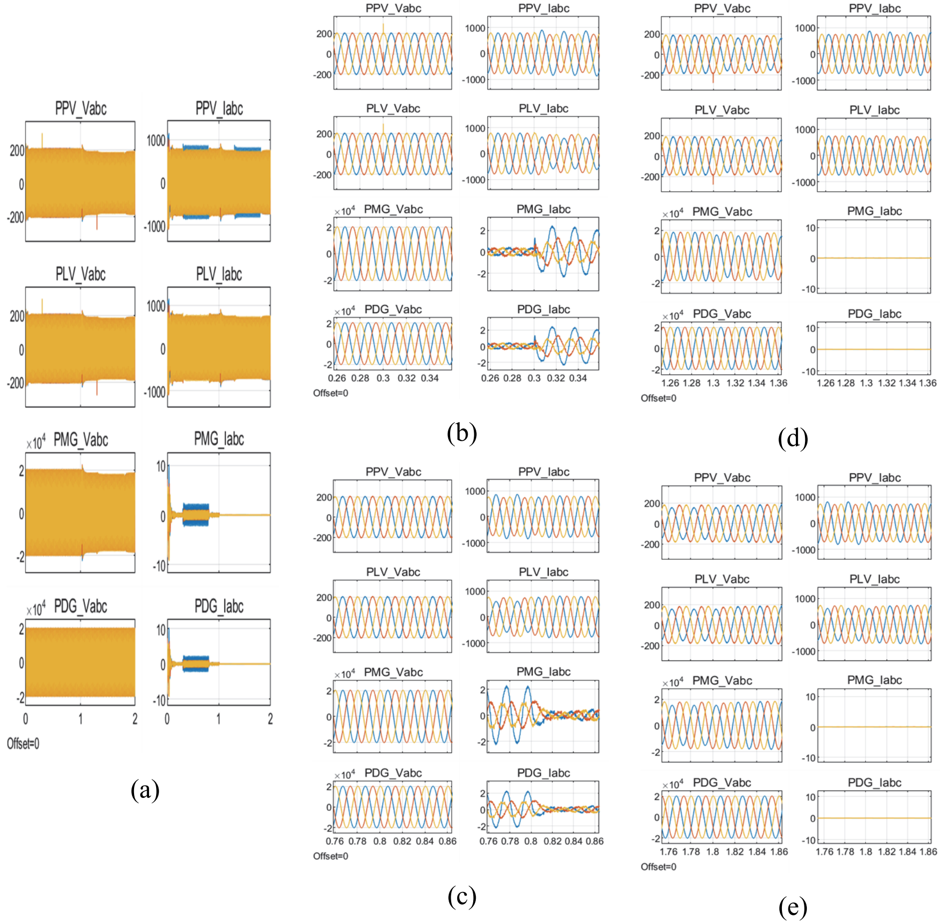

(a) (b) (c) (d) (e)

Figure 4. (a) Simulated results, voltage (in V) and current (in A) waveforms in different points of microgrid, as indicated in Figure 1, Details of voltage (in V) and current (in A) waveforms in different points of microgrid, as indicated in Figure 1: (b) Zoom at 0.3 s (single-phase load connection, grid-connected mode), (c) Zoom at 0.8 s (single-phase load disconnection, grid-connected mode) (d) Zoom at 1.3 s (single-phase load connection, isolated mode), (e) Zoom at 1.8 s (single-phase load disconnection, isolated mode)

It can be observed that, even though the voltage waveforms are not affected considerably due to the synchronization to the grid voltage, the current waveforms in the low voltage feeders are affected considerably and results in unbalanced condition between 0.3s and 0.8s of the simulation time. This study is helpful later in during the validation of algorithm output results using PLECS simulation model.

4.2 Genetic Algorithm Application in Virtual Power Plants

As discussed in literature review, GA is widely used optimization tool for achieving cost minimization. This section is again divided into 4 parts. The first part consists of the defining the objective function and its related constraints for developing the GA. The next parts consists of addition features that can be included in GA to make the system more robust and further reduce the costs.

4.2.1 A Genetic Algorithm for Residential Virtual Power Plants with Electric Vehicle Management Providing Ancillary Services

In order to maximize grid support and economic performance, this study proposes a management system for domestic virtual power plants that combines household loads, solar generation, energy storage, and electric vehicles. The research shows that even small-scale virtual power plants can successfully accomplish technical and financial goals commonly observed in larger systems by comparing different optimization techniques and using a genetic algorithm. The VPP under study encompasses a set of households, a communitarian PV power plant, a battery-based ESS, and EVs.
Eight residences in Denmark and Spain with different demand profiles, a 15 kW common PV plant, a 24 kWh Li-ion energy storage system (ESS), and four electric vehicles (EVs) make up the domestic virtual power plant (VPP) that is modeled in this study. Given the current investment hurdles, the ESS and PV system are sized in accordance with Spanish self-consumption legislation, with battery utilization optimized for cost-efficiency. Spain's time-of-use tariffs encourage EVs with 50 kWh batteries to charge during off-peak hours, which results in a concentrated load in the early morning. The initial findings indicate a self-sufficiency rate of 33.89% and a self-consumption rate of 59.87%. Peak grid injection occurs at midday, when solar generation is at its highest, and peak power demand coincides with EV charging.

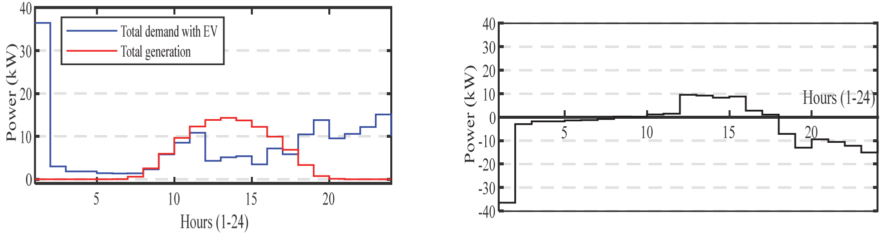

(a) (b)

Figure 5. (a) Initial accumulated demand and generation, excluding ESS; (b) Power interchange with distribution grid in initial situation.

The power exchanged between the entire VPP and the power grid in this initial scenario is depicted in Fig. 5b. The well-known rebound effect caused by time-of-use tariffs makes it clear that the highest demand for electricity happens when EVs are charging. This is followed by high demand hours in the late evening, which are typical of family consumption profiles. However, during midday, when PV plant production is at its peak, the power pumped into the grid reaches its highest value.

The ESS and EVs hourly power plans are optimized using a GA, with an emphasis on charging EVs at night when energy prices are lower and EVs are usually connected. GA is ideally suited for energy management in home virtual power plants because of its evolutionary method, which efficiently explores complex search spaces and steers clear of local optima.

The VPP power balance is defined in (1). Starting from (1), the objective functions are shown in (2) and (3).

$$P_{grid}(h) = P_{PV}(h) - P_{LD}(h) - P_{ESS}(h) - P_{EV}(h) \tag{1}$$

$$f_1 = \sum_{h=1}^{24} P_{grid}^2(h) \tag{2}$$

$$f_2 = \sum_{h=1}^{24} \left[\left(I_{pur}(h) \cdot p_{pur}(h) - I_{sel}(h) \cdot p_{sel}(h) \right) \cdot \left| P_{grid}(h) \right| \right] \tag{3}$$

Objective function f_1 in (2) aims to minimize the power interchanged with the grid. It is useful to maximize SC and SS without considering prices, for example, in TVPP devoted to supporting the distribution grid. CVPP requires economic incentives for final users to be motivated to participate in the VPP; in these kinds of VPP, objective function f_2 in (3) is more appropriate, which aims to minimize the VPP electricity bill.

Constraints for ESS are shown in (4)-(6).

$$-P_{ESSmax} \leq P_{ESS}(h) \leq P_{ESSmax} \tag{4}$$

$$SoC_{lo} \leq SoC(h) \leq SoC_{up} \tag{5}$$

$$|SoC_{in} - SoC(24)| \leq 10\%, \tag{6}$$

where:

$$SoC(h) = SoC_{in} + \sum_{i=1}^{h} \left(I_{ESSch}(i) \cdot P_{ESS}(i) \cdot \eta_{ch} + I_{ESSdi}(i) \cdot \frac{P_{ESS}(i)}{\eta_{di}} \right). \tag{7}$$

The energy storage system (ESS) is limited by its maximum charge/discharge power and a state-of-charge (SoC) range that is established by the manufacturer. Additionally, in order to preserve operational flexibility, the SoC variance over a day must not exceed 10%. Similar restrictions apply to electric vehicle (EV) power, guaranteeing effective and realistic involvement in the energy management of the virtual power plant. Constraints for EV power are shown in (8)-(10).

$$-P_{EVmax} \cdot n_{EV}(h_{EV}) \leq P_{EV}(h_{EV}) \leq P_{EVmax} \cdot n_{EV}(h_{EV}), \ h_{EV} \in nh_{EV} \tag{8}$$

$$P_{EV}(h) = 0, h \notin nh_{EV} \quad (9)$$

$$\sum_{h_{EV}} P_{EV}(h_{EV}) = E_{EVtotal}. \quad (10)$$

Finally, to provide support to the distribution grid, a constraint is also included for P_{grid} to perform peak shaving, as a means of grid congestion prevention (11).

$$|P_{grid}(h)| \leq P_{peak}. \quad (11)$$

Figs. 6 shows the results obtained by the GA when objective function f2 in (3) and constraints (4)-(6) and (8)-(10) are used.

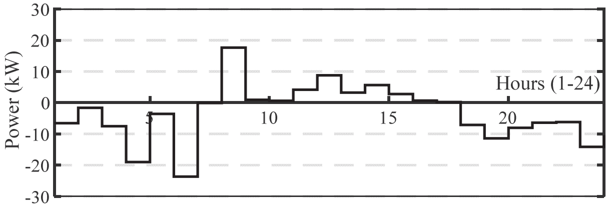

Figure 6. Power interchange with distribution grid, case 2.

In this case, SC is 58.16%, SS is 39.19% and the final bill is 19.95 €/day (a reduction of 15% starting from the base case). This bill is the lowest among the studied cases detrimental to SC and SS rates.

In conclusion, in this study different objective functions and constraints are tested, and the best result is obtained when a single-objective function based on purchase/sale prices is minimized and a peak-shaving constraint is added to regular constraints related to the different energy resources. This technique guarantees a limited peak power interchanged with the distribution grid, as well as minimizing the electricity bill of the whole VPP subject to network constraints, outperforming even a multi-objective optimization technique.

4.2.2 Participation of a Residential Microgrid in Flexibility Markets Providing Ancillary Services

In order to participate in flexibility markets by obtaining financial incentives, this study addresses the cost-effective optimization of energy storage systems' power reservation in a residential microgrid to provide ancillary services. In the study, an energy management system for a home microgrid comprising electric vehicles, photovoltaic generating, domestic loads, and energy storage systems is proposed. By designing and testing a genetic algorithm with appropriate parameters to define new set-points of operation for the energy storage systems and the charging/discharging of electric vehicles, the technical goal of providing ancillary services by reserving a fixed power capacity of the energy storage systems and including grid congestion constraint, as well as the economic goal of lowering electricity bills, are accomplished.

This paper [41] proposes a novel idea to integrate the technical and economic objectives in a residential microgrid (MG) with ESS by using GA to develop an EMS. The optimal charging/discharging of EVs to minimize electricity bill during valley hours as well as incentive-based allocation of energy storages' power capacity to provide ASs to the grid by either supplying or absorbing power are considered as additional constraints in the optimization problem. Moreover, the grid congestion constraint of peak-shaving is also included in the optimization problem to observe different scenarios. Finally, a real-life case study is analysed in which both technical and economic objectives are validated by performing the GA.

$$P_{AS\_up}(h) \leq RP_{up}(h) \tag{11}$$

$$P_{AS\_down}(h) \leq \left| -RP_{down}(h) \right| \tag{12}$$

Here, PAS_up and PAS_down defines the maximum available power allocated for the AS by either supplying or demanding from the grid respectively in kW that are obtained after performing GA. RPup and RPdown represents the reservation power (RP) that is available from the ESS to either increase or decrease the power respectively that are used to define the constraints before performing GA. The reservation price for DERs to provide ASs may be regulated by the Distributed System Operators (DSO) or traded in flexibility markets. This pricing is generally based on multiple bidding strategy which depends on the total production of electricity and the demand during a time slot. In this case study, the reservation allocation pricing for ASs is considered to be constant due to the simplicity of the optimization. The reservation allocation of the ESS depends on the prices offered by the DSO or cleared in the flexibility market. To guarantee the power reservation, constraints are added as shown in equations (11) and (12). The constraints are set in such a way that, the optimal values for the power to increase RPup and the power to decrease RPdown during the 24 hours depends on the distance to the extreme values of SoC and the maximum charging/discharging power PESSmax that limit these values. With this purpose, both reservation power PAS_up and PAS_down are obtained by the GA as optimization variables. The ESS can both supply the power to the grid when necessary to provide ASs as well as demand the power from the grid when required. The power reservation is compensated by means of a reservation price. In the case study, two different types of scenarios have been analysed based on the incentives provided during the allocation of the ESS power capacity. Two different prices have been used to analyse the optimization problem. The AS cost as a compensation payment determined in the flexibility market for the ESS owner to provide the reserved and allocated power is considered to be 50 €/MW/h and 250 €/MW/h. Later, the constraint of peak shaving is added to the optimization problem and the results are analysed in both cases.

In some cases, a penalty is introduced in case the peak power of the demand is exceeded. The penalty cost calculation can be determined by using the following equation.

$$Cost_{max}, P_h = K_p \cdot t_{ep}\sqrt{(P_h - P_c)^2} \tag{13}$$

where, P_c is the contracted power in kW (10kW in this case). Values for tep = 3.424853 and Kp (Tariff 3.0 TD, for consumers connected in LV, with 15 < Pc <100 kW) varies during the different hours of the day and months of the year as in Spanish tariffs.

Applying the above formula results in a total electricity bill of 65.28 €/day and for case 1 and 56 €/day case 2 respectively which is significantly higher than the electricity bill obtained with the peak shaving constraint. In both the cases, only when the peak power demanded exceeds the contracted power of 10kW, a penalty cost is applied according to the regulations determined by Spanish tariffs because it is unfair to the consumers to apply a penalty when supplying a power more than 10kW peak to the grid.

Some of the results discussed above have been demonstrated using the following table.

TABLE I
COMPARATIVE ANALYSIS OF RESULTS

Case number	**0**	**1**	**2**	**1**	**2**
Description	Without ESS (base)	Compn. 50 €/MW/h	Compn. 250 €/MW/h	Compn. 50 €/MW/h + peak shaving (12)	Compn. 250 €/MW/h + peak shaving (12)
SC (%)	59.87	44.62	41.66	**68.42**	64.54
SS (%)	33.89	30.06	28.07	**46.10**	43.48
Electricity bill (€/day)	23.47	14.75	**7.76**	20.1	13.13
Cost saving (%)	0	37.12	**66.92**	14.36	44.1
Extreme power peak (kW)	-36.44	-27.05	-24.94	**-10**	**-10**
P_{AS_up} (kW)	0	0.76	**1.35**	0.09	0.87
P_{AS_down} (kW)	0	0.45	**1.37**	0.76	0.58

In order to provide ancillary services based on incentives or compensation, this study suggests a novel EMS for a residential MG. The ESS reserves an allocated power capacity to participate in the flexibility markets and either supplies or demands the power from the distribution grid. A novel aspect of this study is the inclusion of the best time to schedule EV charging and discharging during valley hours in addition to traditional DERs and residential loads. Additionally, ESS power capacity is reserved. Lastly, an analysis and comparison of the optimization outcomes in various circumstances are conducted. We can conclude that the optimization problem as discussed in case 2 shows the most promising results, with the total bill reduced by 66.92%, when a high compensation is offered for the power reservation and there are no restrictions on the peak power that consumers can demand. In contrast to other circumstances, cost savings are unappealing if there is little incentive to offer auxiliary services.

4.2.3 Guidelines for the Application of Genetic Algorithm

The main novelty of this study [42] is the function of different parameters used in a genetic algorithm, and to find out the best set of parameters in terms of electricity cost reduction, that can be later used as guidelines to design similar types of systems. Simulations are carried out using the genetic algorithm solver that is part of the global optimization toolbox of MATLAB. In this study, we performed four groups of 36 simulations. The simulations are grouped to study the influence of the population size and the number of generations. On the one hand, increasing the first one leads to a broader exploration of solutions during the optimization process. On the other hand, better solutions can be found in subsequent iterations. Therefore, it is expected that increasing these parameters will lead to a better solution. The parameters of population size and number of iterations for each group of simulations are listed in Table 2. Moreover, for each group of simulations, the parameters considered for the study are the following: two crossover operators, three probability values for crossover, two selection operators, and three probability values for the mutation. The mutation operator is fixed, as this is the only option that guarantees the feasibility of the solution, in other words, the constraints of the problem are satisfied. The parameters used for the simulations are summarized in Table 2, and details regarding each operator can be found in.

Table 2. Population and iterations for each group.

Group	Population size	Number of iterations
1	100	200
2	100	500
3	500	200
4	500	500

Table 3. List of parameters analyzed in each group of simulations.

Parameter	Values
Crossover operator	Scattered, Intermediate
Probability of crossover	0.2, 0.5, 0.8
Selection operator	Stochastic-uniform, Roulette-wheel
Mutation operator	Adaptable-Feasible
Probability of mutation	0.2, 0.5, 0.8

The profiles of load consumption, PV generation, and the grid power without any support from storage units are shown in Figure 3, and in this case, the total operation cost results in €2.114 at the end of the day.

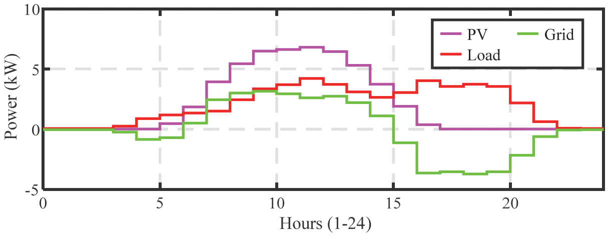

Figure 7. Power profiles for the system without storage units.

The results of group 4 are presented in Table 2, where the best solution corresponds to €0.938, using the Intermediate operator for crossover, and the stochastic-uniform selection. The probabilities of crossover and mutation are set to 80%. In contrast, the worst result is of €1.16 using the scattered crossover and stochastic-uniform selection operators with probabilities of crossover and mutation of 20% for both parameters.

Table 4. Results for simulations of group 4.

Crossover		**Scattered**			**Intermediate**		
P_c^a (%)		**20**	**50**	**80**	**20**	**50**	**80**
Selection		**Stochastic-uniform**					
P_m^b(%)	**20**	1.160	1.053	1.083	0.961	0.986	1.079
	50	1.006	0.979	1.019	0.991	1.128	1.017
	80	1.045	1.067	0.986	0.997	1.035	0.938
Selection		**Roulette-wheel**					
P_m (%)	**20**	0.990	1.111	0.954	1.096	0.960	0.995
	50	0.967	0.997	1.014	0.983	0.972	0.990
	80	0.989	0.993	1.044	0.949	0.958	1.063

The power profiles of the system under study and the SoC of the storage units, for the best result, are shown in Figure 8(a) and Figure 8(b), respectively. In the early hours of the day, power from the grid is taken to charge both the battery and the EV. Later, from t =9 h to t = 15 h, the battery is charged up to its full capacity, and then at t= 17 h, the battery is well utilized to support the load demand during the last hours of the day, when the price reaches the highest values. Moreover, during the last hours of the day the energy interchanged with the grid is reduced compared to the case where the battery is not available. Regarding the SoC profiles, both constraints are satisfied, the electric vehicle is completely charged at = 8h, and the battery SoC reaches 50% at the end of the day.

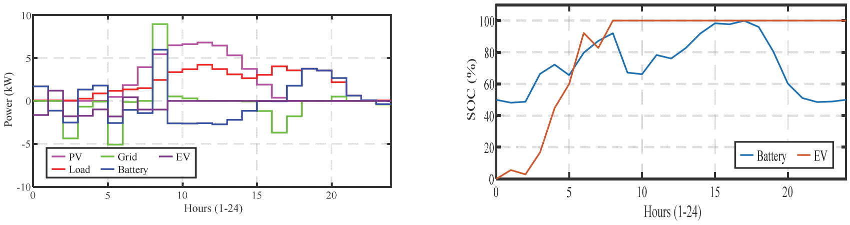

(a) (b)

Figure 8. Simulation of best result case among all groups. (a) Power profiles (b) State of charge of storage units.

Additionally, a comparison of results among the groups was carried out, and the results are summarized in Table 5. The best solutions for each group are shown and the average values and the standard deviation for the 36 simulations in each group are also shown. For each of the best solutions, the corresponding set of options is shown. It is worth noting that, as expected, having more individuals and iterations gives the best result. However, the standard deviation indicates that more consistent results are obtained when the number of iterations is increased, regardless of the number of individuals. Moreover, for three groups, the best results are obtained using the stochastic-uniform selection operator and intermediate crossover operator.

Table 5. Comparison between groups.

Group	Best (€)	Avg.	Standard Deviation	P_c. (%)	P_m (%)	Sel.	Cross.
1	1.0647	1.213	0.076	50	20	*S-u*	*In.*
2	0.958	1.031	0.041	20	80	*S-u*	*Sc.*
3	0.979	1.117	0.087	50	20	*Ro.*	*In.*
4	0.938	1.015	0.054	80	80	*S-u*	*In.*

* *S-u*: Stochastic-uniform, *Ro:* Roulette wheel, *Sc*: Scattered, *In*: Intermediate.

The main contribution of this paper is to use different parameters used in genetic algorithm in a typical energy management system consisting of PV generation, household load, energy storage system and electric vehicle and find out the best set of parameters used in the algorithm solver among two crossover operators, three probability values for crossover, two selection operators, and three probability values for the mutation for the electricity cost reduction. that can be later used as a handbook to design similar types of systems. It can be concluded that, Using the stochastic-uniform selection and the Intermediate operator for crossover, the optimal solution comes out to be €0.938. 80% is the fixed value for the crossover and mutation probabilities. On the other hand, with 20% chances of crossover and mutation for both parameters, the worst outcome obtained with the dispersed crossover and stochastic-uniform selection operators is €1.16. Moreover, higher individuals and iterations yield the best outcome. Regardless of the number of individuals, the standard deviation suggests that increasing the number of iterations yields more consistent findings. This paper will pave the way for designing energy management systems more efficiently. using genetic algorithm and can be used a guideline in terms of the selection of parameters.

4.2.4 Novel Iteration Based Two-Stage Optimization

The study [43] proposes an energy management system for a residential microgrid that includes household loads, photovoltaic generation, energy storage systems and electric vehicles. The economic objective of reducing electricity bill is achieved by designing and testing a novel two-stage optimization consisting of genetic algorithm and gradient based method with suitable parameters to define new set-points of operation for the energy storage systems and the charging/discharging of electric vehicles that can significantly reduce the simulation time as well as solve the problem of not complying with the constraints of genetic algorithm.The different stages of optimization process is illustrated by means of a flowchart in Figure 9.

This study presents a novel approach of integrating the economic objective of price reduction in a residential microgrid (MG) with ESS by developing an EMS utilizing two stage optimizations. The optimal charging/discharging of EVs to minimize electricity bill during valley hours as well as scheduling the energy storages' power to the grid by either supplying during peak hours or demanding power during valley hours are considered as additional constraints in the optimization problem. Moreover, two stage optimizations are performed for an increased reduction of electricity bill by performing GA in the first stage.

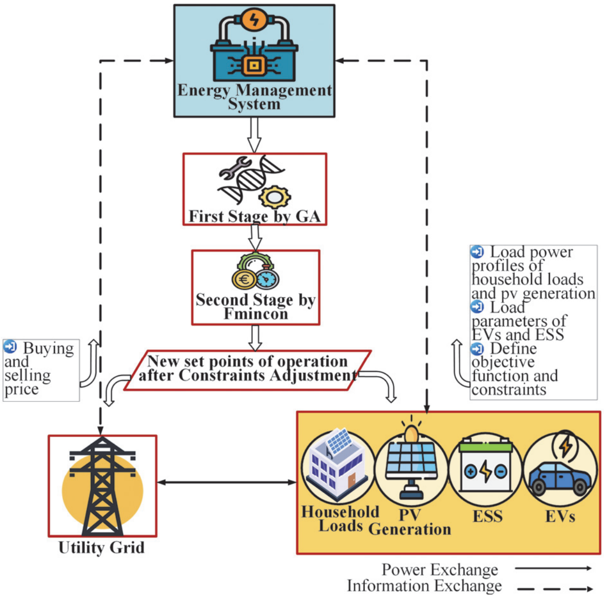

Figure 9. Strategy of two-stage optimization procedure

It can be observed that the results are random each time the algorithm is performed. And so, 1000 iterations are performed and then GBM (Fmincon) is used due to the fast computational nature in the second stage optimization. If any constraints are not met, they are fulfilled analogously. Finally, a real-life case study is analysed in which the economic objectives and the set constraints are validated.

The objective function and its constraints related to the 2nd stage optimization of gradient based method is based on the equations (10-13).

$$min\ f_2(x) = \sum_{h=1}^{24}[f_1(h)] \tag{14}$$

The objective function f_2 is the function to be minimized, typically representing a cost objective in which the output is fed from the 1st stage optimization of GA. The constraints related to the SoC of the ESS and EVs are considered to be the same as before for this optimization problem. Here, x can be defined as:

$$x_{k+1} = x_k - \alpha \nabla F(x_k) \tag{15}$$

Here, $x_k$is the decision variable at iteration k, representing power dispatch decisions, α is the step size (learning rate) and $\nabla F(x_k)$ is the gradient of the objective function, given by:

$$\nabla F(x) = \frac{\partial F(x)}{\partial P_{grid}(h)} \tag{16}$$

For each time step h,

$$\frac{\partial F}{\partial P_{grid}(h)} = I_{pur}(h) \cdot p_{pur}(h) - I_{sel}(h) \cdot p_{sel}(h) \tag{17}$$

Finally, after the 2nd stage optimization, it can be observed that the constraint of the SoC of the EV is not totally fulfilled. The following equation (14) is used to analogously fulfil the required constraint of EVs.

$$E_{EVtotal} = E_{EVtotal} + \max\,(0{,}30000 - E_{EVtotal}) \tag{18}$$

Here, if the total SoC of the EVs do not reach 30 kWh at the end of 8 hours, then the rest of the power is supplied from the grid to charge them 100% during the last hour (7h to 8 h). This occurs due to the absence of “MaxTime” in the GA options. In this way it is possible to reduce simulation time but there is the trade-off of not meeting certain constraints.

To obtain the lowest possible cost, given the random nature of the optimization, the GA together with GBM optimization procedure have been executed 1000 times, with the following results in Figure 10: It can be observed that after 1000 iterations, the SoC constraint of the EVs are not met even for a single time. Hence, it is a necessity to adjust the SoC during the last hour of the EVs charging duration. After these number of attempts, the following minimum prices are obtained:

- Before (Only GA): 17.9375 euros (on iteration 703).
- After 1st Stage (GA + F_{mincon}): 16.7925 euros (in iteration 51).
- After 2nd Stage (GA + F_{mincon} + SoC Adjustment): 17.7674 euros (in iteration 51).

Iteration 51 is considered as the best-case scenario for the case study since the cost is lowest after fulfilling the SoC constraint of the EVs in this case as obtained from Figure 10. The reference solution (attempt 51) is shown in Figure 11.

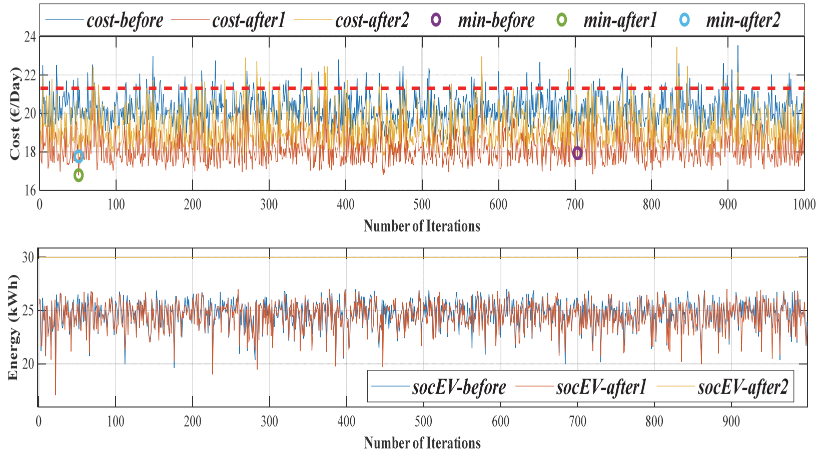

Figure 10. Number of iterations versus change in cost

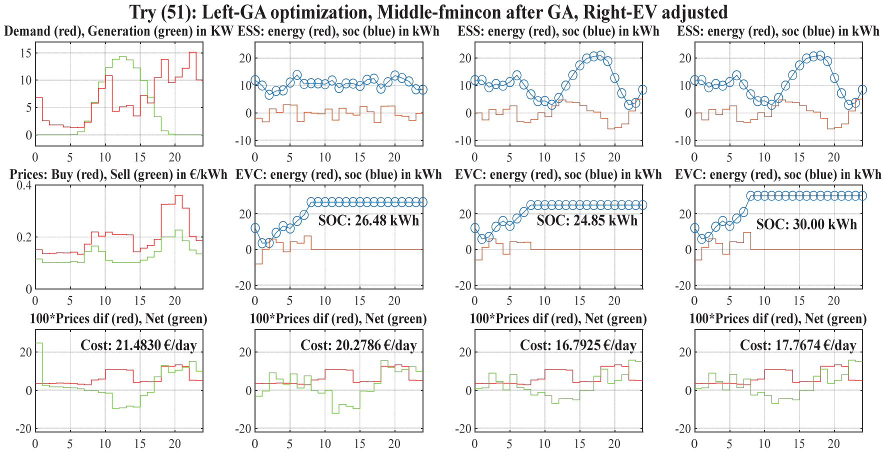

Figure 11. References for the most optimized solution

4.2.4.1 Results Findings:

1. The SoC of the EVs after 2nd stage must be equal to 30kWh and it cannot be greater or lesser.
2. The first step of the optimization process can result in a minimum cost (Before) being lower than the reference in 92.7% of the total cases.
3. It is worth highlighting how it is possible to achieve a minimum price of 18 euros, complying with the requirement of having fully charged electric vehicles

up to 30 kWh. Based on this test, it was decided to take a minimum reference target price of 18 euros.

4. An estimated price improvement of about 3.5 euros (17%) can be achieved.
5. There are attempts that result in a cost higher than the reference cost; these attempts should be discarded, not considering them as valid attempts.
6. The third step (manual adjustment of the state of charge of electric vehicles) is necessary since in most cases with only two steps this constraint has not been guaranteed, remaining below the target value.
7. The minimums in the different steps are not achieved in a coordinated manner in the same attempt, therefore the attempts must be complete, including the three steps. From this moment on, the minimum cost to consider will be the after GBM (Fmincon) cost.
8. With the first and second steps, the charging restriction is not met, leaving the cars charged at an average value of 27 kWh (26.48 kWh for the first step, and 24.85 kWh for the second step). This effect appears to be due to differences in efficiency between charging and discharging.
9. After analysing the results in Figure 6, it can be found that the second step manages to reduce the cost of the first in 99.4% of the cases, while the third only achieves it in 96.8%, since by forcing compliance with the load restriction it forces to purchase the power defect in the load. The second step (After1) manages to reduce the cost on average by 0.7352 euros (4% approx.)
10. The time required to perform the simulation after considering "MaxTime" option in the GA to fully comply with the charging constraint of the EVs takes between 35 to 40 minutes whereas in the proposed method, excluding this option the time required to perform 1000 cases is approximately 4 hours and 6 minutes. However, it can be observed that 40 iterations give satisfactory results which takes 6 minutes and 21 seconds approximately. So, this method reduces the simulation time by more than 75%.

4.2.4.2 Validation using PLECS Simulation Model

This section [44] consists of the validation of the obtained set points of operation after performing the optimization by using a detailed system model that incorporates PECs along with their associated low-level controllers. The simplified diagram of the developed model is shown in Figure **12** depicts a residential grid-connected system with PV generation and a lithium-ion battery serving as the ES device for this study.

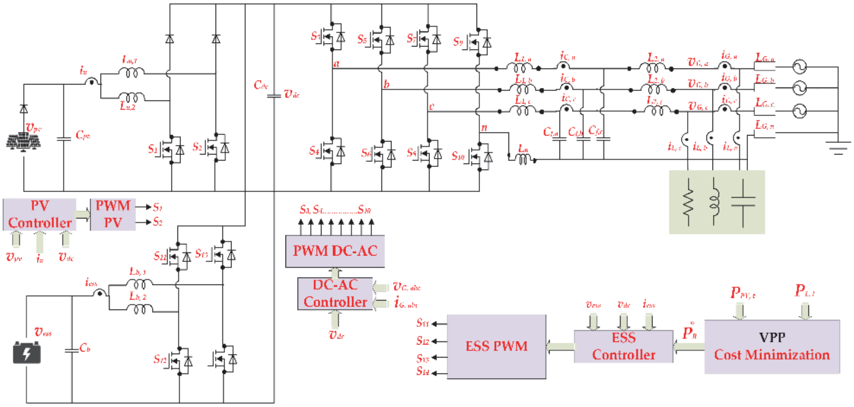

Figure 12. Schematic diagram of the residential system under study

A bidirectional DC–DC converter links the battery to the DC bus, while a boost converter connects the photovoltaic (PV) module to the system. In operation, both DC–DC converters employ an interleaved configuration. This topology was chosen due to its ability to reduce the current stress on semiconductor devices. Furthermore, interleaving allows the filter size to be reduced by a factor of four while maintaining the same input current ripple as conventional converter configurations.

4.3 Business Model for Virtual Power Plants

The graphical user interface based VPP Digital Twin is developed by using MATLAB App Designer. In the GUI, it is possible to define the number of VPPs and MGs. So, from the user's perspective, only the number of VPPs and MGs should be defined. In the initial version, a single VPP can control a maximum of two MGs. However, in the final version of the software, an infinite number of MGs can be controlled by the VPPs in which each element such as ESS, EVs, PV generation of the MGs can be also inputted into the system by the user. The basic UI of the VPP Digital Twin is shown below in Figure **13** and Figure **14**.

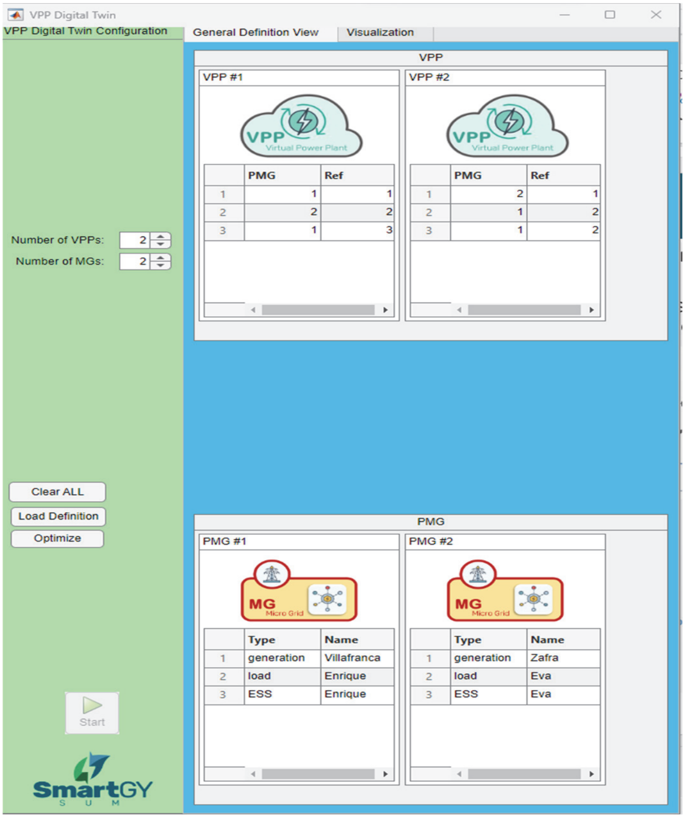

Number of VPPs: 2

Number of MGs: 2

VPP #1

	PMG	Ref
1	1	1
2	2	2
3	1	3

VPP #2

	PMG	Ref
1	2	1
2	1	2
3	1	2

PMG #1

	Type	Name
1	generation	Villafranca
2	load	Enrique
3	ESS	Enrique

PMG #2

	Type	Name
1	generation	Zafra
2	load	Eva
3	ESS	Eva

Figure 13. Graphical User Interface of VPP

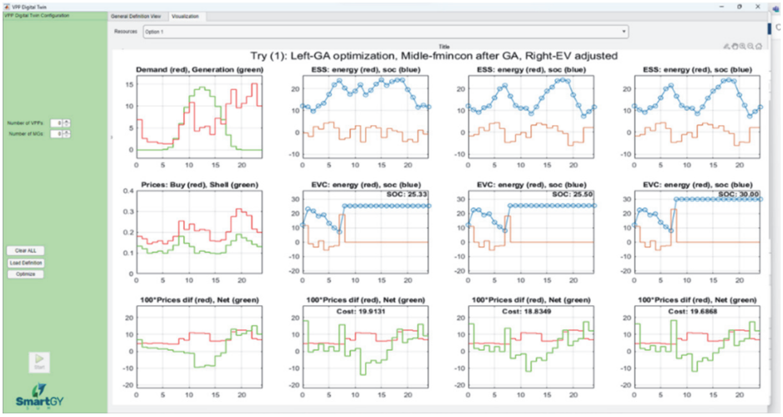

Resources: Option 1

Number of VPPs: 0

Number of MGs: 0

Figure 14. References for the most optimized solution in GUI

First the definitions of the VPPs and MGs must be loaded in the application. Then after optimizing the system, the results can be found in the visualization section as shown below. In this section, all the optimized results as discussed in the above section can be found as desired.

4.3.1 VPPEC Introduction

The name of the application is chosen as VPPEC (Virtual Power Plant for Cost Efficiency) in which the motto is chosen as “Providing Economican Energy for All”. Some of the main features of the application are given below:

- Price Minimization of up to 15%
- Price Minimization of up to 44.1% (Peak Shaving Constraint)
- Price Minimization of up to 66.92% (Providing Ancillary Services)
- User friendly interface
- Personalized services
- Eco-Friendly Solution
- Social Awareness

4.3.2 Market and Impact on Society

VPPs enable market participation for smaller producers, offering ancillary services, peak shaving, demand response, and grid stabilization. In diversified markets, VPPs improve resilience, flexibility, and cost efficiency by dynamically coordinating varied resources. The current VPP Market is USD 48 Million in Spain and USD 1951.2 million globally in which the main customers are commercial VPP users, DSOs and aggregators. The current EMS Market is USD 143.1 Million in Spain and USD 57.33 Billion globally mostly for the EMS Users as shown in Figure 15.

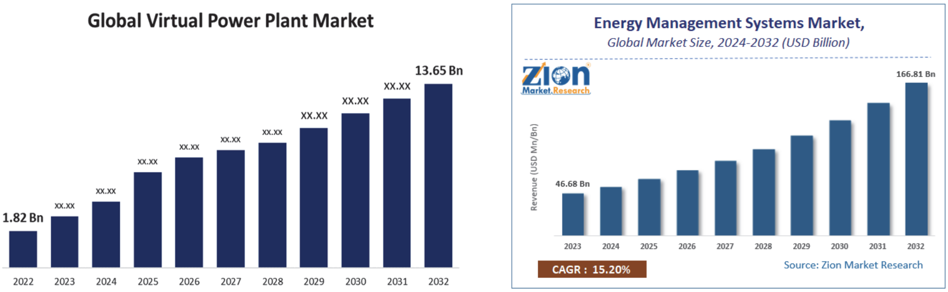

Figure 15. Global VPP and EMS Market

The main business plan is based on the following:

- Initial Application License fee: Ranging from Entry Level at 100 Euro and Premium at 500 Euro.
- Subscription model: 20 or 50 Euro/Month
- 1st year forecast: 1000 Customers at Break-Even (€492K)
- 2nd year forecast: 3000 Customers with a Net profit of €296K (€1.48M)

- 3rd year forecast: 10000 Customers with a Net profit of €984K (€4.92M)
- Equity Share: 20% Share for 50,000 Euros

Conclusions

To conclude, the obtained reference set-points obtained from the developed algorithm were validated by using PLECS simulation model in which there was less than 5% difference which can be considered as negligible.

Acknowledgement

This project has received funding from the European Union's Horizon 2020 research and innovation programme under the Marie Skłodowska-Curie grant agreement No 955614.

References

1. Rathor, Sumit K., and D. Saxena. "Energy management system for smart grid: An overview and key issues." International Journal of Energy Research 44.6 (2020): 4067-4109.
2. Leonori, Stefano, Maurizio Paschero, Fabio Massimo Frattale Mascioli, and Antonello Rizzi. "Optimization strategies for Microgrid energy management systems by Genetic Algorithms." Applied Soft Computing 86 (2020): 105903.
3. Osaba, Eneko, et al. "A tutorial on the design, experimentation and application of metaheuristic algorithms to real-world optimization problems." Swarm and Evolutionary Computation 64 (2021): 100888.
4. Dua, Vivek, Nikolaos A. Bozinis, and Efstratios N. Pistikopoulos. "A multiparametric programming approach for mixed-integer quadratic engineering problems." Computers & Chemical Engineering 26.4-5 (2002): 715-733.
5. S. Katoch, S. S. Chauhan, and V. Kumar, "A review on genetic algorithm: past, present, and future," Multimed Tools Appl, vol. 80, no. 5, pp. 8091–8126, Feb. 2021, doi: 10.1007/s11042-020-10139-6.
6. G. K. Venayagamoorthy, R. K. Sharma, P. K. Gautam, and A. Ahmadi, "Dynamic Energy Management System for a Smart Microgrid," IEEE Transactions on Neural Networks and Learning Systems, vol. 27, no. 8, pp. 1643–1656, Aug. 2016, doi: 10.1109/TNNLS.2016.2514358.
7. M. F. Zia, E. Elbouchikhi, and M. Benbouzid, "Microgrids energy management systems: A critical review on methods, solutions, and prospects," Applied Energy, vol. 222, pp. 1033–1055, Jul. 2018, doi: 10.1016/j.apenergy.2018.04.103.

8. D. H. Wolpert and W. G. Macready, "No free lunch theorems for optimization," in IEEE Transactions on Evolutionary Computation, vol. 1, no. 1, pp. 67-82, April 1997, doi: 10.1109/4235.585893.
9. Y. E. García Vera, R. Dufo-López, and J. L. Bernal-Agustín, “Energy Management in Microgrids with Renewable Energy Sources: A Literature Review,” Applied Sciences, vol. 9, no. 18, Art. no. 18, Jan. 2019, doi: 10.3390/app9183854.
10. International Organization for Standardization, “ISO 9241-210:2019,” ISO, 2019. https://www.iso.org/standard/77520.html
11. Salmon, “What is an energy management system?” MRI Software, Jun. 27, 2023.
12.] K. Zhou, S. Yang, 5.11 Smart Energy Management, Comprehensive Energy Systems, 2018, pp. 423–456, https://doi.org/10.1016/B978-0-12-809597-3.00525-3.
13. A. Lambora, K. Gupta and K. Chopra, "Genetic Algorithm- A Literature Review," 2019 International Conference on Machine Learning, Big Data, Cloud and Parallel Computing (COMITCon), Faridabad, India, 2019, pp. 380-384, doi: 10.1109/COMITCon.2019.8862255.
14. Holland, J. H. (1992). Genetic algorithms. *Scientific American*, *267*(1), 66–73.
15. Genlin, J. (2004). Survey on genetic algorithm. *Computer Applications and Software*, *2*, 69–73.6. Goldberg, D. E. (1990). A note on Boltzmann tournament selection for genetic algorithms and population-oriented simulated annealing. *Complex Systems*, *4*(4), 445–460.
16. Alvi, A.A., Romero-Cadaval, E., González-Romera, E., Hassan, J., Vinnikov, D. (2023). An Overview of the Functions of Smart Grids Associated with Virtual Power Plants Including Cybersecurity Measures. In: Camarinha-Matos, L.M., Ferrada, F. (eds) Technological Innovation for Connected Cyber Physical Spaces. DoCEIS 2023. IFIP Advances in Information and Communication Technology, vol 678. Springer, Cham. https://doi.org/10.1007/978-3-031-36007-7_7
17. Mirjalili, Seyedali, and Seyedali Mirjalili. "Genetic algorithm." *Evolutionary algorithms and neural networks: Theory and applications* (2019): 43-55.
18. Goldberg, D. E. (1990). A note on Boltzmann tournament selection for genetic algorithms and population-oriented simulated annealing. Complex Systems, 4(4), 445–460.
19. Miller, B. L., & Goldberg, D. E. (1995). Genetic algorithms, tournament selection, and the effects of noise. *Complex Systems*, *9*(3), 193–212.
20. Kumar, R. (2012). Blending roulette wheel selection & rank selection in genetic algorithms. *International Journal of Machine Learning and Computing*, *2*(4), 365.
21. Syswerda, G. (1991). A study of reproduction in generational and steady-state genetic algorithms. In *Foundations of genetic algorithms* (Vol. 1, pp. 94–101). Elsevier.
22. Blickle, T., & Thiele, L. (1996). A comparison of selection schemes used in evolutionary algorithms. *Evolutionary Computation*, *4*(4), 361–394.
23. Collins, R. J., & Jefferson, D. R. (1991). *Selection in massively parallel genetic algorithms* (pp. 249–256). University of California (Los Angeles), Computer Science Department.

24. Srinivas,M., & Patnaik, L.M. (1994). Genetic algorithms: A survey. *Computer*, *27*(6), 17–26.
25. Deep, K., & Thakur, M. (2007). A new mutation operator for real coded genetic algorithms. *Applied Mathematics and Computation*, *193*(1), 211–230.
26. Srinivas, M., & Patnaik, L. M. (1994). Adaptive probabilities of crossover and mutation in genetic algorithms. *IEEE Transactions on Systems, Man, and Cybernetics*, *24*(4), 656–667.
27. Neubauer, A. (1997). A theoretical analysis of the non-uniform mutation operator for the modified genetic algorithm. In *IEEE International Conference on Evolutionary Computation* (pp. 93–96). IEEE.
28. Hinterding, R. (1995). Gaussian mutation and self-adaption for numeric genetic algorithms. In *IEEE International Conference on Evolutionary Computation* (Vol. 1, p. 384). IEEE.
29. Tsutsui, S., & Fujimoto, Y. (1993). Forking genetic algorithm with blocking and shrinking modes (fGA). In *ICGA* (pp. 206–215).
30. Oosthuizen, G. D. (1987). Supergran: A connectionist approach to learning, integrating genetic algorithms and graph induction. In *Proceedings of the second International Conference on Genetic Algorithms and their Applications*, July 28–31, 1987 at the Massachusetts Institute of Technology, Cambridge, MA. Hillsdale, NJ: L. Erlhaum Associates.
31. Mauldin, M. L. (1984). Maintaining diversity in genetic search. In *AAAI* (pp. 247–250).
32. Ankenbrandt, C. A. (1991). An extension to the theory of convergence and a proof of the time complexity of genetic algorithms. In *Foundations of genetic algorithms* (Vol. 1, pp. 53–68). Elsevier.
33. A. Arabali, M. Ghofrani, M. Etezadi-Amoli, M. S. Fadali and Y. Baghzouz, "Genetic-Algorithm-Based Optimization Approach for Energy Management," in IEEE Transactions on Power Delivery, vol. 28, no. 1, pp. 162-170, Jan. 2013, doi: 10.1109/TPWRD.2012.2219598.
34. Leonori, S., Paschero, M., Mascioli, F. M. F., & Rizzi, A. (2020). Optimization strategies for Microgrid energy management systems by Genetic Algorithms. *Applied Soft Computing*, *86*, 105903. https://doi.org/10.1016/j.asoc.2019.105903
35. Torkan, R., Ilinca, A., & Ghorbanzadeh, M. (2022). A genetic algorithm optimization approach for smart energy management of microgrids. *Renewable Energy*, *197*, 852-863. https://doi.org/10.1016/j.renene.2022.07.055
36. M. Elsied, A. Oukaour, H. Gualous, R. Hassan and A. Amin, "An advanced energy management of microgrid system based on genetic algorithm," 2014 IEEE 23rd International Symposium on Industrial Electronics (ISIE), Istanbul, Turkey, 2014, pp. 2541-2547, doi: 10.1109/ISIE.2014.6865020.
37. U. Latif, N. Javaid, S. S. Zarin, M. Naz, A. Jamal and A. Mateen, "Cost Optimization in Home Energy Management System Using Genetic Algorithm, Bat Algorithm and Hybrid Bat Genetic Algorithm," 2018 IEEE 32nd International Conference on Advanced Information Networking and Applications (AINA), Krakow, Poland, 2018, pp. 667-677, doi: 10.1109/AINA.2018.00102.

38. Lü, X., Wu, Y., Lian, J., Zhang, Y., Chen, C., Wang, P., & Meng, L. (2020). Energy management of hybrid electric vehicles: A review of energy optimization of fuel cell hybrid power system based on genetic algorithm. *Energy Conversion and Management*, *205*, 112474. https://doi.org/10.1016/j.enconman.2020.112474
39. Wieczorek, M., & Lewandowski, M. (2017). A mathematical representation of an energy management strategy for hybrid energy storage system in electric vehicle and real time optimization using a genetic algorithm. *Applied energy*, *192*, 222-233. https://doi.org/10.1016/j.apenergy.2017.02.022
40. A. A. Alvi, E. Romero-Cadaval, E. González-Romera, D. Vinnikov and J. Hassan, "Performance Evaluation of a Three-Phase PV Power Plant under Unbalanced Conditions with Islanding Detection Reliability Test," 2023 IEEE 17th International Conference on Compatibility, Power Electronics and Power Engineering (CPE-POWERENG), Tallinn, Estonia, 2023, pp. 1-6, doi: 10.1109/CPE-POWERENG58103.2023.10227391.
41. A. A. Alvi, E. González-Romera, E. Romero-Cadaval, D. Vinnikov, M. I. Milanés-Montero and F. Barrero-González, "An Economical Optimization for the Participation of a Residential Microgrid in Flexibility Markets Providing Ancillary Services," 2024 IEEE 18th International Conference on Compatibility, Power Electronics and Power Engineering (CPE-POWERENG), Gdynia, Poland, 2024, pp. 1-6, doi: 10.1109/CPE-POWERENG60842.2024.10604394.
42. A. A. Alvi, L. Martínez-Caballero, E. Romero-Cadaval, E. González-Romera, R. Kot and M. Malinowski, "Guidelines for the Application of Genetic Algorithm in Energy Management System," IECON 2024 - 50th Annual Conference of the IEEE Industrial Electronics Society, Chicago, IL, USA, 2024, pp. 1-6, doi: 10.1109/IECON55916.2024.10905264.
43. A. A. Alvi, E. Romero-Cadaval, E. González-Romera, M. I. Milanés-Montero, F. Barrero-González and L. Martínez-Caballero, "A Novel Iteration Based Two-Stage Optimization in Energy Management Systems Application For Cost Minimization," 2025 IEEE 19th International Conference on Compatibility, Power Electronics and Power Engineering (CPE-POWERENG), Antalya, Turkiye, 2025, pp. 1-6, doi: 10.1109/CPE-POWERENG63314.2025.11027217.
44. Alvi, A.A.; Martínez-Caballero, L.; Romero-Cadaval, E.; González-Romera, E.; Malinowski, M. Iterative Genetic Algorithm to Improve Optimization of a Residential Virtual Power Plant. Energies 2025, 18, 5377. https://doi.org/10.3390/en18205377

MMC Submodule Capacitor Condition Monitoring Considering both *C* and ESR

Shuyu Ou[1], Mahyar Hassanifar[2], Martin Votava[2], Ariya Sangwongwanich[1],
Subham Sahoo[1], Marius Langwasser[2]and Marco Liserre[23], and Frede Blaabjerg[1],

[1] Energy Department, Aalborg University, Pontoppidanstræde 111, 9220 Aalborg Øst, Denmark
[2] Chair of Power Electronics, Kiel University, Kaiserstr. 2, 24143 Kiel, Germany
[3] Fraunhofer Institute for Silicon Technology (ISIT), Kaiserstr. 4, 24143 Kiel, Germany
{so, sssa, ars, fbl}@energy.aau.dk
{mha, mvo, mlan, ml}@tf.uni-kiel.de

Abstract. This chapter proposes a data-driven condition monitoring method for aluminum electrolytic capacitors in modular multilevel converters, with a focus on jointly estimating capacitance and equivalent series resistance (ESR). Unlike conventional approaches that assume ESR is negligible, the proposed method incorporates the coupling effect between capacitance and ESR using a capacitor voltage model and particle swarm optimization (PSO). The method achieves higher estimation accuracy, especially under ESR degradation, and demonstrates that neglecting ESR may lead to incorrect condition assessments. It is validated through experiments on a mission-profile emulator and implementation on a digital signal processor (DSP), highlighting its suitability for edge applications. Comparative analysis with other methods confirms its balanced trade-off between accuracy, computational time, and memory usage.

Keywords: Condition monitoring, MMC, capacitor, PSO.

1 Introduction

Condition monitoring methods are employed to evaluate the health status of the critical components, aiming to mitigate the risk of unplanned failures. In this context, the focus is placed on the submodule capacitor within a modular multilevel converter (MMC), which is of particular interest due to its pivotal role and the high component count inherent in MMC architectures, thereby posing significant reliability challenges [1],[2]. More specifically, the focus of this study is on aluminum electrolytic capacitors, which are widely used due to their low-cost, high power density, and high energy storage capability [3].

Existing condition monitoring methods for capacitors in MMC can be broadly classified into model-based and data-driven methods, as summarized in Table 1. Model-based methods rely on analytical formulations and typically utilize features such as harmonic components in voltage and current [2],[4], voltage ripple characteristics [5], and submodule conduction time [6]. These methods are generally characterized by

Table 6. Existing condition monitoring methods of capacitor in MMC.

Type	Method	Advantage	Disadvantage
Model-based	[2] Use harmonics to estimate *C*	Non-invasive, low computation	Neglecting coupling between *C* and ESR
	[4] Use harmonics to estimate *C*		
	[5] Use voltage ripples to estimate *C*		
	[6] Use conduction time to estimate *C*		
Data-driven	[7] RLS regression for *C*	Robust, accurate	Invasive, training dataset, heavy computation
	[8] WD of the charging transient for ESR		
	[9] WD and CNN for *C* and ESR		

C: Capacitance; ESR: Equivalent-series resistance; WD: Wavelet decomposition; CNN:

low computational requirements and reduced dependency on extensive measurements. However, they are built upon a fundamental assumption that the capacitance (*C*) dominates the impedance, while the equivalent series resistance (ESR) is considered negligible. According to existing methods, this assumption has not been rigorously validated, and its continued use may undermine the accuracy and robustness of condition monitoring results.

Meanwhile, data-driven methods offer the advantage of incorporating ESR estimation by analyzing charging transients, typically measured via additional sensing circuits. Representative techniques include recursive least-square (RLS) [7], wavelet decomposition (WD) [8], and convolution neural network (CNN) [9], which demonstrate improved robustness and accuracy under varying operational conditions. However, these methods generally impose higher computational demands and necessitate supplementary measurement hardware. In particular, CNN-based methods relies on supervised learning, which requires large-scale labeled degradation datasets that span diverse operating scenarios, such as different power levels and ambient temperatures. Acquiring such comprehensive datasets is often time-consuming and resource-intensive, which contributes to the scarcity of publicly available open-source datasets [10].

Based on these observations, there is a need to enhance condition monitoring methods through two key strategies. First, by explicitly incorporating the coupling effect between capacitance and ESR, which is expected to improve the accuracy and reliability of parameter estimation. Second, by adopting computationally efficient algorithms to minimize the demand for processing resources.

Therefore, the coupling between the capacitor parameters is analyzed by modeling them through the capacitor voltage equation. This equation reveals the capacitance contributes to the accumulated variation in capacitor voltage, whereas ESR primarily influences the instantaneous voltage during charging transients. Building on this analysis, a particle swarm optimization (PSO)-based method is proposed to estimate both capacitance and ESR simultaneously.

The remainder of this chapter is organized as follows: Section 2 presents the MMC system architecture and its operational principles. Section 3 details the proposed condition monitoring method. Validation results and comparative analyses are discussed in Sections 4 and 5, respectively. Finally, Section 6 concludes the study and outlines potential directions for future research.

2 System Description

As shown in Fig. 1(a), the modular multilevel converter (MMC) is typically connected between the AC grid (v_a, v_b, v_c) and the DC side (V_{dc}), incorporating a grid-side filter — comprising an inductance L_f and resistance R_f — as well as an arm filter with inductance L_{arm}, and a series of submodules (SM) in each arm. Each submodule adopts a half-bridge configuration, consisting of two insulated gate bipolar transistors (IGBTs), denoted as S_1 and S_2, and two free-wheeling diodes, D_1 and D_2.

The monitored aluminum electrolytic capacitors, denoted as C_{SM}, in Figs. 1(b) and (c), can be represented by an equivalent electrical circuit consisting of a capacitance C, an equivalent series resistance (ESR), and an equivalent series inductance (ESL). The ESL component is typically negligible at frequency below several megahertz [7].

The primary failure mechanism of aluminum electrolytic capacitors is electrolyte evaporation [3], which results in a reduction in capacitance and an increase in ESR. The end-of-life (EOL) criteria of C and ESR are defined as 80% and 200% of their initial value, respectively [3]. Accelerated aging experiments have demonstrated that these two health indicators typically reach their EOL at different times, as illustrated in Fig. 2. Specifically, in Fig. 2 (a), if only capacitance is monitored, the system continues operating during the interval between $t_{R\text{-}EOL}$ and $t_{C\text{-}EOL}$, potentially under degraded ESR conditions without detection.

To further analyze the available measurements related to the submodule capacitor, the capacitor voltage waveform are demonstrated in Fig. 3, where the submodule voltages in both upper and lower arms, denoted as v_{SMu} and v_{SMl}, are regulated by a submodule voltage balancing algorithm [11],[12]. The arm current i_{arm} corresponds to the submodule capacitor current when the switch is S_1 conducting.

3 Proposed Method

The proposed method estimates both the capacitance and ESR by leveraging a capacitor voltage model, time-domain voltage prediction, and a particle swarm optimization (PSO) algorithm, as depicted in Fig. 4. The specific functions of each component within the method are detailed in this section. For illustrative purposes, the following analysis focuses on a single submodule, specifically, one located in the upper arm of SM_1. Applying the method to other submodules is expected to require only minor modifications.

3.1 Input Signal

The input signals consist of a moving window of the submodule voltage v_{SM}, switching signal SW_1, and arm current i_{arm}.

To ensure stable parameter estimation, the input data is segmented into multiple overlapping windows with a fixed temporal shift. This approach reduces estimation variability while limiting the computational burden per execution. Based on systematic testing, each sampling window is set to 5 ms, and the total observation period spans 35 ms, as illustrated in Fig. 4 (a).

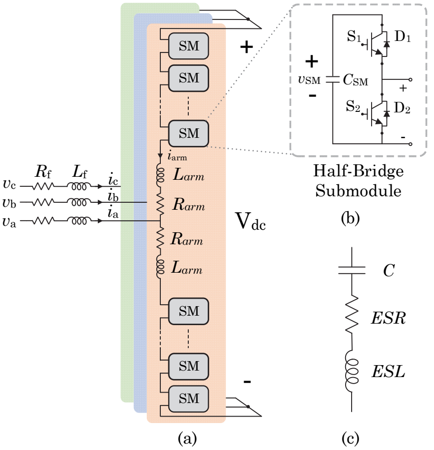

Fig. 15. MMC (a) Converter, (b) Submodule structure, and (c) Equivalent circuit of an electrolytic capacitor.

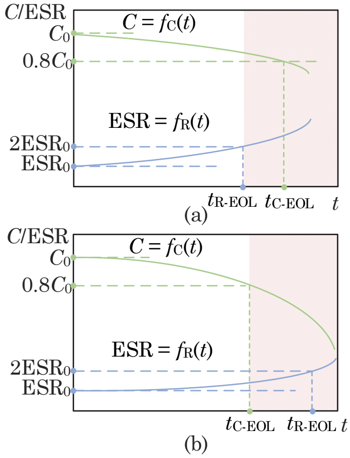

Fig. 2. During degradation, C and ESR shift gradually and eventually they can exceed the end-of-life criteria.

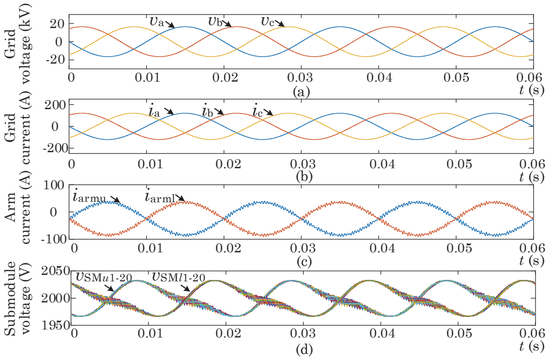

Fig. 3. Typical waveforms of MMC.

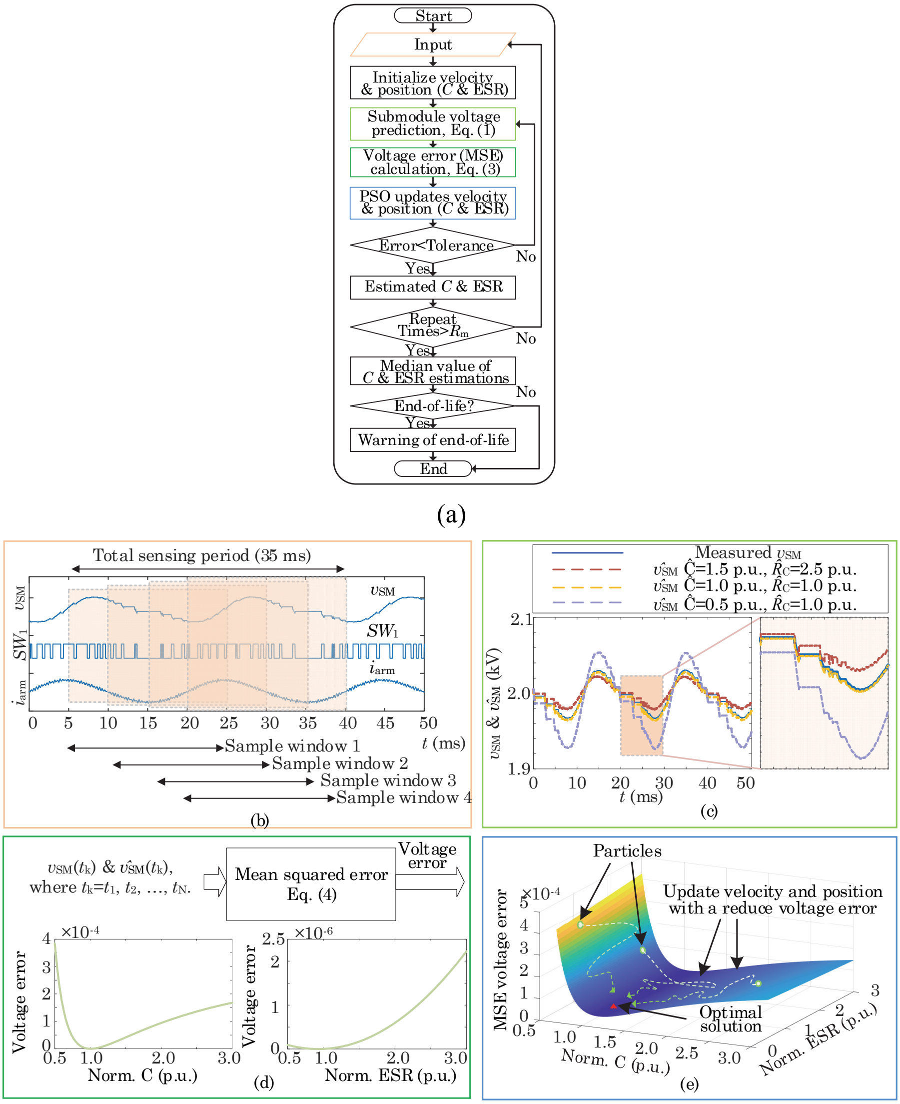

Fig. 4. Proposed method (a) Flowchart, (b) Input signals, (c) Prediction of submodule voltage, (d) Prediction error calculation, and (e) Optimization with PSO.

3.2 Capacitor Voltage Model and Prediction

The input signals are utilized to predict the submodule capacitor voltage using backward Euler in conjunction with the estimated capacitance $\hat{C}$ and ESR $\hat{R}_C$, as expressed in Eq. (1). As evident from the formulation, the capacitance contributes to the cumulative variation in voltage over time, whereas the ESR primarily influences the voltage response at charging and discharging instants.

$$\hat{v}_{SM}(t_k) = \begin{cases} v_{SM}(t_k) & ,k=1 \\ \hat{v}_{SM}(t_{k-1}) + i_C(t_k)T_S / \hat{C} + \hat{R}_C\left[\hat{i}_C(t_k) - \hat{i}_C(t_{k-1})\right] & ,k = 2,3,\ldots,N \end{cases} \tag{1}$$

where t_k denotes the discrete time steps used for voltage prediction, ranging from 1 to N. The capacitor current $i_C(t_k)$ equals the arm current when the switching signal is high. Specifically, SW_1=1 indicates that the upper switch is conducting (on-state), while it is zero corresponding to the off-state, during which the submodule is bypassed.

$$i_C(t_k) = i_{arm}(t_k)SW_1(t_k) \tag{2}$$

The predicted capacitor voltage is then compared with the measured voltage to evaluate the accuracy of parameter estimations, using the mean squared error (MSE) defined in Eq. (3). If the estimated $\hat{C}$ and $\hat{R}_C$ are closely match their actual values, the resulting MSE will approach zero.

$$V_{err} = \frac{1}{V_m^2 N} \sum_{t_k=t_1}^{t_N} (v_{SM}(t_k) - \hat{v}_{SM}(t_k))^2 \tag{3}$$

where V_m^2 is the maximum voltage inside the sampling window.

3.3 Particle Swarm Optimization

Particle swarm optimization (PSO) is a metaheuristic algorithm widely used for parameter estimation due to its low hyperparameter and ease of implementation [13]. The algorithm mimics the social behavior of birds searching for food, where individual particles adjust their positions based on both their own experience and the collective experience of the swarm, thereby converging toward the optimal solution.

The optimization process begins with a population of randomly initialized candidates distributed across the search space. Each candidate, or particle, is assigned an initial velocity v_0 and position x_0, where the subscript zero denotes the starting epoch. Based on their current positions, the objective function is evaluated to assess the quality of each solution. The best position found by the entire swarm is denoted as x_g, while the best position found by each individual particle is represented as x_p. Subsequently, the velocity and position of each particle are updated according to the following equations:

$$v_j = w_j v_{j-1} + c_1 r_{1j}(x_P - x_{j-1}) + c_2 r_{2j}(x_g - x_{j-1}) \tag{4}$$

$$x_j = x_{j-1} + v_j \tag{5}$$

where subscripts j and j-1 refer to the current and previous epochs, respectively. The coefficients c_1 and c_2 represent the cognitive and social components of the velocity update. The terms r_1 and r_2 are randomly distributed between zero and one, introducing stochastic behavior into the search process [13].

In the proposed method, PSO is employed to iteratively update the parameter vector x, which is a two-dimensional vector comprising the estimated capacitance and ESR. During each epoch, both parameters are jointly updated, guiding the solution progressively toward their actual values.

4 Validation

4.1 Mission-profile Emulator

The proposed method is experimentally validated using a mission-profile emulator (MPE). The MPE is designed to replicate the current and voltage waveforms of a submodule, thereby emulating MMC behavior while significantly reducing system complexity and power requirements [14],[15].

The topology of the MPE is depicted in Fig. 5(a), consisting of a device under test (DUT) that represents the target submodule, a full-bridge current generator, and a filter composed of inductance L_f and resistance R_f.

The DUT is operated using switching signals recorded from simulation, allowing it to reproduce voltage and current waveforms closely resembling those of an actual MMC submodule. The full-bridge current generator is controlled via a voltage regulation loop, which maintains the low-pass filtered (LPF) submodule voltage and the arm current i_{arm}, both regulated by proportional-integral (PI) controllers.

The experimental setup and typical waveforms are illustrated in Figs. 5 (b)-(d)., while the corresponding test conditions are summarized in Table 2.

Furthermore, to validate the computational requirement, the proposed method is implemented on a digital signal processor (DSP) TMS320F28069M. This DSP features 256 kB of Flash memory and 100 kB of RAM, which is sufficient to store the collected sampling data, occupying approximately 85 kB. The subsequent parameter estimation results are obtained directly from DSP implementation.

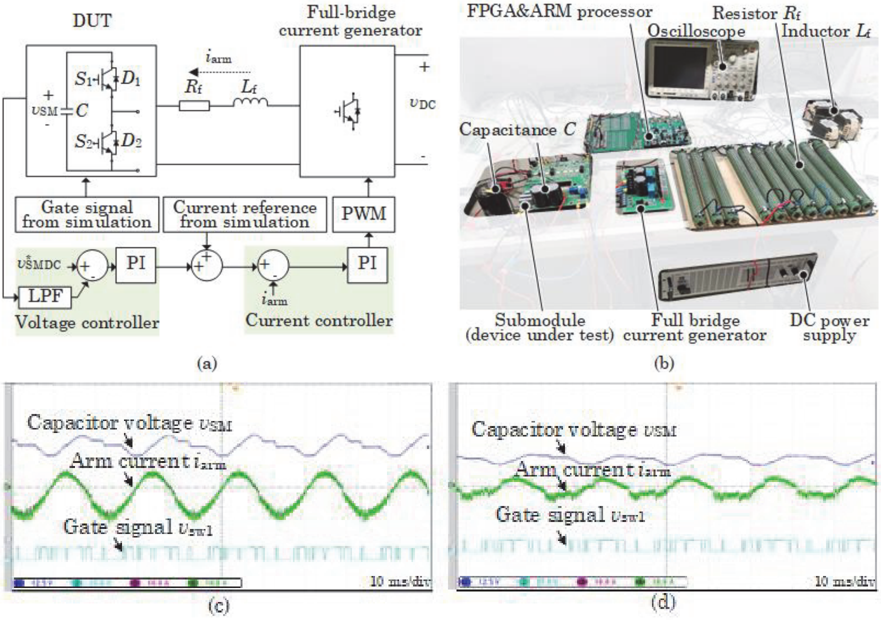

(a) (b)

(c) (d)

Fig. 5. Mission-profile emulator (a) system diagram, (b) topology, and (c-d) typical waveforms.

Table 2. Experimental parameters of the mission profile emulator.

Parameter	Value		Parameter	Value
Input power S_{in}	2 kVA		SM capacitance C	2.26 mF
DC voltage V_{DC}	200 V		SM capacitor ESR	44.12 mΩ
Fundamental freq. f_{g}	50 Hz		Tolerance	10^{-6}
DUT switching freq. f_{SW}	1 kHz		Swarm size	10
Current generator switching freq.	10 kHz		Repeat times R_{m}	5
Sampling window	35 ms		Maximum iteration	100
Sampling freq. f_{sa}	100 kHz		Adaptive inertia weight	[0.1, 1.1]
Voltage loop bandwidth	20 Hz		Cognitive weight c_1	1.49
Current loop bandwidth	800 Hz		Social weight c_2	1.49
Filter inductance L_{f}	5.4 mH		Boundary of C estim.	[1.1, 6.6] mF
Filter resistance R_{f}	1 Ω		Boundary of ESR estim.	[20, 120] mΩ
Prediction steps N	500			

Table 3. Experimental test conditions.

Scenario	1	2	3	4	5	6
V_{SMDC} (V)	50 V			30 V		
I^*_{AC} (A)	9 A	6 A	3 A	9 A	6 A	3 A
C_{err} (%)	0.35	0.18	0.66	0.57	0.83	2.56
$\mathrm{ESR}_{\mathrm{err}}$ (%)	11.47	0.41	19.73	9.71	8.68	5.90

4.2 Estimation Results

The emulated conditions encompass various submodule voltage levels and power levels, as listed in Table 3.

Estimation results are presented in Fig. 6, demonstrating that the predicted submodule voltage closely follows the measured waveform, with instantaneous prediction errors remaining below 0.5 V. The waveforms correspond to two test scenarios—Scenario 1 and Scenario 3 —highlighting the performance under different arm current conditions.

The estimation accuracy for capacitance and ESR is further visualized using boxplots in Fig. 6(c)-(d). In most cases, the median values of the estimated capacitance and ESR fall within ±1% and ±10% of the nominal values, respectively, with the exception of light load conditions represented by Scenario 3 and 6. Despite this deviation, the estimations remain sufficiently accurate to capture end-of-life degradation trends for both C and ESR.

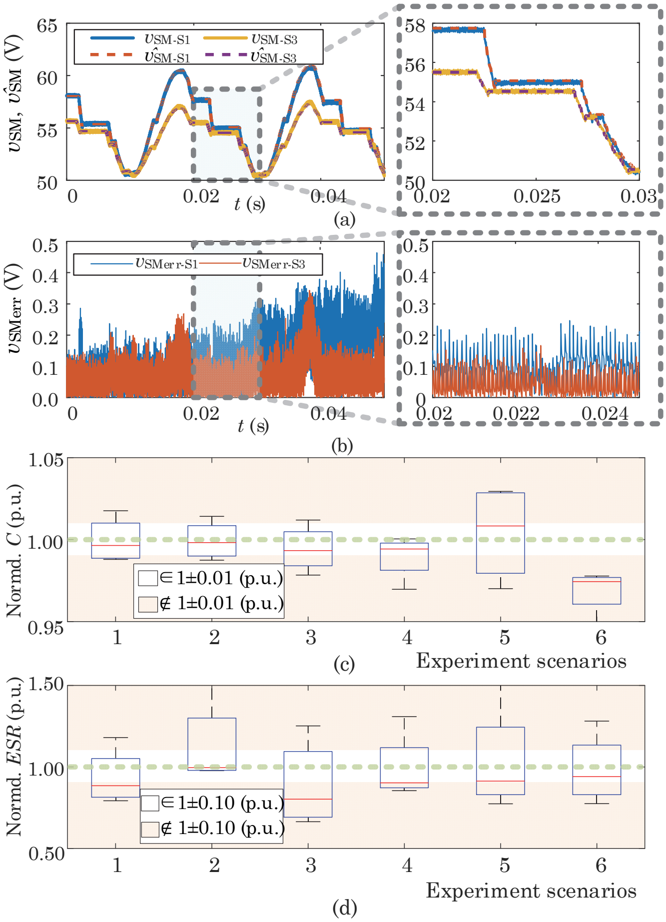

Fig. 6. (a-b) Measurement in solid lines and prediction in dashed lines, and the instantaneous prediction error. Waveforms representing scenario 1 and 3, with different current levels. (c-d) Boxplot of estimation for *C* and ESR.

5 Method Comparison

One of the key contributions of this work lies in the incorporation of the coupling effect between capacitance and ESR in the condition monitoring process. This enhancement enables the proposed method to achieve higher estimation accuracy, particularly under scenarios where the ESR increases significantly from its initial value [16],[17], as illustrated in Fig. 7. The solid curve represents the estimation error curve of *C* under the proposed method, which exhibits minimal sensitivity to ESR variations compared to the dashed curves representing methods that neglect ESR.

The proposed method is further validated by modifying the conventional recursive least square method to incorporate ESR in the estimation process. The modified RLS approach yields similarly low estimation errors as the proposed method.

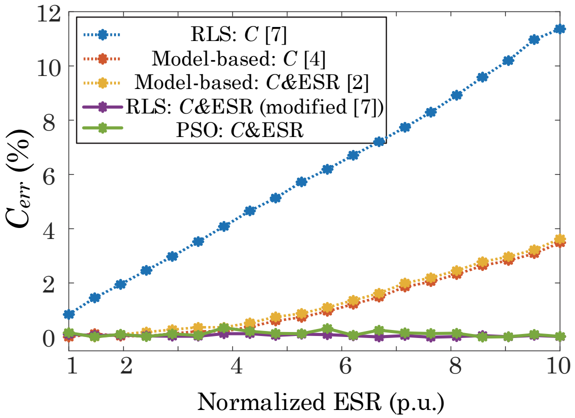

Fig. 7. Compared results of Capacitance estimation error.

Table 4. Compare the computation requirement of condition monitoring methods.

Method	Indicator	Converge time	Sampling window	Memory	Degradation Performance
RLS [7]	C	0.01 s	2 s	Low	Accuracy of C depends on ESR
Model-based [2]		0.004 s			
Model-based [4]	C & ESR	0.28 s			
CNN [10]		Training and monitoring>1000 s	5 s	High	Accuracy of C independent of ESR
PSO (proposed)		0.56 s	0.035 s	Medium	

These methods are also compared in terms of convergence time and memory requirements, as summarized in Table 4. The proposed method offers a balanced trade-off among computation time, memory usage, and degradation tracking performance. In contrast, other methods exhibit limitations, for instance, the CNN-based method [10] has high computation time and memory demand, thereby requiring a high-performance processor.

6 Conclusion and Future Work

In summary, a data-driven condition monitoring method has been proposed to explicitly account for the coupling effect between capacitance and ESR, leading to improved accuracy in degradation estimation. The study also challenges the commonly adopted assumption that ESR can be neglected, demonstrating that this simplification is not always valid and that incorporating the coupling yields more reliable results.

In addition, the proposed method is computationally efficient and has a low memory demand, making it well-suited for implementation on edge platform.

Future work will focus on reducing the sampling frequency to a level closer to the switching frequency, thereby lowering the requirements for sensing circuitry and minimizing data volume.

Acknowledgments. This project is supported by the European Union’s Horizon 2020 research and innovation program under the Marie Skłodowska-Curie grant agreement No. 955614, SMARTGYSUM.
This book chapter is based on a published paper: S. Ou, M. Hassanifar, M. Votava, M. Langwasser, M. Liserre, A. Sangwongwanich, S. Sahoo, and F. Blaabjerg, “Monolithic Data-Driven Condition Monitoring Strategy for MMC Considering C and ES),” *IEEE Trans. Ind. Electron.*, early access, 2025.

References

1. P. T. Lewis, B. M. Grainger, H. A. A. Hassan, A. Barchowsky, and G. F. Reed, “Fault section identification protection algorithm for modular multilevel converter-based high voltage dc with a hybrid transmission corridor,” *IEEE Trans. Ind. Electron.*, vol. 63, no. 9, pp. 5652–5662, Sep. 2016.
2. F. Deng, Q. Heng, C. Liu, X. Cai, R. Zhu, Z. Chen, and W. Chen, “Capacitor esr and c monitoring in modular multilevel converters,” *IEEE Trans. Power Electron.*, vol. 35, no. 4, pp. 4063–4075, 2020.
3. H. Wang and F. Blaabjerg, “Reliability of Capacitors for DC-Link Applications in Power Electronic Converters—An Overview,” *IEEE Trans. on Ind. Applicat.*, vol. 50, no. 5, pp. 3569–3578, Sep. 2014.
4. C. Liu, F. Deng, Q. Yu, Y. Wang, F. Blaabjerg, and X. Cai, “Submodule capacitance monitoring strategy for phase-shifted carrier pulse width modulation-based modular multilevel converters,” *IEEE Trans. Ind. Electron.*, vol. 68, no. 9, pp. 8753–8767, 2021.
5. F. Deng, Q. Wang, D. Liu, Y. Wang, M. Cheng, and Z. Chen, “Reference submodule based capacitor monitoring strategy for modular multilevel converters,” *IEEE Trans. Power Electron.*, vol. 34, no. 5, pp. 4711–4721, 2019.
6. Z. Geng, M. Han, W. Xie, and T. Sun, “A hierarchic capacitor condition monitoring strategy for high-voltage modular multilevel converters,” *IEEE Trans. Power Del.*, vol. 37, no. 6, pp. 5310–5324, Dec. 2022.
7. I. Polanco and D. Duji´c, “Condition health monitoring of modular multilevel converter submodule capacitors,” *IEEE Trans. Power Electron.*, vol. 37, no. 3, pp. 3544–3554, 2022.
8. H. Xia, Y. Zhang, M. Chen, W. Lai, D. Luo, and H. Wang, “Capacitor condition monitoring for modular multilevel converter based on charging transient voltage analysis,” *IEEE Trans. Power Electron.*, vol. 38, no. 3, pp. 3847–3856, 2023.
9. H. Xia, Y. Zhang, M. Chen, D. Luo, W. Lai, and H. Wang, “Capacitor parameter estimation based on wavelet transform and convolution neural network,” *IEEE Trans. Power Electron.*, vol. 39, no. 11, pp. 14 888–14 897, 2024.
10. H. Xia, Y. Zhang, "capCNN dataset: capacitor C and ESR condition monitoring dataset using convolution neural network", *IEEE Dataport*, June 2, 2024, doi:10.21227/0grk-p184.
11. S. Du, A. Dekka, B. Wu, and N. Zargari, Modular Multilevel Converters: Analysis, Control, and Applications. John Wiley & Sons, 2018.

12. B. Wu and M. Narimani, High-power converters and AC drives. John Wiley & Sons, 2017.
13. M. Clerc, Particle Swarm Optimization. U.K., London: ISTE Ltd, 2006.
14. K. Ma, S. Jiang, E. Li, and X. Cai, “Three-phase mission profile emulator for multiple submodules in modular multilevel converter,” *IEEE Trans. Power Electron.*, vol. 36, no. 5, pp. 5213–5222, 2021.
15. E. Li, K. Ma, and K. Han, “Embedded model control for dynamic mission profile emulation of submodule in modular multilevel converter,” *IEEE J. Emerg. Sel. Top. Power Electron.*, 2024.
16. M. Ghadrdan, S. Peyghami, H. Mokhtari, H. Wang, and F. Blaabjerg, “Dissipation factor as a degradation indicator for electrolytic capacitors,” *IEEE J. Emerg. Sel. Top. Power Electron.*, vol. 11, no. 1, pp. 1035–1044, 2023.
17. B. Yao, S. Zhao, Y. Zhang, and H. Wang, “A health indicator of aluminum electrolytic capacitors based on strain sensing,” *IEEE Trans. Power Electron.*, vol. 38, no. 7, pp. 7982–7987, 2023.

Energy Router for Hybrid Microgrids for efficient and robust energy and power management

Mohammadreza Azizi[1,2], Oleksandr Husev[1,3], Oleksandr Veligorskyi[1],
CarlosRoncero-Clemente[2], Ryszard Strzelecki[4]
[1]Department of Radiotechnic and Embedded Systems, Chernihiv Polytechnic National University, Chernihiv, Ukraine
[2]Department of Electric, Electronic and Automation Engineering, University of Extremadura, Badajoz, Spain
[3]Faculty of Electrical Engineering, Warsaw University of Technology, Warsaw, Poland
[4]Faculty of Electrical and Control Engineering, Gdansk University of Technology, Gdansk Poland
M.azizi@stu.cn.ua

Abstract. The use of renewable Photovoltaic (PV) sources and Battery Storage Systems (BSS) in the distribution network and residential buildings in general has been and will continue to be an increasing trend. In the last decade, solar and hybrid inverters have been used as an interface converter between renewable sources, BSS, and the power grid. Given the DC nature of renewable sources and BSSs, the move towards DC nano/microgrids and higher efficiency has been the focus of current research. However, regarding the dominance of the AC network in the distribution sector at present, using hybrid methods seems a possible solution. This study introduces the hybrid multi-port Energy Router (ER) as a reliable solution for integrating the DC system with the AC grid and managing energy flow in different parts. Issues related to safety and grounding are raised, and solutions are presented. Control strategies at different levels are examined, and finally, a reliable and highly reliable Energy Management System (EMS) is presented.

Keywords: Energy router, hybrid microgrid, energy management, flatness-based control theory, dynamic conditions.

1 Introduction

The energy provision has consistently been a major priority for governments worldwide. In recent years, this concern has intensified due to the dual pressures of a gas supply crisis impacting power generation facilities and a surge in electricity demand following the easing of COVID-19 restrictions. These factors have collectively driven electricity prices sharply upward. Simultaneously, the shift toward clean and Renewable Energy Sources (RES) has gained urgency, not only to address environmental concerns but also to curb greenhouse gas emissions. Although numerous countries have integrated RES-based electricity generation into their national strategies and constructed many renewable energy plants, a considerable portion of electricity is still derived from fossil-fuel-based power stations.

Recent data on the European Union's electricity generation mix reveals that approximately 40% of electricity is still generated by combustion plants. In comparison, wind energy contributes around 16%, and solar energy accounts for just 7% [1]. Fig. 1 illustrates the distribution of electricity generation across various sources, along with the breakdown of solar energy production between utility-scale and rooftop systems across EU member states [1]. In 2023, the total solar energy capacity approached 263 GW, with rooftop installations contributing roughly 66% of that total [2].

In 2022, the European Union introduced a strategic roadmap aimed at accelerating the deployment of solar energy solutions [3]. One of its key objectives was to mandate the installation of rooftop solar systems on all new constructions. In parallel with the growing integration of photovoltaic (PV) systems into distribution networks, BSS have witnessed rapid development, particularly for enhancing self-sufficiency and enabling off-grid functionality. Based on data published by SolarPower Europe, battery storage capacity experienced a remarkable surge in 2023, reaching 17.2 GWh, marking a 94% increase compared to the previous year [4].

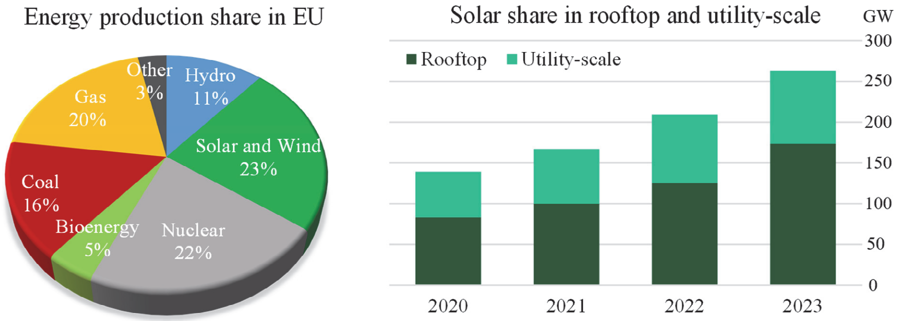

Fig. 1. Energy production shares and solar share in utility-scale and rooftop parts from 2020 to 2023.

With these statistics, it can be said that residential and commercial facilities that utilize a combination of PV arrays and BSS make a significant contribution to decentralized electricity generation. These systems not only ensure a reliable energy supply but also yield economic advantages for owners of distributed energy resources (DERs). Such solutions effectively fulfill the principles of Nearly-Zero Energy Buildings (NZEBs) [5] and Zero Emission Buildings (ZEBs) [6].

On the other side, electricity demand is rising at a rate that surpasses projections for generation capacity expansion. The growing electrification of both public and private transportation further intensifies this issue. Given the inherently intermittent nature of renewable energy sources, network congestion has become a prevalent challenge in many industrialized nations. Without expanding grid capacity and incorporating advanced EMS, maintaining grid stability is increasingly difficult.

Within this framework, the development of advanced control algorithms and comprehensive energy coordination strategies has paved the way for a new class of intelligent and multifunctional power electronics, commonly referred to as Energy Routers (ERs). These interfaces serve as pivotal elements in future smart grids, enabling dynamic energy flow control, real-time optimization, and seamless integration of diverse energy sources and loads within prosumer-based networks.

Considering the increasing expansion of DC systems, the integration method and various connection scenarios in power electronic converters are reviewed in this study. Safety issues related the integration of DC system to AC grid are discussed. Then, the proposed ER structure is described, and control strategies are classified. Finally, the energy management system is reviewed, and a high-reliability method for use in ER is presented. A summary of these discussions is described in the conclusion section.

2 DC System Integration

Given that both PV systems and BSS technologies inherently operate on direct current (DC), the adoption of DC-based architectures in buildings and distributed energy systems has gained considerable attention in recent years as a means of enhancing overall system efficiency. Nevertheless, because the prevailing distribution infrastructure is primarily alternating current (AC)-based, the practical implementation of this concept often involves developing DC or hybrid AC/DC systems that remain connected to the conventional AC grid. As shown in Fig. 2, the future grid architecture visualizes LVDC networks operating in synergy with existing AC infrastructure, offering a more efficient and flexible energy ecosystem [7]. As can be seen, there are AC, DC, and hybrid buildings in the distribution network, and this can lead to more compatibility with renewable resources and DC loads.

Various approaches exist for connecting DC microgrids to AC grids. Traditionally, a transformer is recommended to ensure galvanic isolation and enhance system reliability. Early configurations employed a low-frequency transformer followed by an AC-DC interface converter [8]. However, due to the bulky size and weight of such transformers, high-frequency isolation techniques have gained popularity. In these modern configurations, an AC-DC converter is used first, followed by a high-frequency isolated DC-DC converter incorporating a compact transformer [9]–[11]. These solutions offer galvanic isolation, suppress leakage currents, and improve reliability. Nevertheless, the presence of a transformer increases system cost, size, and may reduce overall efficiency.

While many studies advocate for isolated architectures in LVDC-to-AC interconnections, isolation is not strictly necessary, particularly in hybrid AC/DC systems [12]. Transformerless configurations are a viable alternative, involving only a single-stage AC-DC interface without a transformer. Depending on design requirements, converters such as full-bridge, NPC, ANPC, or T-type can be utilized. In transformerless designs, safety considerations become especially critical. Leakage current mitigation must be addressed through advanced converter topologies or modified modulation techniques that decouple the AC and DC domains [13]–[20].

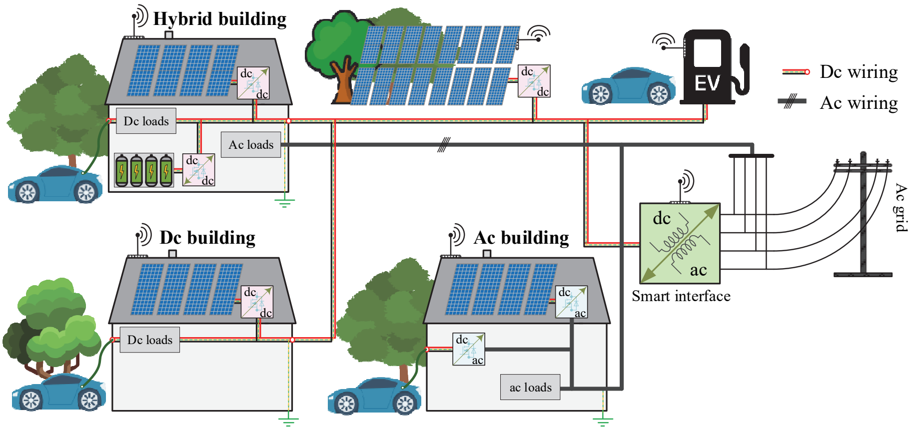

Fig. 2. Future energy distribution system.

Fig. 3 illustrates various potential configurations for connecting future residential buildings to the electrical grid. In scenario (a), a conventional AC-based system is depicted, which represents the most common current topology. Most commercially available hybrid inverters are designed to operate based on this setup. Scenario (b) presents a hybrid AC/DC architecture, where AC loads remain connected to the main grid, while DC loads are powered via a 48 V DC bus. This configuration aligns with the ER concept. In scenario (c), the internal infrastructure of a Zero Emission Building (ZEB) is fully DC, interfaced with the AC grid through an isolated AC-DC converter. Lastly, scenario (d) considers a fully DC architecture, in which PV arrays, energy storage units, and DC loads are connected directly to the DC bus via individual DC-DC converters. Despite its efficiency advantages, the implementation of scenarios (c) and (d) remains constrained due to the limited development of standardized DC systems and the availability of DC-compatible end-use devices.

To assess and compare the efficiency and power losses across these configurations, real-world electricity consumption profiles for residential buildings were used [21]. The case study assumes a building located in Berlin, equipped with a 5-kW photovoltaic system and a battery storage unit with a capacity of 5 kWh. Simulations were conducted for two representative days: one in June, with maximum solar irradiance, and one in December, with minimal sunlight. Losses were calculated for all system components, assuming uniform and negligible efficiency degradation due to load scaling. The comparative results are depicted in Fig. 4.

As expected, the pure DC configuration (scenario d) exhibited the lowest overall power losses on both test days, underscoring the efficiency potential of fully DC systems. However, this outcome, though intuitive, cannot be universally applied, particularly when compared with the conventional AC scenario (a), which demonstrated relatively higher energy losses. Of particular interest is the hybrid AC/DC system (scenario b), which offers a balanced trade-off between infrastructure compatibility and performance. In regions with temperate climates and minimal seasonal variation in solar radiation, such systems can operate with high energy autonomy. In these cases, the interlink converter between AC and DC domains is used minimally, thereby preserving system efficiency. Conversely, in regions with significant climatic variation, reliance on the AC grid increases, potentially reducing overall efficiency due to the lower performance of isolated AC-DC conversion interfaces.

Several recent studies [22]-[25] have also explored and compared the efficiency of DC versus AC residential nanogrids under varying configurations of photovoltaic and storage capacities. In particular, reference [23] evaluates the performance of an office building and demonstrates that transitioning to a DC-based infrastructure can enhance overall system efficiency by approximately 11% to 17%. Moreover, it is important to highlight that the redesign and optimization of currently available AC appliances for DC operation can further improve energy efficiency. A clear example lies in motor-driven devices commonly used for applications such as air conditioning, refrigeration, and household cleaning. Research findings indicate that transitioning to brushless DC (BLDC) motors could yield significant energy savings, up to 50% in heating applications, 30–50% in cooling, and 5–15% in cleaning systems [26].

Consequently, while the long-term transition from AC to DC systems and end-use devices remains a complex and gradual process, the hybrid AC/DC approach, as exemplified by the ER configuration (scenario b), emerges as a practical and forward-looking solution. This architecture not only bridges existing AC infrastructure with the growing DC demands but also offers a scalable pathway toward higher efficiency in both current and future nanogrid implementations.

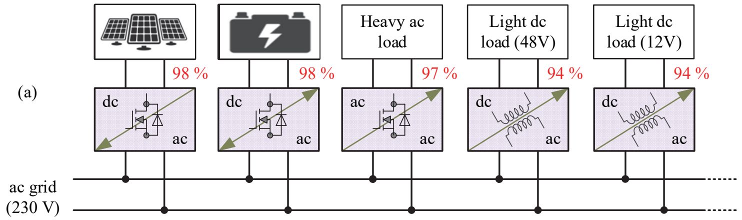

Classical non effective and non-efficient system (ac)

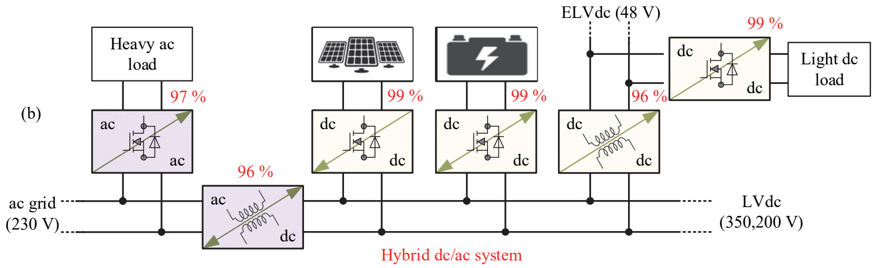

Hybrid dc/ac system

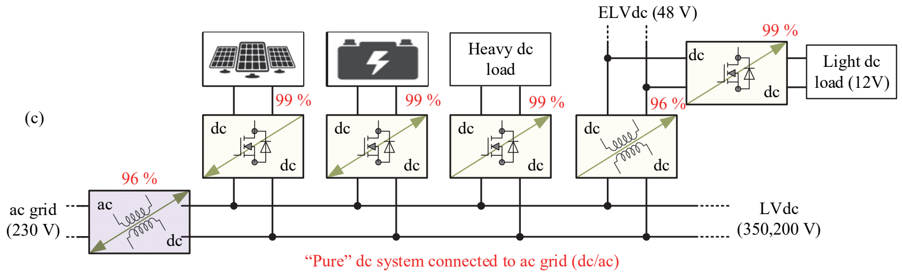

“Pure” dc system connected to ac grid (dc/ac)

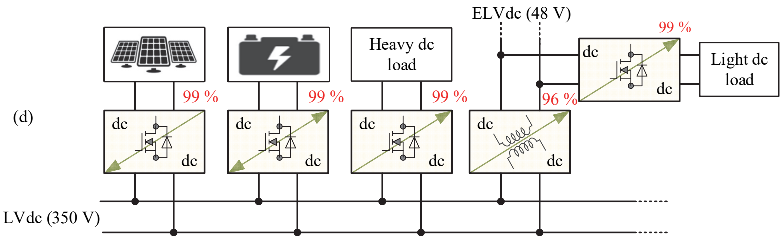

Pure dc system connected to dc grid (dc)

Fig. 3. Different scenarios for connecting ZEB to the power grid.

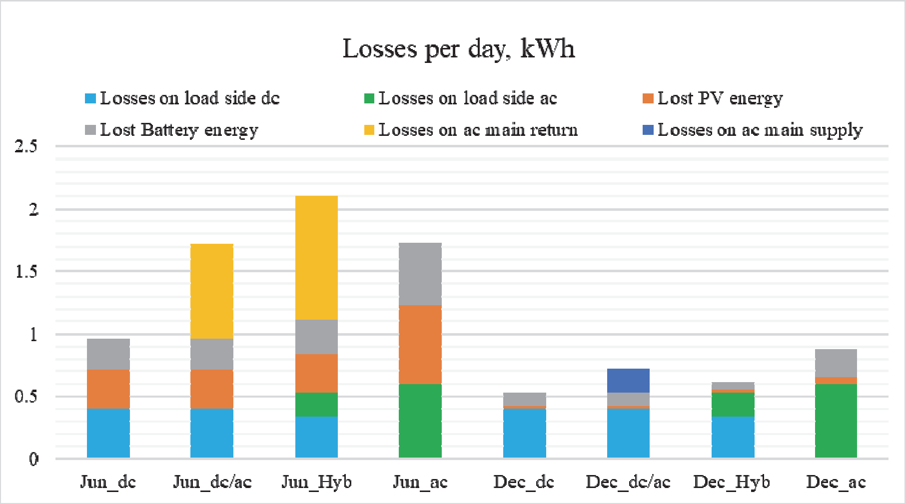

Fig. 4. Losses for four scenarios of connecting NZEBs to the grid for a day in June and a day in December based on the electricity consumption profile in [21].

3 Possible ER configurations

Considering the above, the ER configuration corresponds to the layout illustrated in Fig. 5(a). It closely resembles hybrid inverter architectures but incorporates relays as optional components to enable load-shifting capabilities and to support a DC interface for supplying light DC loads. Additionally, an optional isolated DC-DC converter may be integrated to connect with an external DC microgrid, serving as a supplementary power source. The inclusion of relays becomes unnecessary if the loads possess IoT-based communication features, which is increasingly common in modern appliances. Given that only electrical isolation between future AC and DC networks is considered acceptable in the current context, maintaining isolation between hybrid AC/DC systems and DC microgrids is essential. However, since interactions with DC microgrids are anticipated to be occasional, they are unlikely to lead to notable energy inefficiencies.

An alternative topology, receiving growing attention, is shown in Fig. 5(b). In this arrangement, the internal DC bus is directly linked to the DC microgrid, which acts as the primary power source. Simultaneously, due to the isolation standards between AC and DC systems, an isolated interlink converter becomes a necessary component. This configuration may become viable when heavy-duty DC appliances emerge alongside conventional AC counterparts. These integrated systems can coordinate power flow among generation units, energy storage, and end-use devices, and they may be designed as a unified power electronics module offering comprehensive functionalities such as energy monitoring and embedded components. Energy management strategies (EMS) will also be executed through this architecture, utilizing real-time data and optimization algorithms.

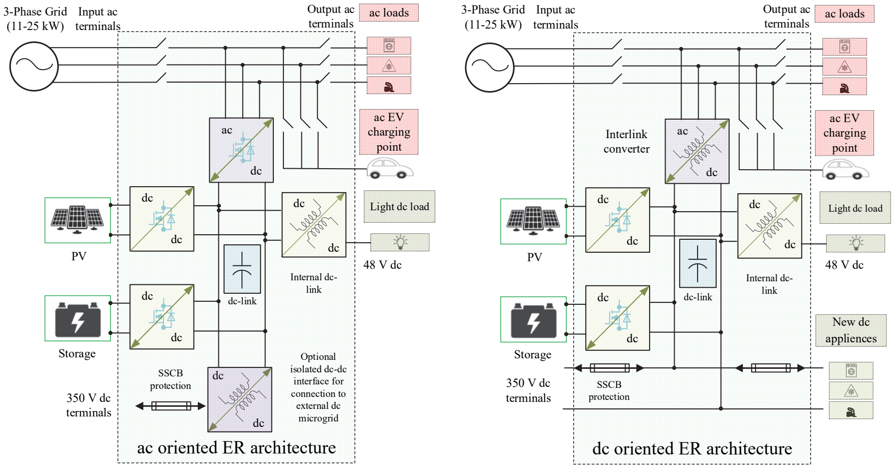

(a) (b)

Fig. 5. The possible overall structure of ER. (a) in case of ac domination, (b) dc domination.

4 Safety Issues

Although the integration of DC architectures can significantly reduce conversion losses and improve system performance, a major obstacle remains: the lack of comprehensive standards governing DC systems. These standards must address critical aspects such as appropriate voltage levels, grounding methodologies, and protection mechanisms. As in AC systems, ensuring robust protection in DC nanogrids is also crucial to safeguard both users and equipment. A typical DC nanogrid may include interconnected PV modules, BSS, DC loads, and electric vehicles (EVs), all of which necessitate proper protective measures to ensure operational safety [27].

Considering that the ER is poised to serve not only as an advanced EMS component but also as a critical interface between AC and DC microgrids. This dual functionality introduces new design and operational challenges, particularly concerning safety protocols, leakage currents, and grounding techniques. While galvanic isolation is not mandatory in hybrid AC/DC systems, such as those utilized in conventional hybrid inverters, it becomes indispensable when interfacing separate AC and DC microgrids.

As previously discussed, traditionally, isolation has been achieved through low-frequency transformers, which provide robust electrical separation. However, the high-frequency isolation techniques, often embedded within isolated power electronic converters, offer a compact and cost-effective alternative that is far more suitable for household environments [28]. Nevertheless, even high-frequency isolation cannot eliminate associated issues. For instance, when interconnecting a three-phase AC grid with a two-wire DC system, a DC common-mode voltage offset may arise. If the isolation barrier degrades over time or multiple parallel converters are present, this bias can result in unintended DC leakage currents (Fig. 6(a)) [29].

Grounding strategies, essential in both AC and DC systems, exhibit notable differences in implementation. In the DC domain, various grounding methods exist for linking the system to protective earth, each with specific trade-offs regarding safety and electromagnetic compatibility [30]–[32]. To suppress DC leakage currents effectively, specially tailored grounding approaches must be applied (Fig. 6(b)).

In specific cases, particularly those involving hybrid AC grids connected to individual DC systems rather than full DC microgrids, a non-isolated configuration remains viable. One such solution involves the use of a common-ground structure [33], [34], in which the negative terminal of the DC-link is directly tied to the neutral line of the AC grid. This approach stabilizes the common-mode voltage at zero, thereby preventing leakage current circulation. Moreover, it enables one side of the system to be grounded safely (Fig. 6(c)).

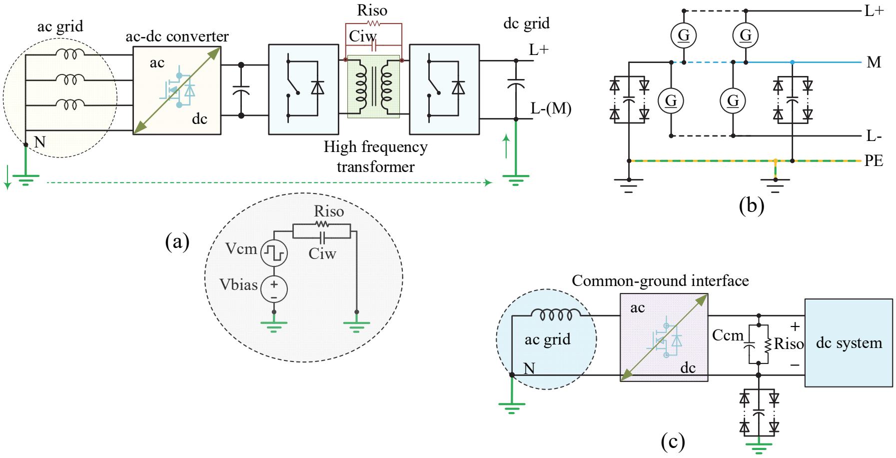

Fig. 6. Grounding and isolation between dc and ac grids with a common-mode voltage bias (a), recommended grounding in dc systems to avoid dc leakage currents (b), common-ground interface as a solution to have grounding on both sides without leakage current problem (c).

5 Proposed ER and Control Strategy

Fig. 7 illustrates the architecture of the proposed Single-Cell Three-Phase (SC-TP) ER. On the grid side, a single-stage common-ground inverter is utilized, capable of both voltage step-up and step-down operations [35]. A central DC bus (shown in blue) forms the backbone of the system, linking all power sources, inverters, and DC loads. This configuration not only ensures system-wide interconnection but also provides expandability by supporting future integration with other nanogrids.

AC loads are positioned between the inverter and the grid, allowing uninterrupted operation in both grid-connected and islanded modes. Relay switches are installed on the grid, inverter, and AC load sides to manage phase selection and routing. Although the DC bus can interact with all three AC phases, it does so sequentially rather than simultaneously. To minimize phase imbalance, common in three-phase residential or commercial setups, the system actively detects and limits consumption on the most loaded phase. This strategic control enhances energy efficiency and provides a cost-effective alternative to traditional three-cell (TC) designs by eliminating the need for multiple converter stages.

PV and Battery Storage System (BSS) units are interfaced with the DC bus through dedicated DC-DC converters. The PV converter operates in both buck and boost modes depending on panel voltage, while the BSS employs a bidirectional interleaved converter for efficient high-current charge and discharge management. The common-ground design reduces leakage current risks and establishes a shared ground between AC and DC domains, thereby improving system protection [36]. Additionally, a Solid-State Circuit Breaker (SSCB) is incorporated for fast fault response and improved safety [37].

The SC-TP configuration, as justified in [38], offers enhanced PV self-consumption, reduced phase imbalance, and significantly lower cost compared to traditional TC setups. It also provides better integration with distributed energy sources, contributing to improved grid stability and resilience. To fully realize these benefits, the topology relies on a Smart Energy Management Algorithm (SEMA) running alongside low-level control loops. While SEMA is critical for balancing and optimizing performance, its detailed implementation is beyond the scope of this section.

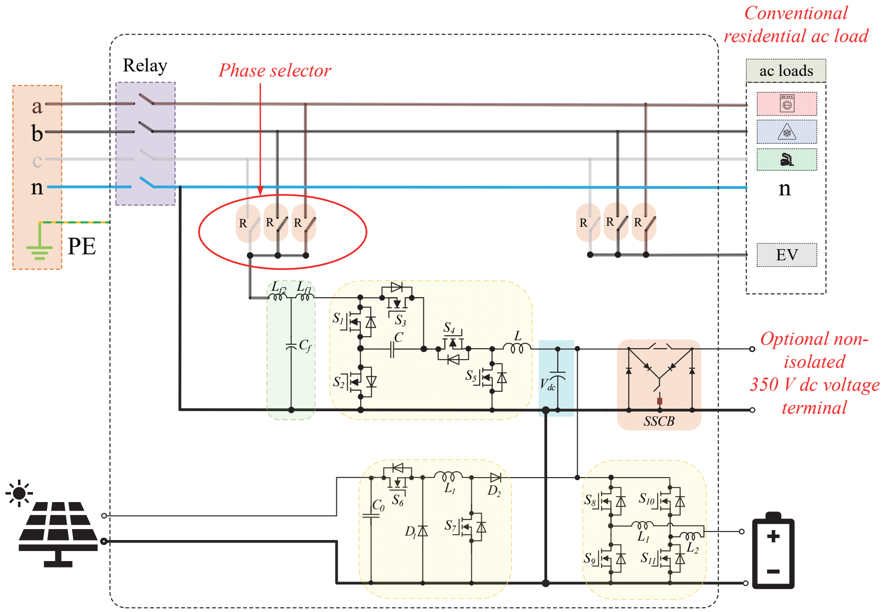

Fig. 7. Schematic diagram of the ER.

Beyond the structural design and protection mechanisms, one of the most pressing challenges in ER systems lies in the precise control and coordinated management of power flows across its various components. In this context, devising efficient control strategies and hierarchical control architectures remains a prominent area of ongoing research. Fig. 8 provides an overview of the multi-level control strategy employed in the ER.

As illustrated in Fig. 8, the control hierarchy of the ER is composed of multiple levels. In the low-level control layer encompasses fundamental functions such as grid current regulation, DC-link voltage stabilization, and grid synchronization. These elements form the core operational layer, ensuring stable and reliable interaction between the ER and the main grid. The mid-level control manages component-level functions, including PV power tracking, battery charging/discharging, and load prioritization. At the high level, broader tasks are addressed, including EMS coordination, data communication, and cloud-based optimization.

In the low-level, various strategies have been explored for grid-connected inverter control, with conventional methods largely centered around Proportional-Integral (PI) controllers implemented in the dq reference frame [39]. In low-level control, the inverter control strategy consists of an outer PI loop for DC-link voltage regulation, complemented by a Phase-Locked Loop (PLL) for synchronization with the AC grid. The PI controller generates a reference current (i_g^*), which is compared with the measured grid current (i_g). The resulting error signal is then fed into a Proportional-Resonant (PR) controller, which computes the modulation reference voltage to ensure accurate grid current tracking. While PR controllers offer superior steady-state performance under sinusoidal conditions, particularly in tracking and harmonic compensation, they are notably difficult to tune and typically exhibit poor transient response [40]. Conversely, PI controllers are favored in many industrial settings due to their simplicity, low implementation complexity, and minimal computational burden. However, their performance can be adversely affected by slow dynamic response, reduced effectiveness in disturbance rejection, and heightened sensitivity to system parameter uncertainties and grid disturbances [41], [42].

The control block diagrams for the PV and BSS converters are illustrated in the mid-level control system. In both cases, the reference currents (I_{PV}^* and I_{BSS}^*) are defined either based on the grid connection status, instructions from the EMS, or via DC-link voltage deviations processed through outer PI loops. These reference currents are then compared to the actual measured currents, and the error signals are managed by inner PI controllers to generate the modulation signals for the respective converters.

At the high level, the EMS is responsible for determining reference values based on real-time energy consumption, load profiles, and the State of Charge (SoC) of the BSS. Depending on the system design, EMS can operate locally through rule-based logic or leverage cloud-based platforms that integrate advanced communication protocols and optimization algorithms.

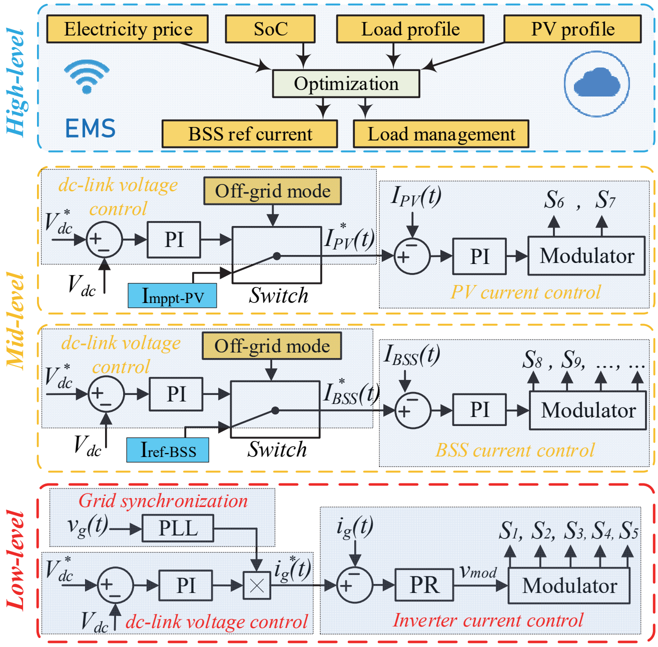

Fig. 8. The simplified block diagram of the applied control strategy in ER for different control levels.

6 Flatness-based control (FBC) for low-level control

Recent studies primarily focus on conventional control strategies designed to regulate link and manage power exchange with the grid. While these methods demonstrate acceptable performance, they often exhibit relatively slow dynamic responses.

To enhance control system response under dynamic conditions, alternative approaches such as Model Predictive Control (MPC), adaptive controller, Fuzzy Logic Controller (FLC), and Sliding Mode Control (SMC) have been explored in the literature [43]–[45]. In [43], MPC is employed to control the load-side inverter in a back-to-back ER, while the dc link is controlled using a PI controller, and the grid-side inverter is managed with a Proportional-Resonant (PR) controller. Although the PR controller has proven effective for grid-connected inverters, its tuning process remains complex [46]. SMC is robust and has a fast dynamic response, but the practical implementation is complex due to high-frequency oscillations near the sliding surface [45]. Given that the ER integrates multiple links, including PV, battery storage, DC and AC loads, and the grid, any sudden change in these components can introduce disturbances into the system. Therefore, a control system capable of delivering a fast, robust, and precise response under dynamic conditions is essential.

Among the control methods suitable for dynamic conditions and nonlinear systems, Flatness-Based Control (FBC) theory has been introduced as a reliable solution [47]. This control method, initially introduced by Fliess, demonstrates excellent performance in managing nonlinear systems and provides robust capabilities for systems with multiple state variables and inputs. However, like other advanced control strategies, FBC imposes certain conditions that must be met. Similar to MPC, it first requires an accurate mathematical model of the system. Additionally, the system should be differentially flat, ensuring that the overall conditions of the flat system are met. In contrast, compared to methods such as MPC, FBC offers a lower computational burden. While MPC requires solving an optimization problem at each time step, FBC relies on analytical relationships, making it computationally more efficient. This control approach has been successfully applied across various domains, including mechanical and chemical systems, aerospace, and power systems, demonstrating its capability to manage nonlinear and dynamic systems while ensuring fast and stable responses. Over the past decade, several studies have explored the application of FBC in power electronics, yielding promising results in dynamic conditions [48]–[51].

Employing FBC improves overall system performance and stability by offering fast dynamic response and robust control of nonlinear systems, which significantly reduces voltage and current fluctuations. Based on the definition, a system is considered differentially flat if a set of flat outputs can be found such that all state variables and inputs can be expressed as a function of these flat outputs and their derivatives. From a mathematical point of view:

If the system $\dot{x} = f(x, u)$ has a state $x \in R_n$, and an input $u \in R_m$, then the system is differentially flat if an output $y \in R_m$, can be found in the form:

$$y = \phi\left(x, u, \dot{u}, \dots, u^{(l)}\right), \tag{1}$$

when,

$$x = \varphi\left(y, \dot{y}, \dots, y^{(r)}\right), \tag{2}$$

and,

$$u = \psi\left(y, \dot{y}, \dots, y^{(r+1)}\right). \tag{3}$$

Then, the system is differentially flat, and the mapping of (φ, ψ) is called Lie-Backlund isomorphism, which defines a flat system. *l* and *r* are also the number of time derivatives.

FBC is a model-based control system that needs equations to define the system. Therefore, the system is modeled with corresponding equations, and then it is proved that the system with the considered inputs and outputs is differentially flat. For the described ER in Fig..7, FBC is applied to control the DC-link voltage by setting the reference current of the inverter in an outer loop. Afterwards, in an inner loop, applied to the output LC filter of the inverter to generate a voltage reference and control the inverter current. Detailed processes are described in the following subsections. In this study, the reference currents for the PV and storage battery power converters are set by EMS and then tracked by conventional PI controllers.

6.1 DC-link voltage control using FBC

As mentioned previously, the DC-link voltage in grid-connected mode is controlled in an outer loop by regulating the inverter reference current. To reach that, the inverter power is calculated by applying FBC. For this purpose, the total power in the DC-link is calculated. The EMS sets the PV and battery power. DC load power can also be measured through the DC load current. Thus, the energy in the DC-link is:

$$e_{dc} = \frac{1}{2} C_{dc} V_{dc}^2, \tag{4}$$

where e_{dc} is the energy in the link, C_{dc} is the capacitance value of DC-link capacitor, and V_{dc} is the DC-link voltage. From the power point of view, the power in the DC-link is the derivative of energy, which is of the total power in the dc link. Note that the power injected into the DC-link is considered positive:

$$\dot{e}_{dc} = P_{PV} \pm P_{BSS} - P_{dc} \pm P_{Inv}, \tag{5}$$

where P_{PV} is the PV power, P_{BSS} is the battery power, P_{dc} is the power of dc loads, and P_{Inv} is the inverter power. Defining the following parameters as the flat system terms:

$$\begin{cases} y = e_{dc} \\ x = V_{dc}\,, \\ u = P_{Inv} \end{cases} \tag{6}$$

where y is the flat output, x and u are the control variable and control input, respectively.

Then, rewriting (4) to obtain V_{dc}:

$$V_{dc} = \sqrt{\frac{2e_{dc}}{C_{dc}}} \Rightarrow x = \varphi(y). \tag{7}$$

Therefore, the state variable (V_{dc}) is a function of flat output (e_{dc}). Also, from (5), and rewriting P_{dc} in terms of V_{dc}:

$$P_{Inv} = P_{PV} + P_{Bat} - \frac{V_{dc}^2}{R_{dc}} - \dot{e}_{dc} = P_{PV} + P_{Bat} - \frac{2e_{dc}}{C_{dc}R_{dc}} - \dot{e}_{dc} \Rightarrow \quad u = \psi(y, \dot{y}), \tag{8}$$

which proves that the input variable is a function of flat output and its derivative.

Considering the flat system criteria, it can be concluded that this system is differentially flat. Using a linearizing feedback control law with the following equation, $\dot{e}_{dc}$ can be achieved:

$$(\dot{y} - \dot{y}_{Ref}) + K_{11}(y - y_{Ref}) + K_{12} \int_0^t (y - y_{Ref}) d\tau = 0 \tag{9}$$

while y_{Ref} is the reference value of the control output, and $\dot{y}$ is the output derivative. Also, K_{11} and K_{12} are the coefficients and must comply with the following polynomial:

$$p(s) = s^2 + 2\zeta\omega_n s + \omega_n^2, \tag{10}$$

which K_{11} and K_{12} are defined as follows:

$$K_{11} = 2\zeta\omega_n, \qquad K_{12} = \omega_n^2, \tag{11}$$

while ζ and ω_n are the desired dominant damping ratio and natural frequency, respectively. These parameters are set knowing the switching frequency f_{sw} of the system.

Finally, getting $\dot{e}_{dc}$ in equation (8), P_{Inv} can be obtained. Obtaining P_{Inv}, the inverter reference current can be easily calculated. Since the reference current is needed for inverter control and the control structure is based on *dq* transformation, the following equation should be used to obtain the *dq* component of the reference current.

$$\begin{bmatrix} i_d \\ i_q \end{bmatrix} = \frac{1}{(v_d^2 + v_d^2)} \begin{bmatrix} v_d & v_q \\ v_q & -v_d \end{bmatrix} \cdot \begin{bmatrix} P_{Inv} \\ Q_{Inv} \end{bmatrix}, \tag{12}$$

while P_{Inv} is calculated in (8), Q_{Inv} is set to zero, v_d and v_q are measured in the *dq* form of the grid voltage.

6.2 Inverter control using FBC

FBC is also used in an inner loop to control the inverter current. For this purpose, equations related to the ac-side output filter and also the *dq* components of inverter reference currents, which were calculated in (12), are needed. Fig. 9 shows the inverter and its LC filter between the inverter and grid. *αβ* to *dq* domain transfer is applied for this control system. The process of applying *dq* transformation for a single-phase system is described in [52].

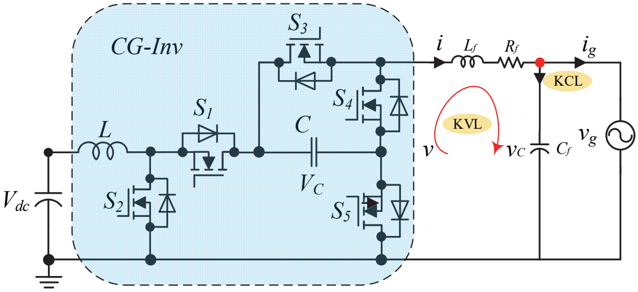

Fig. 9. The ER inverter and its LC filter.

Fig. 9. ER inverter and its LC filter.

To extract the system equations, Kirchhoff's Voltage Law (KVL) and Kirchhoff's Current Law (KCL) are applied on the output side of the inverter and the following equations in the dq frame are obtained:

$$\frac{di_d}{dt} = \frac{1}{L_f}\left(v_d - v_{Cd} - R_f i_d\right) + \omega i_q, \tag{13}$$

$$\frac{di_q}{dt} = \frac{1}{L_f}\left(v_q - v_{Cq} - R_f i_q\right) - \omega i_d, \tag{14}$$

$$\frac{dv_{Cd}}{dt} = \frac{1}{C_f}\left(i_d - i_{gd}\right) + \omega v_{Cq}, \tag{15}$$

$$\frac{dv_{Cq}}{dt} = \frac{1}{C_f}\left(i_q - i_{gq}\right) - \omega v_{Cd}. \tag{16}$$

where L_f, R_f, and C_f are the LC filter inductor, resistance, and capacitor, respectively. i_d, i_q, are *dq* components of the inverter reference current, and v_d and v_q are dq components of the inverter output voltage. i_{gd}, i_{gq}, v_{Cd}, and v_{Cg} are also the *dq* components of the grid current and the voltage across the filter capacitor, respectively. Finally, ω is the angular frequency.

To meet the conditions of the flat system, the following definitions are assumed:

$$y = \begin{bmatrix} i_d \\ i_q \end{bmatrix}, \quad x = \begin{bmatrix} i_d \\ i_q \end{bmatrix}, \quad u = \begin{bmatrix} v_d \\ v_q \end{bmatrix}. \tag{17}$$

From (17) it is clear that $x=y$, and then $x=\varphi(y)$, which means the state variable is a function of flat output.

Then from (13), it can be written,

$$u_1 = L_f \dot{i}_d + R_f i_d - \omega L_f i_q + V_{Cd} \Rightarrow u_1 = \psi(y_1, \dot{y}_1, y_2), \tag{18}$$

and from (14), we can write:

$$u_2 = L_f \dot{i}_q + R_f i_q i + \omega L_f i_d + V_{Cq} \Rightarrow u_2 = \psi(y_2, \dot{y}_2, y_1). \tag{19}$$

Therefore, the input variables can also be expressed in terms of flat outputs and their derivatives, meaning the considered system is differentially flat. Using the same linearizing feedback control law as (9) and finding appropriate coefficients that satisfy the criteria in (10) will be found. Then, using (18) and (19), v_d,v_q will be achieved. Once v_d,v_q are obtained, *dq* to *αβ* transformation will be used, and vα is sent as a reference voltage for the modulation block.

The general control system proposed to control the DC-link voltage and inverter current is illustrated in Fig. 10. As can be seen, FBC is first used in an outer loop to obtain the reference current of the inverter, which is responsible for DC-link voltage control. Then, another FBC is used in an inner loop to control the inverter current. As is clear, the reference current obtained in the first part is fed to the second part of the control system. It should also be pointed out that the red circle in Fig. 10(a) exhibits the control equation in (9).

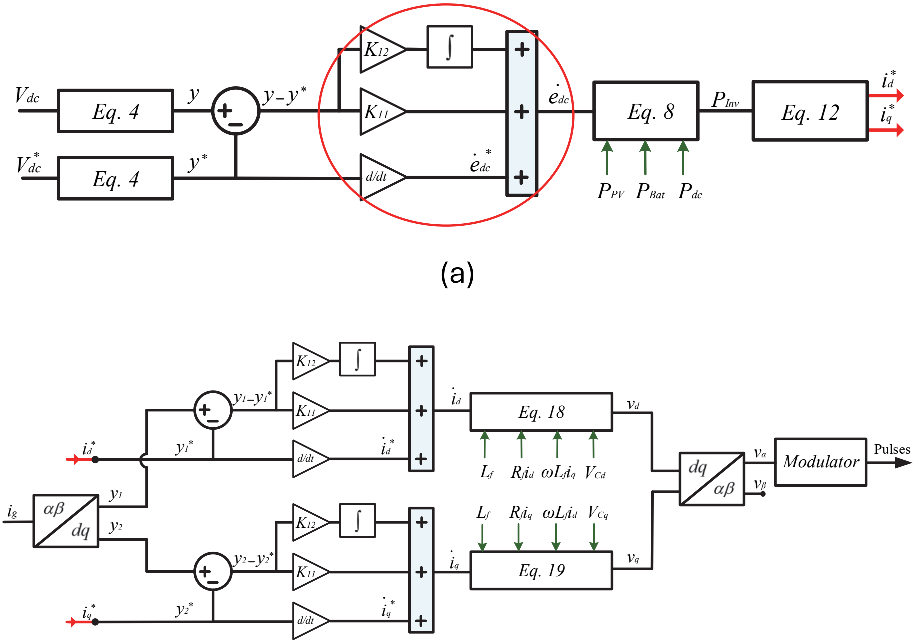

(a)

(b)

Fig. 10. Proposed control scheme. (a). FBC for DC-link control through inverter reference current. (b). FBC for controlling the inverter current.

7 Energy Management System for ER

Nowadays, the Internet of Things (IoT) plays a pivotal role in the daily operations of numerous industries, with a broad range of applications spanning smart cities, smart grids, and smart homes. IoT technologies facilitate the collection, processing, analysis, and utilization of data to support management and optimization tasks, addressing essential requirements such as comfort, usability, security, and energy efficiency [53]. In line with this technological evolution, modern buildings are increasingly integrating IoT under the concept of smart buildings, a trend that has gained significant momentum in recent years. Through IoT-based systems, building operations can benefit from remote monitoring, intelligent temperature and lighting control, and enhanced energy performance, all of which contribute to cost reduction while improving occupant comfort [54].

Simultaneously, the increasing demand for electrical energy has spurred interest in the on-site integration of Distributed Generation (DG)—particularly PV systems—alongside BSS in residential and commercial buildings. This integration has led to a growing need for robust EMS to coordinate and optimize the production, storage, and consumption of energy, with the ultimate goal of achieving ZEBs. This transition has been made feasible through advancements in power electronic converters and microcontroller technologies.

In the context of EMS, various control strategies can be employed depending on system architecture and communication capabilities [55]. One of the most widely used approaches for power sharing in microgrids is droop control, which can be adapted for use in ERs as well. Ideally, this strategy enables autonomous power sharing based on predefined droop coefficients, eliminating the need for communication links. This plug-and-play, low-cost, and scalable solution remains a preferred option among power electronics researchers [56]. However, droop control is not without its limitations. Challenges such as impedance-dependent performance, inaccurate power distribution, and slow transient response have been identified as key drawbacks [57]-[58]. These issues have motivated the exploration of enhanced or alternative control strategies that can provide better accuracy and dynamic performance, especially in complex and highly dynamic smart building environments. Consequently, various enhancements to conventional droop control have been proposed to address its inherent limitations. These include adaptive droop control [59]-[60], robust droop control [61], and neural network-based droop control [62]. The latter leverages input-output data to train a neural network that adjusts droop characteristics dynamically. In another approach [63], voltage droop control is combined with a secondary communication-based control layer, aiming to improve overall performance. The secondary controller determines setpoints based on optimization schemes, enabling better voltage and current regulation under varying operating conditions.

To manage multiple control objectives, the distributed hierarchical control paradigm typically structured into two or three levels has become a common framework for DC microgrids [64]. At the primary level, a local droop-based controller maintains system stability and enables plug-and-play functionality. Higher-level controllers use low-bandwidth communication for coordination [65], where consensus algorithms are widely adopted to ensure reliable data exchange and agreement among distributed units [66]. At the tertiary level, optimization techniques can be implemented to maximize system efficiency and economic operation [67].

However, despite these improvements, distributed control whether hierarchical or not cannot ensure optimal power flow from an economic perspective. Achieving global optimization requires centralized communication, data acquisition, computation, and management. The foundational step in this approach involves monitoring and measuring all aspects of the system production, storage, and consumption and transmitting this data to a centralized EMS.

With the rapid adoption of full digitalization in new buildings and the interconnection of all energy assets within a central control platform, the initial investment for implementing centralized systems has become less of a concern. Most modern EMS platforms are now cloud-based, offering scalability, flexibility, and high computational capacity for handling vast amounts of energy-related data. The cloud infrastructure facilitates advanced analytics, real-time monitoring, and even machine learning-based forecasting and decision-making. As a result, cloud-based EMS emerges as a powerful, accurate, efficient, and cost-effective solution for smart buildings and microgrids. Nonetheless, this architecture also comes with drawbacks, primarily the single-point-of-failure risk and reduced system reliability in the event of communication loss. Moreover, the operational costs of continuous communication can be significant in large-scale implementations [68].

To overcome the aforementioned limitations, a hybrid control paradigm is emerging, which combines cloud-based EMS with Edge Computing Platforms (ECP) deployed at the ER level [68]. In this architecture, most of the computationally intensive tasks are performed in the Cloud Computing Platform (CCP), including long-term forecasting and global optimization based on comprehensive datasets. At the local level, only simple real-time tasks remain, which are manageable by the embedded computing resources within inverters and local controllers. These include adapting or fine-tuning the control strategies provided by the CCP using real-time measurements from the ER such as local generation, consumption, battery state of charge, and the status of switchable loads. This reduces the computational load and maintenance requirements at the edge, while allowing faster response times and increased autonomy. Moreover, since edge devices do not require continuous communication with the cloud, they can operate independently for short-term decision-making in the event of communication loss, thereby alleviating communication burdens. The architecture also benefits from the flexibility and scalability of cloud computing software updates, control algorithms, and optimization strategies can be remotely updated at the CCP. Additionally, a single CCP instance can serve multiple independent buildings, further reducing implementation costs.

In summary, the integration of CCP with ECP offers a flexible, scalable, and cost-effective control solution. It enables global economic optimization based on predictive analytics and aggregated data an objective that decentralized EMS approaches cannot fully achieve. Furthermore, a local droop control strategy can still be maintained as a fallback mechanism in the event of communication failure, thus enhancing system reliability.

This hybrid cloud-edge control approach, illustrated in Fig. 11, ensures autonomous operation when needed and effectively addresses the single-point failure issue, while also minimizing communication costs compared to traditional centralized EMS solutions.

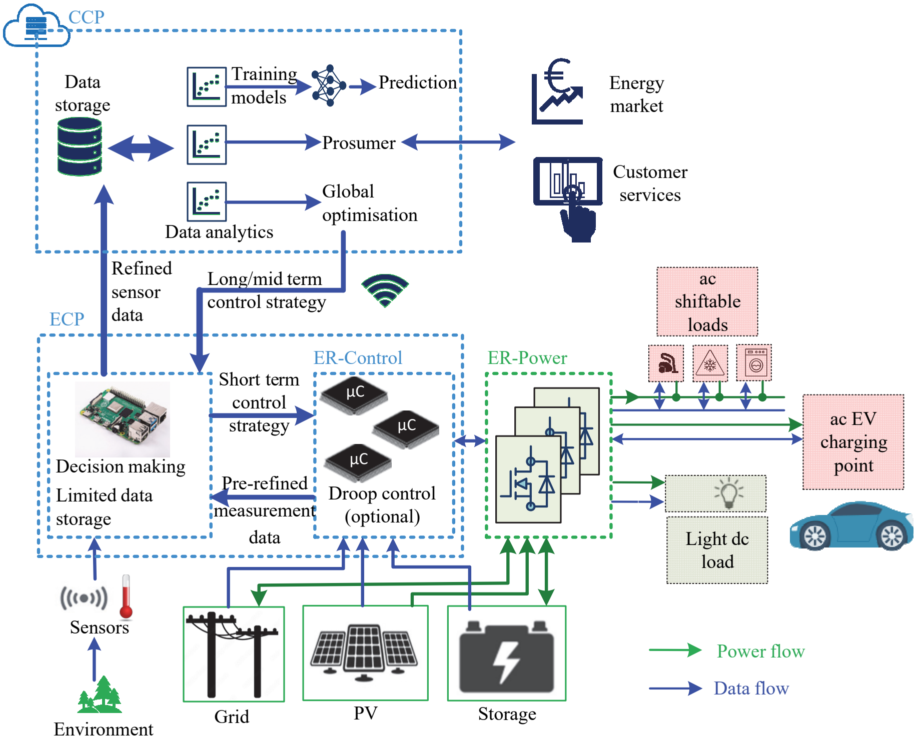

Fig. 11. Hybrid CCP/ ECP for ER control.

8 Conclusion

With the increasing penetration of renewable energy sources and BSS, alongside the adoption of concepts such as NZEB, demand-side load shifting and EMS tools are becoming critical components of next-generation residential infrastructures. At the same time, transitioning toward DC and hybrid-compatible architectures is essential to leverage the higher efficiency of DC-based systems.

This study analyzes and compares multiple scenarios for DC system integration. Subsequently, prospective configurations for future ERs are explored. Safety concerns related to leakage currents are addressed, and corresponding mitigation strategies are proposed. Finally control strategy was discussed at different levels, and at the high-level layer, a robust EMS framework is introduced to support system digitalization while ensuring high reliability.

Acknowledgments. This project has received funding from the European Union's Horizon 2020 research and innovation programme under the Marie Skłodowska-Curie grant agreement No 955614.

References

1. https://www.consilium.europa.eu/en/infographics/how-is-eu-electricity-produced-and-sold.
2. https://www.solarpowereurope.org/press-releases/new-report-eu-solar-reaches-record-heights-of-56-gw-in-2023-but-warns-of-clouds-on-the-horizon
3. https://energy.ec.europa.eu/system/files/2022-05/COM_2022_221_2_EN_ACT_part1_v7.pdf
4. https://www.solarpowereurope.org/press-releases/new-analysis-reveals-european-solar-battery-storage-market-increased-by-94-in-2023
5. E. Tsioumas, N. Jabbour, M. Koseoglou, D. Papagiannis and C. Mademlis, "Enhanced Sizing Methodology for the Renewable Energy Sources and the Battery Storage System in a Nearly Zero Energy Building," in IEEE Trans. on Power Electron., vol. 36, no. 9, pp. 10142-10156, Sept. 2021.
6. https://ec.europa.eu/commission/presscorner/detail/en/ip_21_6683
7. O. Husev, D. Vinnikov, S. Kouro, F. Blaabjerg and C. Roncero-Clemente, "Dual-Purpose Converters for DC or AC Grid as Energy Transition Solution: Perspectives and Challenges," in IEEE Ind. Electron. Magazine, Early access.
8. N. Papanikolaou, A. Kyritsis, M. Loupis, C. Tzotzos and E. Zoga, "Design Considerations for Single-Phase Line Frequency Transformers Applied at Photovoltaic Systems," in IEEE Power and Energy Technology Systems Journal, vol. 2, no. 3, pp. 82-93, Sept. 2015.
9. M. A. Hannan et al., "State of the Art of Solid-State Transformers: Advanced Topologies, Implementation Issues, Recent Progress and Improvements," in IEEE Access, vol. 8, pp. 19113-19132, 2020.
10. X. She, A. Q. Huang and R. Burgos, "Review of Solid-State Transformer Technologies and Their Application in Power Dis-tribution Systems," in IEEE Journal of Emerging and Selected Topics in Power Electronics, vol. 1, no. 3, pp. 186-198, Sept. 2013.
11. M. -H. Ryu, H. -S. Kim, J. -W. Baek, H. -G. Kim and J. -H. Jung, "Effective Test Bed of 380-V DC Distribution System Using Isolated Power Converters," in IEEE Transactions on Industrial Electronics, vol. 62, no. 7, pp. 4525-4536, July 2015.
12. IEEE Standard for Interconnection and Interoperability of Distributed Energy Resources with Associated Electric Power Systems Interfaces--Amendment 1: To Provide More Flexibility for Adoption of Abnormal Operating Performance Category III," in IEEE Std 1547a-2020 (Amendment to IEEE Std 1547-2018) , vol., no., pp.1-16, 15 April 2020.
13. G. Buticchi, D. Barater, E. Lorenzani and G. Franceschini, "Digital Control of Actual Grid-Connected Converters for Ground Leakage Current Reduction in PV Transformerless Systems," in IEEE Transactions on Industrial Informatics, vol. 8, no. 3, pp. 563-572, Aug. 2012.
14. T. R. Oliveira, W. W. A. G. Silva, S. I. Seleme and P. F. Donoso-Garcia, "PLL-Based Feed-Forward Control to Attenuate Low-Frequency Common-Mode Voltages in Transformerless LVDC Systems," in IEEE Transactions on Industry Applica-tions, vol. 55, no. 3, pp. 3151-3159, May-June 2019.
15. J. Qiu, Y. He, C. Lei, Q. Jiao and J. Liu, "An Improved LMSVM Method for Leakage Current Suppression and Neutral-Point Voltage Control in Transformerless NPC Three-Level Inverters," in IEEE Journal of Emerging and Selected Topics in Power Electronics, vol. 10, no. 3, pp. 3100-3113, June 2022.
16. L. Zhou, F. Gao and T. Xu, "Implementation of Active NPC Circuits in Transformer-Less Single-Phase Inverter With Low Leakage Current," in IEEE Transactions on Industry Applications, vol. 53, no. 6, pp. 5658-5667, Nov.-Dec. 2017.
17. S. Iturriaga-Medina et al., "Leakage-Ground Currents Compensation in a Transformerless HB-NPC Topology Using a DC-link-Tied LC Filter for Photovoltaic Applications," in IEEE Journal of Emerging and Selected Topics in Power Electronics, vol. 10, no. 4, pp. 4725-4737, Aug. 2022.

18. G. Escobar, P. R. Martinez-Rodriguez, S. Iturriaga-Medina, J. C. Mayo-Maldonado, J. Lopez-Sarabia and O. M. Miche-loud-Vernackt, "Mitigation of Leakage-Ground Currents in Transformerless Grid-Tied Inverters via Virtual-Ground Con-nection," in IEEE Journal of Emerging and Selected Topics in Power Electronics, vol. 8, no. 3, pp. 3111-3123, Sept. 2020.
19. S. Rivera, R. Lizana F., S. Kouro, T. Dragičević and B. Wu, "Bipolar DC Power Conversion: State-of-the-Art and Emerging Technologies," in IEEE Journal of Emerging and Selected Topics in Power Electronics, vol. 9, no. 2, pp. 1192-1204, April 2021.
20. S. Dey, V. K. Bussa and R. K. Singh, "Transformerless Hybrid Converter With AC and DC Outputs and Reduced Leakage Current," in IEEE Journal of Emerging and Selected Topics in Power Electronics, vol. 7, no. 2, pp. 1329-1341, June 2019.
21. F. Melzi, A. Same, M. Zayani, and L. Oukhellou, “A Dedicated Mixture Model for Clustering Smart Meter Data: Identification and Analysis of Electricity Consumption Behaviors,” Energies, vol. 10, no. 10, p. 1446, Sep. 2017.
22. A. Stippich et al., "From Ac to Dc: Benefits in Household Appliances," International ETG Congress, Bonn, Germany, 2017, pp. 1-6.
23. D. L. Gerber, V. Vossos, W. Feng, A. Khandekar, C. Marnay, B. Nordman, "A simulation based comparison of AC and DC power distribution networks in buildings," in proc. of IEEE Second International Conference on DC Microgrids (ICDCM), Nuremburg, Germany, 2017, pp. 588-595.
24. A. Goikoetxea, J. M. Canales, R. Sanchez, P. Zumeta, "DC versus AC in residential buildings: Efficiency comparison," Eurocon 2013, Zagreb, Croatia, 2013, pp. 1-5.
25. A. Santos, G. Duggan, S. Frank, D. Gerber, D. Zimmerle. "Endpoint use efficiency comparison for ac and dc power distribution in commercial buildings." Energies, 14, no. 18 (2021): 5863.
26. H.E. Gelani, F. Dastgeer, M. Nasir, S. Khan, J.M. Guerrero. "Ac vs. dc distribution efficiency: Are we on the right path?." Energies 14, no. 13 (2021): 4039.
27. M. Najafzadeh, R. Ahmadiahangar, O. Husev, I. Roasto, T. Jalakas and A. Blinov, "Recent Contributions, Future Prospects and Limitations of Interlinking Converter Control in Hybrid AC/DC Microgrids," in IEEE Access, vol. 9, pp. 7960-7984, 2021.
28. M.-H. Ryu, H.-S. Kim, J.-W. Baek, H. -G. Kim and J. -H. Jung, "Effective Test Bed of 380-V DC Distribution System Using Isolated Power Converters," in IEEE Trans. on Ind. Electron., vol. 62, no. 7, pp. 4525-4536, July 2015.
29. M. Azizi, O. Husev, O. Veligorskyi, M. Turzvński and R. Strzelecki, "Dc Leakage Current in Isolated Grid-Connected dc Nanogrid - Origins and Elimination Methods," 2024 IEEE 18th International Conference on Compatibility, Power Electronics and Power Engineering (CPE-POWERENG), Gdynia, Poland, 2024, pp. 1-6.
30. J. Mohammadi, F. Badrkhani Ajaei and G. Stevens, "Grounding the DC Microgrid," in IEEE Trans. on Ind. Appl., vol. 55, no. 5, pp. 4490-4499, Sept.-Oct. 2019.
31. M. Azizi, O. Husev, O. Veligorskyi, S. Rahimpour, C. Roncero-Clemente, “Grounding and Isolation Requirements in DC Microgrids: Overview and Critical Analysis,” Energies, vol. 16, no. 23, p. 7747, Nov. 2023, doi: 10.3390/en16237747.
32. H. Yan Lu, Jian Guo Zhu and S. Y. R. Hui, "Experimental determination of stray capacitances in high frequency transformers," in IEEE Trans. on Power Electron., vol. 18, no. 5, pp. 1105-1112, Sept. 2003.
33. O. Husev, N.V. Kurdkandi, M.G. Marangalu, D. Vinnikov and S. H. Hosseini, "A New Single-Phase Flying Inductor-Based Common Grounded Converter for Dual-Purpose Application," in IEEE Trans. on Ind. Electron., vol. 70, no. 8, pp. 799 7913-7923, Aug. 2023.
34. R. Barzegarkhoo, S. S. Lee, Y. P. Siwakoti, S. A. Khan and F. Blaabjerg, "Design, Control, and Analysis of a Novel Grid-Interfaced Switched-Boost Dual T-Type Five-Level Inverter With Common-Ground Concept," in IEEE Transactions on Industrial Electronics, vol. 68, no. 9, pp. 8193-8206, Sept. 2021.
35. S. S. Lee, C. Shen Lim, Y. P. Siwakoti and K. -B. Lee, "Single-Stage Common-Ground Boost

Inverter (S2CGBI) for Solar Photovoltaic Systems," 2019 IEEE Energy Conversion Congress and Exposition (ECCE), Baltimore, MD, USA, 2019, pp. 4229-4233.

36. O. Husev, N.V. Kurdkandi, M.G. Marangalu, D. Vinnikov and S. H. Hosseini, "A New Single-Phase Flying Inductor-Based Common Grounded Converter for Dual-Purpose Application," in IEEE Trans. on Ind. Electron., vol. 70, no. 8, pp. 799 7913-7923, Aug. 2023.
37. S. Rahimpour, O. Husev and D. Vinnikov, "A Family of Bidirectional Solid-State Circuit Breakers with Increased Safety in DC Microgrids," in IEEE Transactions on Industrial Electronics, vol. 71, no. 9, pp. 10919 10929, Sept. 2024, doi: 10.1109/TIE.2023.3337493.
38. H. N. Hokmabad, T. H. Shahsavar, O. Matiushkin, T. Jalakas, O. Husev and J. Belikov, "Single Cell Energy Router Justification for Three Phase Near Zero Energy Buildings," 2025 IEEE Applied Power Electronics Conference and Exposition (APEC), Atlanta, GA, USA, 2025, pp. 1622-1628.
39. O. Kukrer, S. Bayhan and H. Komurcugil, "Model-Based Current Control Strategy With Virtual Time Constant for Improved Dynamic Response of Three-Phase Grid-Connected VSI," in IEEE Transactions on Industrial Electronics, vol. 66, no. 6, pp. 4156-4165, June 2019.
40. O. Husev, C. Roncero-Clemente, E. Makovenko, S. P. Pimentel, D. Vinnikov and J. Martins, "Optimization and Implementation of the Proportional-Resonant Controller for Grid-Connected Inverter With with Significant Computation Delay," in IEEE Transactions on Industrial Electronics, vol. 67, no. 2, pp. 1201-1211, Feb. 2020.
41. L. Rosado, J. Samanes, E. Gubia and J. Lopez, "Selective Harmonic Mitigation: Limitations of Classical Control Strategies and Benefits of Model Predictive Control," in IEEE Transactions on Industry Applications, vol. 59, no. 5, pp. 6082-6094, Sept.-Oct. 2023.
42. Ranjan Bana, M. Amin and M. Molinas, "ANN-Based Surrogate PI and MPC Controllers for Grid-Connected VSC System: Small-Signal Analysis and Comparative Evaluation," in IEEE Journal of Emerging and Selected Topics in Power Electronics, vol. 12, no. 1, pp. 566-578, Feb. 2024.
43. M. Najafzadeh, N. Strzelecka, O. Husev, I. Roasto, K. Nassereddine, D. Vinnikov, and R. Strzelecki, "Grid-forming operation of energy-router based on model predictive control with improved dynamic performance," Energies, vol. 15, no. 11, p. 4010, 2022.
44. M. Merai, M. W. Naouar, I. Slama-Belkhodja and E. Monmasson, "An Adaptive PI Controller Design for DC-link Voltage Control of Single-Phase Grid-Connected Converters," in IEEE Transactions on Industrial Electronics, vol. 66, no. 8, pp. 6241-6249, Aug. 2019.
45. B. Long, P. J. Lu, K. T. Chong, J. Rodriguez and J. M. Guerrero, "Robust Fuzzy-Fractional-Order Nonsingular Terminal Sliding-Mode Control of LCL-Type Grid-Connected Converters," in IEEE Transactions on Industrial Electronics, vol. 69, no. 6, pp. 5854-5866, June 2022.
46. O. Husev, J. Belikov, O. Matiushkin, D. Vinnikov, R. Ahmadiahangar and N. V. Kurdkandi, "Optimal Tuning of Resonant- and Repetitive-Based Controller for Single-Phase Buck–Boost Inverter With Unfolding Circuit," in IEEE Journal of Emerging and Selected Topics in Industrial Electronics, vol. 3, no. 4, pp. 954-965, Oct. 2022.
47. M. Fliess, J. Levine, P. Martin and P. Rouchon, "A Lie-Backlund approach to equivalence and flatness of nonlinear systems," in IEEE Transactions on Automatic Control, vol. 44, no. 5, pp. 922-937, May 1999.
48. P. Mungporn et al., "Dynamics improvement of 3-phase inverter with output LC-filter by using differential flatness based control for grid connected applications," in Proceedings of the 2016 19th International Conference on Electrical Machines and Systems (ICEMS), Chiba, Japan, 2016, pp. 1-6.
49. H. Renaudineau, D. Lopez, F. Flores-Bahamonde and S. Kouro, "Flatness-based control of a boost inverter for PV microinverter application," 2017 IEEE 8th International Symposium on Power Electronics for Distributed Generation Systems (PEDG), Florianopolis, Brazil, 2017, pp. 1-6.

50. H. A. Khalid, C. Cecati, N. A. Al-Emadi, A. Gastli and L. Ben-Brahim, "Differential Flatness-Based Performance Enhancement of a Vector Controlled VSC With an LCL-Filter for Weak Grids," in IEEE Access, vol. 9, pp. 33557-33568, 2021.
51. M. Mehrasa, E. Pouresmaeil, S. Taheri, I. Vechiu and J. P. S. Catalão, "Novel Control Strategy for Modular Multilevel Converters Based on Differential Flatness Theory," in IEEE Journal of Emerging and Selected Topics in Power Electronics, vol. 6, no. 2, pp. 888-897, June 2018.
52. C. Roncero-Clemente, E. Romero-Cadaval, O. Husev and D. Vinnikov, "P and Q control strategy for single phase Z/qZ source inverter based on d-q frame," 2014 IEEE 23rd International Symposium on Industrial Electronics (ISIE), Istanbul, Turkey, 2014, pp. 2048-2053.
53. D. Minoli, K. Sohraby and B. Occhiogrosso, "IoT Considerations, Requirements, and Architectures for Smart Buildings—Energy Optimization and Next-Generation Building Management Systems," in IEEE Internet of Things Journal, vol. 4, no. 1, pp. 269-283, Feb. 2017.
54. C. Balasubramanian and R. L. Raja Singh, "IoT Based Energy Management System in Smart Grid," 2023 Innovations in Power and Advanced Computing Technologies (i-PACT), Kuala Lumpur, Malaysia, 2023, pp. 1-6.
55. I. Fagarasan, I. Stamatescu, N. Arghira, D. Hossu, A. Hossu and S. S. Iliescu, "Control Techniques and Strategies for Microgrids: Towards an Intelligent Control," 2017 21st International Conference on Control Systems and Computer Science (CSCS), Bucharest, Romania, 2017, pp. 630-635.
56. Yantao Liu, Wei Deng, Peng Yang, Yuting Teng, Xue Zhang, Yanhong Yang, Wei Pei, Dispatchable Droop Control Strategy for DC Microgrid, Energy Reports, Volume 9, Supplement 12, 2023, Pages 98-102, ISSN 2352-4847.
57. Usman Bashir Tayab, Mohd Azrik Bin Roslan, Leong Jenn Hwai, Muhammad Kashif, A review of droop control techniques for microgrid, Renewable and Sustainable Energy Reviews, Volume 76, 2017, Pages 717-727, ISSN 1364-0321.
58. Shu Godwill Ndeh, Divine Khan Ngwashi, Lawrence K. Letting, Chu Donatus Iweh, Emmanuel Tanyi, Power sharing enhancement through a decentralized droop-based control strategy in an islanded microgrid, e-Prime - Advances in Electrical Engineering, Electronics and Energy, Volume 7, 2024, 100433, ISSN 2772-6711.
59. W. Wang, X. Lei, B. Wei, K. He and P. Yang, "Research on Adaptive Droop Control Strategy of DC Active Power and Voltage in DC Microgrid," 2023 International Conference on Power Energy Systems and Applications (ICoPESA), Nanjing, China, 2023, pp. 627-632.
60. S. Prakash, V. Nougain and S. Mishra, "Adaptive Droop-Based Control for Active Power Sharing in Autonomous Microgrid for Improved Transient Performance," in IEEE Journal of Emerging and Selected Topics in Power Electronics, vol. 9, no. 3, pp. 3010-3018, June 2021.
61. Q. -C. Zhong, "Robust Droop Controller for Accurate Proportional Load Sharing Among Inverters Operated in Parallel," in IEEE Transactions on Industrial Electronics, vol. 60, no. 4, pp. 1281-1290, April 2013.
62. A. Basati, A. Fakharian and J. M. Guererro, "An intelligent droop control for improve voltage regulation and equal power sharing in islanded DC microgrids," 2017 5th Iranian Joint Congress on Fuzzy and Intelligent Systems (CFIS), Qazvin, Iran, 2017, pp. 190-195.
63. T. L. Vandoorn, J. D. M. De Kooning, B. Meersman and L. Vandevelde, "Communication-based secondary control in microgrids with voltage-based droop control," PES T&D 2012, Orlando, FL, USA, 2012, pp. 1-6.
64. L. Meng, T. Dragicevic, J. Roldán-Pérez, J. C. Vasquez and J. M. Guerrero, "Modeling and Sensitivity Study of Consensus Algorithm-Based Distributed Hierarchical Control for DC Microgrids," in IEEE Transactions on Smart Grid, vol. 7, no. 3, pp. 1504-1515, May 2016.
65. R. Li, S. Liu, M. Xia and X. Liu, "Analysis of Effects of Communication Conditions on Distributed Secondary Control for DC Microgrids," 2020 IEEE 9th International Power Electronics and Motion Control Conference (IPEMC2020-ECCE Asia), Nanjing, China,

2020, pp. 2933-2938.

66. A. Lahmer, J. -W. Chang, H. Jeong and S. Chae, "Distributed Hierarchical Control of Energy Storage Systems in a DC Microgrid under Consensus Based Adaptive Droop Control Method," 2023 11th International Conference on Power Electronics and ECCE Asia (ICPE 2023 - ECCE Asia), Jeju Island, Korea, Republic of, 2023, pp. 568-573.
67. L. Meng, T. Dragicevic, J. M. Guerrero and J. C. Vasquez, "Dynamic consensus algorithm based distributed global efficiency optimization of a droop controlled DC microgrid," 2014 IEEE International Energy Conference (ENERGYCON), Cavtat, Croatia, 2014, pp. 1276-1283.
68. S. Wang, X. Wang and W. Wu, "Cloud Computing and Local Chip-Based Dynamic Economic Dispatch for Microgrids," in IEEE Transactions on Smart Grid, vol. 11, no. 5, pp. 3774-3784, Sept. 2020.

Multiterminal bidirectional EV charging station with V2G functionality, powered from LV DC traction grid

Mykola Lukianov[1], Ryszard Strzelecki[2], Enrique Romero-Cadaval[3]

[1]Faculty of Electrical and Control Engineering, Gdańsk University of Technology,
Gdańsk, Gabriela Narutowicza 11/12, 80-222, Poland (e-mail: mykola.lukianov@pg.edu.pl)

[2]Faculty of Electrical Engineering, Gdynia Maritime University,
Gdynia, 81-87 Morska St., Poland, (e-mail: r.strzelecki@we.umg.edu.pl)

[3]Electrical, Electronic and Control Engineering Department, University of Extremadura,
Badajoz, Av. de Elvas, s/n, 06006, Spain (e-mail: eromero@unex.es)

Abstract. The rapid adoption of electric vehicles, now comprising around 20% of the global automotive market, calls for a strategic expansion of charging infrastructure. Urban areas face particular challenges due to limited space and the high cost of installing new high-power chargers. A promising solution is to leverage existing low-voltage DC traction grids—commonly used for trams and metros—for EV charging. This approach reduces infrastructure costs and allows efficient use of existing substations and power electronics. This book chapter discusses a scalable multiport Current-Fed Multi-Active Bridge DC-DC converter to support multiterminal EV charging stations connected to DC traction networks. The multiport architecture enables flexible power flow, bidirectional operation, and shared use of converter components across multiple EVs and energy storage units. In addition to cost and space efficiency, the system enhances grid stability, allows recuperation of regenerative braking energy from public transport, and supports smart grid functions such as vehicle-to-grid and vehicle-to-vehicle energy exchange.

Keywords: bidirectional EV charging; traction grids; DC/DC converters; smart charging; V2G services.

1 Introduction

In recent years, the number of electric vehicles (EVs) worldwide has been growing at an unprecedented rate, with annual sales increasing year over year. As a result, EVs now account for approximately 20% of the global automotive market [1]. This rapid adoption contributes significantly to reducing local air pollution and greenhouse gas emissions, particularly in densely populated urban areas. However, to fully realize the environmental and energy benefits of EVs, it is critical that their charging infrastructure is strategically developed, utilizing renewable energy sources and advanced power electronics technologies to ensure efficient, scalable, and sustainable integration with the power grid. One of the primary challenges accompanying this growth is the increasing demand for publicly accessible EV charging stations, especially in cities.

Installing high-power chargers in urban areas typically requires substantial investments in new infrastructure, including medium-voltage substations, transformers, and dedicated power converters. These upgrades are not only costly but are also often constrained by limited space and regulatory barriers in built-up areas. Moreover, integrating a large number of EV chargers into existing grids can lead to considerable stress on the grid, including voltage fluctuations, transformer aging, and power quality issues, especially when fast charging is involved [2]. To address these challenges, recent research and urban energy planning efforts have explored the possibility of leveraging existing infrastructure to support EV charging needs. One promising approach is to utilize low-voltage direct current (LV DC) traction grids—already present in many European cities for light rail, trams, and metro systems—as a backbone for EV charging stations [3]. These traction grids are typically underutilized during off-peak hours and at night when public transport is inactive, yet remain operational and capable of supplying power. By connecting EV chargers to these existing DC networks, it is possible to significantly reduce the installation and operational costs associated with building new charging infrastructure. This approach is particularly effective in locations where multiple vehicles are typically parked and can be charged simultaneously, such as near residential buildings, transit hubs, or parking lots adjacent to rail lines. Implementing multiterminal charging stations in such areas makes efficient use of space and resources, enabling multiple EVs to share power electronics and grid access infrastructure.

Beyond cost and space efficiency, integrating EV charging with LV DC traction grids offers several technical advantages. These include the ability to mitigate LV DC traction grid voltage surges and sags through controlled power exchange, improving overall grid stability, and utilize regenerative braking energy from public transport systems to charge EVs, rather than dissipating it in resistive braking elements [4]. Moreover, EVs equipped with bidirectional chargers can participate in vehicle-to-grid applications, discharging stored energy during grid demand peaks, thereby supporting grid and reducing the impact of load fluctuations. In this way, EVs can function as distributed energy storage units within a smart grid ecosystem. In this book chapter, the use of a Current-Fed Multi-Active Bridge (CF-MAB) DC-DC converter is studied, as a potential solution for providing bidirectional EV charging from the LV DC traction grids. The CF-MAB converter is a multiport power converter that allows multiple EVs and a battery energy storage system be connected to a common DC bus with high flexibility and efficiency. Compared to conventional charging station architectures—where each EV or battery storage unit requires a separate dedicated converter—the multiport CF-MAB converter topology reduces the total number of components, leading to cost savings, simplified thermal management, and enhanced system reliability. Each port of the MAB converter can operate independently, supporting flexible energy flow modes such as vehicle-to-grid (V2G), vehicle-to-vehicle (V2V), and energy exchange with a stationary battery. This modular and scalable architecture is well-suited to multiterminal charging stations and can be adapted to varying numbers of EVs or different grid conditions. Furthermore, the CF-MAB-based system contributes to stabilizing the voltage of the LV DC traction grid at the point of connection and optimizes the usage of surplus energy, such as that generated by rail transport regenerative braking.

2 State of EVs market and EVs charging

2.1 Electromobility and EV chargers development trends Formulas

Electric car sales continue to grow, surpassing 17 million in 2024 and accounting for more than one in five cars sold globally. They are steadily becoming a mass-market option in more countries. Despite concerns over tight profit margins, volatile battery metal prices, inflation, and the reduction of subsidies in some regions, global sales remain strong. In the first quarter of 2024, electric car sales rose about 25% compared to the same period in 2023, similar to growth in 2022. In Europe, one in five new cars sold was electric, maintaining the previous year's share. Sales share increased in 14 of 27 EU countries, but declined or stalled in others, including Germany and France, mainly due to subsidy changes. Germany ended subsidies in late 2023, while France has gradually scaled back its incentives, limiting bonuses for higher-income buyers and narrowing eligibility in early 2024 [5].

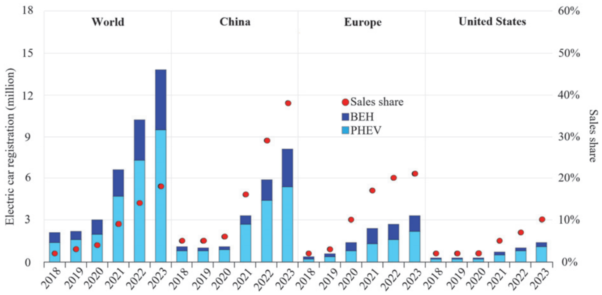

Fig. 2. Electric car registrations and sales share in China, United States and Europe, 2018-2023.

Home charging remains the most common option for EV owners. In Europe and the U.S., over two-thirds of chargers are in urban areas, where most public infrastructure still relies on slow chargers (≤22 kW). Only 15% of urban public chargers in Europe exceed this power. However, expanding public charging is essential for wider EV adoption, especially for people without home charging access. In 2024, public charging points in Europe grew by over 35%, surpassing 1 million. Yet, deployment varies widely by country. The Netherlands leads with over 180,000 public chargers, followed by Germany (160,000) and France (155,000). Under the STEPS scenario, public chargers in Europe are expected to double by 2030 to more than 2 million, with fast chargers making up 30% of the total—up from less than 20% in 2024. This would boost public charging capacity to 115 GW. To meet 2030 goals, Europe needs to install around 210,000 public chargers annually. Several countries have set ambitious national targets: France aims for 400,000 public chargers by 2030, the UK for 300,000, and Germany has proposed 1 million—though this figure has faced criticism for being excessive. EU regulation is also pushing deployment forward. The AFIR mandates fast chargers of at least 150 kW every 60 km along major road networks by 2025, increasing minimum total power output per station to 600 kW by 2027. Additionally, the revised

EU Energy Performance in Buildings Directive supports private charging rollout by requiring pre-cabling in buildings to avoid costly retrofits later.

2.2 Bidirectional charging perspectives

From the other side, mass electric vehicles charging can significantly impact the power grid in a negative way, creating significant technical challenges, such as grid overloads, especially during peak charging hours, leading to voltage instability, increased wear on infrastructure, the need for costly grid upgrades, and potential disruptions in electricity supply if not properly managed. Several measures can turn these impacts into opportunities for flexibility. In Table 1, four phases are outlined, each reflecting greater flexible EV load and rising system demand for flexibility, starting with a V1G grid compliant charging, ending with aggregated V2G bidirectional charging. The core strategy is to maximize managed charging over unmanaged charging.

Table 7. Vehicle to grid integration levels [6, 7].

	Grid compliant charging	**Level 1 – V1G Smart Charging**	**Level 2 – V1G Cooperative smart charging**	**Level 3 – V2G Bidirectional charging**	**Level 4 – V2G Aggregated charging**
Description	-Unidirectional charging -Compliant EV charging from grid to EV -Power levels are low in order to be controlled by DSO	-Unidirectional smart charging -Charging power can be regulated by EV user, home management system or DSO in automatic regime remotely according to needs	-Unidirectional charging -EV charging profiles is set according to monetary reasons, grid constrains etc. -EV aggregation in order to have more power (local, per charging spot)	-Bidirectional charging -Energy can be transferred from battery to customers home/load -Supports behind the meter services -Charging is motivated by economical or sustainability reasons	-Bidirectional charging -EV charging goes beyond customers own needs (aggregation function, balancing services, economic profits). -Aggregation across large area (city, country)
Requirements	-Local regulations (grid codes, IEC 61851, IEC 60364 series…)	-IEC 61851 -DIN-SPEC 70121 -OCPP 1.6 -Demand-response -Opt-out possibilities	-Level 1 + -ISO/IEC15118 -OCPP 1.6 -EV and Grid Telematics -Time of Use metering	-Level 2 + -ISO/IEC15118-20 -EEBus	-Level 3 + -ISO-15118-20-2022, CHAdeMO

Measures include providing locational signals, applying non-firm connections during peak times, requiring storage or associated fees, and linking connection fees to demand or controllability. Policy tools such as tariff design, flexibility markets, and wholesale market participation can support this. Although individual EVs may be too small to participate in markets, standardization and interoperability can enable aggregation. Coordinated EV charging, aligned with renewable generation, can be incentivized through renewable capacity contracting. To realize these benefits, policy makers should promote smart-readiness through clear control standards, easily implementable by EV producers and monetary reward for EV owners.

However, the challenge of implementing controlled bidirectional charging and enabling EV participation in the aforementioned services is further complicated by the fact that vehicles from different manufacturers are equipped with different charging connectors, have varying power ratings, and adhere to different charging standards. EV chargers are commonly categorized by their power output into slow and fast chargers, with ultra-fast chargers considered a subset of the latter. Several international standards define and classify these systems, including IEC 61851-1, SAE J1772, and CHAdeMO. These standards specify power levels for both AC and DC charging modes (see Table 2). Slow charging generally refers to AC Levels 1 and 2, which rely on onboard chargers. Under the IEC standard, this corresponds to a maximum power of 22 kW, while under SAE it is up to 19 kW. Notably, within the SAE classification, only AC Level 3 refers to an off-board charger capable of delivering fast charging above 50 kW. Fast charging, particularly DC fast charging, is defined in standards such as SAE CCS, IEC 61851-23, and CHAdeMO. These systems typically deliver power in the 50–240 kW range, with ultra-fast chargers—like the EVTEC TERRA HP 350—providing up to 350 kW. To accommodate both AC and DC charging, EVs are usually equipped with two charging ports or a combined inlet. For AC, common connector types include J1772 Type 1, Type 2, GB/T-AC, and Tesla. For DC, standards include CHAdeMO, GB/T-DC, and Tesla DC. Integrated systems such as CCS1, CCS2, and ChaoJi allow both AC and DC charging through a single interface.

Table 2. Charging standards description [8].

Type	**Level**	**Charger location**		**Hours to charge 300 km**	**Specification**		
		On-board	**Off-board**		**Voltage (V)**	**Current (A)**	**Power (kW)**
				SAE			
AC	Level 1	+	−	7 - 17	120	12 - 16	≤ 1.92
	Level 2	+	−	0.4 - 1.2	240	80	1.92-19.2
	Level 3	−	+	0.5 - 1	480	≥ 100	≥ 50
				IEC			
	Level 1	+	−	2 - 3	250 - 450	16	4-7
	Level 2	+	−	1 - 2		63	22
				SAE			
DC	Level 1	−	+	0.4 - 1.2	200 - 600	80	36
	Level 2	−	+	0.2 - 0.4		200	90
	Level 3	−	+	0.2		400	240
				CHAdeMO			
	Fast Charging	−	+	≥ 0.5	≤ 480	200	≥ 135

Many of today's charging standards are evolving to support bidirectional power flow, enabling V2G and vehicle-to-home (V2H) applications. CHAdeMO has long supported bidirectional charging, while CCS is gradually adding V2G functionality through updates like ISO 15118-20. However, integrating V2G into ultra-fast chargers raises practical concerns. These chargers are typically used when drivers need rapid energy replenishment—often during travel or emergencies—so activating V2G in such scenarios would delay charging and run counter to user expectations. As a result, enabling bidirectional flow at high-power stations may be inefficient or even counterproductive. Slow AC chargers are much better suited for grid services like frequency regulation, voltage support, or energy balancing. EVs connected to these chargers—often overnight or during the workday—offer grid operators a stable and predictable energy resource. Mid-range fast chargers (below 50 kW) present a more nuanced case. They appeal to users needing moderate top-ups and can be effective for short-duration grid services (0 - 30 seconds) like frequency regulation or post-blackout stabilization, where energy drawn from the EVs battery is minimal. However, relying on mid-power fast chargers is less convincing for long-duration grid services such as peak shaving, capacity market participation, or backup power during outages, which require extended energy discharge and could conflict with user charging needs. As a result, aligning charger type and power level with appropriate V2G use cases is critical and remains a major challenge for widespread V2G deployment.

3 Suitable urban connection LV DC connection vs AC connection.

To avoid overloading the low-voltage network, public EV charging stations are often connected to the medium-voltage (MV) grid through a low-frequency (LF) distribution transformer, as illustrated in Table 3a. While AC-based charging is the more commonly used and researched approach, it comes with notable drawbacks: it requires an additional AC/DC conversion stage and a large LF transformer. These components increase installation costs, reduce energy efficiency, and enlarge the physical footprint of the charging station. A more cost-effective alternative is to make use of existing infrastructure—specifically, urban traction grids, which are already well-developed in many large cities. Integrating EV chargers with these grids offers several mutual advantages:

- Voltage stabilization and energy recovery: DC traction grids can experience significant voltage fluctuations, during electric trains acceleration and deceleration. Traditionally, on-board energy storage systems, located on a moving train are used to smooth these instabilities. However, connected to the traction grid bidirectional EV chargers can serve the same purpose.

- Reactive power support: Traction lines often suffer from reactive power imbalances, particularly during periods of low activity (e.g., night time), when active power consumption is minimal. Although reactive power compensators are typically installed to handle this issue, EV chargers can partially offset the need for them by acting as an additional load.

- Lower charger installation costs: Smart charging strategies can shift EV charging to periods of low traction demand, such as off-peak hours, minimizing the risk of grid overload. By aligning EV charging with the power availability in traction systems, both the traction grid and EV infrastructure can benefit from more balanced and cost-effective energy use.

Table 3. Urban EV charger connection points.

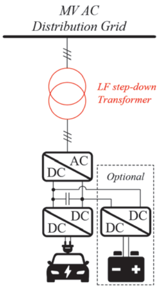 a) MV AC Distribution grid connection through LF-step down transformer	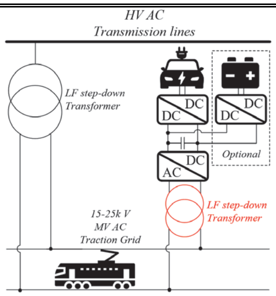 b) MV AC Traction Grid connection using a LF-step-down transformer
-Reliable -Low voltage fluctuations in the point of connection *-Significant installation costs* *-Requires additional AC-DC conversion stage* *-Bulky LF transformer*	*-Significant installation costs* *-MV AC Traction grid voltage fluctuations* *-Requires additional AC-DC conversion stage* *-Bulky LF transformer*
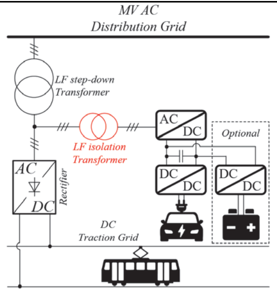 c) AC connection at traction substation through LF isolation transformer	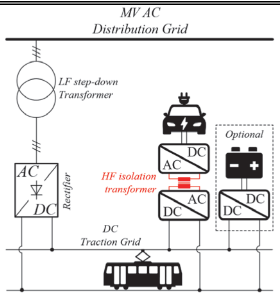 d) DC connection through High frequency isolation DC-DC converter
-Reliable -Low voltage fluctuations in the point of connection *-Requires additional AC-DC conversion stage* *-Bulky LF transformer*	-No AC-DC stage -Reduced installation costs -Small HF-isolation transformer *-LV DC traction grid voltage fluctuations*

Several connections of EV charging infrastructure into railway traction systems are presented in Table 3b, c, d. A MV AC traction connection typically involves interfacing directly with the traction grid using a LF step-down transformer, which comes with notable drawbacks. The LF transformer required is physically large, whereas MV AC traction grids are prone to voltage fluctuations, which can compromise the stability of EV charging. Moreover, this topology necessitates an additional AC-DC conversion stage, increasing system complexity, energy losses and costs. Alternatively, connecting to the AC side of a traction substation through a LF isolation transformer offers improved stability (Table 3c). In the proximity to the traction substation, voltage is more stable and predictable, enhancing the reliability of EV charging. However, similar to the MV approach, it still requires a bulky LF transformer and a subsequent AC-DC conversion stage, which adds to the system's footprint and operational losses. Other possible solution is a DC connection to the traction grid via a high-frequency isolated DC-DC converter. This approach eliminates the need for an intermediate AC-DC conversion stage, reducing component count and overall installation costs. The use of a high-frequency transformer allows for much smaller and lighter equipment, facilitating integration in constrained environments. However, the main drawback is the fluctuations of the DC traction voltage, which can change significantly, depending on train operation and load conditions.

In urban environments, the most prevalent DC traction grids include MV DC (typically operating at 1.5 kV or 3 kV) for suburban trains and metro systems, and LV DC systems (600–750 V) for trams and trolleybuses [9]. MV DC traction grids experience substantial voltage fluctuations—ranging from approximately 1.0 kV up to 3.6 kV and sudden load changes. This imposes higher technical requirements on the isolation and control stages of the DC-DC converter, often necessitating the use of advanced topologies such as multilevel or cascaded converters to ensure safe operation and high efficiency. In contrast, LV DC traction grids present a less demanding environment for EV charger integration. Although they still experience voltage variation, the range is narrower and easier to manage from a converter design standpoint. Furthermore, light rail systems in cities are typically well-developed, with many substations located at street level, which simplifies physical access for integration. From a power-matching perspective, power demand required for EVs multiport charging station aligns more closely with the power levels typical in light rail networks. This enhances the feasibility and efficiency of using EV batteries to absorb regenerative braking energy. Therefore, further study focuses on the integration of EV chargers into LV DC traction grids, which offers a balanced trade-off between technical complexity and practical implementation benefits.

The integration of battery energy storage (BES) systems into EV charging infrastructure is usually optional, however, it offers technical and economic advantages. Battery storage helps mitigating voltage fluctuations in DC traction grid, when aggregated EVs charging/discharging power is not enough for the required service, or there are no EVs connected. Additionally, BES allows providing longer term services – being used as a reserve battery for capacity market and electricity trading. As a result, studied solution includes a storage battery, used for a more flexible system operation.

4 Suitable converter topologies to integrate lots of EVs to the grid

To integrate multiple EVs and BES system into LV DC traction grids, different architectural options are available. A straightforward approach involves connecting each EV through an independent converter, for example, single-phase dual active bridge (DAB) converter, while the BES is interfaced using an interleaved three-phase boost converter (Fig. 2). This method supports scalability, by simply adding more DAB modules per each additional EV, ensures EV ports galvanic isolation and independent control of both EVs and BES. However, the trade-off is a higher component count required. Additionally, while the BES stabilizes the traction grid voltage, it does it in some range ΔV_{DC}. This means EVs still face unstable input voltages, which can complicate the DAB operation.

For the solutions requiring multiple loads and sources connection, the multiple active bridge (MAB) converter has been explored extensively [10]. It uses a shared transformer core to interconnect multiple active bridges, reducing the total number of switches. However, in multi-terminal EV charging stations—where each EV requires different voltage and power—this topology becomes difficult to manage due to inter-port dependencies. To tackle this, a variant using single-phase transformers was proposed in [11], allowing independent operation of multiple EVs while still minimizing switch count. Despite this improvement, it lacks a dedicated port for BES and still exposes EVs to the unstable traction grid voltage. A more refined solution involves using the current-fed dual active bridge (CF-DAB) converter [12], which combines a DAB converter with a boost stage. This topology adjusts the voltage on an auxiliary DC-link capacitor to match the EV voltage, ensuring perfect matching and stable operation even when the grid voltage fluctuates. While both single-phase [13] and multi-phase [14] CF-DAB designs improve voltage matching, they lack scalability, typically supporting only a few ports. Alternative is a studied current-fed multi active bridge converter, that integrates the benefits of a MAB with a single-phase transformers [11] and CF-DAB [13] topologies, while supporting scalable EV port expansion. Studied converter (Fig. 3) includes a dedicated BES port, and ensures all EVs are charged from a stable DC voltage node, while keeping the switch count low.

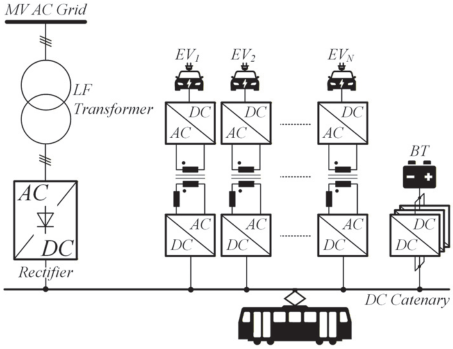

Fig. 2. The conventional way of integrating multiple EV charging stations and battery energy storage into a low-voltage DC traction grid.

Table 4. Comparison of storage battery and EV charger topologies.

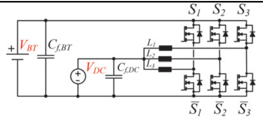 a) 3-phase Interleaved boost	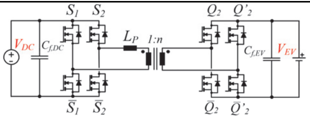 b) Dual Active Bridge
-Simple structure and low cost -Power distribution between phases -Modular structure -Low ripples *-Non isolated, thus, suitable as second stage for EV charging, or as a converter for BES connection*	-High efficiency -High power density -Simple control *- Reduced efficiency during V_{DC} and V_{EV} mismatch* *- EVs charging from an unstable traction grid voltage V_{DC}*
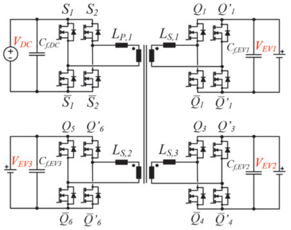 c) Multi-Active Bridge with common core transformer	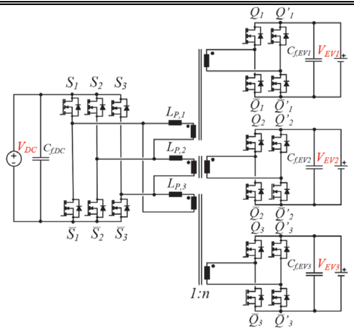 d) Multi-Active Bridge with single phase transformers
-Multiple ports connection is possible, with reduced number of switches *-Complex control* *-Ports interdependence, which becomes more challenging as the number of ports increases* *- Reduced efficiency during V_{DC} and V_{EV} mismatch* *- EVs charging from an unstable traction grid voltage V_{DC}*	-Multiple ports connection is possible, with reduced number of switches -Ports are independent from each other, thus, scalability is improved *- Reduced efficiency during V_{DC} and V_{EV} mismatch* *- EVs charging from an unstable traction grid voltage V_{DC}*
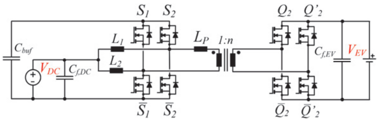 e) Single Phase CF-MAB	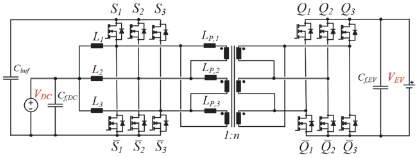 f) Three Phase CF-MAB
-Improved efficiency during V_{DC} and V_{EV} mismatch due to utilization of a buffer capacitor C_{buf} *-Lacks scalability*	-Improved efficiency during V_{DC} and V_{EV} mismatch due to utilization of a buffer capacitor C_{buf} -Higher power deliver capability then of a single-phase version *-Lacks scalability*

5 Studied CF-MAB converter solution

5.1 Bidirectional charging perspectives

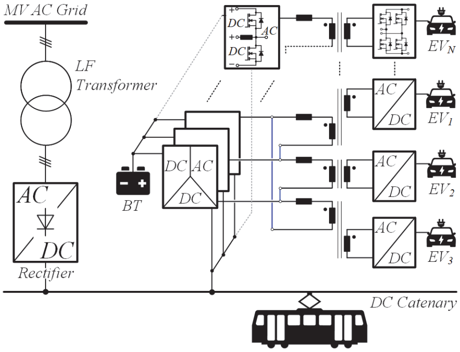

Fig. 3. Multi-terminal EV charging station using the studied multiport converter connected to a low-voltage DC traction grid.

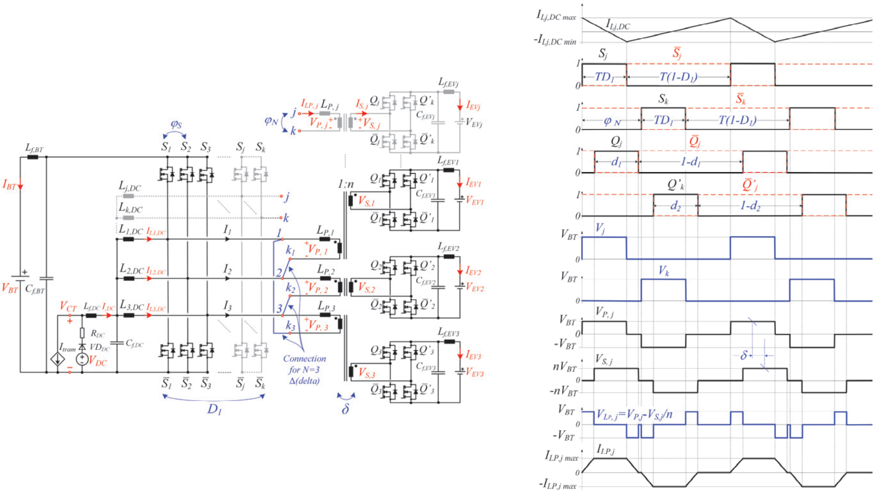
a) b)

Fig. 4. CF-MAB converter topology for an arbitrary numer of EVs (a) and its working diagrams (b).

The converter being analyzed (Fig. 4a) includes a port for connection to a DC grid, a non-isolated port for battery (BT) storage, and N isolated output ports for EV charging. On the input side, it uses N interleaved half-bridge stages that operate with phase shifts, similar to an interleaved boost converter. These stages boost the DC grid voltage V_{DC} to match the battery voltage V_{BT} during charging, and step down V_{BT} to match V_{DC} during discharging. As a result, the buffer battery voltage V_{BT} always has to be higher than the DC grid voltage. The upper switches on the primary side S_1, ... , S_N operate with a duty cycle D_1, determined by equation (1), while the lower switches $\overline{S}_1$, ... , $\overline{S}_N$ operate complementarily with a duty cycle of $1\text{-}D_1$.

$$D_1 = T_S / T = V_{DC} / V_{BT} \tag{1}$$

where $T=T_S+T_{\overline{S}}$, T_S - switch on time.

The control pulses for the input-side switches S_1, S_2, ..., S_N are phase-shifted by an angle φ_S, which is determined by the number of EV ports and given by $\varphi_S = 2\pi/N$, where number of ports $N = 3,5...$

The EV charging outputs are implemented using N full-bridge AC-DC converters, each electrically isolated from the primary side by a single-phase transformer. The transformer windings are connected to the midpoints of the input-stage converter bridges, as illustrated Fig. 4a. The connection points labeled "j" and "k" correspond to transformer winding terminals, with their indices defined as follows:

$$k = \left(j + (N-1)/2\right) - N \cdot \left\lfloor \left(2j + N - 1\right)/2N \right\rfloor \tag{2}$$

where $j=1,2, ... , N$; $\lfloor\ \rfloor$ – floor function.

The phase voltages V_j and V_k between points "j" and "k" are shifted relative to each other by a phase angle φ_N. In the simplest case, when $N=3$, the transformer windings are connected in a delta (Δ) configuration, resulting in a phase shifts of $\varphi_S=\varphi_N=120^{\circ}$. For the system with more output ports, the phase shift φ_N is calculated using expression $\varphi_N = \pi(N\text{-}1)/N$, where $N=3, 5, 7…$

Each isolated output of the converter includes four switches Q_j , Q'_k , $\overline{Q}_j$, $\overline{Q}'_k$, configured in a full bridge to support bidirectional power flow. Switch Q_j operates with a phase shift δ relative to the input side switch S_j, while Q'_k operates with the same phase shift δ relative to S_k. The control signals for Q_j and Q'_k are phase shifted by the angle φ_N. When the phase shift $\delta=0$ and the input and output voltages are perfectly matched (i.e. $V_{BT} \cdot n=V_{EV}$), the transformer primary and secondary voltages are identical in both waveform and amplitude. In this case, the voltage across the leakage inductor $L_{P,j}$ is zero, and no power is transferred through the transformer. In such case, operation of each EV port comparable to a single-phase Dual Active Bridge (DAB) converter, consisting of switches S_j, $\overline{S}_j$, S_k, $\overline{S}_k$ on the input side and Q_j, Q'_k, $\overline{Q}_j$, $\overline{Q}'_k$ on the output side. By adjusting the phase shift δ, the voltage across the transformer leakage inductor $L_{P,j}$ changes, thereby controlling the power delivered to the EV port. Detailed descriptions of the converter's operation using Single-Phase Shift (SPS) modulation [15] and modified Dual-Phase Shift (DPS) modulation [16] can be found in prior publications.

When the battery-side voltage perfectly matches the EV port voltage (i.e. $n \cdot V_{BT}=V_{EV}$, with n being the transformer turns ratio), SPS modulation produces a transformer current waveform where the current drops to zero during zero-voltage intervals. However, any mismatch between nV_{BT} and V_{EV} creates a volt-second imbalance across the transformer's leakage inductor $L_{P,j}$, leading to non-zero current intervals (Fig. 5b) and increased RMS current. To reduce transformer RMS current, various DAB control methods are used—among them, Triple Phase Shift (TPS) modulation [17] is the most advanced. However, TPS cannot be applied in the CF-MAB converter, as input-side parameters are constrained: changing φ_N disrupts interleaving between input phases, and modifying D_1 affects the battery current I_{BT}. This limits control of the isolated output ports to just two degrees of freedom: d_2 and δ. Thus, the converter uses a modified DPS modulation scheme (where the duty cycle is not fixed at 0.5). This allows d_2 to be adjusted to ensure volt-second balance across the transformer—achieving $nV_{BT}{\cdot}d_1=V_{EV}{\cdot}d_2$, —while δ is used to control the EV port output power $P_{EV,N}$.

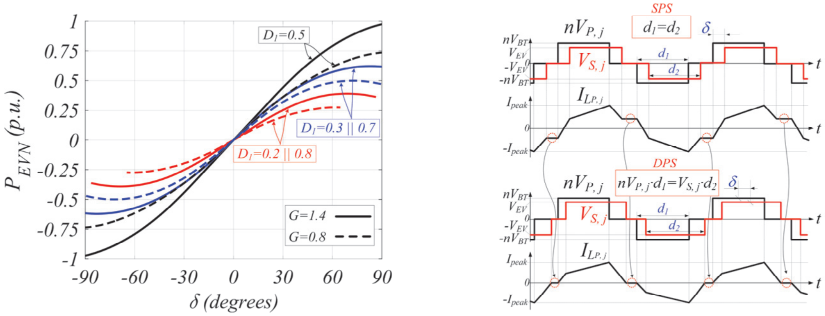

a) b)

Fig. 5. a) Characteristics of the CF-MAB converter EV ports for different values of D_1 and for varying voltage mismatch ratio ($G=V_{BT}\cdot n / V_{EV}$). The converter operation is symmetric with respect to $D_1=0.5$; therefore, values $D_1=m$ and $D_1=1\text{-}m$ yield the same regulation behavior, assuming V_{BT} remains constant; b) shows the primary and secondary transformer voltages and currents under SPS and modified DPS modulation.

In general, the power delivered to the EV port under this modulation scheme is defined by the equation (3). As can be seen, across all eight operating modes, the output power $P_{EV,N}$ depends not only on the phase shift δ, but also on the primary-side duty cycle D_1 and the voltage mismatch ratio G (Fig. 5a):

$$P_{EV,N} = \frac{V_{EV\,N} \cdot V_{BT}}{n \cdot f_{sw} \cdot L_{P,N}} \cdot f(\delta, D_1, G) \tag{3}$$

where $f(\delta, D_1, G)$ - is a mode-dependent function detailed in [18].

5.2 Bidirectional charging perspectives

To quantitatively evaluate the RMS current values in the CF-MAB converter switches, a comparison was made with the most conventional configurations: series (Fig. 6a) and parallel (Fig. 6b) connections of a 3-phase interleaved boost converter and three independent DAB converters. In both cases, the 3-phase interleaved converter is used to connect the BT port, while the DAB converters are used to charge the EVs. The power delivered to the BT and EV ports is kept the same across all configurations.

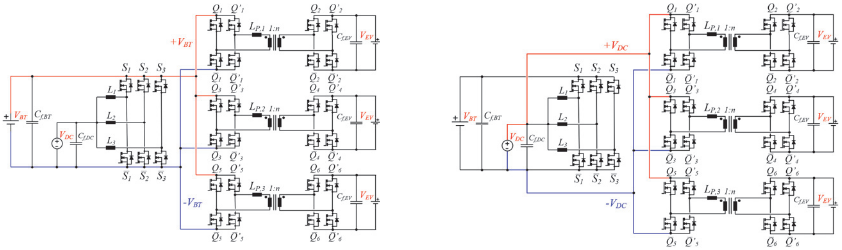

a) Series connection b) Parallel connection

Fig. 6. EV charging station architectures using series-connected converters (where the BT is charged from the DC grid and EVs are charged from the BT) and parallel-connected converters (where both the BT and EVs are charged directly from the DC grid).

In all configurations, under peak load conditions, the average current through the interleaved boost inductors is the same. In the series configuration, peak power is reached when both the BT and all EV ports transfer maximum power to the DC grid. In contrast, in the parallel configuration, peak power is reached when the BT supplies power both for EV charging and DC grid stabilization. The formulas used to calculate the RMS currents for the CF-MAB converter and conventional solutions are presented in Table 5.

Table 5. Comparison of storage battery and EV charger topologies. Comparison of storage battery and EV charger topologies.

<table>
<tr><td colspan="4">Average input inductor current (For all connections: Series, Parallel and CF-MAB)</td></tr>
<tr><td colspan="3">$$I_{Lj,DC,AVG} = \frac{I_{BT} + \sum_{N} \frac{V_{EV,N} \cdot I_{EV,N}}{V_{BT}}}{3 \cdot D_1}$$</td><td>(4)</td></tr>
<tr><td colspan="4">BT port switches RMS currents</td></tr>
<tr><td>3-phase interleaved boost</td><td></td><td>CF-MAB interleaved side</td><td></td></tr>
<tr><td>$$I_{\bar{S}j}rms = \sqrt{\frac{1}{T}\int_{0}^{T(1-D_1)} I^2_{Lj,DC}(t)dt}$$
$$I_{Sj}rms = \sqrt{\frac{1}{T}\int_{T(1-D_1)}^{T} I^2_{Lj,DC}(t)dt}$$</td><td>(5)</td><td>$$I_{\bar{S}j}rms = \sqrt{\frac{1}{T}\int_{0}^{T(1-D_1)-\alpha_1} \left(I_{Lj,DC}(t) - I_j(t)\right)^2 dt}$$
$$I_{Sj}rms = \sqrt{\frac{1}{T}\int_{T(1-D_1)-\alpha_1}^{T-\alpha_1} \left(I_{Lj,DC}(t) - I_j(t)\right)^2 dt}$$
(6)
where $I_j(t) = I_{LP,j}(t) - I_{LP,k}(t)$.</td><td></td></tr>
<tr><td colspan="4">EV ports switches RMS currents</td></tr>
<tr><td>DAB converter full bridges</td><td></td><td>CF-MAB converter full bridge</td><td></td></tr>
<tr><td>$I_{Sj}rms = \frac{I_{LP,RMS}}{\sqrt{2}}$, $I_{Q}rms = \frac{I_{LP,RMS}}{n \cdot \sqrt{2}}$</td><td>(7)</td><td>$I_{Q}rms = \frac{I_{LP,RMS}}{n \cdot \sqrt{2}}$</td><td>(8)</td></tr>
</table>

RMS transformer current, represented by Fourier Series (For all connections: Series, Parallel and CF-MAB)

$$I_{LP,j}rms=\sqrt{\sum_{m=1,2,3\ldots}\left[\frac{\sqrt{2}}{m^2\omega_0\pi L_{P,j}}\sqrt{A^2-2AB\cos(m\cdot\omega_0\delta)+B^2}\right]^2}$$
$$A=V_{BT}\cdot\left[\cos(m\cdot(\alpha_1+d_1))-\cos(m\cdot\alpha_1)\right] \qquad \textbf{(9)}$$
$$B=\frac{V_{EV}}{n}\cdot\left[\cos(m\cdot(\alpha_2+d_2))-\cos(m\cdot\alpha_2)\right]$$

where $\alpha_1,\alpha_2,d_1,d_2$ - modified DPS modulation parameters for a CF-MAB converter (Fig. 7) and are specified in [18]. In case of SPS modulation (for CF-MAB) $\alpha_1=\alpha_2$, $d_1=d_2$ and for a typical SPS for DAB $\alpha_1=\alpha_2=0$, $d_1=d_2=0.5T$.

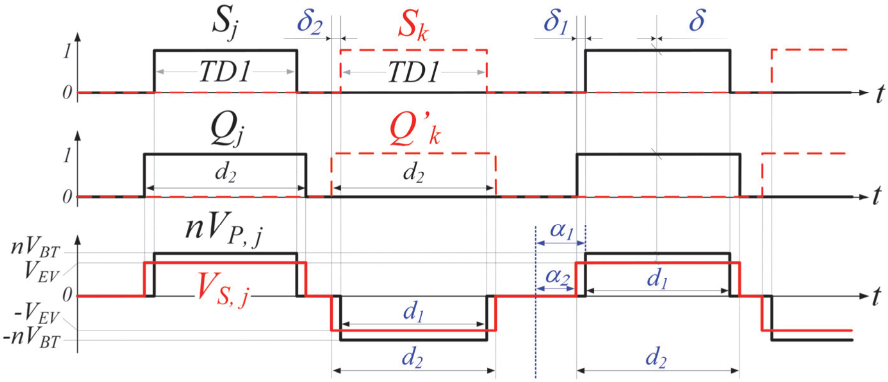

Fig. 7. Modified DPS modulation variables, used for RMS currents calculation.

Using the formulas above, RMS currents for the three configurations were compared. The normalized sum of the system's switch RMS currents is shown in Fig. 8a. Separate bars for the BT and EV ports are included to highlight the differences between the converters. As shown, the parallel configuration results in higher RMS currents at the EV ports. This is because the EV port inputs are connected directly to the DC grid, which has a lower voltage—meaning higher currents are needed to deliver the same power compared to the series connection, where the DABs are powered from the higher-voltage BT port.

For the CF-MAB converter, the RMS current in the input switches is generally higher than in the series and parallel configurations. The total RMS current at the output EV ports is also slightly higher for the CF-MAB, which is attributed to differences in modulation strategies between CF-MAB and DAB. In the case of the classical DAB, standard SPS modulation is used with both the primary and secondary duty cycles set to 0.5. In contrast, the CF-MAB in both SPS and DPS operates with duty cycle lower than 0.5. This results in slightly higher RMS currents due to lower utilization of the transformer and switches, which is feature of the CF-MAB design.

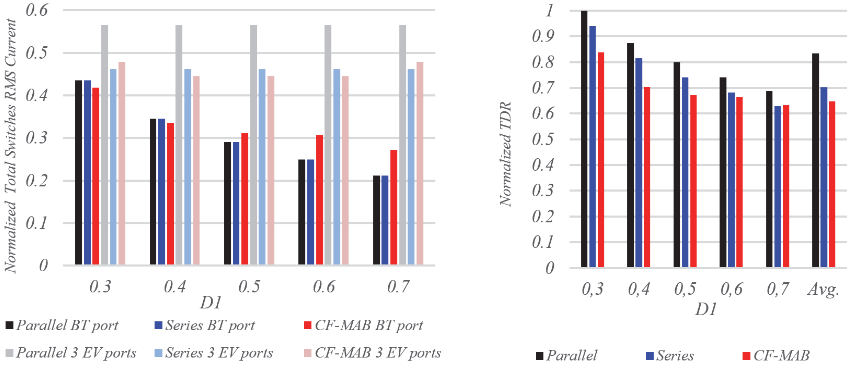

a) b)

Fig. 8. Comparison of CF-MAB, parallel and series connection of battery and EV chargers to the DC traction grid by normalized total switches RMS currents (a) and total devices rating (b).

However, the total RMS current does not fully reflect the differences between the solutions, because the CF-MAB and conventional configurations differ in the number of switches and their voltage ratings. To account for this, a Total Device Rating (TDR) coefficient is introduced, which considers both the number of switches and their electrical stress (i.e., peak voltage and RMS current):

$$TDR = \sum_{k=1}^{z} V_k ds \cdot I_k rms \tag{20}$$

where $V_k ds$ is a k is the maximum drain-source voltage of the k-th transistor, and $I_k rms$ is its RMS current.

The results (Fig. 8b) show that, in all cases, the CF-MAB converter has a lower TDR due to the reduced number of switches. This suggests that the CF-MAB could potentially be less costly than both the series and parallel alternatives.

5.3 Converter control system

The main goals of the converter control are to ensure efficient EV charging without overloading the substation and to stabilize the traction catenary voltage by managing bidirectional power flow between the catenary and both the buffer battery BT and EVs. These objectives are achieved by continuously monitoring the catenary voltage V_{CT} and dynamically adjusting the charging/discharging currents of the BT and EVs to counteract voltage fluctuations. A catenary-voltage-based control approach is adopted due to its simplicity and low cost, as it does not require additional communication links between the charging station and the substation [19]. The overall control system (Fig. 9) is divided into a high-level control (Fig. 9a), which sets the current references I^{ref}_{BT} and I^{ref}_{EVN} based on V_{CT}, and a low-level control (Fig. 9b), which ensures these reference values are accurately tracked.

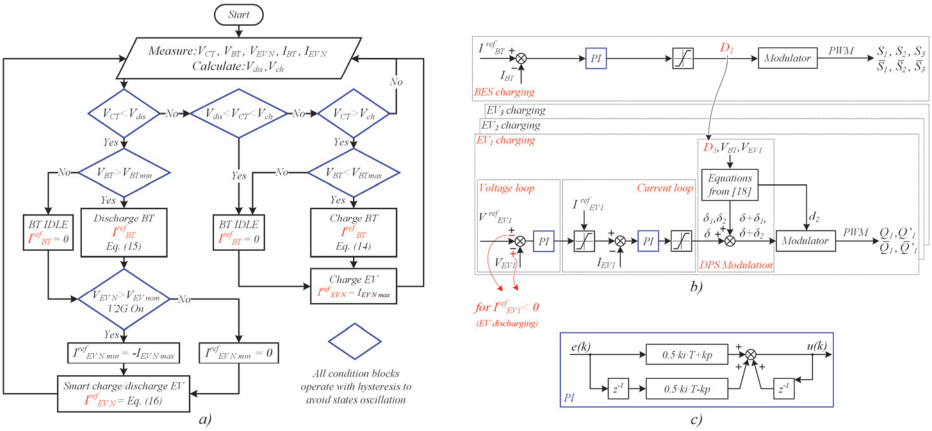

Fig. 9. a) High-level control algorithm of the catenary-based system, which determines the reference battery current $I^{ref}{}_{BT}$ and reference EV port currents EVs $I^{ref}{}_{EVN}$; b) Low-level control system, which receives $I^{ref}{}_{BT}$ and $I^{ref}{}_{EVN}$ from the high-level controller and, through closed-loop regulation, maintains these values by adjusting the input-side duty cycle D_1 and the phase shift δ for each EV port; c) Structure of the digital PI controllers used in the control system.

The control algorithm begins by measuring key system parameters: voltages V_{CT}, V_{BT}, V_{EVN} and currents I_{BT}, I_{EVN}. It then computes the charge and discharge thresholds V_{ch} and V_{dis} using equations (11). These thresholds are adjusted to balance the State Of Charge (SOC) of the buffer battery and to prevent overcharging or deep discharging, particularly during dynamic load conditions caused by varying EV charging demand. Based on a comparison of the measured V_{CT} with these thresholds, the control system determines whether the BT should be in charging, discharging, or idle mode.

$$V_{ch}(i)=V_{adj}(i)+V^{nom}{}_{ch},\ V_{dis}(i)=V_{adj}(i)+V^{nom}{}_{dis} \tag{31}$$

where $V^{nom}{}_{ch}$, $V^{nom}{}_{dis}$ represent the default charging and discharging voltage thresholds when the catenary is unloaded.

The adjustment term $V_{adj}(i)$ is dynamically regulated by a controller defined as follows:

$$\begin{aligned}&V_{adj}(i)=V_{adj}(i-1)+e_{SOC}(i-1)\cdot(0.5\cdot ki\cdot T_{SOC}-kp)+\\&+e_{SOC}(i)\cdot(0.5\cdot ki\cdot T_{SOC}+kp)\end{aligned} \tag{42}$$

$$e_{SOC}(i)=(SOC_{BT}(i)-SOC^{nom}{}_{BT}) \tag{13}$$

where kp and ki are the proportional and integral gains respectively, T_{SOC} is the SOC measurement interval, e_{SOC} is the error between the measured and desired SOC. The reference charging and discharging currents are calculated using equations (14) and (15):

$$BT\ charging\!: V_{ch}(i)=V_{adj}(i)+V^{nom}{}_{ch},\ V_{dis}(i)=V_{adj}(i)+V^{nom}{}_{dis} \tag{54}$$

$$\textit{BT discharging:}\quad I^{ref}{}_{BT} = (V_{CT} - V_{dis}) \cdot k_{BT}\ , \tag{15}$$

$$\textit{EV smart charging:}\ I^{ref}{}_{EV\,N} = I^{ref}{}_{EV\,N\,\max} + (V_{CT} - V_{dis}) \cdot k_{EV}\ , \tag{16}$$

where $k_{BT} = I^{ref}{}_{BTmax} / \Delta V_{CTmax}$, $k_{EV} = 2 \cdot I^{ref}{}_{EVmax} / \Delta V_{CTmax}$.

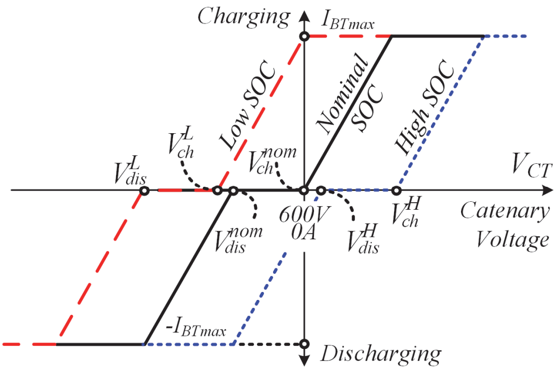

Fig. 10. Charge/discharge behavior of the buffer battery as a function of its state of charge SOC_{BT}.

The droop coefficient k_{BT} is defined based on the maximum allowable voltage deviation ΔV_{CTmax} during the catenary voltage stabilization process. When the catenary voltage V_{CT} is sufficiently high, the high-level control charges EVs with the maximum current $I^{ref}{}_{EVN} = I_{EVNmax}$. If V_{CT} falls below the discharging threshold V_{dis} the EVs switch to a smart charging mode, governed by equation (16).

The buffer battery (BT) is typically kept at a medium SOC level, allowing it to either absorb or supply power when needed. Due to this balancing strategy, there is no need for a constant-voltage charging mode or voltage regulator in the BT control loop. Instead, the BT current I_{BT} is regulated using a single PI controller, which compares the measured current with the reference $I^{ref}{}_{BT}$ and adjusts the duty cycle D_I accordingly (Fig. 9b). Nonetheless, high-level control continuously monitors the BT voltage, ensuring it remains within the permissible range V_{BTmin} to V_{BTmax}; charging or discharging is halted if these limits are exceeded.

EV charging and discharging follow a constant-current/constant-voltage (CC/CV) method. This is implemented via a conventional two-stage control loop, where current and voltage errors—calculated as the difference between reference values $I^{ref}{}_{EVN}$, $V^{ref}{}_{EVN}$ and the measured currents I_{EVN}, V_{EVN}—are fed into their respective PI controllers. These controllers generate the required phase shift δ for each EV port. During the transition from charging to discharging mode, the signs of $V_{refEV\,N}$ and $V_{EV\,N}$ are inverted to ensure proper operation of the saturation block that limits I_{refEVN}. All PI controllers are implemented digitally in the z-domain, using bilinear transformation of the standard s-domain PI controller transfer function (see Fig. 9c).

5.4 Simulation, HIL experimental results and prototype.

Simulation and HIL verification of the proposed converter were carried out for three EV ports (N=3), using parameters listed in Table 6.

Table 6. CF-MAB HIL model parameters

Parameter	Value
DC grid voltage V_{DC}	600 V
DC grid resistance R_{DC}	0.2 Ohm
Battery nominal voltage V^{nom}_{BT}	1200 V
Battery capacitance C_{BT}	10.5 Ah
Battery resistance R_{BT}	0.1 Ohm
Battery maximum current I^{max}_{BT}	250 A
EV voltage $V_{EV1}, V_{EV2}, V_{EV3}$	345 V
EV maximum current I^{max}_{EV1} , I^{max}_{EV2} , I^{max}_{EV3}	125 A
Transformer ratio $1{:}n$	0.28
DC side inductance $L_{1,DC}, L_{2,DC}, L_{3,DC}$	10·50 uH
Primary inductance $L_{P,1}, L_{P,2}, L_{P,3}$	10·30 uH
Battery side capacitor $C_{f,\,BT}$	10·470 uF
Battery and EV sides inductances $L_{f,\,BT,}\,L_{fEV}$	10·10 uH
EV side capacitor C_{fEV}	10·1 mF
DC filter inductance $L_{f,DC}$	8 uH
DC filter capacitor $C_{f,DC}$	4 mF
Discretization step size*, Tstep*	8 us
HIL switching frequency f_{sw}	2.5 kHz

In the considered scenario, the EV charger is located at some distance from the traction substation, while a tram operates nearby. This setup leads to fluctuations in the catenary voltage V_{CT} relative to the nominal DC voltage V_{DC}. During tram acceleration, the voltage V_{CT} drops due to the resistance R_{DC} of the catenary, while during tram braking, V_{CT} rises due to recuperated braking energy. According to EN 50163, for a 600 V DC traction grid, such fluctuations can reach ±33%, with the upper limit constrained by the braking chopper, which dissipates energy in a resistor when V_{CT} reaches 800V.

Switched-model simulation results (Fig. 11) display the input boost inductor current $I_{LN,DC}$, transformer primary voltage $V_{P,N}$ and currents $I_{LP,N}$, secondary voltages $V_{S,N}$ under various conditions: a), c) EVs and BT charging, which occurs during normal line operation (no tram present), as well as during tram braking, when breaking energy is recuperated and used for BT and EVs charging; b), d) BT and EVs discharging, which occurs during tram acceleration, when power from BT and EVs is send to the DC grid to reduce voltage drop. Each EV port has different voltage levels, which for cases (a) and (b) correspond to fully discharged electric car $V_{EV1}=288\ V$, fully charged $V_{EV3}=400\ V$ and with a nominal voltage $V_{EV2}=345.6\ V$, which is matched with a nominal battery voltage $V_{BT}=1200\ V$ by a transformer with a ratio $n=0.288$. All ports use modified DPS modulation, ensuring zero current flow during zero voltage intervals across the transformer. As expected, due to the symmetrical regulation characteristics, the phase shift δ between the primary and secondary voltages is identical in magnitude but opposite in sign for forward and reverse power flow.

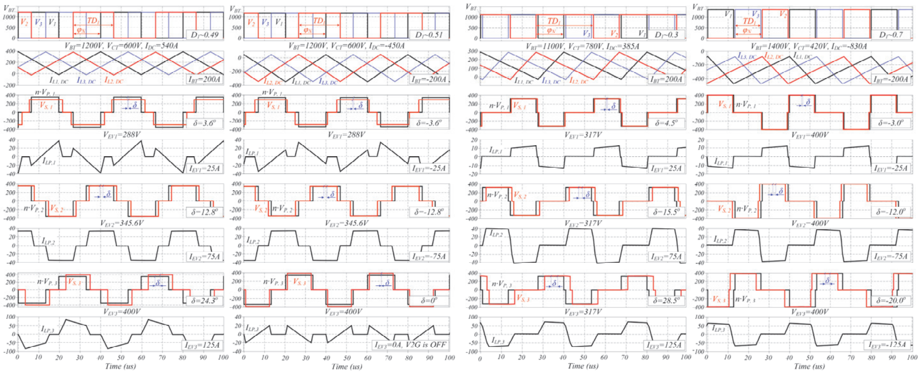

a) charging, D_I~0.49 b) discharging, D_I~0.51 c) charging, D_I~0.3 d) discharging, D_I~0.7

Fig. 11. Switched model simulation results for $N=3$, with different EV and BT ports load. Results are shown for different cases: EVs and BT are charging (a, c), consuming power from grid, and discharging (b, d), supplying power to DC grid. Cases (a,b) simulated with D_I~0.5 and nominal catenary and battery voltage (V_{BT}=1200V, V_{CT}=600V), whereas (c) corresponds to D_I~0.3, with V_{BT}=1100V, V_{CT}=780V and (d) to D_I~0.7, with V_{BT}=1400V, V_{CT}=420V.

Fig. 11 presents simulation results for various loading conditions of EV and BT ports. Cases (a) and (b) illustrate operation at D_1~0.5, with nominal V_{BT}=1200V and V_{CT}=600V, leading to symmetrical zero-voltage intervals on both transformer sides. However, during real-time operation, both V_{BT} and V_{CT} vary due to changes in BT state of charge and tram activity. These variations cause D_I to adjust accordingly. Cases (c) and (d) demonstrate operation with D_I~0.3 and D_I~0.7 respectively. Despite different voltages (V_{BT}=1200V in (c) and V_{BT}=1400V in (d)), the current and voltage waveforms remain similar due to the converter's symmetrical regulation characteristics. A lower battery voltage in (c) requires a higher phase shift δ to achieve the same port power compared to (d). In all scenarios, each EV port operates independently. For instance, EV1 can be charged while EV2 is discharged—enabling vehicle-to-vehicle (V2V) energy transfer—without impacting other ports. Power exchange in this mode occurs through the BT port capacitor $C_{f,BT}$ without affecting BT current I_{BT}.

To validate the converter performance, a hardware-in-the-loop (HIL) experiment was conducted. The hardware portion was simulated using PLECS RT Box 1, while control was implemented on a TMS320F28379D signal processor (Fig. 12).

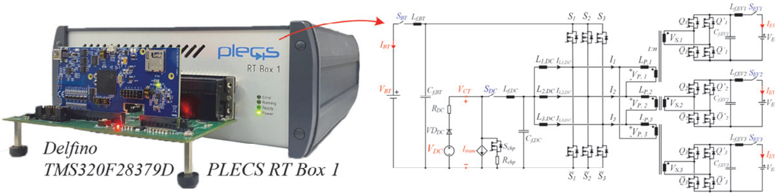

Fig. 12. HIL experimental setup for converter control verification (N=3).

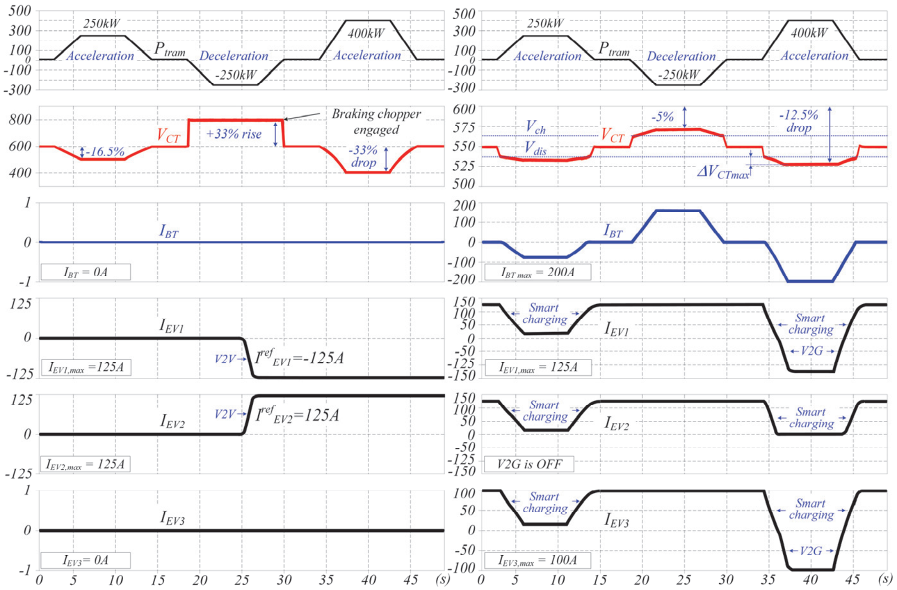

a) DC grid stabilization is OFF
EV1 and EV2 operate in V2V mode

b) DC grid stabilization is ON

Fig. 13. HIL simulation results for case when system is turned OFF (a), and for the normal system operation (b) with EVs and BT operating bidirectionally.

The results (Fig. 13a) confirm that during tram operation at selected power levels V_{CT} fluctuates within ±33% of the nominal 600 V DC grid voltage. In case (a), DC grid stabilization is disabled, while EV1 and EV2 operate in V2V mode. EV1 discharges at 100 A and EV2 charges at 100 A, without impacting the performance of other ports. Energy is exchanged via the BT port capacitor $C_{f,BT}$ with zero average current flow through I_{BT}. In contrast, when DC grid stabilization is enabled (Fig. 13b), voltage drops in V_{CT} are reduced to −12.5%, and voltage surges are eliminated thanks to bidirectional charging of BT and EVs. During normal operation V_{CT}, does not rise above V_{DC}, which is attributed to the load presented by the charging EVs. For example, bidirectional charging is disabled for EV2 (based on user preference), while other EVs continue to operate bidirectionally. When the voltage drop is minimal, smart charging is applied across all EVs to reduce power draw. However, under significant voltage drop conditions, EVs inject power back into the grid to support voltage stabilization.

The next step in the research is assembling a lower-power experimental prototype to verify the theoretical results obtained. The developed prototype (Fig. 14) has three output ports for charging electric vehicles, a port for connecting a battery, and a port for connecting to a DC grid. The prototype will be tested under laboratory conditions at a power level of 20 kW. A key aspect of the testing is verifying proper operation in bidirectional mode for all ports, as well as performance across the full range of traction grid voltages and vehicle battery voltages.

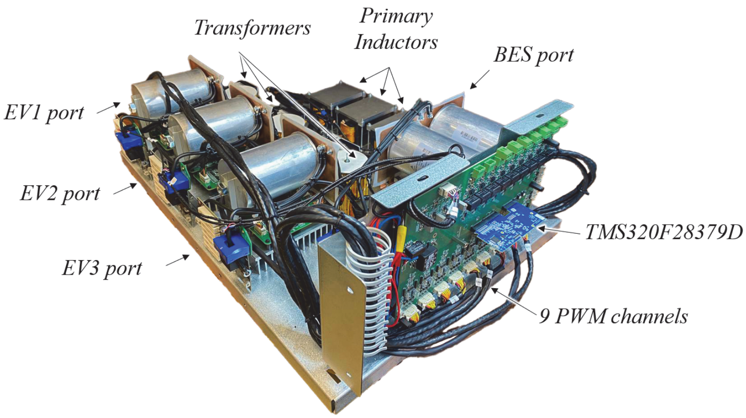

Fig. 14. CF-MAB converter 20kW prototype.

5 Conclusions

A scalable multiport Current-Fed Multi-Active Bridge DC-DC converter enables multiterminal EV charging from existing LV DC traction grids, eliminating the need for dedicated transformers and rectifiers, and reducing infrastructure costs. The converter supports independent, bidirectional charging for multiple EVs and integrates a buffer battery for DC grid voltage stabilization and recuperation of braking energy from traction systems. Shared use of power components reduces the number of switches required (6N vs. 8N+6 in conventional systems), making the CF-MAB converter more economical. At the same time, EV ports are powered from a stabilized capacitor voltage at the BES port, simplifying the EV charging control process. Additionally, the applied improved battery SOC balancing maintains the buffer battery at optimal levels regardless of load conditions or the number of connected EVs. Simulation and HIL results show catenary voltage surge reductions of up to 30% and voltage drop reductions of 10–12.5%. The application of the proposed modified DPS modulation, instead of classical single-phase shift modulation, reduces RMS currents in the transformer by up to 5.7% on average, with differences reaching 43.6% under low-power conditions and extreme voltage mismatches.

Acknowledgments. This project has received funding from the European Union's Horizon 2020 research and innovation programme under the Marie Skłodowska-Curie grant agreement No 955614.

References

1. European Alternative Fuels Observatory, "Charging Ahead: Accelerating the Roll-Out of EU Electric Vehicle Charging Infrastructure," May 2024. [Online]. Available: https://shorturl.at/LD7OV [Accessed: May 8, 2025]
2. M. Yilmaz and P. T. Krein, "Review of the Impact of Vehicle-to-Grid Technologies on Distribution Systems and Utility Interfaces," in IEEE Transactions on Power Electronics, vol. 28, no. 12, pp. 5673-5689, Dec. 2013, doi: 10.1109/TPEL.2012.2227500.
3. M. Lukianov, I. Verbitsky, E. R. Cadaval, R. Strzelecki, "An Overview of Bidirectional EV Chargers: Empowering Traction Grid-Powered Chargers," in Power Systems Research and Operation. Studies in Systems, Decision and Control, vol 512, Springer, Cham, 2024, doi:10.1007/978-3-031-44772-3_9
4. K. Smith, L. Hunter, S. Galloway, C. Booth, C. Kerr and M. Kellett, "Integrated Charging of EVs Using Existing LVDC Light Rail Infrastructure: A Case Study," 2019 IEEE Third International Conference on DC Microgrids (ICDCM), Matsue, Japan, 2019, pp. 1- 7, doi: 10.1109/ICDCM45535.2019.9232726.
5. International Energy Agency (IEA), "Global EV Outlook. 2025," Apr. 2023. [Online]. Available: https://www.iea.org/reports/global-ev-outlook-2025 [Accessed: May 19, 2025]
6. International Energy Agency (IEA), "Grid Integration of Electric Vehicles," Apr. 2021. [Online]. Available: https://www.iea.org/reports/grid-integration-of-electric-vehicles [Accessed: May 8, 2025]
7. CharIN, "V2G - Vehicle to Grid," [Online]. Available: https://www.charin.global/technology/v2g/ [Accessed: May 8, 2025]
8. A. Ahmad, Z. Qin, T. Wijekoon and P. Bauer, "An Overview on Medium Voltage Grid Integration of Ultra-fast Charging Stations: Current Status and Future Trends," IEEE Open Journal of the Industrial Electronics Society, no. 3, pp. 420 - 447, 6 2022.
9. CENELEC, "EN 50163:2004 – Railway Applications – Supply Voltages of Traction Systems, " 2004. [Online]. Available: https://standards.iteh.ai/catalog/standards/clc/a150c612-ccc5-4de1-853a-7d1dfe70f3e1/en-50163-2004 [Accessed: May 8, 2025]
10. A. Shekhar, G. C. R. Mouli, S. Bandyopadhyay and P. Bauer, "Electric Vehicle Charging with Multi-Port Converter based Integration in DC Trolley-Bus Network," 2021 IEEE 19th International Power Electronics and Motion Control Conference (PEMC), Gliwice, Poland, 2021, pp. 250-255, doi: 10.1109/PEMC48073.2021.9432590.
11. J. Böhler, F. Krismer, T. Sen and J. W. Kolar, "Optimized Modulation of a Four-Port Isolated DC–DC Converter Formed by Integration of Three Dual Active Bridge Converter Stages," 2018 IEEE International Telecommunications Energy Conference (INTELEC), Turino, Italy, 2018, pp. 1-8, doi: 10.1109/INTLEC.2018.8612312.
12. M. Uno, M. Sato, Y. Tada, S. Iyasu, N. Kobayashi and Y. Hayashi, "Partially Isolated Multiport Converter With Automatic Current Balancing Interleaved PWM Converter and Improved Transformer Utilization for EV Batteries," in IEEE Transactions on Transportation Electrification, vol. 9, no. 1, pp. 1273-1288, March 2023, doi: 10.1109/TTE.2022.3175032.
13. G. -J. Su and L. Tang, "A Reduced-Part, Triple-Voltage DC–DC Converter for EV/HEV Power Management," in IEEE Transactions on Power Electronics, vol. 24, no. 10, pp. 2406-2410, Oct. 2009, doi: 10.1109/TPEL.2009.2026989.
14. Z. Wang and H. Li, "A Soft Switching Three-phase Current-fed Bidirectional DC-DC Converter With High Efficiency Over a Wide Input Voltage Range," in IEEE Transactions on Power Electronics, vol. 27, no. 2, pp. 669-684, Feb. 2012, doi: 10.1109/TPEL.2011.2160284.
15. M. Lukianov, E. R. Cadaval, G. Arena and R. Strzelecki, "Partially Isolated Multi-Active Bridge DC-DC Converter with Bidirectional EV Charging Ports," 2024 IEEE 18th International Conference on Compatibility, Power Electronics and Power Engineering (CPE-POWERENG), Gdynia, Poland, 2024, pp. 1-7, doi: 10.1109/CPE-POWERENG60842.2024.10604312.
16. M. Lukianov, P. Derkacz and R. Strzelecki, "Multi Active Bridge converter with DPS modulation for bidirectional EV charging from DC traction grid," IECON 2024 - 50th Annual Conference of the IEEE Industrial Electronics Society, Chicago, IL, USA, 2024, pp. 1-7, doi: 10.1109/IECON55916.2024.10905342.
17. F. An, W. Song, K. Yang, S. Yang and L. Ma, "A Simple Power Estimation With Triple Phase-Shift Control for the Output Parallel DAB DC–DC Converters in Power Electronic Traction Transformer for

Railway Locomotive Application," in IEEE Transactions on Transportation Electrification, vol. 5, no. 1, pp. 299-310, March 2019, doi: 10.1109/TTE.2018.2876057

18. M. Lukianov, “Regulation Characteristic Formulas for Scalable CF-MAB converter, operating with DPS modulation”, Mendeley Data, V1, 2025, doi: 10.17632/m73wxt8pzd.1
19. T. Suzuki, H. Hayashiya, T. Yamanoi and K. Kawahara, "Introduction and Practical Use of Energy Storage System with Lithium-ion Battery for DC Traction Power Supply System", in IEEJ Journal of Industry Applications, 2016, Volume 5, Issue 1, pp. 20-25, Jan. 2016, doi:10.1541/ieejjia.5.20

Edge computing platform (ECP) for Fault Tolerant, High Reliable and Resilient Power Electronic in Prosumers Applications

Cheikh Elekbir Sidi Lekhel[1], Rita Mbayed[2], Oleksandr Velihorskyi[3],
Oleksandr Husev[4], and Eric Monmasson[1]

[1] SATIE, CY Cergy Paris Université, Paris, France
{cheikh-elkebir.sidi-lekhel, eric.monmasson}@cyu.fr
[2] SATIE, Université Gustave Eiffel, Paris, France
rita.mbayed@esiee.fr
[3] Embedded Systems Dept., Chernihiv Polytechnic National University, Chernihiv, Ukraine
alexveligorsky@gmail.com
[4] Department of Industrial Electronics, Warsaw University of Technology, Warsaw, Poland
oleksandr.husev@pw.edu.pl

Abstract. Battery degradation is a decisive factor influencing the economic viability of residential photovoltaic-battery systems. Existing approaches often decouple sizing from operational decisions, risking accelerated aging and compromised performance. This chapter proposes a two-stage optimization framework: first, system sizing determines the optimal PV and battery capacities, estimated lifetime, and annual degradation losses by incorporating consumption and weather data. The resulting configuration is then fixed for day-ahead operation, where a degradation cost model consistent with the sizing assumptions is integrated into the daily optimization. Seasonal simulations show that the proposed sizing approach estimates a battery lifetime of approximately 13–14 years by integrating both calendar and cyclic degradation effects. This con- figuration achieves a system payback time of about 7 years. While, the proposed day-ahead optimization yields daily savings compared to full grid supply, reaching €1.31 in summer and €6.80 in winter. The chapter finally discusses a deployable cloud/edge EMS architecture and the use of multiparametric optimization to support fast real-time control under uncertainty.

Keywords: PV-battery systems, sizing optimization, battery degradation, day-ahead control.

1 Introduction

The foundation for deploying smart Energy Management Systems (EMS) in residential applications has become increasingly viable due to recent technological and economic advances. The declining cost of photovoltaic (PV) panels and Battery Energy Storage Systems (BESS), particularly lithium-ion batteries with long service life, has made energy self-generation and storage more accessible.

Moreover, the development of Energy Router (ER) converters provides a fundamental infrastructure for optimal managing power flows between the grid, PV systems, storage units, and household loads [1]. These fundamentals now make it possible to implement cost-effective EMS solutions that are perfectly suited to the needs of residential consumers.

To assess the practical feasibility and economic performance of such systems, various sizing methodologies have been developed. These approaches aim to determine optimal configurations of PV and BESS components that minimize over- all costs while meeting energy demands under different usage and environmental scenarios. For instance, [2] investigates optimal sizing and energy management for smart homes, while [3] incorporates operational optimization to determine battery capacity in Australian households. Battery degradation plays a critical role in such assessments, models accounting for calendar and cyclic aging ex- plored in [5][6]. Additionally, the widespread use of lithium-ion batteries with high efficiency and long life in residential settings is presented in [13].

A critical factor in the optimal sizing and long-term cost estimation of PV- BESS systems is the battery lifetime, which directly impacts both the frequency of replacements and the total economic viability. Unlike fixed-lifetime assumptions used in many conventional models, real battery lifetime depends heavily on usage, including depth of discharge and charge/discharge rates. These factors influence the degradation process, which combines both calendar aging (time-based degradation) and cyclic aging (usage-based degradation). Modeling this degradation is essential for ensuring that sizing decisions reflect realistic performance expectations over the system lifespan.

While long-term battery lifetime estimation is essential for proper system sizing, its value lies not in planning replacement but in integrating it into daily operation. In practice, respecting the degradation limits inferred during sizing requires establishing a coherent relationship between sizing and day-ahead optimization. Without such coordination, short-term decisions can lead to accelerated aging, undermining long-term system viability. To address this, several works have introduced degradation-aware models that integrate degradation cost models into short-term decision-making. For instance, in [7], a two-stage EMS is proposed that incorporates battery degradation cost to guide operation. A MILP-based model considering Depth of Discharge and SoC limitations was developed in [8], while [21] proposed a cost function based on SoH degradation, ensuring compliance with end-of-life criteria. These strategies could ensure that day-ahead energy management aligns with long-term objectives, preserving battery health while minimizing operational costs.

This chapter proposes a framework that bridges battery degradation modeling, system sizing, and day-ahead EMS optimization. The starting point (Section 2) represents the targeted application and case study. section 3 presents the development of a battery degradation model, capturing both calendar and cyclic aging. System operation and power flow is presented in section 4. This enables an estimation of battery lifetime under realistic operating conditions. Next, this degradation model is integrated into a joint system sizing approach (Section 5), where the optimal number of PV panels and batteries, as well as the annual battery losses, are determined.

To link these long-term objectives to short-term EMS operation, a day-ahead optimization framework is developed (Section 6) by proposing a short-term degradation cost model is integrated into day-ahead optimization.

The chapter concludes with the presentation of a two-level EMS architecture and proposed business model (Section 7), combining Cloud Computing and embedded Edge Computing to support future implementation.

2 Case study

This work targets a typical residential household equipped with a self-consumption system combining PV generation and BESS, as shown in Figure 1. The house- hold is connected to the electrical grid under a time-of-use (ToU) tariff structure, allowing both import and export of electricity. The objective is to optimize both system sizing and day-ahead (short-term) operation to minimize energy costs while accounting for battery degradation.

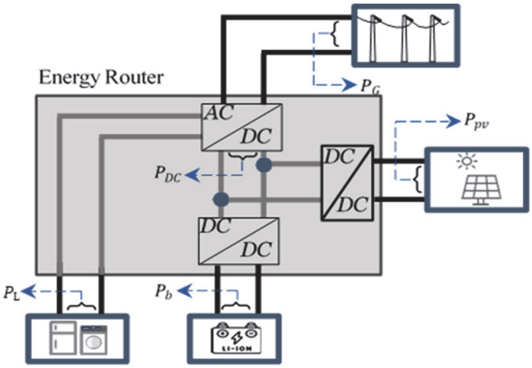

Fig. 1: System considered

The system includes key physical components: residential loads with varying demand profiles, rooftop PV panels sized to fit typical installation limits for single-family homes, and lithium-ion batteries sized to balance generation and consumption over daily and seasonal cycles. An ER converter coordinates power flows between the PV system, BESS, grid, and household loads, enabling flexible energy management. Realistic consumption, local weather data, and dynamic electricity pricing are considered to capture practical operational conditions.

3 Battery Lifetime Modeling

The BESS cost constitutes a substantial portion of the total investment in residential PV-battery systems, both in terms of initial capital and future replacement expenses. This highlights the need for smart charging strategies and effective BESS management. However, BESS lifetime is often a major source of uncertainty during system sizing, as it strongly depends on how the battery is used. If not handled carefully, the degradation behavior of the BESS can fluctuate significantly, which directly impacts its performance and economic viability. Different sizing approaches often assume a fixed BESS lifetime, ignoring the significant role of degradation in determining its actual lifespan. Such simplifications may lead to an underestimation of the real replacement needs and long-term operational costs. Other approaches concentrate primarily on cyclic aging, overlooking calendar aging effects, which can also accelerate degradation particularly when the battery remains at high SoC levels for prolonged periods [4].

Various BESS degradation models are found in the literature, with a focus on physico-chemical, empirical, or semi-empirical approaches [9]. For energy management purposes, semi-empirical models are the most widely adopted [10][11], as they offer a balance between accuracy and computational efficiency. More detailed models, such as electrochemical or thermal degradation models, impose high computational requirements, making their integration into optimization frameworks more complex [12].

This section is dedicated to modeling BESS lifetime as a function of degradation. The objective is to establish a representation that can be effectively incorporated into both operational control and sizing processes, allowing for a more realistic and integrated energy management strategy.

3.1 Battery degredation model

In recent years, the most commonly used batteries for residential PV-battery systems is lithium-ion batteries, particularly $LiFePO_4$, due to their long lifetime and high efficiency [13]. Hence, this battery is used and evaluated in degradation studies.

The degradation of lithium-ion batteries is typically characterized by two interconnected processes: calendar aging and cyclic aging [15]. Calendar aging refers to the decline in battery performance over time, regardless of usage, while cyclic aging is related to the number of charge-discharge cycles the battery can complete before reaching its end-of-life (EOL).

The overall battery degradation is calculated by combining the effects of calendar aging and cyclic aging at each time step, as shown in Equation (1).

$$Q_{t,F} = Q_{t,F}^{cyc} + Q_{t,F}^{cal} \tag{1}$$

where $Q_{t,F}^{cyc}$ represents the degradation due to cyclic aging, and $Q_{t,F}^{cal}$ corresponds to calendar aging.

A semi-empirical model for the calendar aging of $LiFePO_4$ batteries is proposed in [16]. This model depends on temperature and SoC. For residential applications, the temperature is typically close to ambient conditions. Therefore, it is fixed at 25°C to analyze the impact of SoC variation alone. The model is given in Equation (2).

$$Q_{t,F}^{cal}(\mathrm{T}, SoC_t) = (\beta_1 \cdot SoC_t^{\beta_2} + \beta_3)(\beta_4 T^{\beta_5} + \beta_6) d^{\beta_7} \tag{2}$$

Where β_1 to β_7 are fitting parameters.

Cycle aging can be modeled as a function of SoC, C-rate, or the energy throughput of the battery. In Equation (3), cyclic degradation is expressed based on the energy throughput, taking into account N_b, the number of batteries installed, E_b the energy capacity of each battery and N_{cyc}, the number of battery cycles.

$$Q_{t,F}^{cyc} = 0.5 \frac{\sum P_{t,b} \cdot \Delta t}{N_{cyc} N_b E_b} \tag{3}$$

Where $P_{t,b}$ is the battery power at time step t, defined as the charging or discharging power exchanged with the battery. Δt is the time step duration.

3.2 State of Health (SoH) and battery lifetime modeling

The battery SoH is modeled based on the capacity fade $Q_{t,F}$. It starts from an initial value $SoH_i = 1$ when the battery is new and unused, and decreases over time as capacity fade increases due to the aging process. The battery reaches its EoL when SoH drops to a final value $SoH_f = 0.8$ [17]. As shown in Equation 4.

$$SoH_{t,b} = SoH_{t-1,b} - 0.2 \cdot Q_{t,F} \tag{4}$$

where 0.2 is the degradation coefficient, such that a complete degradation level (i.e., $Q_{t,F} = 1$) corresponds to a state of health SoH = 0.8, which is considered the EoL threshold SoH_f.

To better understand how to model the aging process of batteries, it is important to examine the evolution of their capacity fade over time. Figure 2 illustrates the general degradation trend of lithium-ion batteries, as shown in [14][15]. The capacity starts at its initial value with zero capacity fade and gradually decreases due to the combined effects of calendar and cyclic aging. Once the battery reaches the EoL threshold, typically defined at 80% of the initial capacity, degradation accelerates rapidly and the remaining capacity becomes unpredictable.

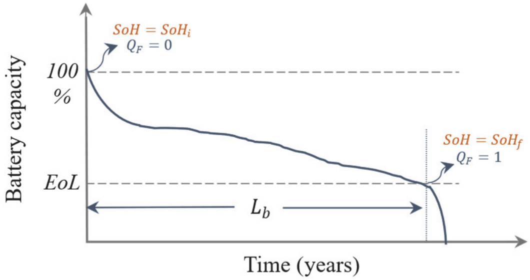

Fig. 2: General trend of battery degradation based on time

To capture this behavior, the battery service duration L_b is modeled as a function of annual degradation rate, denoted by L_{loss}, quantifies the yearly reduction in battery capacity due to aging. As given in Equation (5).

$$L_b = \frac{SoH_i - SoH_f}{L_{loss}} \tag{5}$$

where L_{loss} is the total annual scaled degradation of the batteries is calculated in Equation (6).

$$L_{loss} = 0.2 \cdot \beta \sum_{t=1}^{n} (Q_{t,F}^{cyc} + Q_{t,F}^{cal}) \tag{6}$$

where β is a scaling parameter that depends on the time resolution of the data used in the optimization either weekly, as in sizing, or daily, as in short-term day-ahead optimization in order to annualize the degradation.

4 System operation model

From the power flow representation in Figure 3, the operation model of the system can be formulated by considering power limitations and physical constraints.

Power constraints must be satisfied at each time step t, as the optimization is carried out using real data with a fixed interval Δt over a predefined time horizon.

Limitation on the maximum contracted power exchange between the grid and the system is expressed in equation (7) and (8).

$$0 \leq P_{t,G\to(b,L)} \leq P_G^{max} \tag{7}$$

$$0 \leq P_{t,(pv,b)\to G} \leq P_G^{max} \tag{8}$$

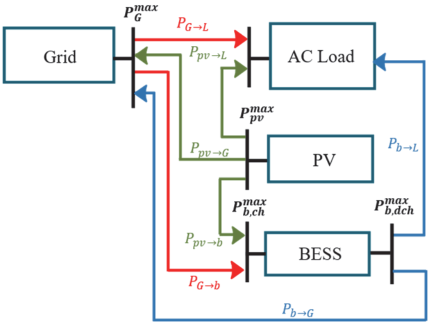

Fig. 3: Power flow representation

Equations (9) and (10) present models for PV generation, which take into account the solar irradiance incident on the PV modules and their temperature to determine the instantaneous normalized output power [18][19].

$$T_{pv}(\mathrm{t}) = T_a(\mathrm{t}) + \frac{NOCT - 20}{800}\,\mathrm{G(t)} \tag{9}$$

$$p_{pv}(\mathrm{t}) = p_{pv,m}(1 - K_T(T_{pv}(\mathrm{t}) - T_s)) \cdot \frac{G(t)}{G_s} \tag{10}$$

Where p_{pv} denotes the instantaneous output power of a PV module, while $p_{pv,m}$ refers to its rated power. K_T is the temperature coefficient of the PV cell, T_{pv} is the cell temperature, and T_s is the reference temperature under Standard Test Conditions. G represents the actual solar irradiance, G_s is the irradiance under STC, T_a is the ambient temperature, and NOCT stands for the Nominal Operating Cell Temperature.

The maximum PV output constraint is defined in Equation (11).

$$0 \leq P_{t,pv\rightarrow(L,b,G)} \leq P_{pv}^{max} \tag{11}$$

Equation (12) presents the battery energy balance, accounting for charging and discharging processes. The term $SoH_{t,b}$ is included to reflect the impact of degradation on the battery storage capacity over time.

$$E_{t,b} = E_{t-1,b} + (\eta_{b,c}P_{t,(pv,G)\rightarrow b} - \frac{P_{t,b\rightarrow(G,L)}}{\eta_{b,d}})\Delta t \cdot SoH_{t,b} \tag{12}$$

The lower and upper bounds of the charging and discharging power of the battery storage unit are defined in Equations (13) and (14).

$$0 \leq P_{t,(pv,G)\rightarrow b} \leq P_{b,ch}^{max} \tag{13}$$

$$0 \leq P_{t,b\rightarrow(G,L)} \leq P_{b,dis}^{max} \tag{14}$$

Equation (15) defines the SoC of the battery as the ratio of the stored energy Et,b to the total battery capacity $N_b\mathrm{E}_b$, providing a normalized measure of the battery available energy at a given time. Meanwhile, Equation (16) imposes constraints on the minimum and maximum allowable SoC levels.

$$SoC_{t,b} = \frac{\mathrm{E}_{t,b}}{N_b\mathrm{E}_b} \tag{15}$$

$$SoC_b^{min} \leq SoC_{t,b} \leq SoC_b^{max} \tag{16}$$

The C-rate of the BESS is determined based on its charging and discharging operations, as shown in Equation (17).

$$C_{t,rate} = \frac{\mathrm{P}_{t,b}}{N_b\mathrm{E}_b} \tag{17}$$

The constraints on DC-side power limitation, simultaneous battery charging and discharging, and power exchange with the grid are given in Equations (18), (19), and (20), respectively. In addition, the power flow balance to the load is enforced by the constraint in Equation (21).

$$P_{t,pv\rightarrow(L,G)} + P_{t,b\rightarrow(L,G)} \leq P_{DC}^{max} \tag{18}$$

$$P_{t,b\rightarrow(L,G)} \cdot P_{t,(pv,G)\rightarrow b} = 0 \tag{19}$$

$$P_{t,G\rightarrow(L,b)} \cdot P_{t,(pv,b)\rightarrow G} = 0 \tag{20}$$

$$P_{t,L} = P_{t,G\rightarrow L} + P_{t,b\rightarrow L} + P_{t,pv\rightarrow L} \tag{21}$$

Equation (22) represents the energy cost associated with power exchange with the grid. It accounts for the energy consumed from the grid by both the batteries and the loads, calculated according to the ToU tariff. It also includes the energy fed back into the grid, which consists of contributions from both the BESS and the PV system.

$$C_{t,G} = P_{t,G\rightarrow(L,b)} \cdot \Delta t \cdot ToU_t - P_{t,(pv,b)\rightarrow G} \cdot \Delta t \cdot FiT_t \tag{22}$$

where FiT_t is the energy price for selling electricity back to the grid. It represents 80% of ToU_t, excluding applicable taxes.

This system operation model allows for integration into the sizing process, making the combined sizing and operation model more realistic for predicting actual system costs and estimating battery lifetime.

5 Sizing approach

For sizing PV and BESS in residential applications, the most commonly used approach involves modeling investment, replacement, and maintenance costs over the project lifetime typically 20 years. To integrate operational costs and account for the impact of battery degradation, an annualized cost-based sizing approach is used. In this method, project lifetime costs are converted to equivalent yearly values. This allows annual battery capacity losses to be consistently linked with annual costs, ensuring realistic and comparable optimization results.

The expenses include the cost of PV panels, BESS capacity, and the ER. The PV system lifetime is considered fixed, as it typically exceeds the 20-year (L_{pr}) project duration. The ER is assumed to have a lifespan of 15 years, and its replacement is accounted for accordingly. Therefore, the BESS is the only component whose performance and cost are significantly affected by degradation.

5.1 Annualized cost

The total cost includes the initial investment cost, replacement cost, and maintenance cost. Equation (23) presents the initial investment cost of the complete system, incorporating the Capital Recovery Factor (CRF) to account for annual loan interest i_L payments on the total cost of all components over M years.

$$C_{Capital} = \sum\nolimits_j C_{Cap,j} \cdot \frac{i_L(1+i_L)^M}{(1+i_L)^M - 1} \cdot \frac{M}{L_{pr}} \tag{23}$$

The total initial investment cost $C_{Capital}$ of the system can be broken down by component as follows: Equation (24) defines the investment cost of the photovoltaic system, where N_{pv} is the number of PV panels and $C_{Cap,1}$ is the unit cost of one panel.

$$C_{Cap,pv} = N_{pv} \cdot C_{Cap,1} \tag{24}$$

Equation (25) expresses the battery storage system investment, where N_b is the number of battery units and $C_{b,1}$ is the cost per battery. The ER, acting as the power converter, is assumed to be a single unit with a fixed cost C_{ER}.

$$C_{Cap,b} = N_b \cdot C_{b,1}, \qquad C_{Cap,ER} = C_{ER} \tag{25}$$

The replacement cost accounts only for the BESS and the ER and is calculated to cover future replacements. It includes the Sinking Fund Factor (SFF) to determine the periodic deposit required to accumulate the future amount, based on the interest rate of a savings account i_{sa}. The corresponding calculation is shown in Equation (26).

$$C_{Replacement} = \sum\nolimits_j C_{Rep,j} \cdot \frac{i_{sa}}{(1+i_{sa})^{L_j} - 1} \cdot (1 - \frac{L_j}{L_{pr}}) \tag{26}$$

The battery replacement cost is calculated based on the number of battery units N_b and the unit cost $C_{b,1}$. Similarly, the ER replacement cost is assumed to be a fixed amount C_{ER}, as shown in Equation (27).

$$C_{Rep,b} = N_b \cdot C_{b,1}, \qquad C_{Rep,ER} = C_{ER} \tag{27}$$

The annual maintenance cost is estimated as 1% of the capital cost of each component, assuming a uniform maintenance rate across all components, as shown in Equation (28).

$$C_{Maintenance} = \sum\nolimits_j C_{Rep,j} \cdot 1\% \tag{28}$$

5.2 Joint sizing approach

Once the models for sizing and operating costs are defined, a joint sizing and operation approach can be established. The main idea of this approach is to integrate running costs based on real consumption data, weather conditions, and energy prices for a realistic case study. The optimization problem is then formulated as follows.

$$min\ C_{Tot} = C_{Capital} + C_{Replacement} + C_{Maintenance} + C_{operation} \tag{29}$$

$$Subject\ to: \begin{cases} Constraints\ in: (7) - (8), (11), (13) - (14), (16), \\ and\ (18)\ to\ (21) \\ N_{pv} \leq N_{pv,max} \\ C_{INV} \leq C_{INV,max} \end{cases} \tag{30}$$

Where:

$$C_{operation} = \beta \sum_{t=1}^{n} C_{t,G} \tag{31}$$

The number of PV panels selected by the optimization must not exceed the available physical space for their installation. Additionally, the initial investment cost is constrained by the maximum budget allocated for the system.

The optimization procedure starts by uploading the input data, including the household consumption profile, corresponding weather data, and the applicable ToU tariff. It proceeds with the initialization of model parameters, such as PV module characteristics and battery specifications.

Throughout the optimization loop, the number of PV panels and the BESS size are selected. For each configuration, power flow is simulated, battery SoC and aging are calculated, and energy costs are evaluated based on real consumption data, weather, and energy prices.

The algorithm computes the total cost, including investment, replacement, maintenance, and operational costs. Constraints such as SoC bounds, power limits, and battery degradation are checked. If all constraints are satisfied and the stopping criteria are met, the optimization converges to the optimal solution. The optimization is handled using MATLAB fmincon solver with an interior-point algorithm, subject to nonlinear constraints and configured to run in parallel with strict tolerance settings for constraint satisfaction, step size, and optimality. However, the optimization process determines the L_{loss}, creating a trade-off between L_{loss} and the number of batteries N_b. This trade-off is illustrated in Figure 4, which shows the replacement cost as a function of L_{loss} and N_b.

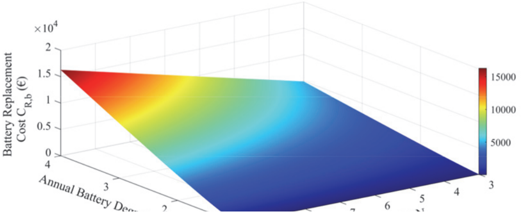

Fig. 4: Replacement cost variation with L_{loss} and N_b

The optimization tends to minimize the replacement cost either by selecting a higher number of batteries, which reduces degradation, or by avoiding high L_{loss} values that would result in frequent replacements.

5.3 Sizing Results

To evaluate the proposed approach, different scenarios based on solar irradiance levels are considered. Each scenario is built by selecting one representative week of consumption along with the corresponding solar irradiance and temperature data (with a time step of one hour), which is then annualized to serve as input for the optimization process. The objective is to determine the optimal selection of N_b and N_{pv}, along with the associated operational cost, annualized total cost, and corresponding battery lifetime.

Both self-consumption and grid-selling scenarios are analyzed to assess the impact of incorporating battery degradation under different conditions and its influence on dynamic lifetime estimation.

Table 1 presents the optimization results under three irradiance levels (high, medium, and low) and two operation strategies: self-consumption and selling to the grid.

Table 8: Optimization results under different irradiance and selling strategies

	Self Consumption				Selling to the Grid Option			
	N_{pv}^{op}	N_b^{op}	L_{loss}	L_b	N_{pv}^{op}	N_b^{op}	L_{loss}	L_b
High irradiance	24	5	1.58	12.6	25	5	1.59	12.57
Medium irradiance	16	3	1.33	15	25	7	1.37	14.5
Low irradiance	25	7	1.59	12.5	25	7	1.73	11.52

The analysis reveals that irradiance level strongly influences the optimal system configuration. Under high irradiance, a reduced number of PV panels are sufficient for self-consumption (N_{pv}^{op} = 24) compared to low irradiance conditions, which require the maximum number of panels (N_{pv}^{op} = 25). A similar trend is observed for battery sizing. Medium irradiance conditions result in a reduced battery configuration (N_b^{op}= 3), reflecting a favorable balance between energy generation and consumption.

It should be noted that consumption and energy prices also play a significant role in system sizing. In the medium irradiance scenario, the reduced selection of both PV and battery capacity is partly due to lower overall energy demand during the selected period. Additionally, the peak consumption aligns better with the solar generation profile, improving self-consumption efficiency and reducing the need for storage or excess generation capacity.

When grid-selling is enabled, the system tends to size the PV system at its upper bound (N_{pv}^{op}= 25) across all irradiance levels to maximize revenue. This shift comes with an increase in battery usage, especially under medium irradiance (N_b^{op}= 7) compared to only 3 in the self-consumption case. Notably, in the low irradiance case,

L_{loss} increases from 1.59% to 1.73% and L_b drops to 11.52 years, indicating that maximizing profit through export comes at the cost of higher battery degradation.

The number of batteries N_b^{op} and the annual degradation rate L_{loss} exhibit a clear inverse relationship. Increasing N_b^{op} helps reduce L_{loss}, thereby extending the battery lifetime L_b, as observed in the medium irradiance case, where N_b^{op} increases from 3 to 7 under the selling scenario. However, in grid-selling scenarios, the system tends to exploit battery cycling more intensively to maximize revenue, resulting in higher L_{loss} and lower L_b, even when N_b^{op} is high.

Table 2 presents the cost results for three representative weeks, each associated with a different solar irradiance level and mapped to a corresponding season. Since a typical year is composed of such seasonal variations, this approach provides an estimate of the annual degradation rate L_{loss} and a more realistic evaluation of system performance. For this purpose, all optimization runs were conducted with a fixed number of PV panels N_{pv}^{op} = 25 and batteries N_b^{op} = 7 across all scenarios. These values were selected based on the optimal system sizing identified in the previous table. This setup ensures that the analysis reflects realistic operational conditions throughout the year, focusing specifically on the scenario where selling electricity back to the grid is enabled, which is the adopted case.

Table 9: Cost breakdown and battery degradation under fixed PV and BESS configuration

Total capital cost (€/year)	Total maintenance cost (€/year)	Total replacement cost (€/year)	Annual imported energy cost (€/year)	Annual exported energy cost (€/year)	Annual operational cost (€/year)	Overall cost (€/year)	L_{loss} (%)	L_b
516.6	90.75	86.85	4231.23	- 531.28	3700	4394.2	1.47	13.6

The results in Table 2 show that, under the fixed configuration, the annual degradation rate L_{loss} is 1.47%, corresponding to a battery lifetime L_b of approximately 13.6 years. These values confirm the effectiveness of the selected system sizing in limiting battery wear while maintaining operational performance throughout the year. The moderate degradation rate ensures fewer replacements, contributing to a balanced trade-off between investment and operational cost.

Figure 5 shows the power flow dynamics, battery SoC, and C-rate behavior over a representative day in the average irradiance scenario with grid selling enabled. The C-rates for both charging and discharging remain below 0.3, indicating moderate battery usage and controlled cycling. The battery is primarily charged during low-tariff periods and discharged during high-tariff periods, reflecting the optimization objective to reduce energy costs and increase revenue through grid export. All operational constraints are respected, including those on power flow and battery SoC, as shown in the figure.

Figure 6 illustrates the payback time when considering the option of selling electricity back to the grid. It shows two curves: the first represents the cumulative cost over 20 years when all the energy demand is met only from the grid. The second curve represents the cumulative cost of the PV-BESS system integrated with an energy router. This cost includes the initial investment (distributed over M years), replacement and maintenance costs, as well as operational costs calculated as the cost of energy purchased from the grid minus the revenue from energy sold back to the grid. As shown in the figure, the payback time is approximately 7 years, indicating that the adoption of such a system becomes more economically beneficial in the long term.

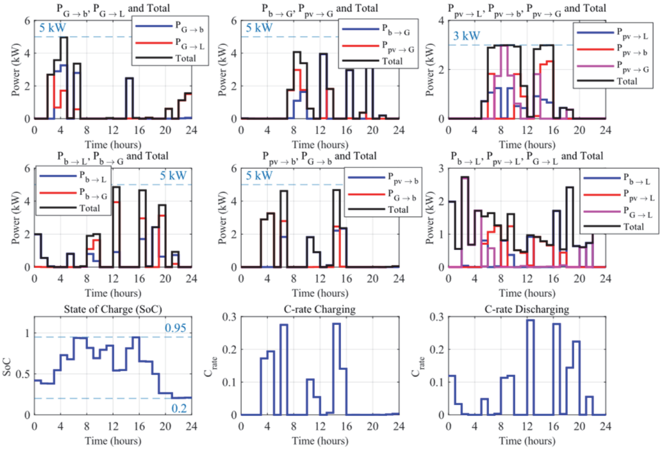

Fig. 5: Power flow, SoC, and C-rate profiles for a representative day under average irradiance

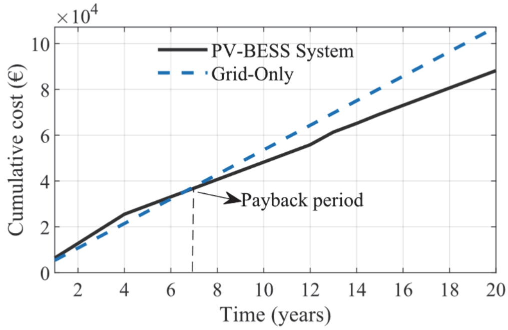

Fig. 6: Payback time analysis for PV-BESS System with energy export to the Grid

6 Day-Ahead Operation and Energy Management

For day-ahead operation, the focus shifts to the EMS, which becomes central to optimizing energy flow in real time. The presence of the ER converter enables the dynamic coordination of power exchange between the PV system, BESS, the grid, and the residential load. The proposed EMS is designed to operate over a 24 hours horizon where it predicts both energy consumption and PV generation. These forecasts, combined with day-ahead energy prices, serve as inputs for the day-ahead optimization.

The day-ahead optimization is applied within the household EMS and is structured in two main layers, as shown in Figure 7. The upper layer is the EMS, which collects historical system data, integrates weather forecasts, and predicts PV output and electricity demand. Using this information, the optimization problem is solved to determine the most cost-effective strategy for managing energy flow over the next 24 hours. The resulting power references are then sent to the lower layer, consisting of the physical system: the residential load, PV panels, BESS, and the grid, all interconnected via the ER converter, which executes the optimal energy dispatch in real-time operation.

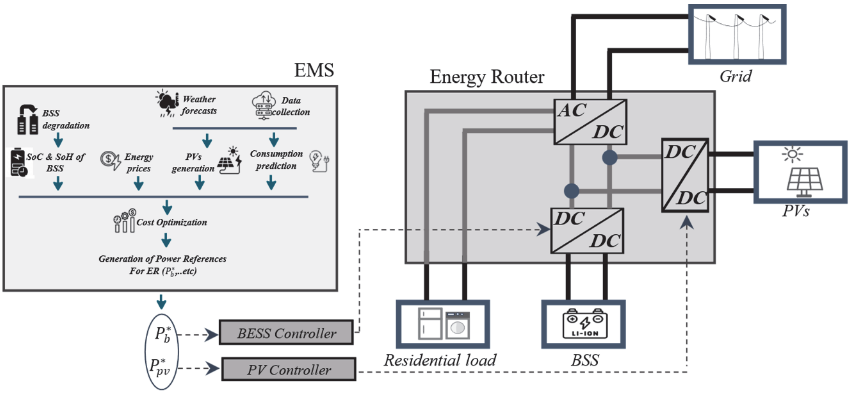

Fig. 7: Architecture of the proposed Short-Term EMS

6.1 Day-Ahead optimization

The developed day-ahead optimization strategy aims to minimize the total operational cost of a residential PV-battery system while accounting for short-term battery degradation effects. To ensure the approach realistically captures battery wear in daily operations, the optimization is formulated to be battery aging-aware by integrating degradation cost models directly into the objective function. Several degradation modeling approaches exist in the literature to quantify the impact of battery usage on lifetime, such as SoH-based models that compute cost as a function of SoH loss [21], and FEC-based models that use Full Equivalent Cycles to estimate degradation [22]. These models are used to link short-term energy management decisions with long-term battery degradation dynamics.

6.1.1 Optimization formulation

The day-ahead optimization problem is formulated to minimize the total operational cost over a 24-hour time horizon with a fixed step time, typically set to 5 minutes. The objective function, presented in (32), includes three main components: the cost of electricity purchased from the grid, the revenue from energy exported to the grid, as detailed in Equation (22) in the case study and system operation model section, and the degradation cost of the battery $C_{d,F}^{Model}$, which accounts for both calendar and cyclic aging effects, as introduced in the battery degradation model section. This integrated formulation ensures that the optimization not only minimizes daily operational costs but also balances short-term economic benefits with long-term battery health preservation. The optimization is formulated as follows.

$$min\ C_{Daily} = C_{d,F}^{Model} + \sum_{t=1}^{n} C_{t,G} \tag{32}$$

$$Subject\ to: \begin{cases} Constraints\ in: (7)-(8), (11), (13)-(14), (16), \\ \qquad and\ (18)\ to\ (21) \end{cases} \tag{33}$$

The optimization includes all operational constraints previously defined in the system operation model section, covering power balance, maximum power limits, and charging/discharging constraints.

6.1.2 Battery degradation cost modeling

A commonly used approach in EMS is to convert battery degradation into a monetary cost, enabling the integration of long-term battery wear into short-term operational decisions. This formulation helps prevent excessive degradation due to daily cycling and ensures that optimal control strategies account for battery aging [22][9][21].

Two widely adopted models for estimating battery aging costs are the SoH-based model and the (FEC)-based model:

1) SoH-Based Model This approach calculates degradation cost based on the loss in battery SoH over time. The idea is to penalize each loss of SoH proportionally to the initial capital cost of the battery. The total cost over a prediction horizon is given by:

$$C_{d,F}^{SoH} = \sum_{t=1}^{n} \frac{-c_f \cdot N_b E_b}{1 - SoH_f} \Delta SoH_{t,b} \tag{34}$$

Where:

- c_f is the battery cost per kWh [€/kWh],
- E_b is the nominal capacity of the battery [kWh],
- $\Delta SoH_{t,b}$ is the SoH degradation during time step t.

2) FEC-Based Model This model assumes that battery degradation is mainly due to the number of charge-discharge cycles. The total battery life is characterized by a predefined number of Full Equivalent Cycles (FECs), after which the battery reaches its end of life. The cost per time step is calculated as:

$$C_{d,F}^{FEC} = \sum_{t=1}^{n} \frac{c_f \cdot N_b E_b}{N_{Cyc}} \Delta FEC_{t,b} \tag{35}$$

Where:

– $\Delta FEC_{t,b}$ is the fraction of a full cycle consumed at time step t.

This approach may underestimate degradation under conditions where calendar aging dominate.

3) Proposed degradation cost model Unlike the previous models, the proposed approach incorporates both the physical degradation of the battery and the financial impact of its future replacement by considering the effect of interest rates. This choice is motivated by the fact that in the system sizing stage, the battery replacement cost was discounted using a sinking fund approach, which

ensures financial consistency between long-term investment planning and short- term operational decisions.

$$C_{d,F}^{deg-rep} = c_f \cdot N_b E_b \cdot \frac{i_{sa}}{(1+i_{sa})^{\frac{SoH_i - SoH_f}{0.2 \cdot \gamma \cdot Q_{d,F}}} - 1} \cdot \frac{1}{\gamma} \tag{36}$$

Where:
– In the daily case, γ is set to 365.
Where:

$$Q_{d,F} = \sum_{t=1}^{n} Q_{t,F} \tag{37}$$

This model ensures consistency with the economic assumptions used during the sizing phase and reflects more accurately the financial consequences of battery wear. It is especially useful for applications where the EMS must balance cost savings and asset longevity while respecting financial return criteria.

6.1.3 Seasonal performance analysis of the proposed model

To evaluate the sensitivity of the proposed degradation-integrated cost model to seasonal conditions, the day-ahead optimization was applied to two representative days: one in summer and one in winter (Figure 8). These test cases reflect typical consumption behaviors under different environmental and pricing conditions. The optimization problem was solved with a temporal resolution of 5 minutes (Δt = 5 min). Both energy prices and household demand exhibit seasonal variability, winter presents higher consumption and significantly elevated energy tariffs compared to summer. This allows for a comprehensive assessment of how the proposed EMS strategy responds to seasonal fluctuations in both grid dynamics and household energy behavior, particularly with respect to battery usage, degradation impact, and cost-effectiveness.

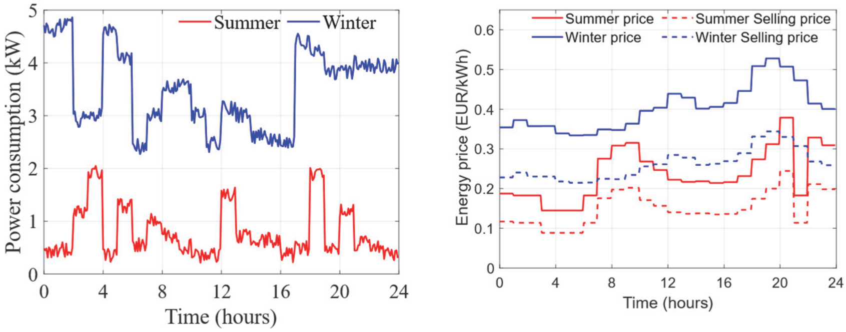

(a) Consumption profiles (b) Energy prices

Fig. 8: Seasonal variations in consumption and energy prices

Figure 9-a illustrates the evolution of battery SoH under both winter and summer conditions, starting from the same initial value. As shown, the degradation is more significant in the winter case. This is primarily due to higher energy demand, more intensive cycling, which amplify both calendar and cyclic aging effects. In contrast, the summer scenario demonstrates a slower degradation trend, reflecting less stressful operating conditions for the battery. Figure 9-b shows the battery SoC profiles over 24 hours. During winter, the battery reaches its lower SoC limit (SoC_{min} = 0.2), indicating important discharging to meet demand. This increases cycling-related stress. In summer, the battery operates within a narrower and more stable SoC range, benefiting from higher PV generation and lower consumption.

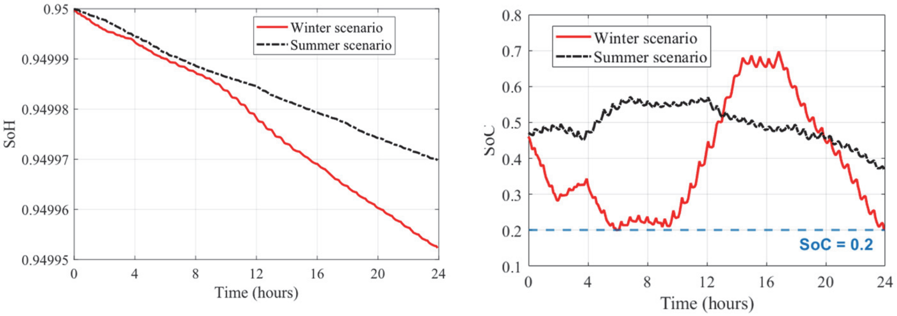

(a) SoH evolution

(b) SoC evolution

Fig. 9: SoH and SoC profiles for different seasonal scenarios

As shown in Table 3, the PV-battery system leads to cost savings in both summer and winter scenarios. The Grid-only cost represents the case where all electricity is drawn from the grid without any local generation or storage. The Final cost excludes the degradation cost, which is treated as a penalty reflecting battery wear. Despite higher degradation in winter, the system yields greater savings due to higher consumption and electricity prices, emphasizing the economic advantage of the proposed day-ahead optimization.

Table 10: Cost comparison between summer and winter scenarios

Cost component	Summer (€/day)	Winter (€/day)
Imported cost	3.6711	27.2072
Exported cost	- 0.6435	- 0.0030
Battery degradation cost	0.2310	0.4395
Final cost (without degradation)	3.0276	27.2042
Grid-only cost	4.3380	34.0158
Potential savings	1.3104	6.8086

7 Business Model Perspective and Deployment Roadmap

To translate the proposed degradation-aware sizing and day-ahead EMS into a deployable solution, we consider a hybrid Cloud/Edge architecture designed for residential prosumers equipped with PV, BESS, and an ER as shown in figure 10. The key technical challenge for real deployment is that uncertainty (load, PV generation, tariffs, and user behavior) requires frequent decision updates, while embedded controllers must remain fast, reliable, and privacy-preserving.

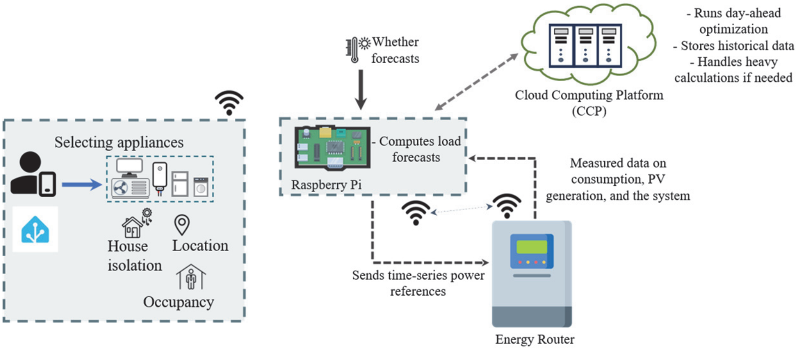

Fig. 10: Two-level EMS architecture with CCP and ECP

Architecture (two-level Table 4):

Edge Computing Platform (ECP): implemented on a low-cost Raspberry Pi 4 integrated with Home Assistant. The ECP handles data acquisition (smart meter, PV, BESS, ER), provides the user interface, performs local short-term consumption prediction, and executes real-time decision making by computing power references for the ER. High-frequency household data can be stored locally by default, supporting privacy and resilience (operation continues even if connectivity is degraded).

Table 11: ECP/CCP Split of Responsibilities

Edge Computing Platform (ECP): Raspberry Pi	Cloud Computing Platform (CCP): Cloud Service
• Data acquisition (smart meter, PV, BESS, Energy Router) • Home Assistant UI (user-friendly) • Local consumption prediction • Real-time decision making (compute power references for ER) • Local storage (default)	• Day-ahead optimization (heavy compute) • Multiparametric optimization to compute critical regions • Tariff/forecast processing • Policy distribution + updates • Optional cloud storage (limited retention)
Uploads: aggregated day-ahead forecast (and optional consented aggregates), not raw sensitive signals by default.	Returns: compact policy packages (critical regions) enabling fast real-time control on the ECP.
Operates in Real-time.	Runs on schedule (daily + every 4 hours).

Cloud Computing Platform (CCP): runs the computationally intensive day-ahead optimization and periodically performs multiparametric optimization to generate Critical Regions (CRs). These policies are transmitted to the ECP, enabling real-time optimal control without solving heavy optimization problems on the embedded device.

7.1 Role of multiparametric optimization under uncertainty

Instead of relying on continuous cloud control, the CCP converts the day-ahead problem into a set of critical regions that map uncertain/variable parameters to an optimal control law. This approach ensures that the ECP can react in real time with minimal computation and latency, while still following an optimization-consistent strategy.

Value proposition:

The solution targets measurable outcomes already demonstrated by the research results:

1) reduced electricity cost through optimized scheduling under ToU and export rules.
2) improved asset durability by explicitly accounting for battery degradation (calendar + cyclic).
3) practical feasibility through a low-cost embedded implementation. The availability of an open-access residential load profile predictor already implemented on Raspberry Pi 4 supports immediate prototyping and future replication across sites and climates [20].

7.2 Go-to-market logic

A realistic adoption path is through PV+BESS+ER installers and integrators, where the end user bears installation costs as part of the global installation/retrofit project, while the EMS provider supplies the ECP package and software onboarding. A recurring subscription can cover CCP services (day-ahead optimization, critical-region updates, cybersecurity maintenance, tariff updates, and technical support), with multi-tenant cloud execution reducing marginal compute cost per household.

7.3 Roadmap

The next step is to close the loop in a real case study by finalizing:

(i) the CCP day-ahead optimization based on multiparametric optimization.
(ii) the ECP real-time execution layer that computes ER power references from the received CRs. A preliminary cost assessment (edge hardware, local storage, and cloud compute) enables feasibility evaluation before customization and full experimental validation on the ER prototype.

8 Conclusion and Perspectives

This chapter presented a degradation-consistent framework for residential PV–battery systems, linking battery lifetime modeling, system operation, sizing, and day-ahead optimization. A semi-empirical LiFePO4 model combining calendar and cyclic aging was used to track SoH and quantify annual degradation losses, enabling sizing decisions that reflect realistic replacement needs and economic impact. The resulting configuration was then used in a day-ahead EMS where battery aging is monetized through a degradation cost model consistent with the sizing stage. Seasonal case studies indicate annual capacity fade typically in the 1.3–1.7% range, yielding an estimated lifetime of about 13–14 years, while export-enabled scheduling improves profitability with a payback time close to 7 years and daily savings compared to grid-only operation.

Future work will focus on experimental validation on a residential application with an ER and full implementation using a two-level cloud/edge EMS. Multiparametric optimization will be used to handle uncertainty and to deliver compact "critical-region" policies from the cloud, enabling fast real-time control on embedded hardware while preserving privacy and reliability.

Acknowledgments. This project has received funding from the European Union's Horizon 2020 research and innovation programme under the Marie Skłodowska-Curie grant agreement No 955614.

References

1. Azizi, M., Husev, O., Mbayed, R., Monmasson, E., Martins, J., Veligorskyi, O.: En- ergy Router: A Sustainable Solution for Future Residential Buildings. IEEE Power Electron. Mag. 12(1), 75–86 (2025)
2. Bhamidi, L., Sivasubramani, S.: Optimal sizing of smart home renewable energy resources and battery under prosumer-based energy management. IEEE Syst. J. 15(1), 105–113 (2021)
3. Wu, Y., Liu, Z., Liu, J., Xiao, H., Liu, R., Zhang, L.: Optimal battery capacity of grid-connected PV-battery systems considering battery degradation. Renew. Energy 181, 10–23 (2022)
4. Das, A., Wu, D., Bhatti, B.A., Kamaludeen, M.: Approximate Dynamic Program- ming With Enhanced Off-Policy Learning for Coordinating Distributed Energy Re- sources. IEEE Trans. Sustain. Energy 15(3), 1614–1626 (2024)
5. Lam, L., Bauer, P.: Practical capacity fading model for Li-Ion battery cells in electric vehicles. IEEE Trans. Power Electron. 28(12), 5910–5918 (2013).
6. Schmitt, J., Rehm, M., Karger, A., Jossen, A.: Capacity and degradation mode estimation for lithium-ion batteries based on partial charging curves at different current rates. J. Energy Storage 59, 106517 (2023)
7. Nizami, M.S.H., Hossain, M.J., Fernandez, E.: Multiagent-based transactive energy management systems for residential buildings with distributed energy resources. IEEE Trans. Ind. Inform. 16(3), 1836–1847 (2020)
8. Liu, C., Ma, H., Zhang, H., Shi, X., Shi, F.: A MILP-based battery degradation model for economic scheduling of power system. IEEE Trans. Sustain. Energy 14(2), 1000–1009 (2023)
9. Collath, N., Tepe, B., Englberger, S., Jossen, A., Hesse, H.: Aging aware operation of lithium-ion battery energy storage systems: A review. J. Energy Storage 55(C), 105634 (2022)
10. Li, S., Zhao, P., Gu, C., Huo, D., Li, J., Cheng, S.: Linearizing Battery Degradation for Health-Aware Vehicle Energy Management. IEEE Trans. Power Syst. 38(5), 4890–4899 (2023)
11. Mulleriyawage, U.G.K., Shen, W.X.: Optimally sizing of battery energy storage ca- pacity by operational optimization of residential PV-battery systems: An Australian household case study. Renew. Energy 160, 852–864 (2020)

12. Ghanaee, E., P´erez-D´ıaz, J.I., Ferna´ndez-Mun˜oz, D., Na´jera, J., Chazarra, M., Castan˜o-Solis, S.: Optimal Scheduling of a Hybrid Wind–Battery Power Plant in the Day-Ahead and Reserve Markets Considering Battery Degradation Cost. In: Proc. Int. Conf. Smart Energy Systems and Technologies (SEST), pp. 1–6. IEEE, Torino (2024)
13. Choi, D., Shamim, N., Crawford, A., Huang, Q., Vartanian, C.K., Viswanathan, V.V., Paiss, M.D., Alam, M.J.E., Reed, D.M., Sprenkle, V.L.: Li-ion battery tech- nology for grid application. J. Power Sources 511, 230419 (2021)
14. Xu, B., Oudalov, A., Ulbig, A., Andersson, G., Kirschen, D.S.: Modeling of Lithium-Ion Battery Degradation for Cell Life Assessment. IEEE Trans. Smart Grid 9(2), 1131–1140 (2018)
15. Khezri, R., Steen, D., Wikner, E., Tuan, L.A.: Optimal V2G Scheduling of an EV With Calendar and Cycle Aging of Battery: An MILP Approach. IEEE Trans. Transp. Electrific. 10(4), 10497–10507 (2024)
16. Goebel, C., Hesse, H., Schimpe, M., Jossen, A., Jacobsen, H.-A.: Model-Based Dispatch Strategies for Lithium-Ion Battery Energy Storage Applied to Pay-as-Bid Markets for Secondary Reserve. IEEE Trans. Power Syst. 32(4), 2724–2734 (2017)
17. Zou, B., Peng, J., Li, S., Li, Y., Yan, J., Yang, H.: Comparative study of the dynamic programming-based and rule-based operation strategies for grid-connected PV-battery systems of office buildings. Appl. Energy 305, 117875 (2022)
18. Yang, H., Gong, Z., Ma, Y., Wang, L., Dong, B.: Optimal two-stage dispatch method of household PV-BESS integrated generation system under time-of-use elec- tricity price. Int. J. Electr. Power Energy Syst. 123, 106244 (2020)
19. Baniasadi, A., Habibi, D., Al-Saedi, W., Masoum, M.A.S., Das, C.K., Mousavi, N.: Optimal sizing design and operation of electrical and thermal energy storage systems in smart buildings. J. Energy Storage 28, 101186 (2020)
20. Lekhel, C.E.S., Mbayed, R., Velihorskyi, O., Husev, O., Monmasson, E.: Generic residential load profile generator based on weather data and occupancy. Math. Com- put. Simul. 237, 102310 (2025)
21. Hesse, H., Kumtepeli, V., Schimpe, M., Reniers, J., Howey, D., Tripathi, A., Wang, Y., Jossen, A.: Ageing and efficiency aware battery dispatch for arbitrage markets using mixed integer linear programming. Energies 12(6), 999 (2019)
22. Collath, N., Cornejo, M., Engwerth, V., Hesse, H., Jossen, A.: Increasing the life- time profitability of battery energy storage systems through aging-aware operation. Appl. Energy 348, 121531 (2023)

A Centralized Energy Management System for Droop-Controlled DC Nanogrids Using Binary Setpoint Shifting

Sayeed Hasan[1] , Neelesh Yadav[1],Andrii Chub[1], Andreii Blinov[1], Dmitri Vinnikov[1]

[1] Department of Electrical Power Engineering and Mechatronics
Tallinn University of Technology
{sayeed.hasan, neelesh.yadav, andrii.chub, andrei.blinov, dmitri.vinnikov}@taltech.ee}

Abstract. AC microgrids and nanogrids have reached a mature stage in terms of efficiency, operational flexibility, and resilience. However, in recent decades, DC microgrids have gained significant attention as a promising alternative for both industrial and residential applications. Modern DC-DC converters now offer high efficiency across a wide range of use cases, from general-purpose to specialized applications. Replacing conventional AC-based components with DC systems can further reduce energy losses and unlock greater operational flexibility. Among various DC architectures, droop-controlled DC microgrids stand out for their adaptability, resilience, and stable performance. Even with fixed droop curves, DC microgrids provide a degree of operational flexibility. However, integrating an Energy Management System (EMS) to control droop-regulated assets can significantly enhance this flexibility, enabling a wider range of operational modes and dynamic responses. This chapter provides an overview of EMS for DC microgrids and presents simulation results and experimental validation of a centralized EMS with binary shifting from a 350V DC nanogrid testbed.

Keywords: DC droop control, Setpoint shifting, DC nanogrid, energy management, Battery Management.

1 Introduction

With the global population rising rapidly and fossil fuel reserves gradually depleting, the world has increasingly shifted toward renewable energy over the past few decades. This transition is also driven by concerns over geopolitical stability, the urgent need for energy independence, and the push to mitigate climate change. The European Union, through initiatives like the Green Deal, has set an ambitious goal to become carbon neutral by 2050. As a result, member states are adopting policies to cut emissions. For example, since 2020, Estonia has mandated that all new residential buildings meet the nearly zero-energy building (nZEB) standard, corresponding to energy performance class A. This standard necessitates that buildings are constructed using energy-efficient solutions and renewable energy technologies in a technically reasonable manner [1].

However, the growing integration of renewables into the grid introduces challenges such as grid congestion and harmonic distortion. While renewable energy installations

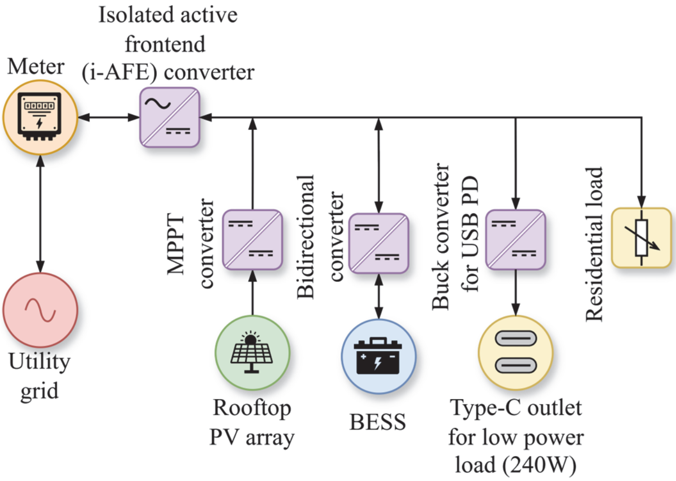

Fig. 3. Typical DC droop-controlled residential nanogrid/microgrid.

were once viewed as highly profitable, widespread adoption could drive down energy prices, potentially reducing return on investment. In such cases, prosumers may benefit more by consuming or storing their excess energy for use during peak price periods rather than selling it to the grid. Effective EMS approaches can make this strategy feasible.

Currently, most renewable integration relies on traditional AC systems using line-frequency converters. However, AC microgrids present limitations, including multiple conversion stages, bulkier infrastructure, and reduced control flexibility. Additionally, essential resources like copper and iron are also becoming scarce, making conventional AC setups less efficient in terms of both energy and material use.

These challenges can be addressed by adopting droop-controlled DC microgrids. DC microgrids offer benefits like fewer power conversion stages and the need for only one grid-interface converter, leading to higher efficiency, greater operational flexibility, and reduced use of raw materials. As illustrated in Fig. 1, a typical DC nanogrid configuration demonstrates this streamlined and resource-efficient design. In the droop control approach, each asset is assigned a specific operating voltage range by applying a droop coefficient (virtual resistance) to the converter [2]. Converters and loads are given unique droop curves based on their power ratings and capabilities, enabling efficient power sharing and the implementation of various operating modes across different voltage bands.

The concept of DC droop control is derived from its AC counterpart, where power sharing among multiple sources is governed by system frequency [3]. This case, however, limits the controllability of AC systems as the stable operating frequency band is quite narrow. In most cases, energy management in AC systems is event or mode-triggered, focusing primarily on maintaining a stable reference voltage rather than enabling dynamic, fine-grained control.

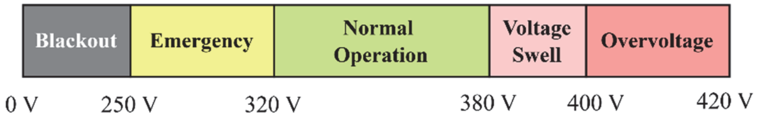

Fig. 2. DC residential microgrid/nanogrid operating bands according to Current/OS.

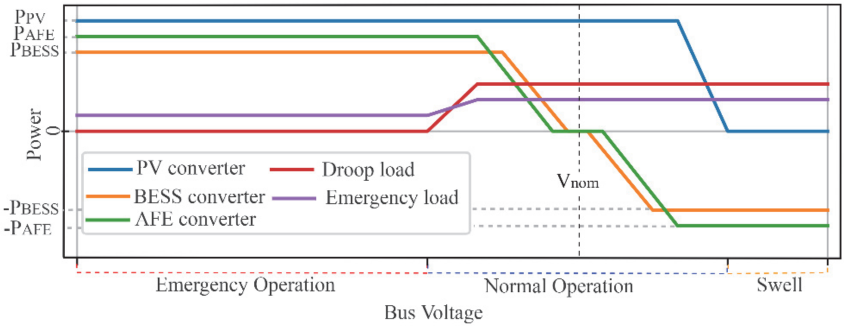

Fig. 3. Piecewise droop curves of different converters and loads in a DC microgrid.

In contrast, DC droop-controlled microgrids offer greater flexibility, as the operating voltage ranges are wider and can be tailored, and droop curves can take various forms: linear, piecewise linear, or even nonlinear [4][5]. Even with fixed droop curves, significant operational flexibility can be realized, such as maximizing self-consumption or increasing energy export to the grid. The operating range of a DC droop-controlled system is illustrated in Fig. 2, while Fig. 3 presents a representative droop curve used within this range.

In the literature, energy management in DC microgrids or nanogrids is typically categorized into three hierarchical control architectures: centralized, decentralized, and distributed control. In centralized systems, each converter in the microgrid communicates directly with a central EMS, which collects data from all converters and sends back optimal power setpoints based on system-wide analysis. In decentralized architectures, there is no communication between converters or with a central EMS; instead, each converter independently makes decisions based solely on local information, such as the DC bus voltage or the state of charge (SOC) of its connected energy storage system. Distributed systems, on the other hand, involve peer-to-peer communication among converters. Each converter exchanges information with others and adjusts its power setpoints collaboratively, without relying on a central controller. A simplified illustration of different EMS architectures comprising distributed generating units(DGs) is presented in Fig. 4[6].

Several research studies have been conducted on implementing energy management strategies in DC microgrids. In [7], a standalone DC microgrid comprising photovoltaic (PV) panels, fuel cells (FC), batteries, and supercapacitors (SC) is managed using fuzzy logic and PI controllers. Reference [8] discusses a SOC-driven, condition-based energy management approach for an islanded DC microgrid with a similar configuration.

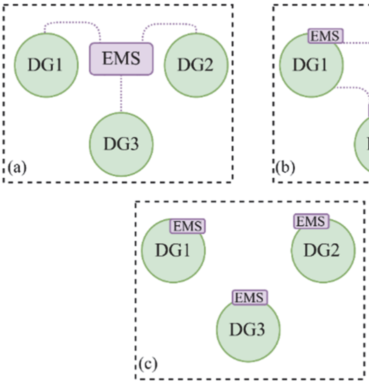

Fig. 4. DC microgrid/nanogrid EMS architecture, (a) Centralized, (b) distributed, and (c) decentralized.

In [9], a rule-based EMS is developed for a standalone DC microgrid incorporating PV, FC, SC, batteries, and an electric vehicle. This EMS addresses issues such as DC bus voltage stability and power-sharing fluctuations caused by renewable generation variability and load dynamics. Its effectiveness is validated through hardware testing and MATLAB Simulink simulations, demonstrating improved voltage stability and energy source coordination. Indirect battery management in a droop-controlled microgrid is explored in [10]. In [11], the proposed EMS uses battery SOC as a dynamic droop coefficient for power distribution, stabilizing bus voltage, and balancing energy storage levels. The strategy includes a secondary control layer that monitors both bus voltage and SOC, enabling seamless transitions between operational modes under various microgrid conditions. In [12], an EMS is proposed that utilizes an adaptive droop control algorithm to maintain DC bus voltage, especially during the islanded operation, where voltage regulation is more challenging. It employs a nonlinear droop profile with four tunable parameters, optimized for stable and efficient performance across different load and generation scenarios.

In [13], an optimized droop control strategy is introduced for DC microgrids with parallel-connected batteries. The focus is on mitigating SOC imbalances that lead to battery degradation. The strategy incorporates actual battery capacity data into the control logic, enabling proportional power sharing and SOC equalization. In [14], a centralized EMS is proposed for maximizing the utilization of PV and battery energy storage system (BESS) through multi-objective optimization techniques. This includes linear programming for energy scheduling and mixed-integer linear programming for intelligent load shedding. In [15], an EMS for an isolated DC microgrid based on fuzzy logic control (FLC) is presented, which efficiently manages power generation and demand. The FLC adjusts the fuel cell output in response to the power gap and battery SOC, enhancing the overall efficiency and reliability of the microgrid.

Conventional energy management strategies often face certain limitations. They either depend on computationally intensive algorithms or require a reliable and fast communication link to enable frequent data exchange between the EMS and power converters within the nanogrid. However, DC microgrids with piecewise droop curves inherently operate within well-defined voltage bands, offering an opportunity to reduce the need for continuous EMS intervention. This work aims to leverage that characteristic by developing an EMS approach that minimizes the frequency of setpoint updates sent to the converters. The goal is to simplify control by reducing the EMS's direct involvement in real-time operations. To achieve this, a mode-based, condition-triggered EMS architecture is proposed. This approach allows the system to operate autonomously within predefined voltage ranges, only adjusting the droop curve when certain operational thresholds are crossed, thereby improving reliability and reducing communication overhead.

2 Methodology

2.1 Droop curve shifting

Considering voltage-power (V–P) droop control, the basic expression for the n_{th} converter in a nanogrid is given by:

$$V_{ref} = k_p.P_{max} + V_{bus} \tag{1}$$

For a piecewise linear droop curve, within the segment defined by voltage setpoints V_a and V_b, the power output can be calculated as:

$$P_{out} = \frac{V_{bus} - V_a}{k_p} + P_a \tag{2}$$

Where the droop coefficient is:

$$K_p = \frac{V_a - V_b}{P_a - P_b} \tag{3}$$

When droop setpoint shifting is applied, both voltage reference points are moved to new values within the allowable operating range, denoted as V_a* and V_b*. Consequently, the updated droop coefficient and resulting power output are given by:

$$k_p^* = \frac{V_a^* - V_b^*}{P_a - P_b} \tag{4}$$

$$P_{out}^* = \frac{V_{bus}}{k_p^*} + P_a \tag{5}$$

By shifting the droop curve, the power output of a converter can be adjusted, enabling or enforcing specific operating modes. In essence, energy management in droop-controlled microgrids can be effectively implemented through this approach.

One of the primary goals of this work was to minimize the frequency of interactions between the nanogrid and the EMS, meaning that droop curve setpoint shifting should occur infrequently. To achieve this, a simple EMS strategy based on conditional logic was implemented. The EMS evaluates predefined operating conditions to determine when setpoints should be adjusted. These conditions include defined operating bands to prevent excessive communication, which could otherwise overload the network and complicate system control.

Each converter operates in telemetry mode, periodically sending measured input and output parameters to the EMS. The EMS checks these values against the predefined conditions but only sends new setpoint data if one or more of the condition bands are exceeded. Four key parameters were selected to perform droop curve shifting:

1. Power consumption, derived from telemetry data, is categorized into high, medium, and low prices.

2. Electricity price, retrieved via DSO APIs, categorized into high, medium, and low prices.

3. Power surplus or deficit, inferred from deviations in DC bus voltage, and

4. Battery SOC, also obtained from telemetry. Modes change depending on available energy based on the SOC's upper and lower limits.

To validate this approach, the droop shifting control is applied exclusively to the BESS converter in this study. Moreover, the droop curve shifting is implemented symmetrically, with a fixed voltage offset for each shift, hence the term binary shifting. Fig.5 depicts a flow chart for applying shifting based on the conditions of the four parameters.

The flowchart illustrates that electricity prices are divided into three categories: high, medium, and low. These are determined based on historical hourly price data and assigned percentile ranges. Similarly, overall power consumption (excluding ESS charging power) is classified into the same three tiers based on different load levels.

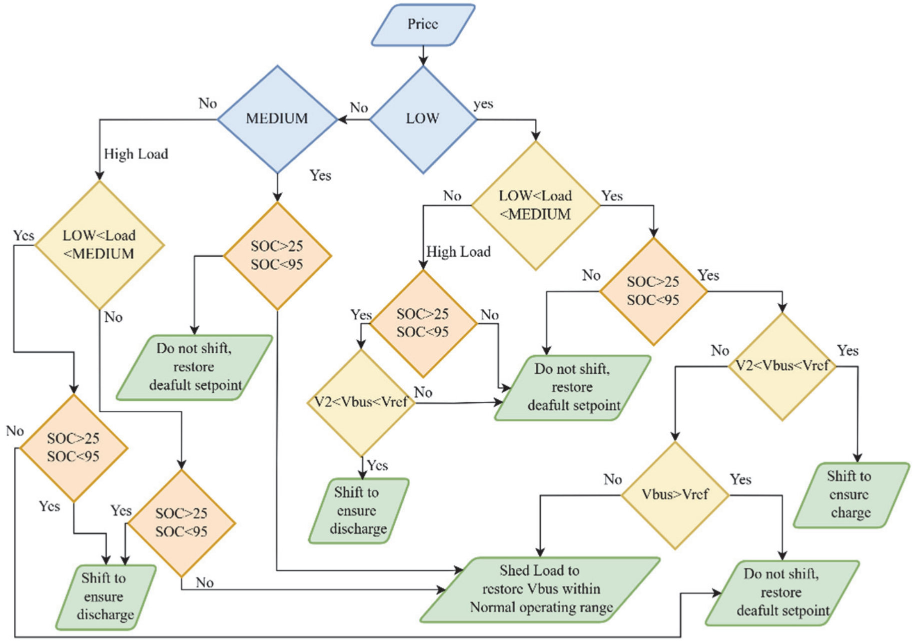

Fig. 5. Flowchart of droop curve shifting based on different operating conditions

When the electricity price is in the medium range, the EMS does not perform any droop curve shifting for the BESS converter, unless the battery is depleted. In that case, if the load is high, the EMS attempts to shed non-critical loads.

For low-price conditions, if the consumption is low to medium and there is an opportunity to charge the battery from the grid, the EMS shifts the droop curve to initiate charging. If PV generation is available, the system prioritizes charging from PV instead. However, if the load is high and there's a power deficit (i.e., $V_{bus} < V_2$, where V_2 is the voltage threshold just above the lower bound of the normal operation band, typically 320 V), the EMS shifts the curve to the left to enable battery discharge. If the BESS is unavailable, it again resorts to shedding non-essential loads. If surplus power is detected, the system reverts the curve to its original state.

Under high-priced conditions, the EMS always shifts the droop curve to prioritize battery discharge, regardless of load conditions. If the battery is depleted during high load, non-critical loads are shed to maintain system stability. This method is tested in the RT box simulation as well as in a 350 V DC microgrid.

2.1 RT Box Simulation Model

Before implementing droop curve shifting for converter control in real hardware, a simulation model was developed to emulate the behavior of the nanogrid. To closely replicate real-world operation, the same communication microcontroller used in the actual system was also used as the input source for a hardware-in-the-loop (HIL) simulation setup. For this purpose, the microgrid model was simulated using PLECS Standalone with RT-Box 1. Communication with the EMS was handled by the ESP32-C3 microcontroller, which is also used in the physical system (discussed in the next section).

However, newer RISC-V-based ESP32 variants lack onboard digital-to-analog converters (DAC), which are essential for providing analog signals required for droop curve shifting or for injecting real-time mission profiles into the simulation. There are two ways to overcome this: generate PWM and average out the PWM signal using an RC filter, or an external DAC chip connected to the ESP32 via Inter-Integrated Circuit(I^2C) protocol. For this experiment, the second option is chosen. A Raspberry Pi 4 is used to process feedback data, compute the necessary symmetrical droop shifting values, and send them to the ESP32 via Message Queuing Telemetry Transport (MQTT) protocol, and the microcontroller emulates the behavior of a BESS converter.

In the simulation, all current-fed converters are represented as average models using controlled current sources. These sources are driven by custom C-scripts containing predefined droop parameters. Real-time analog values from the DAC are read by the RT-Box, filtered, scaled, and then passed to the C-script controlling the BESS converter within the simulation. A simplified schematic of the system is shown in Fig. 6.

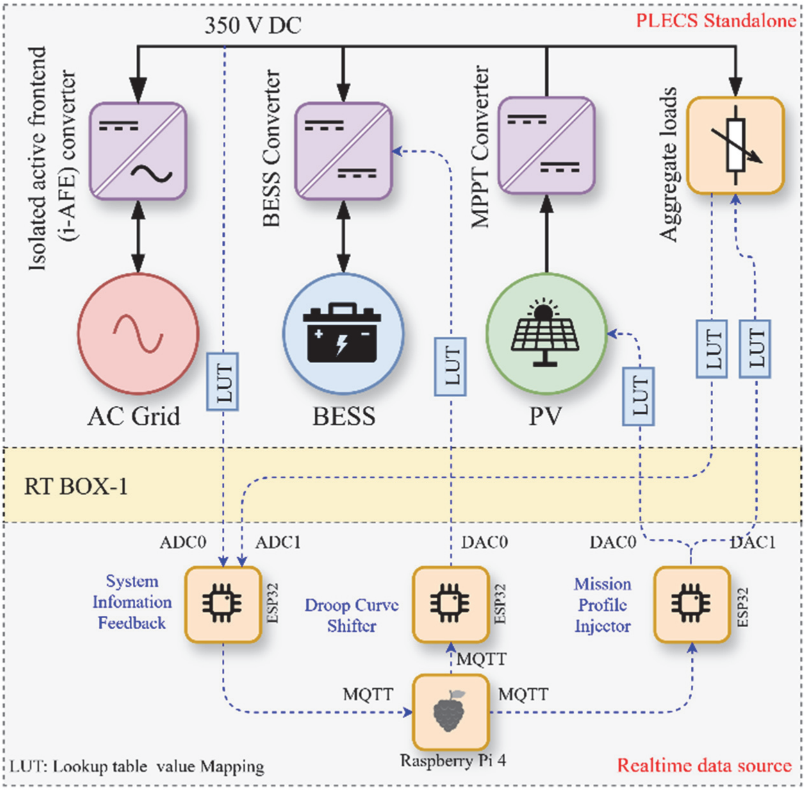

Fig. 6. Real-time simulation model of the nanogrid with the proposed droop curve shifting.

The simulation input mission profile for a day, shown in Fig. 7, is a synthetic dataset generated using a Python script. The mission profile was generated in a way that it can have both surplus and deficit scenarios. For the price information, a synthetic hourly price of energy was chosen; the price curve is shown in Fig.8.

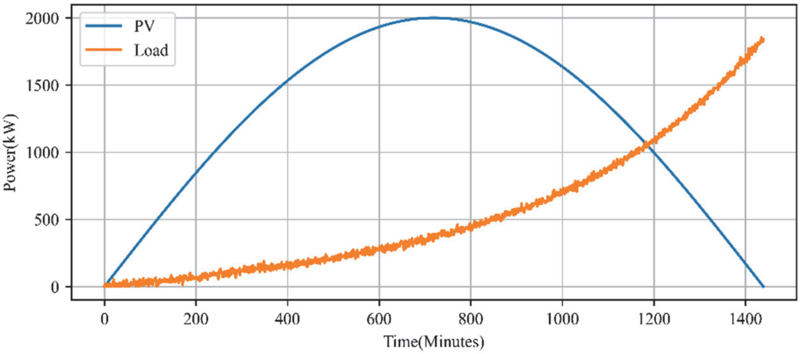

Fig. 7. Input mission profile for HIL simulation.

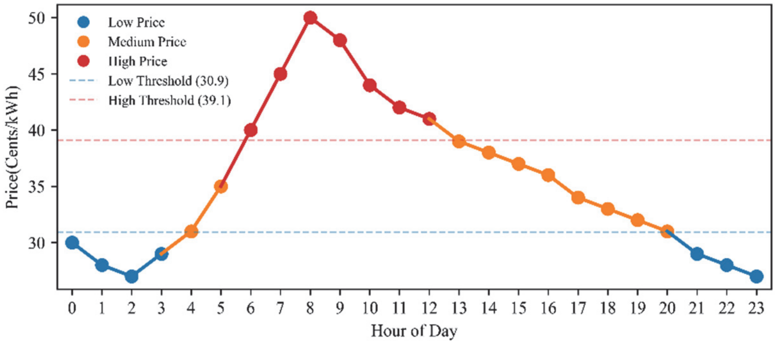

Fig. 8. Synthetic price curve with classification.

The data injector modules are illustrated in Fig. 9. Three ESP32 units are connected to the RT-Box 1: one functions as the BESS converter, adjusting the droop curve according to incoming setpoints; another receives system feedback from the RT-Box; and the third injects the mission profile. The complete setup is depicted in Fig. 10.

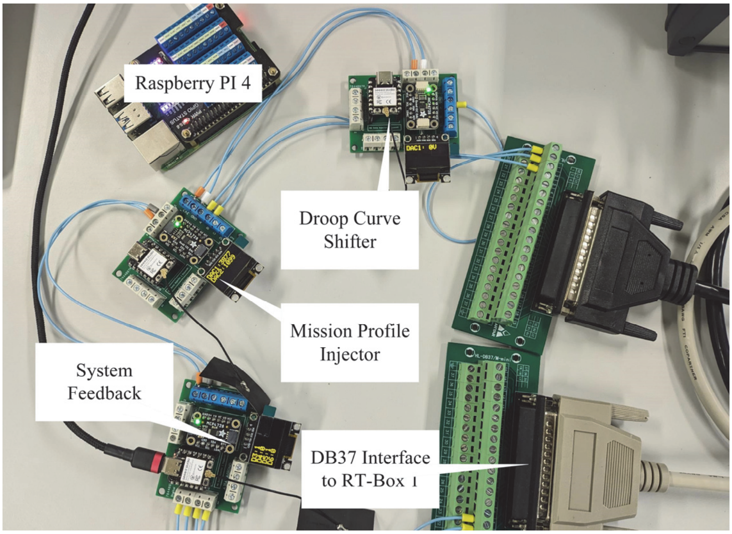

Fig. 9. Mission Profile injector, simulation feedback module, and droop curve shifter modules.

2.2 350 V DC Nanogrid Test Setup

In the prototype BESS converter, the actual microcontroller used for primary control was STM32G4, and for secondary communication, ESP32-S3 was used. Both the microcontrollers share information through a hardware Universal Asynchronous Receiver/Transmitter (UART) port set at 115200bps speed. ESP32 connects to EMS

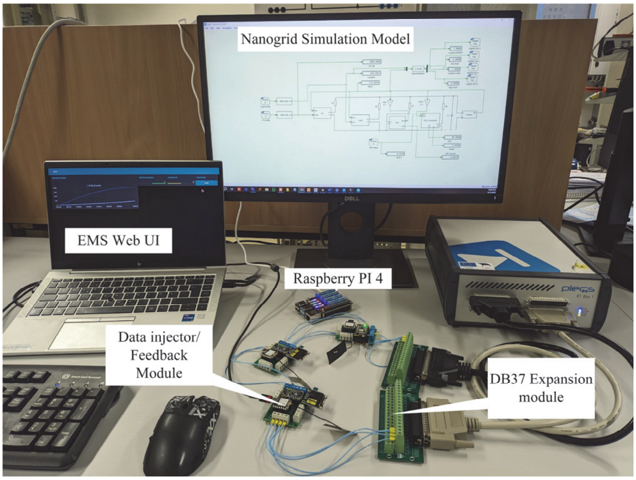

Fig. 40. Experimental setup for HIL simulation.

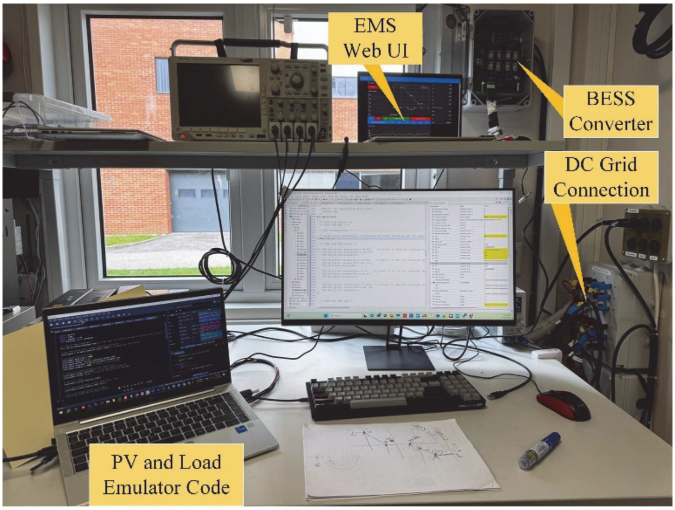

Fig. 51. Experimental setup in DC 350 V residential nanogrid testbed.

hardware via a wireless local area (WLAN) network to reduce the amount of latency in the communication. The EMS hardware processes the data and creates a JavaScript object notation (JSON) format containing all 6 coordinates for the droop curve. Which is received by ESP32 and pushed to the main microcontroller through UART. Then the converter moves toward the new setpoints through a current ramp up or down to maintain operational stability.

For simulating the residential load and PV generation, an ITECH IT6006C power supply was connected to the DC bus, and it was connected to a host computer via USB and controlled using a Python script using the Pyvisa library and the value for PV generation and load consumption was loaded to the power supply through a web interface. The 350VDC microgrid setup is shown in Fig. 11.

Table 12. Input parameters of different components used in the simulation and tests

Parameters	Simulation Model	DC test nanogrid
AFE converter (kW)	3	2.5
BESS converter(kW)	1.5	1
PV converter (kW)	2	1
Peak load (kW)	2	2

2.2 System parameters for both simulation and real testing

For the HIL simulation, the converter parameters differed from those used in the real-world tests. Additionally, the converter configurations varied between the two setups. The specific simulation parameters are presented in Table 1. The converters used in the DC test nanogrid are designed for higher power capacities, but their output has been intentionally limited through the configuration of their droop curves.

3 Result analysis

3.1 HIL setup using RT-Box 1

From Fig. 12, it can be observed that the EMS did not shift the droop curves during periods when electricity prices were in the medium range. Similarly, during high-price hours, sufficient PV generation was available, so no curve shifting occurred. The EMS initiated droop curve shifts by -25 volts during low-price periods, at around 200 minutes, and again around 1200 minutes to charge the battery. At 1200 minutes, in the absence of PV generation, the charging began via the AFE converter, causing a drop in bus voltage compared to the previous operating condition. After charging, the curve was shifted back to its original position, prompting the battery to start discharging. As a result, the voltage returned to the earlier level, and the AFE converter power injection decreased.

3.2 Results from the test nanogrid

In the experimental nanogrid setup, a partial power converter (PPC) was used as the BESS converter. To ensure system safety and avoid overstressing the hardware, the droop setpoint shift range was limited to ±6V. Due to this limitation, not all operating modes demonstrated in the simulation phase could be replicated in the hardware test. However, to validate the concept, test conditions were manually configured by inputting different electricity price levels.

Fig. 13 shows an oscillogram from the hardware test, while Fig. 14 shows data from an external power monitor, demonstrating the system's response to various test scenarios. Four distinct conditions, combining varying load demands and electricity price levels, were introduced as inputs to the EMS.

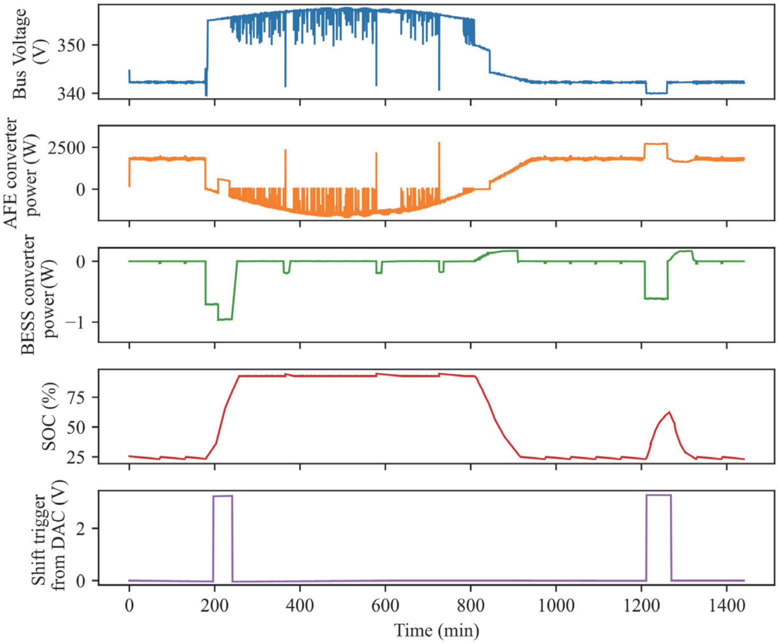

Fig. 62. Bus voltage, converter power, and shifting command from the simulation.

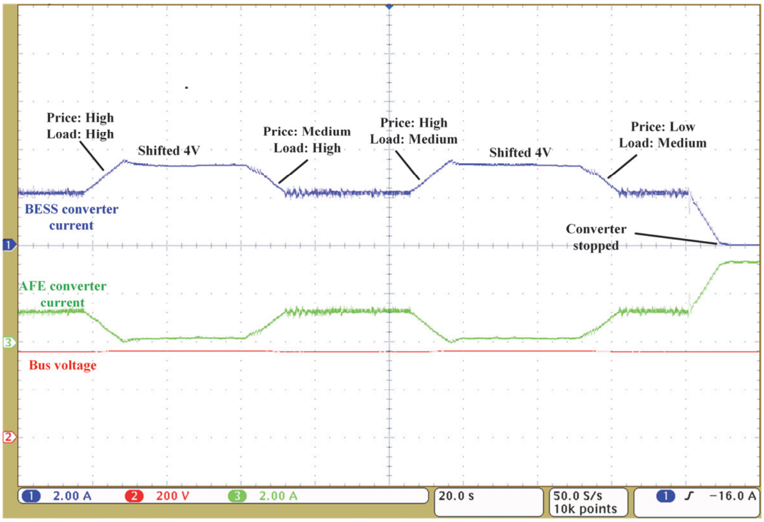

Fig. 73. AFE and BESS converter oscillogram from test nanogrid setup.

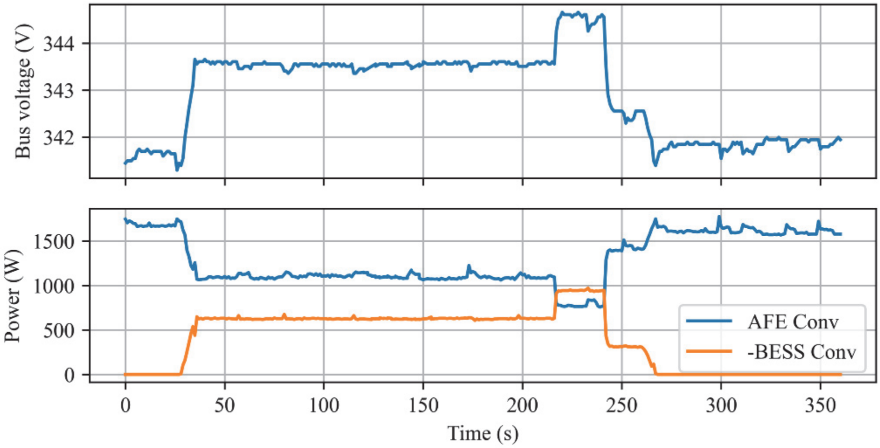

Fig. 84. Snippet of change of power of converter from the test nanogrid setup (data from external power monitor).

Based on these conditions, the EMS adjusted the droop curve accordingly. As a result of the droop shifting, the BESS converter changed its current output, either increasing or decreasing the power injection, demonstrating the effectiveness of voltage-based setpoint control in real-time operation. Although constrained in its full functionality, the test successfully showcased the responsiveness of the BESS converter to EMS-driven droop control under simplified conditions.

4 Conclusion

This work presents an energy management strategy designed to benefit from the inherent flexibility of droop-controlled DC nanogrids. By introducing a mode-based, condition-triggered centralized EMS architecture, the system significantly reduces the need for frequent setpoint updates, minimizing real-time EMS intervention and simplifying overall control. The converters operate autonomously within predefined voltage bands, and droop curve adjustments are only triggered when specific operating thresholds are exceeded. This reduces communication overhead and enhances system reliability. Symmetrical droop curve shifting was employed for adjusting the converter power output. The proposed approach was validated through both HIL simulations and experiments in a real residential DC nanogrid testbed. Results demonstrate that the system can effectively limit EMS-to-converter control actions without compromising performance. Future work will focus on expanding EMS integration across multiple converters and refining inter-converter power-sharing strategies.

Acknowledgments. This work was supported in part by the European Union's Horizon 2020 research and innovation programme under the Marie Sklodowska-Curie grant agreement no. 955614, in part by the Estonian Research Council under Grant PRG1086, and in part by the Estonian Centre of Excellence in Energy Efficiency, ENER, funded by the Estonian Ministry of Education and Research under Grant TK230, and in part by the Estonian Research Council through the funding of the international multilateral partnership IMPRESS-U project "EAGER: Adaptive Infrastructure Recovery from Repeated Shocks through Resilience Stress Testing in Ukraine."

References

1. Energy performance and indoor climate | Majandus- ja Kommunikatsiooniministeerium, https://mkm.ee/en/construction-and-residential-sector/environmental-sustainability/energy-performance-and-indoor, last accessed 2025/05/22.
2. De Santana Borges, J., Freitas, C.M., Monteiro, L.F.C.: Control of DC-DC converters in DC microgrids: adaptation of virtual DC machine control. In: 2024 16th Seminar on Power Electronics and Control (SEPOC). pp. 1–6 (2024). https://doi.org/10.1109/SEPOC63090.2024.10747470.
3. Roasto, I., Blinov, A., Vinnikov, D.: Droop Control with Incorporated Dead Zone for Indirect Energy Management in DC Nanogrids. In: 2024 IEEE 21st International Power Electronics and Motion Control Conference (PEMC). pp. 1–6 (2024). https://doi.org/10.1109/PEMC61721.2024.10726394.
4. Roasto, I., Blinov, A., Vinnikov, D., Mackay, L., Jalakas, T.: DC Droop Control Strategies and Tuning Principles. In: 2023 IEEE 64th International Scientific Conference on Power and Electrical Engineering of Riga Technical University (RTUCON). pp. 1–6 (2023). https://doi.org/10.1109/RTUCON60080.2023.10412947.
5. Current/OS Technical Rules - Direct Current Distribution Redefined, https://currentos.org/technical-rules/, last accessed 2025/05/22.
6. Ali, S., Zheng, Z., Aillerie, M., Sawicki, J.-P., Péra, M.-C., Hissel, D.: A Review of DC Microgrid Energy Management Systems Dedicated to Residential Applications. Energies. 14, 4308 (2021). https://doi.org/10.3390/en14144308.
7. Rajput, A.K., Lather, J.S.: Adaptive energy management strategy for a DC microgrid using intelligent Controller. Smart Science. 13, 77–93 (2025). https://doi.org/10.1080/23080477.2024.2444756.
8. Berboucha, A., Aissou, S., Colak, I., Djermouni, K., Belkaid, A., Amirouche, E., Kayisli, K.: Energy Management of DC Microgrid-based Photovoltaic/Battery and Super Capacitor. In: 2024 13th International Conference on Renewable Energy Research and Applications (ICRERA). pp. 1316–1321 (2024). https://doi.org/10.1109/ICRERA62673.2024.10815364.
9. Safder, M.U., Hossain, M.A., Sanjari, M.J., Lu, J.: Rule-based energy management system for autonomous voltage stabilization in standalone DC microgrid. Energy Science & Engineering. 12, 4278–4296 (2024). https://doi.org/10.1002/ese3.1873.
10. Roasto, I., Blinov, A., Vinnikov, D.: Novel droop control strategy for indirect battery management in DC nanogrids. PEAS. 73, 345 (2024). https://doi.org/10.3176/proc.2024.4.03.
11. Wang, J., Dai, L., Qiao, X., Bai, B., Wu, X., Zhao, D.: Energy management strategy of microgrid energy storage unit based on adaptive droop control. In: 2022 IEEE 17th Conference on Industrial Electronics and Applications (ICIEA). pp. 1014–1018 (2022). https://doi.org/10.1109/ICIEA54703.2022.10006327.

12. Hajebrahimi, H., Kaviri, S.M., Eren, S., Bakhshai, A.: A New Energy Management Control Method for Energy Storage Systems in Microgrids. IEEE Trans. Power Electron. 35, 11612–11624 (2020). https://doi.org/10.1109/TPEL.2020.2978672.
13. Ferahtia, S., Djerioui, A., Rezk, H., Chouder, A., Houari, A., Machmoum, M.: Adaptive Droop based Control Strategy for DC Microgrid Including Multiple Batteries Energy Storage Systems. Journal of Energy Storage. 48, 103983 (2022). https://doi.org/10.1016/j.est.2022.103983.
14. Bhattar, C.L., Chaudhari, M.A.: Centralized Energy Management Scheme for Grid Connected DC Microgrid. IEEE Systems Journal. 17, 3741–3751 (2023). https://doi.org/10.1109/JSYST.2022.3231898.
15. Oussama, H., Amine, H.M., Mohamed Amine, S., Aissa, B., Abdeselem, C., Othmane, A.: Intelligent Energy Management Strategy For Multi-Sources Isolated DC-Microgrid. In: 2023 Second International Conference on Energy Transition and Security (ICETS). pp. 1–5. IEEE, Adrar, Algeria (2023). https://doi.org/10.1109/ICETS60996.2023.10410815.

Optimizing Energy Management Systems in Smart Buildings Through Practical Deployment of Edge-Based Non-Intrusive Load Monitoring

Luis E. Garcia-Marrero[1,2,*], Giovanni Petrone[1], and Eric Monmasson[2]

[1] Dipartimento di Ingegneria dell'Informazione ed Elettrica e Matematica Applicata (DIEM), University of Salerno, Fisciano, 84084, Italy
[2] Systèmes et Applications des Technologies de l'Information et de l'Energie Laboratory, CY Cergy Paris University, Cergy-Pontoise, 95031, France

Abstract. This chapter presents the practical implementation of a Non-Intrusive Load Monitoring (NILM) framework for real-time energy monitoring in residential environments. The work builds on the O2RE (Online, Real-time, Robust, and Edge-driven) algorithm, previously developed by the authors, which is optimized for execution on low-cost, resource-constrained edge devices. The system disaggregates aggregated household electricity consumption into individual appliance-level estimates, supporting energy awareness and enabling integration with Energy Management Systems (EMS). The framework was implemented on a Raspberry Pi and integrated into the open-source Home Assistant platform, allowing real-time data visualization, historical tracking, and seamless control within a smart home ecosystem. Experimental verification using real-world consumption data demonstrates that the solution operates reliably over long periods while meeting real-time processing requirements. This work confirms the feasibility of deploying NILM technology in practical residential settings through accessible hardware and open-source tools.

Keywords: Non-Intrusive Load Monitoring, Edge Computing, Residential Energy Management, Real-Time Energy Disaggregation, Smart Home Automation

1 Introduction

The building sector accounts for a significant portion of electricity consumption and greenhouse gas emissions in industrialized countries. Addressing this challenge requires more efficient energy use and better management of household electricity demand. Recent advancements in smart grid technologies have enabled detailed monitoring of consumption patterns through smart meters, demand-side management tools, and real-time data infrastructure [1]. These capabilities improve fault detection [2], enhance load forecasting [3], and support demand response strategies [4].

---

[*] This project has received funding from the European Union's Horizon 2020 research and innovation program under the Marie Skłodowska-Curie grant agreement No 955614.

Traditionally, centralized cloud computing has supported smart grid applications, but it presents limitations such as bandwidth constraints, latency, data transmission overhead, and privacy concerns [5, 6]. Edge computing (EC) addresses these challenges by processing data near its source, reducing transmission requirements and enhancing privacy through local control [6, 7]. EC also supports the use of cost-effective, resource-constrained hardware, making advanced monitoring technologies more accessible.

In this context, Non-Intrusive Load Monitoring (NILM) emerges as an effective solution for appliance-level consumption tracking without the need for individual sensors. By operating locally on edge devices, NILM enables real-time analysis, improves user awareness of energy usage, and supports energy-saving behaviors. Furthermore, NILM can be integrated into Energy Management Systems (EMS) to automate responses to demand response signals, electricity prices, and incentive programs. Manual control of appliances in response to dynamic pricing is impractical for most users, but NILM enables consumer-specific optimizations that lower energy costs while preserving comfort [8].

Various methods have been proposed to solve the NILM problem. Hidden Markov Models (HMMs) and their extensions have been widely used [9, 10], but their dependence on extensive submetered data or long training periods limits their applicability. To address these constraints, training-less approaches have gained attention. These include Integer Programming [11, 12], Graph Signal Processing [13, 14], the Population-Based Incremental Learning algorithm [15], subtractive clustering [16], and the balanced window technique [17].

Deep Learning has also become a dominant approach, with architectures based on CNNs [18], RNNs [19], and LSTMs [20]. However, their practical deployment faces three main challenges. First, generalization remains difficult due to variability in appliance behavior and the lack of labeled data across households [21, 22]. Second, the opacity of deep learning models hinders explainability and model refinement [22]. Third, even compressed models often exceed the computational limits of edge devices [23–26], and their impact on generalization performance has not been thoroughly validated.

This chapter describes the implementation of the O2RE (Online, Real-time, Robust, and Edge-driven) NILM framework, an algorithm previously proposed by the same authors [15]. O2RE is designed for real-time operation on constrained edge devices, using a dynamic structure that updates appliance state probabilities upon event detection while preserving historical and temporal information with minimal memory usage. The method also handles unknown and constantly-on loads, enhancing its robustness in real households. We deployed O2RE on a low-cost edge device and integrated it into an open-source home automation platform that ensures local control and privacy. This implementation demonstrates the feasibility of deploying NILM in practical residential energy management systems.

2 NILM O2RE Framework

The O2RE (Online, Real-time, Robust, and Edge-driven) framework, introduced in [15], focuses on the practical deployment of a real-time NILM algorithm suitable for operation at approximately 1 Hz on constrained edge devices. The method accounts for the presence of unknown loads, modeled as finite state machines or constantly-on appliances. At its core, the framework maintains a dynamic structure S_P, where each element $S_{P_{i,j}}$ represents the probability that appliance i is in state j. This structure is updated sequentially in response to detected events using a dynamic programming algorithm, allowing efficient storage of historical and temporal information.

To identify the operating state of each appliance, the structure S_P is incorporated into a state-based optimization process using the Population-Based Incremental Learning (PBIL) algorithm. Unlike traditional metaheuristics, PBIL enhances computational efficiency by evolving a single probability vector rather than a population of individual solutions. This vector is iteratively updated based on the performance of sampled solutions, reducing the computational load typically associated with approaches such as Genetic Algorithms [15].

2.1 NILM Preliminaries

The goal of the NILM problem is to estimate the real power consumption of N individual appliances at time t, denoted as $[\hat{p}_1(t), \dots, \hat{p}_N(t)]$, using only the aggregated power measurement $P(t)$. These estimates aim to approximate the actual appliance-level consumptions $[p_1(t), \dots, p_N(t)]$.

$$P(t) = \sum_{i=1}^{N} p_i\,(t) + B(t) + \eta(t) \qquad (1)$$

The aggregated power consumption $P(t)$ is composed of the power signals from N monitored appliances $p_i(t)$, a base load $B(t)$ representing the steady-state consumption of unknown appliances, and a residual term $\eta(t)$. The residual term accounts for measurement noise and the consumption of unmonitored or unmodeled loads. Each appliance is modeled using a Finite State Machine (FSM) (Figure 1), which defines a set of discrete operating states and the permissible transitions between them.

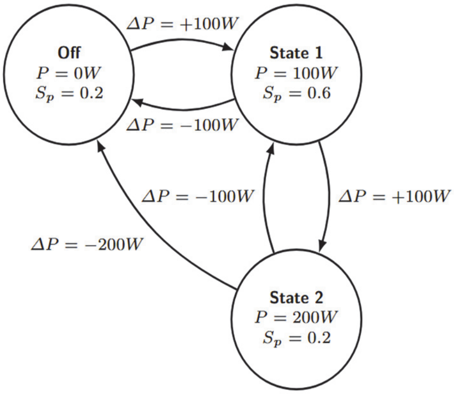

Figure 1: Finite State Machine Model. The diagram shows the power consumption for each state (P) and the probability (S_p) of being in that state at a given time t. Transitions between states are labeled with power differences (ΔP) [15].

Let $P_{i,j}$ denote the nominal power of appliance i when operating in state j, where $0 \leq j \leq M_i$ and M_i is the number of "On" states for appliance i. The estimated power consumption $\hat{p}_i(t)$ at any time t can therefore take one of the discrete values in the set $\{P_{i,0}, P_{i,1}, \dots, P_{i,M_i}\}$. Based on this formulation, the NILM problem becomes one of identifying the operating state indicator vector S that best represents the actual state of the appliances. Each element $S_{i,j}$ is defined as follows:

$$S_{i,j} = \begin{cases} 1 & \text{if appliance } i \text{ is operating in state } j \\ 0 & \text{otherwise} \end{cases} \qquad (2)$$

S.T:

$$\sum_{j=0}^{M_i} S_{i,j} = 1 \quad \text{for each appliance } i \qquad (3)$$

Constraint (3) implies that any appliance always operates exactly in one of the given states. Equation (1) can now be rewritten in terms of $S_{i,j}$ as follows:

$$P(t) = \sum_{i=1}^{N} \sum_{j=0}^{M_i} S_{i,j}(t) P_{i,j} + B(t) + e(t) \qquad (4)$$

Here, $e(t)$ represents the total error term, which includes the residual $\eta(t)$ (as defined in Equation 1) along with the additional error introduced by the estimation of $p_i(t)$. A straightforward criterion for determining $S_{i,j}$ is to minimize the absolute value of the error term $|e(t)|$:

$$|e(t)| = |P(t) - B(t) - \sum_{i=1}^{N} \sum_{j=0}^{M_i} S_{i,j} P_{i,j}| \qquad (5)$$

An important discrimination feature for NILM algorithms operating at sampling frequencies around 1 Hz is the power difference between consecutive steady states. Let $\overline{P}_{\text{curr}}$ denote the power value of the current steady state and $\overline{P}_{\text{prev}}$ the value of the previous steady state. The edge E is then defined as:

$$E = \overline{P}_{\text{curr}} - \overline{P}_{\text{prev}} \qquad (6)$$

Given the sampling frequency used, it is reasonable to assume that the edge E results from a state change in a single appliance. Under this assumption, E can serve as a key discrimination feature. However, due to transient spikes and fluctuations in the signal, the reliability of this feature strongly depends on the effectiveness of the steady-state detection method applied.

2.2 O2RE: High-level architecture

O2RE framework evolves a dynamic structure S_P, where $S_{P_{i,j}}$ denotes the probability that appliance i is in state j. Unlike a fixed-dimension matrix, S_P supports a variable number of states per appliance. S_P is sequentially updated upon detecting a significant edge (event-based) or inconsistencies with the total aggregated power. After updating S_P an appliance might still be associated with multiple states with varying probabilities. To define a unique state for each appliance, S_P is integrated into a state-based optimization algorithm by employing the total matching criterion and possibly other additional criteria. The functioning of the O2RE framework is depicted in Algorithm 1, as originally presented in [15].

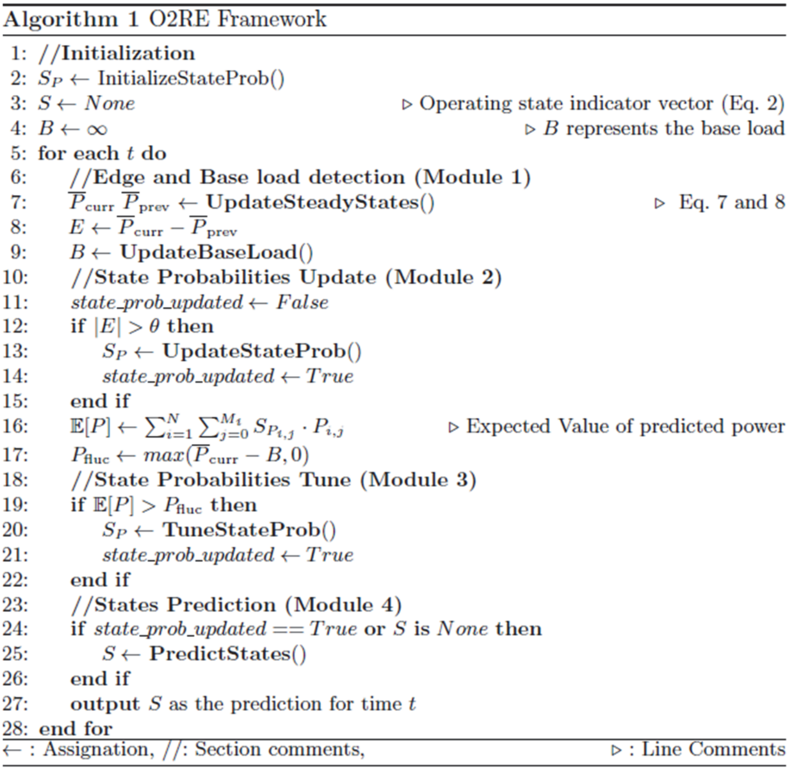

Algorithm 1 O2RE Framework

```
//Initialization
$S_P \leftarrow$ InitializeStateProb()
$S \leftarrow None$                                    ▷ Operating state indicator vector (Eq. 2)
$B \leftarrow \infty$                                  ▷ $B$ represents the base load
for each $t$ do
    //Edge and Base load detection (Module 1)
    $\overline{P}_{\text{curr}}\ \overline{P}_{\text{prev}} \leftarrow$ UpdateSteadyStates()       ▷ Eq. 7 and 8
    $E \leftarrow \overline{P}_{\text{curr}} - \overline{P}_{\text{prev}}$
    $B \leftarrow$ UpdateBaseLoad()
    //State Probabilities Update (Module 2)
    $state\_prob\_updated \leftarrow False$
    if $|E| > \theta$ then
        $S_P \leftarrow$ UpdateStateProb()
        $state\_prob\_updated \leftarrow True$
    end if
    $\mathbb{E}[P] \leftarrow \sum_{i=1}^{N} \sum_{j=0}^{M_i} S_{P_{i,j}} \cdot P_{i,j}$     ▷ Expected Value of predicted power
    $P_{\text{fluc}} \leftarrow max(\overline{P}_{\text{curr}} - B, 0)$
    //State Probabilities Tune (Module 3)
    if $\mathbb{E}[P] > P_{\text{fluc}}$ then
        $S_P \leftarrow$ TuneStateProb()
        $state\_prob\_updated \leftarrow True$
    end if
    //States Prediction (Module 4)
    if $state\_prob\_updated == True$ or $S$ is $None$ then
        $S \leftarrow$ PredictStates()
    end if
    output $S$ as the prediction for time $t$
end for
```

$\leftarrow$: Assignation, //: Section comments, ▷ : Line Comments

2.3 O2RE: Low level design

Edge Detection (Module 1). The edge detection algorithm begins by assessing whether the system is likely in a steady state, taking into account the power grid noise variance σ_g^2. For this purpose, the three-point method is employed [16], which is both simple and effective. Given the current aggregated power sample $P(t)$, the method computes the local average power $\mu_P(t)$ and the local variance $\sigma_P^2(t)$ around $\mu_P(t)$.

$$\mu_P(t) = \frac{1}{3}\sum_{i=1}^{3} P\,(t - i\Delta t) \qquad (7)$$

$$\sigma_P^2(t) = \frac{1}{3}\sum_{i=1}^{3} (P(t - i\Delta t) - \mu_P(t))^2\,. \qquad (8)$$

If $\sigma_P(t) < \sigma_g$, the system is likely in a steady state, and the steady state values are updated accordingly: $\overline{P}_{\text{prev}} = \overline{P}_{\text{curr}}$ and $\overline{P}_{\text{curr}} = \mu_P(t)$. This procedure forms the core of the UpdateSteadyStates function in Algorithm 1. A significant edge is then identified when Equation 6 yields $|E| > \theta$, where θ is a predefined threshold satisfying $\theta \geq \sigma_g$.

Base load detection (Module 1). Accurate estimation of the base load is essential for improving the performance of NILM algorithms, especially those based on state modeling. The base load reflects the steady-state consumption of appliances that operate continuously. It is estimated sequentially, as outlined in Algorithm 2 [15].

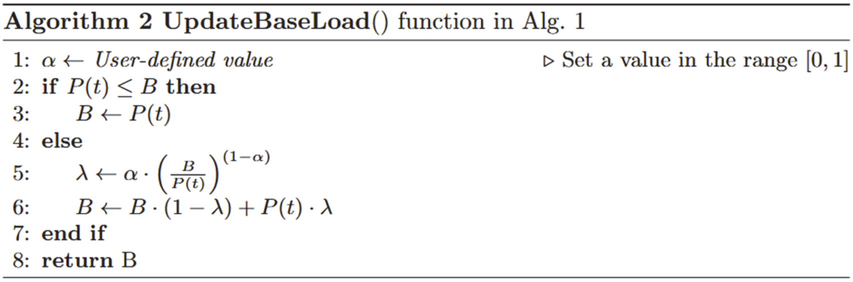

Algorithm 2 UpdateBaseLoad() function in Alg. 1

```
$\alpha \leftarrow$ User-defined value                ▷ Set a value in the range $[0, 1]$
if $P(t) \leq B$ then
    $B \leftarrow P(t)$
else
    $\lambda \leftarrow \alpha \cdot \left(\frac{B}{P(t)}\right)^{(1-\alpha)}$
    $B \leftarrow B \cdot (1 - \lambda) + P(t) \cdot \lambda$
end if
return B
```

Probabilistic model for power state transitions in FSM appliances (Module 2). If the random fluctuations of the power transition in load i from state j to state k is represented with the random variable $\Delta P_{i,j,k}$, we define the transformed random variable $\Delta\tilde{P}_{i,j,k}$ as:

$$\Delta\tilde{P}_{i,j,k} = \operatorname{sgn}(\Delta P_{i,j,k}) \cdot \ln(|\Delta P_{i,j,k}|) \qquad (9)$$

$$\mu_{\Delta\tilde{P}_{i,j,k}} = \operatorname{sgn}(P_{i,k} - P_{i,j}) \cdot \ln(|P_{i,k} - P_{i,j}|) \qquad (10)$$

$$\Delta\tilde{P}_{i,j,k} \sim \mathcal{N}(\mu_{\Delta\tilde{P}_{i,j,k}}, \sigma^2_{\Delta\tilde{P}}) \qquad (11)$$

Where $\operatorname{sgn}(.)$ is the sign of the given argument. Here it is assumed $\Delta\tilde{P}_{i,j,k}$ to be normal distributed with mean $\mu_{\Delta\tilde{P}_{i,j,k}}$ and variance $\sigma^2_{\Delta\tilde{P}}$. On the other hand, it is considered a fixed value of the variance $\sigma^2_{\Delta\tilde{P}}$, and this is a tunable parameter of the algorithm.

Likelihood calculation given an appliance state transition (Module 2). Once an edge E is detected, the objective is to assign a likelihood value $L(E \mid T_{ijk})$ to each appliance state transition T_{ijk}. Based on the model described in Equations 9 to 11, and by normalizing each distribution to the standard normal distribution $\mathcal{N}(0,1)$ using $\tilde{x} = \frac{x-\mu}{\sigma}$, is obtained:

$$x_{ijk} = \frac{\tilde{E} - \mu_{\Delta\tilde{P}_{ijk}}}{\sigma_{\Delta\tilde{P}}} \qquad (12)$$

Where:

$$\tilde{E} = \operatorname{sgn}(E)\ln(|E|) \qquad (13)$$

By evaluating x_{ijk} in the probability density function of the standard normal distribution, the corresponding likelihoods are computed as follows:

$$L(E|T_{ijk}) = \frac{1}{\sqrt{2\pi}} e^{-\frac{x^2_{ijk}}{2}} \qquad (14)$$

Likelihood of unknown state transition (Module 2). It is assumed that unknown loads may be present in the aggregated power signal. Consequently, a detected change E might result from a transition in an unmonitored appliance rather than from any of the N monitored devices. To assign a likelihood to such unknown transitions, this work adopts the concept of an improper constant density defined over the entire Euclidean space, as shown in Equation 15.

$$L(E|UnkTrans) = \delta \qquad (15)$$

The constant $\delta > 0$ represents the improper constant density and is a configurable parameter of the algorithm. The underlying idea is that transitions located in low-density regions, where $L(E \mid T_{ijk}) < \delta$, are unlikely to explain the observed edge E. In such cases, it is more plausible that the edge was caused by a different, unmonitored transition.

Conditional probability calculation (Module 2). Once the likelihoods are computed, a probability is assigned to each possible event, conditioned on the observed edge E. The set of events includes all possible state transitions of the monitored appliances as well as the unknown transition event. Let $\Pr(T_{ijk} \mid E)$ denote the probability that the transition of appliance i from state j to state k caused the edge E, and $\Pr(\mathrm{UnkTrans} \mid E)$ the probability that the change was due to an unknown load. Applying Bayes' theorem, we obtain:

$$Pr(T_{ijk}|E) = \frac{L(E|T_{ijk})Pr(T_{ijk})}{\sum_{\substack{\forall i'j'k' \\ j'\neq k'}} L(E|T_{i'j'k'})Pr(T_{i'j'k'}) + UTT} \qquad (16)$$

Here, $\mathrm{UTT} = L(E \mid \mathrm{UnkTrans}) \cdot \Pr(\mathrm{UnkTrans})$ represents the unknown transition term, and $\Pr(T_{ijk})$ and $\Pr(\mathrm{UnkTrans})$ are the prior probabilities. In Equation 16, the indices i', j', k' iterate over all appliances and their possible state transitions. The denominator in Equation 16 is a direct application of the Law of Total Probability, since the set of all state transitions and the unknown transition event are mutually exclusive and collectively exhaustive. Initial values for $\Pr(T_{ijk})$ and $\Pr(\mathrm{UnkTrans})$ can be set to $\frac{1}{M+1}$, where M is the total number of possible state transitions across all appliances, implying an equal prior probability for each event.

Updating sequentially the appliance state probabilities (Module 2). In (17) is shown the equation to calculate the updated state probabilities sequentially.

$$\begin{aligned} S'_{P_{i,j}} &= [\sum_{j\neq k} Pr(T_{ikj}|E) \cdot S_{P_{i,k}}] \\ &+[(1 - \sum_{j\neq k} Pr(T_{ijk}|E)) \cdot S_{P_{i,j}}] \end{aligned} \qquad (17)$$

The first term in Equation 17 computes the probability that appliance i transitions to state j from any other state k. The second term represents the probability that appliance i remains in state j without any change. By assigning $S_{P_{i,j}} = S'_{P_{i,j}}$, the updated state probabilities are stored in $S_{P_{i,j}}$.

State Probabilities Tuning (Module 3). The tuning phase is designed to keep S_P robust in the presence of anomalous conditions. In this work, tuning is triggered when the expected power consumption $\mathbb{E}[P]$ exceeds the fluctuating power P_{fluc}. The fluctuating power P_{fluc} is defined as the maximum between zero and the difference between the current steady-state power $\overline{P}_{\text{curr}}$ and the base load B. In essence, P_{fluc} represents the non-constant portion of the total power, which is expected to encompass the consumption of all FSM-modeled appliances.
As we are assuming that the appliances are independent, the expected value of power can be defined as

$$\mathbb{E}[P] = \sum_{i=1}^{N} \sum_{j=0}^{M_i} S_{P_{i,j}} \cdot P_{i,j} \qquad (18)$$

If $\mathbb{E}[P] > P_{\text{fluc}}$, this suggests an overestimation of power consumption, indicating that some appliances may have been incorrectly assigned to an on-state. To address this, S_P is adjusted to ensure that $\mathbb{E}[P] \leq P_{\text{fluc}}$, while minimizing deviation from the original state distribution. The deviation is quantified using relative entropy (also known as Kullback–Leibler divergence) [27] between the original and the updated S_P.

States Prediction (Module 4). We propose a modified Population-Based Incremental Learning algorithm (PBIL) [28] for this step. The standard PBIL algorithm was designed for binary vector encoding but can be extended to consider integer vector encoding. In this case, the probability vector is defined as: $\overrightarrow{Pr} = [\overrightarrow{Pr_1}, \ldots, \overrightarrow{Pr_N}]$, where $\overrightarrow{Pr_i} = [p_1, \ldots, p_{M_i}]$ (M_i is the length of the vector $\overrightarrow{Pr_i}$), and $\sum_{j=1}^{M_i} p_j = 1$. PBIL is an iterative algorithm in which a set pop of S_z solutions is sampled from the probability vector $\overrightarrow{Pr}$ each iteration. Then, the probability vector $\overrightarrow{Pr}$ is learned toward the best sample $\vec{B}$ in pop, according to the problem-specific fitness function. To maintain diversity, a mutation process is carried out, learning the vector $\overrightarrow{Pr_i}$ towards a neutral vector $\vec{M_i}$ with a certain probability $\overrightarrow{p_m}$, and the cycle is repeated. Here we consider the Total Matching Criterion and the state probabilities S_P as the bases for the fitness function. The first criterion considered is the minimization of $|e(t)|$ in (5). The second criterion is the maximization of the probability of a given solution S. As we are assuming that appliances are independent, this probability can be defined as $Pr = \prod_{i=1}^{N} [\sum_{j=0}^{M_i} S_{i,j} \cdot S_{P_{i,j}}]$. An equivalent computationally robust formulation of this criterion is the minimization of minus the logarithm of the probability (19):

$$-\ln(Pr) = -[\sum_{i=1}^{N} \ln(\sum_{j=0}^{M_i} S_{i,j} \cdot S_{P_{i,j}})] \qquad (19)$$

To select the best sample from the population pop, two ranking arrays are defined based on distinct evaluation criteria: $rank\_e$ for error minimization and $rank\_p$ for power plausibility. Specifically,

-$rank\_e[i]$ denotes the rank of the i-th sample $pop[i]$ when the population is sorted by the first criterion in ascending order.
-$rank\_p[i]$ denotes the rank of $pop[i]$ when sorted by the second criterion in ascending order.

The best sample $\vec{B}$ from the population is determined by selecting the individual $pop[i]$ that minimizes the maximum of its ranks across the two evaluation criteria. Formally, this is expressed as:

$$\vec{B} = pop[i] \quad \text{where} \quad i = \underset{i}{\operatorname{argminmax}}(rank\_e[i], rank\_p[i]) \qquad (20)$$

Algorithm 3 presents the pseudocode for the state prediction module, which represents the base of the function PredictStates in Algorithm 1 [15].

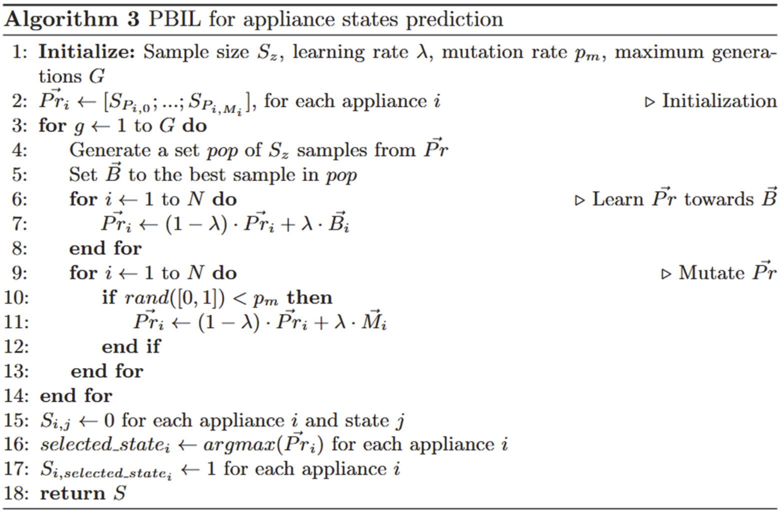

Algorithm 3 PBIL for appliance states prediction

```
Initialize: Sample size $S_z$, learning rate $\lambda$, mutation rate $p_m$, maximum generations $G$
$\vec{Pr_i} \leftarrow [S_{P_{i,0}}; ...; S_{P_{i,M_i}}]$, for each appliance $i$    ▷ Initialization
for $g \leftarrow 1$ to $G$ do
    Generate a set $pop$ of $S_z$ samples from $\vec{Pr}$
    Set $\vec{B}$ to the best sample in $pop$
    for $i \leftarrow 1$ to $N$ do    ▷ Learn $\vec{Pr}$ towards $\vec{B}$
        $\vec{Pr_i} \leftarrow (1-\lambda) \cdot \vec{Pr_i} + \lambda \cdot \vec{B_i}$
    end for
    for $i \leftarrow 1$ to $N$ do    ▷ Mutate $\vec{Pr}$
        if $rand([0,1]) < p_m$ then
            $\vec{Pr_i} \leftarrow (1-\lambda) \cdot \vec{Pr_i} + \lambda \cdot \vec{M_i}$
        end if
    end for
end for
$S_{i,j} \leftarrow 0$ for each appliance $i$ and state $j$
$selected\_state_i \leftarrow argmax(\vec{Pr_i})$ for each appliance $i$
$S_{i,selected\_state_i} \leftarrow 1$ for each appliance $i$
return $S$
```

3 O2RE: Practical implementation in an Edge Device

This section presents the practical implementation of the O2RE framework in an edge device, which provides real-time information to the users about some appliances of interest. The integration of this NILM algorithm in an open-source framework for home automation is also described, designed to be an Internet of Things ecosystem-independent integration platform and central control system for smart home devices, with a focus on local control and privacy. This integration facilitates the use of the NILM technology in real cases and motivates the development of future integrations to accomplish important goals in Energy Management Systems.

3.1 Block diagram of the prototype

A block diagram of the real-time NILM prototype is presented in Figure 2, from Aggregated Power to Appliance-Level Disaggregation:

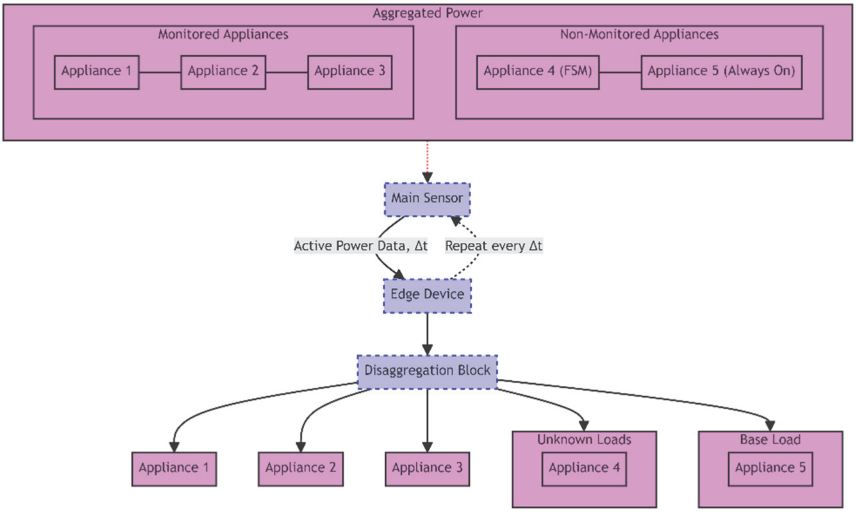

Figure 2: Non-Intrusive Load Monitoring (NILM) Process: From Aggregated Power to Appliance-Level Disaggregation

A detailed explanation of the diagram is provided in the following. The section Monitored Appliances (FSM) represents the set of N monitored appliances, each labeled as "Appliance 1", "Appliance 2", and so on, up to "Appliance 3" in this case. These appliances are finite state machines (FSMs). Each appliance's power consumption contributes to the aggregated power measurement. The block Non-Monitored Appliances is divided into two subcategories: Appliance 4 (FSM), is an example of an appliance that operates with distinguishable states but is not included in the monitored set. Its consumption is part of the aggregated power, yet is not individually tracked or estimated by the NILM process. Appliance 5 (Always On) represents appliances contributing to the base load B(t). These are typically always-on devices whose consumption is steady and contributes a constant load over time. Main Sensor is the central device capturing the aggregated power consumption P(t), which is the sum of the power from all appliances (monitored and non-monitored), the base load, and any residual noise or unaccounted-for consumption. Edge Device (Disaggregation

Block): Acts as the computational heart of the NILM system. It continually fetches the aggregated active power from the Main Sensor with frequency Δt and employs algorithms to disaggregate this data in real-time. Each monitored appliance's estimated consumption is output separately, allowing for detailed analysis and monitoring of individual appliances. Unknown Loads represents the disaggregated component attributed to FSM appliances not monitored. This block would include the estimated consumption of "Appliance 4" in this context. Base Load reflects the constant power consumption part of the aggregated signal, including "Appliance 5 (Always On)" in this diagram. This load is steady and contributes to the overall consumption without significant variation over short periods.

3.2 Integration in an open-source framework for home automation

Integrating NILM into home automation frameworks is a key step towards enhancing its practical application. For our integration, we have selected Home Assistant as the home automation platform of choice. This decision is based on its open-source nature and extensive compatibility with a wide array of devices and protocols, enabling NILM to reach a broader audience. Moreover, for users who have already integrated Home Assistant into their homes, the addition of our NILM algorithm does not require any extra hardware investments. This aspect is crucial, as it lowers the barriers to adoption and integration, making it feasible for more users to take advantage of NILM technology.

Home Assistant (https://www.home-assistant.io/) is an open-source home automation platform designed to control and monitor a wide array of smart home devices. Developed with privacy and local control in mind, it runs locally, ensuring that your data remains within your home and does not rely on cloud services. This platform supports thousands of smart devices across various brands and ecosystems, allowing users to seamlessly integrate lighting systems, thermostats, smart plugs, sensors, cameras, and more. One of the core strengths of Home Assistant is its highly customizable nature. Users can create unique automations and scripts to make devices work together based on time, location, sensor readings, and other triggers. It features a user-friendly interface that can be accessed through web browsers on desktops, tablets, and smartphones, enabling users to manage their smart home from anywhere.

3.3 Hardware of the prototype

The prototype for our NILM system is built upon the versatile and cost-effective Raspberry Pi platform, specifically utilizing the Raspberry Pi 3B and 4 models. These selections are based on several key attributes that align with the requirements of NILM processes, namely their computational capabilities, connectivity options, and the feasibility of hosting Home Assistant directly on the device. Within our prototype block diagram, the Raspberry Pi functions as the Edge Device that is responsible for the real-time processing of aggregated power data received from the Main Sensor Fig. 2. In this case, the connection to the Main Sensor can be established through GPIO pins for direct measurement or via wireless protocols supported by smart meters.

While our NILM prototype is designed around the Raspberry Pi 3B and 4 models due to their exceptional balance of cost-effectiveness, performance, and direct compatibility with Home Assistant, it is noteworthy that the architecture of our system permits the use of other computing units supported by Home Assistant as well. This flexibility in hardware selection allows for the adaptation of our NILM system to various operational needs and preferences, expanding its applicability and potential user base.

3.4 Experimental verification of the prototype

The experimental verification of our NILM prototype utilized the Raspberry Pi 3 and Raspberry Pi 4 models. The aim was to assess the system's ability to disaggregate power consumption effectively and to ensure stable, long-term operation. We also verified the system's real-time performance to confirm it meets the requirements for timely data processing. For this reason, our prototype was tested for a continuous period of one month, simulating a main sensor that sends data at a frequency of 6 seconds.

Simulation of the Main Sensor. To simulate real-world energy consumption data for our experiments, we used the UK-DALE dataset [29], which contains detailed energy usage data from UK households. Instead of relying on physical sensors, we simulated a main sensor by wirelessly transmitting this real, publicly available data to the Home Assistant OS running on the Raspberry Pi. This method allowed us to evaluate the prototype under various conditions and scenarios, closely mimicking real household energy consumption patterns. For this proposes, an addon was created in Home Assistant that implements a web server that listens to queries. Through a specific endpoint, the server returns the aggregated active power coming from the UK-DALE dataset, that better matches the actual time of the server. Then, it was created a REST sensor in Home Assistant that uses this endpoint to fetch each 6 seconds a value of the active power (6s is the same frequency as UKDALE-DATASET).

NILM Integration with Home Assistant. A significant aspect of our experimental setup was the integration of the NILM prototype with Home Assistant. By running Home Assistant directly on the Raspberry Pi, we were able to create virtual sensors within the platform to report the NILM disaggregation results. This integration facilitated a seamless flow of information, where the disaggregated energy consumption data for each monitored appliance, as well as for the base load and unknown loads, was estimated and displayed within Home Assistant in real time. The creation of virtual sensors in Home Assistant for each appliance of interest allowed us to not only monitor their power consumption in real-time but also to utilize this data for further automation and energy management tasks within the smart home environment. This level of integration highlights the potential of NILM technologies to enhance energy awareness and efficiency in residential settings.

Experimental Outcomes. The initial step to replicate the experimental prototype is selecting and installing the appropriate operating system for your hardware. Figure 3 illustrates the Raspberry Pi Imager utility, a user-friendly tool designed to simplify the installation of different operating systems on a Raspberry Pi. Highlighted within this tool is the option to install Home Assistant. Whether you are configuring a Raspberry Pi 4/400 or a Raspberry Pi 3, the Imager provides a straightforward path to embedding Home Assistant into your hardware.

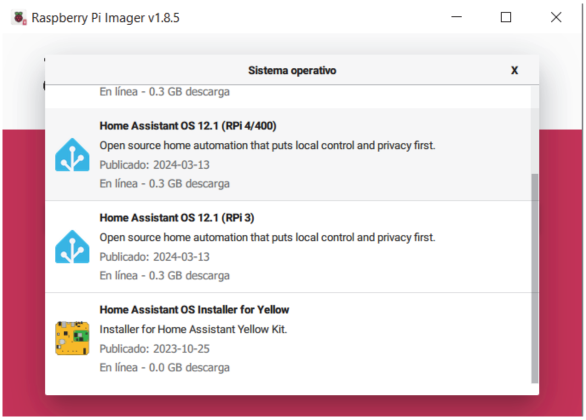

En línea - 0.3 GB descarga

Home Assistant OS 12.1 (RPi 4/400)
Open source home automation that puts local control and privacy first.
Publicado: 2024-03-13
En línea - 0.3 GB descarga

Home Assistant OS 12.1 (RPi 3)
Open source home automation that puts local control and privacy first.
Publicado: 2024-03-13
En línea - 0.3 GB descarga

Home Assistant OS Installer for Yellow
Installer for Home Assistant Yellow Kit.
Publicado: 2023-10-25
En línea - 0.0 GB descarga

Figure 3: Installation of Home Assistant OS for a Raspberry Pi

We then connected the Raspberry Pi to a router (Figure 4), in such a way that by connecting devices as phones, tablets, and laptops to the Wi-Fi created in the router, we can visualize and control the Home Assistant running environment.

Figure 4: Raspberry Pi unit connected to a router, serving as a central hub for smart home automation and energy monitoring tasks.

Once you have access to the Home Assistant OS, the next step is to install the NILM integration into the /config/custom_components folder. For this, it is necessary to have the Command Prompt addon or the Visual Studio Code addon installed. During the installation, the user must first configure the integration. For this, we provide an easy-to-use user interface shown in Figure 5.

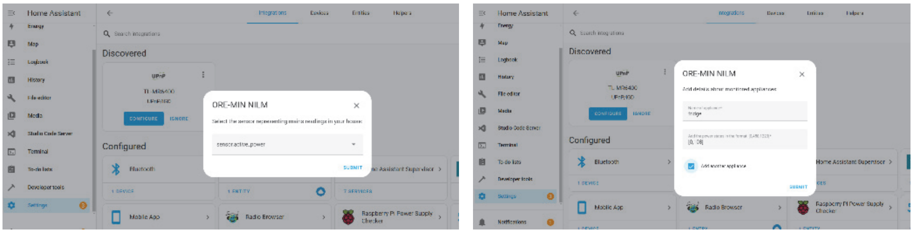
ORE-MIN NILM

Select the sensor representing mains readings in your house

sensor.active_power

SUBMIT

ORE-MIN NILM

Add details about monitored appliances

fridge

[0, 108]

☑ Add another appliance

SUBMIT

(a): Details about monitored appliances (b): Sensor representing mains readings

Figure 5: Configuration of the NILM integration

When the NILM integration is installed and running, the user can visualize in real time, the power consumption of the configured appliances in the Home Assistant Dashboard. In addition, we provide a sensor for the Base Load and other for the Unknown Applianes that can also be visualized (Figure 6(a)). The integration also allows the user to inspect the power consumption history for each monitored appliance as shown in Figure 6(b) and Figure 6(c). By examining the historical power consumption data, users can better understand how their behaviors impact their energy bills, allowing them to make informed decisions about where to cut back on usage to save on costs.

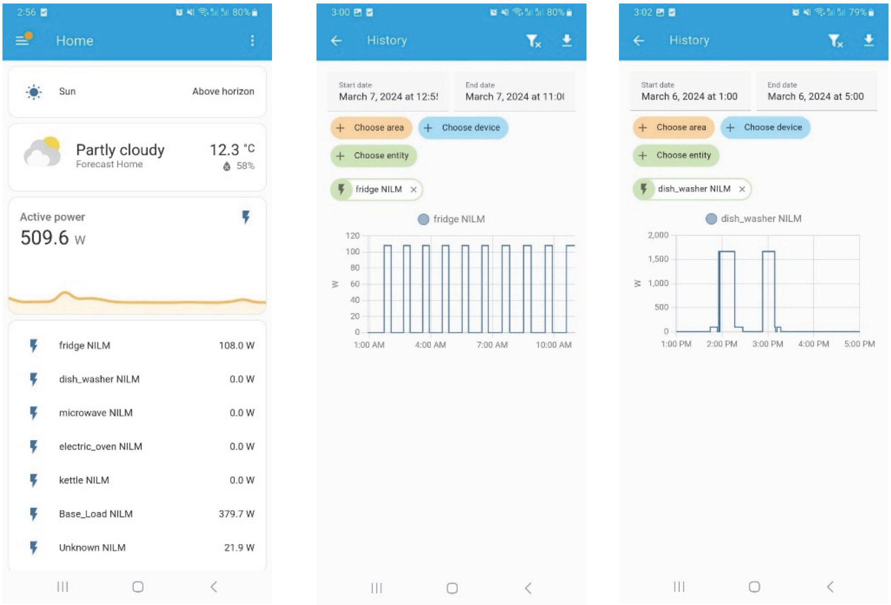
Sun Above horizon

Partly cloudy 12.3 °C
Forecast Home 58%

Active power
509.6 W

fridge NILM	108.0 W
dish_washer NILM	0.0 W
microwave NILM	0.0 W
electric_oven NILM	0.0 W
kettle NILM	0.0 W
Base_Load NILM	379.7 W
Unknown NILM	21.9 W

Start date March 7, 2024 at 12:5!
End date March 7, 2024 at 11:0(

fridge NILM

Start date March 6, 2024 at 1:00
End date March 6, 2024 at 5:00

dish_washer NILM

(a):Real-Time Information of Power Consumption. (b):NILM History of the Fridge (c):NILM History of the Dish Washer

Figure 6: Home Assistant Information

In addition to the visualization of the active power in real time for each monitored appliance, the user can also visualize the flow of energy in their homes. In the Energy section inside Home Assistant, it can be observed the total energy as well as the energy for each monitored device (Figure 7). By making energy consumption data accessible and easy to understand, users can become more energy-conscious, often leading to behavior changes that prioritize energy efficiency.

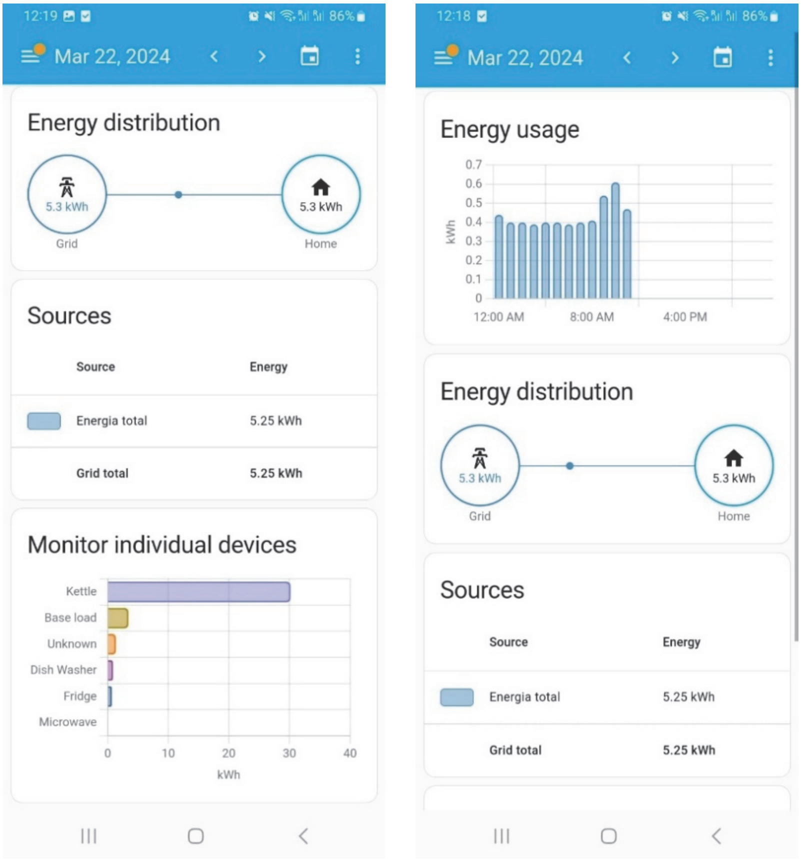

Source	Energy
Energia total	5.25 kWh
Grid total	5.25 kWh

Source	Energy
Energia total	5.25 kWh
Grid total	5.25 kWh

(a): Energy Usage and Distribution (b): Energy Distribution and Sources

Figure 7: Total Energy and Individual Appliances Energy

Computational capabilities. An experimental comparison with state-of-the-art methods of the performance capabilities of the proposed algorithm was presented in the original paper [15]. Here, we are going to concentrate on the computational capabilities of the algorithm and verify its capabilities for real-time feedback to the user. For this purpose, it was measured the running time for each time step, for an instance of the algorithm running on a Raspberry Pi 3 with Home Assistant. Raspberry Pi 3 is the edge device with less computational capabilities of the analyzed.

Table 1 presents the performance Analysis of the NILM Algorithm Across Normal and Critical Detection Intervals. This table summarizes the mean running times under regular conditions and during critical edge detection events (running time > 0.5 seconds).

Table 1: Timing Statistics with Confidence Intervals

Statistic	**Time (seconds)**
Mean (All)	0.0149
Mean (> 0.5 s)	1.1666
95% Confidence Interval Lower Bound (All)	0.0140
95% Confidence Interval Upper Bound (All)	0.0158
95% Confidence Interval Lower Bound (> 0.5 s)	1.1484
95% Confidence Interval Upper Bound (> 0.5 s)	1.1849

Table 1 presents an analysis of the NILM algorithm running times, with a focus on its performance during critical situations where an edge is detected. An edge signifies a notable change in energy consumption, triggering the algorithm to update its predictions. This updating process is the most computationally intensive, resulting in longer running times. To accurately reflect the algorithm’s performance, especially in these key moments, we specifically highlight the mean running time for instances exceeding 0.5 seconds. This approach ensures a comprehensive understanding of how the algorithm behaves when it is most needed, offering insights into its efficiency and responsiveness during essential prediction updates.

The overall mean running time of approximately 0.0149 seconds indicates that, under normal conditions, the NILM algorithm operates with high efficiency. However, the analysis also highlights instances where the running time exceeds 0.5 seconds, notably when an edge is detected, and the algorithm updates its predictions. These instances, while less frequent, are critically important as they reflect the algorithm’s response to significant changes in energy consumption patterns. The mean running time for these instances is around 1.1666 seconds, indicating that while the algorithm takes longer to process these significant events, it still does so in a fast manner, and the method can handle frequency in the order of 1.5 seconds in a Raspberry Pi 3 running Home Assistant. These results suggest that our method is well-suited for real-time monitoring.

The inclusion of a 95% confidence interval for both the general running times and those exceeding 0.5 seconds adds a layer of statistical robustness to our analysis. The narrow confidence interval for the overall running times underscores the reliability of the

NILM algorithm's performance under standard operating conditions. In contrast, the specific analysis of running times over 0.5 seconds provides a focused understanding of the algorithm's behavior during important moments of energy consumption change.

4 Conclusion

This work demonstrates the practical deployment of an edge-based NILM system as an effective solution for optimizing energy management in smart buildings. The O2RE framework, previously developed by the authors, was implemented on low-cost hardware and integrated into the Home Assistant platform, enabling real-time appliance-level monitoring without reliance on cloud services or submetered training data.

The system was tested on Raspberry Pi 3 and 4 devices, showing reliable and stable operation over a one-month period using real-world data from the UK-DALE dataset. The NILM integration within Home Assistant provided live monitoring, historical tracking, and visualization of energy use, allowing users to better understand and manage their consumption.

Performance evaluation showed that the algorithm maintained a low average processing time of 0.015 seconds under normal conditions, and around 1.17 seconds during critical appliance switching events. These results confirm that the method supports real-time operation even on constrained edge devices.

Overall, the implementation confirms the feasibility of embedding NILM into residential energy systems. Its flexibility, compatibility with home automation platforms, and accessibility through low-cost hardware highlight its potential for broader adoption in real-world applications.

Acknowledgments. This project has received funding from the European Union's Horizon 2020 research and innovation program under the Marie Skłodowska-Curie grant agreement No 955614.

References

1. Thomas, D., Deblecker, O., Ioakimidis, C.S.: Optimal operation of an energy management system for a grid-connected smart building considering photovoltaics' uncertainty and stochastic electric vehicles' driving schedule. Applied Energy. 210, 1188–1206 (2018). https://doi.org/10.1016/j.apenergy.2017.07.035.
2. Chakraborty, S., Das, S.: Application of smart meters in high impedance fault detection on distribution systems. IEEE Transactions on Smart Grid. 10, 3465–3473 (2019). https://doi.org/10.1109/TSG.2018.2828414.
3. Brucke, K., Arens, S., Telle, J.-S., Steens, T., Hanke, B., Maydell, K. von, Agert, C.: A non-intrusive load monitoring approach for very short-term power predictions in commercial

buildings. Applied Energy. 292, 116860 (2021). https://doi.org/10.1016/j.apenergy.2021.116860.

4. Huang, Y., Wang, L., Guo, W., Kang, Q., Wu, Q.: Chance constrained optimization in a home energy management system. IEEE Transactions on Smart Grid. 9, 252–260 (2018). https://doi.org/10.1109/TSG.2016.2550031.
5. Feng, C., Wang, Y., Chen, Q., Ding, Y., Strbac, G., Kang, C.: Smart grid encounters edge computing: Opportunities and applications. Advances in Applied Energy. 1, 100006 (2021). https://doi.org/10.1016/j.adapen.2020.100006.
6. Liu, Y., Yang, C., Jiang, L., Xie, S., Zhang, Y.: Intelligent edge computing for IoT-based energy management in smart cities. IEEE Network. 33, 111–117 (2019). https://doi.org/10.1109/mnet.2019.1800254.
7. Kumari, P., Mishra, R., Gupta, H.P., Dutta, T., Das, S.K.: An energy efficient smart metering system using edge computing in LoRa network. IEEE Transactions on Sustainable Computing. 7, 786–798 (2022). https://doi.org/10.1109/tsusc.2021.3049705.
8. Cimen, H., Cetinkaya, N., Vasquez, J.C., Guerrero, J.M.: A microgrid energy management system based on non-intrusive load monitoring via multitask learning. IEEE Transactions on Smart Grid. 12, 977–987 (2021). https://doi.org/10.1109/tsg.2020.3027491.
9. Makonin, S., Popowich, F., Bajić, I.V., Gill, B., Bartram, L.: Exploiting HMM sparsity to perform online real-time nonintrusive load monitoring. IEEE Transactions on Smart Grid. 7, 2575–2585 (2016). https://doi.org/10.1109/TSG.2015.2494592.
10. Kumar, P., Abhyankar, A.R.: A time efficient factorial hidden markov model based approach for non-intrusive load monitoring. IEEE Transactions on Smart Grid. 1–1 (2023). https://doi.org/10.1109/TSG.2023.3245019.
11. Dash, S., Sodhi, R., Sodhi, B.: An appliance load disaggregation scheme using automatic state detection enabled enhanced integer programming. IEEE Transactions on Industrial Informatics. 17, 1176–1185 (2021). https://doi.org/10.1109/tii.2020.2975810.
12. Balletti, M., Piccialli, V., Sudoso, A.M.: Mixed-integer nonlinear programming for state-based non-intrusive load monitoring. IEEE Transactions on Smart Grid. 13, 3301–3314 (2022). https://doi.org/10.1109/tsg.2022.3152147.
13. He, K., Stankovic, L., Liao, J., Stankovic, V.: Non-intrusive load disaggregation using graph signal processing. IEEE Transactions on Smart Grid. 9, 1739–1747 (2018). https://doi.org/10.1109/tsg.2016.2598872.
14. Zhao, B., Li, X., Luan, W., Liu, B.: Apply graph signal processing on NILM: An unsupervised approach featuring power sequences. Sensors. 23, 3939 (2023). https://doi.org/10.3390/s23083939.
15. Garcia-Marrero, L.E., Monmasson, E., Petrone, G.: Online real-time robust framework for non-intrusive load monitoring in constrained edge devices. Applied Energy. 378, 124814 (2025). https://doi.org/10.1016/j.apenergy.2024.124814.
16. Henao, N., Agbossou, K., Kelouwani, S., Dubé, Y., Fournier, M.: Approach in nonintrusive type i load monitoring using subtractive clustering. IEEE Transactions on Smart Grid. 8, 812–821 (2017). https://doi.org/10.1109/TSG.2015.2462719.
17. Liu, B., Luan, W., Yang, J., Yu, Y.: The balanced window-based load event optimal matching for NILM. IEEE Transactions on Smart Grid. 13, 4690–4703 (2022). https://doi.org/10.1109/tsg.2022.3179440.
18. Zhang, C., Zhong, M., Wang, Z., Goddard, N., Sutton, C.: Sequence-to-point learning with neural networks for non-intrusive load monitoring. Proceedings of the AAAI Conference on Artificial Intelligence. 32, (2018). https://doi.org/10.1609/aaai.v32i1.11873.
19. CAVDAR, I.H., FARYAD, V.: New design of a supervised energy disaggregation model based on the deep neural network for a smart grid. Energies. 12, (2019). https://doi.org/10.3390/en12071217.

20. Mauch, L., Yang, B.: A new approach for supervised power disaggregation by using a deep recurrent LSTM network. In: 2015 IEEE global conference on signal and information processing (GlobalSIP). pp. 63–67 (2015). https://doi.org/10.1109/GlobalSIP.2015.7418157.
21. Schirmer, P.A., Mporas, I.: Non-intrusive load monitoring: A review. IEEE Transactions on Smart Grid. 14, 769–784 (2023). https://doi.org/10.1109/TSG.2022.3189598.
22. Rafiq, H., Manandhar, P., Rodriguez-Ubinas, E., Ahmed Qureshi, O., Palpanas, T.: A review of current methods and challenges of advanced deep learning-based non-intrusive load monitoring (NILM) in residential context. Energy and Buildings. 305, 113890 (2024). https://doi.org/10.1016/j.enbuild.2024.113890.
23. Kukunuri, R., Aglawe, A., Chauhan, J., Bhagtani, K., Patil, R., Walia, S., Batra, N.: EdgeNILM: Towards NILM on edge devices. In: Proceedings of the 7th ACM international conference on systems for energy-efficient buildings, cities, and transportation. ACM (2020). https://doi.org/10.1145/3408308.3427977.
24. Sykiotis, S., Athanasoulias, S., Kaselimi, M., Doulamis, A., Doulamis, N., Stankovic, L., Stankovic, V.: Performance-aware NILM model optimization for edge deployment. IEEE Transactions on Green Communications and Networking. 7, 1434–1446 (2023).
25. Lu, Z., Cheng, Y., Zhong, M., Luan, W., Ye, Y., Wang, G.: LightNILM: Lightweight neural network methods for non-intrusive load monitoring. In: Proceedings of the 9th ACM international conference on systems for energy-efficient buildings, cities, and transportation. ACM (2022). https://doi.org/10.1145/3563357.3566152.
26. Luan, W., Zhang, R., Liu, B., Zhao, B., Yu, Y.: Leveraging sequence-to-sequence learning for online non-intrusive load monitoring in edge device. International Journal of Electrical Power and Energy Systems. 148, 108910 (2023). https://doi.org/10.1016/j.ijepes.2022.108910.
27. MacKay, D.J.C.: Information theory, inference and learning algorithms. Cambridge University Press, Cambridge, England (2003).
28. Baluja, S.: Population-based incremental learning: A method for integrating genetic search based function optimization and competitive learning. School of Computer Science, Carnegie Mellon University Pittsburgh, PA (1994).
29. Kelly, J., Knottenbelt, W.: The UK-DALE dataset, domestic appliance-level electricity demand and whole-house demand from five UK homes. Scientific Data. 2, (2015). https://doi.org/10.1038/sdata.2015.7.

Energy Communities Enablers: Techno-Economic Optimization Analysis of Renewable Energy System for Electric Vehicle charging Station

S.M. Masum Ahmed[1,2], Annamaria Bagaini[1], Tania Molteni[1], Edoardo Croci[1],

[1] Centre for Research in Geography, Resources, Environment, Energy and Networks (GREEN), Bocconi University, Via Guglielmo Roentgen, 1, 20136 Milan, Italy
{masum.ahmed, annamaria.bagaini, tania.molteni, edoardo.croci}@unibocconi.it
[2] Department of Electrical, Electronic and Control Engineering, School of Industrial Engineering, University of Extremadura, Campus Universitario, Av. de Elvas, s/n, 06006 Badajoz, Spain
sahmedn@alumnos.unex.es

Abstract. Energy Communities (ECs) aim to foster collaborative, citizen-driven clean energy transitions. Within the EU, they are formally defined as Renewable Energy Communities (RECs) and Citizen Energy Communities (CECs). These initiatives promote citizen participation in decentralized energy production and in delivering energy services. Examples may include services to the grid; services to members; and services directed to external clients. Moreover, they contribute to reducing greenhouse gas emissions, enhancing energy security, and lowering dependence on fossil fuels by fostering cleaner and more efficient energy systems. However, ECs face significant barriers to growth, including social, economic, institutional, and technological challenges. Overcoming these requires suitable enablers, such as smart metering and accessible renewable energy technologies. Many studies focus on EC enablers by categorizing them into technical, institutional, social, and economic enablers. Among technical enablers, Renewable Energy Sources (RES)-powered Electric Vehicle Charging Stations (EVCS) are gaining increasing relevance support the optimization of renewable energy generation and enable G2V and V2G operations. These functions enhance self-consumption, provide flexibility services to the grid, and supply backup storage to local communities, while potentially generating additional revenues when serving external clients who pay for charging their vehicles. Despite these potential benefits, RES-powered EVCS are rarely integrated into the main activities of ECs, and their feasibility remains underexplored in the literature. This study addresses this gap by validating RES-powered EVCS as effective enablers through two techno-economic feasibility analyses, applied to real case studies. The analyses combine software-based optimisation (HOMER) with a mathematical optimisation approach. Results demonstrate that RES-powered EVCS can substantially reduce both energy costs for local communities and CO_2 emissions, by enhancing and optimising onsite RES generation. These findings provide policymakers, researchers, and energy planners with evidence-based insights. They confirm that integrating RES and e-mobility solutions, can strengthen ECs, expand their impact, and create profitable opportunities for investors, prosumers, and consumers alike.

Keywords: Energy Communities · Energy optimization · Enabler · Renewable energy · EV Charging Station

1 Introduction

Fossil fuels remain a primary energy source in the European Union (EU); however, their extensive use significantly contributes to greenhouse gas (GHG) emissions, air pollution, and global warming. Moreover, the EU faces economic and geopolitical risks due to its heavy dependence on imported fossil fuels [1]. In response, the EU has set renewable energy targets to reduce CO_2 and enhance energy security. The EU Renewable Energy Directive (RED II) 2018/2001, set a target of 32% renewable energy in the energy mix by 2030 [2], which was increased to 42.5% in RED III (EU Directive 2023/2413). These shifting targets underscore the need to accelerate the transition to Renewable Energy Sources (RES) powered energy generation. Therefore, it is crucial to reduce reliance on fossil fuels to achieve long-term sustainability and energy autonomy with benefits in terms of energy costs for final users.

Local RES production is essential to decarbonise energy generation and improve energy democratization. Therefore, Energy Communities[2] (ECs) can play a pivotal role in engaging people in local RES generation specifically in RECs [3] and in transforming citizens from passive consumers to active prosumers [4]. Nevertheless, ECs are more of an exception than a rule in the Europe energy system, with approximately 10,000 EC initiatives establishing around 22,000 projects that account for between 7 and 10 GW of capacity [5]. Considering that the total renewable capacity in the EU is 848 GW, ECs represent only 0.82% to 1.17% of this total renewable capacity.

The full potential of ECs expansion cannot be fully achieved because of a set of barriers hindering them, including technical, institutional, social, and economic barriers. However, appropriate enablers[3] (such as smart metering, availability of renewable energy technology, etc.) are essential to overcoming these barriers. Many studies focus on EC enablers by categorizing them into technical, institutional, social, and economic enablers. Institutional enablers can positively affect organizations, institutions, and communities by helping end users (EC members) access services [6]. Key enablers include a liberalized energy market and a stable regulatory framework for ECs [7]. Moreover, economic enablers are mechanisms, policies, and support systems that aid the financial aspects and economic growth of projects [8, 9]. The crucial enablers that can play a pivotal role for ECs are access to financial support (including grants and subsidies) and crowdfunding [7]. A social enabler is a personal behaviour (ECs member traits), a policy, or awareness that facilitates participation (interaction between members of ECs) to achieve social goals more frequently [10, 11]; key enablers include trust, and community-based networks [12]. Furthermore, a technical

---

[2] *"Energy communities enable collective and citizen-driven energy actions to support the clean energy transition"* [35].

[3] An enabler is an approach or technology that facilitates or smooths the operation of a system, including technical, economic, social, and institutional [12].

enabler is a technological solution, including both hardware (equipment) and software, that enhances operations and management and reduces the costs of projects, including EC projects [13, 14]. Crucial enablers include the availability of RES technology options, net metering, and Electric Vehicle Charging Stations (EVCS) (Vehicle-to-Grid (V2G) and Grid-to-Vehicle (G2V) [15]).

Among technical enablers is raising in relevance the role of EVCS integrated into RES-based production. However, this technical enabler is rarely included in the main activities of ECs, despite its crucial importance in decarbonizing the transportation sector, reduce energy costs and optimize energy consumption for local communities. Also, there is a lack of academic studies validating whether these enablers are effective or not through techno-economic feasibility analyses. The role of RES-powered EVCS in ECs is underexplored, with few studies focusing on its practical application and management. Additionally, thorough evaluations of their technological feasibility, including integration with RES, storage, and V2G systems, as well as their economic viability, are limited.

Therefore, the objective of this study is to assess the techno-economic feasibility of EVCS powered by RES, with the aim of validating their role as effective enablers for ECs. By doing so, the study seeks to expand the functional scope of ECs beyond energy production and self-consumption, enabling them to actively contribute to the decarbonization of the mobility sector through e-mobility solutions. The research methodology combines a comprehensive review of the existing literature with empirical validation through case studies. First, the study analyses the definition and scope of ECs as outlined in the European regulatory frameworks. It then identifies and categorizes potential enabling factors from the literature, with a particular focus on the integration of RES-powered EVCS. Finally, the role of these EVCS is evaluated through techno-economic optimization analyses applied to two representative case studies, in order to assess their viability and contribution to EC development.

To this end, the chapter is organized into the following sections. Section 2 outlines the definitions of ECs by the EU, characteristics, and the EU member state's transposition situation of REC and CEC definitions. Section 3 reviews the existing literature on the enablers for the development of ECs, with a particular emphasis on technical and economic factors. In Section 4, two techno-economic analyses are presented with an aim to formulate concrete proposals that can enhance knowledge about the EVCS as an enabler for ECs, which are validated through two case studies. Finally, Section 5 offers the main conclusions of this study.

2 ECs definition by EU and member states' transposition of REC and CEC

There are two definitions of ECs available in the EU directives. First, the recast on RED II (EU) 2018/2001 mentioned EC as a REC [16]. Furthermore, common rules under the IEMD (EU) 2019/942 mentioned another definition of EC as a CEC [17]. The RED II emphasizes the promotion of renewable energy, while IEMD's main purpose is the completion of the internal market. Furthermore, both directives explicitly accept that the consumer is *“at the heart of the energy markets”*, which is expressed as an *“Active Consumer”* in the IEMD and as a *“Renewable Self-consumer”* in the RED II [18].

The REC is a legal entity based on voluntary and open participation. REC is autonomous, which is managed by shareholders or members (natural persons, SMEs or local authorities, including municipalities) that are situated near (proximity) to the renewable energy projects which are owned and constructed by a legal entity. Moreover, the CEC is a legal entity based on voluntary and open participation. In contrast, CEC is controlled by shareholders or members, including natural people and local authorities (municipalities, or small enterprises and micro-enterprises). Several similarities are discovered between the two EC definitions, such as open and voluntary involvement in both CEC and REC. Main features considered to compare REC and CEC include ‘membership status,’ ‘autonomy,’ ‘management of EC,’ ‘geographical limitation,’ ‘primary purpose,’ and ‘activities,’ which are found in the literature [19] (regarding ***‘membership*** status’ means what kind of members can participate in ECs; the ***‘primary purpose’*** is to provide economic, environmental and social benefits are toward ECs members and shareholders rather than concentrating on financial benefits for companies; ***‘Activities’*** are also similar in both aspects including generation, distribution, consumption, energy storage, aggregation, energy supply and distributing energy-related services. Furthermore, a few key differences are found between them in terms of ***‘degree of autonomy’*** and ***‘geographical limitations’ means any geographical proximity limitations that all members, and authorities need to follow for joining an EC***. Key aspects and differences between REC and CEC are summarized in Table 1 [19].

Table 13. Key aspects of REC and CEC.

Main features	REC	CEC
EU directive	Directive (EU) 2018/2001 (RED II)	Directive (EU) 2019/942
Membership Status	Open and voluntary involvement; the shareholders or members are individuals, micro, Small or Medium-sized Enterprises (SMEs) or local authorities	Open and voluntary involvement; members or shareholders are individuals, local authorities, including municipalities, or small enterprises
Degree of Autonomy	Autonomous	Not Autonomous, (restricted decision making of large energy companies in EC)
Management of EC	Efficiently managed by shareholders or members that reside close to the RES projects which owned and constructed by the REC	Efficiently managed by members or shareholders; the decision-making abilities should be limited to those members that are not connected with large-scale commercial activity
Geographical limitation	Reside close to REC	No limitation
Primary purpose	To deliver environmental, economic or social benefits to EC’s members or shareholders instead of focusing on financial gains	To deliver environmental, economic or social benefits to EC’s members or shareholders instead of focusing on financial gains
Activities	Generation, distribution, consumption, energy storage,	Generation, distribution, energy supply, consumption, energy sharing,

	aggregation, energy supply and distributing energy-related services	aggregation, energy storage, energy-efficiency services and EV charging-services

REC and CEC definitions can help the EU member states to understand how they can transpose these definitions to their national and regional level. Specifically, these directives are binding legislative instruments requiring member states to develop or adapt their national legal frameworks, ensuring alignment with the EU renewable energy targets and the empowerment of ECs. These directives seek to accelerate the proliferation of ECs and substantially increase the share of renewables in the EU's energy portfolio. This directly supports the EU's overall objectives of reducing GHG emissions, boosting energy autonomy, and achieving climate neutrality by 2050. However, the national and EU-level regulations can be different from each other, which sometimes can create confusion.

Furthermore, the revised RED III (EU Directive 2023/2413) establishes an aim of 42.5% for RES in final energy consumption. RED III strengthens the role of RECs in the EU's energy transition by encouraging them to participate in electricity markets by enabling its contribution to providing flexibility services like demand response, energy storage, and EV integration (smart and bidirectional EV charging). Also, the directive stresses local governments engage with network operators to ensure that grid development aligns with energy-saving goals and community-based renewable initiatives. Moreover, RED III declares that the licensing process for solar systems up to 100 kW must be finished within a month, and if there is no response, the systems will be automatically approved. This step will facilitate the integration of small-scale renewable energy. The registration procedure should be made easier for installations of less than 50 kW. RED III promotes the simplification of renewable energy system implementation, especially for small solar panel implementation, to facilitate ECs and self-consumption [20].

2.1 EU member state's transposition situation of REC and CEC

The transposition of the RED II and the IEMD EU directives into national laws is necessary to define national policies that aim to support and boost citizen-centred initiatives and strengthen citizens' rights within the energy market. Although the deadline for transposing RED II was 30 June 2021, not all member states have fully integrated it into their national legislation. Similarly, IEMD was not transposed by all Member States appropriately, despite the deadline being set for December 2020. Member States can decide to merge CECs and RECs definitions in a unique EC model to avoid confusion and facilitate the creation of ECs. In case Member States decide to maintain the two concepts, their definitions, and relation should be coherent with the EU dispositions.

The REScoop transposition tracker (2024) categorized the transposition situation of EU Member States into 4 different categories: *'Bad transposition'*, *'Substantial deficiencies'*, *'Average progress'*, and *'Good practice',* based on *'Criteria of EU definition reflected in national definition'*, '*Level of detail in the elaboration of principles contained in EU criteria'*, *'Clearly defined purpose'*, *'Legal entities* *allowed'*, *'Citizen participation is ensured'*, and *'Coherency between both definitions'*. *'Bad transposition'* means either that Member States do not have draft legislation for EC development, or they are working on the draft legislation but have not started to implement it at national or regional levels. The *'substantial deficiencies'* of transposition category indicates that Member States have regulations regarding REC or CEC, but several aspects are missing, such as citizen participation not always ensured, and blurring definitions of CEC and REC that hinder a successful EC development. *'Average progress'* of transposition means that there is legislation for ECs, but those are not fully compliant with the EU legislation. *'Good practice'* of transposition indicates that EU Member States fully transpose the EU directives in the national legislation. In this case, Member States set proper rules considering any aspects concerning the EC setup and implementation, such as EC governance and legal forms allowed, membership and voting rules, ownership and control rights, proximity requirements, energy sharing rules, and roles of the current status of nation energy market operators, etc. The current transposition situation of EU Member States is in Table 2 [21].

Table 2. Transposition Situation of EU Member States.

Transposition Situation	Member States
Good Practice	Belgium, Czech Republic, Denmark, France, Ireland, Italy
Average progress	Cyprus, Germany, Greece, Latvia, Lithuania, Slovenia, Spain
Substantial deficiencies	Austria, Bulgaria, Croatia, Estonia, Finland, Hungary, Luxembourg, Malta, Poland, Portugal, Romania, Slovakia
Bad Transposition	Sweden

Figure 1 illustrates the transposition situation of the EU Member States [21]. Where one Member State is in the bad transposition category, twelve Member States in the substantial deficiencies, seven Member States are in average progress of transposition, and six Member States are in good practice of transposition [21].

The EU has established several directives and regulations that can promote the development of ECs capable of participating in the entire energy value chain. However, as mentioned earlier, ECs are still in their infancy stage and have not yet fully developed since there are many barriers, including technical [22], economic [23], institutional [24], and social/behavioural barriers [22, 24] to their development. Thus, many scholars have focused on analysing how ECs can overcome these barriers through a set of technical, economic, institutional, and social enablers, which can facilitate EC operation, reduce operational barriers, and support the rollout of EC initiatives in the EU. Therefore, the next section identifies and discusses the key enablers of ECs found in the literature.

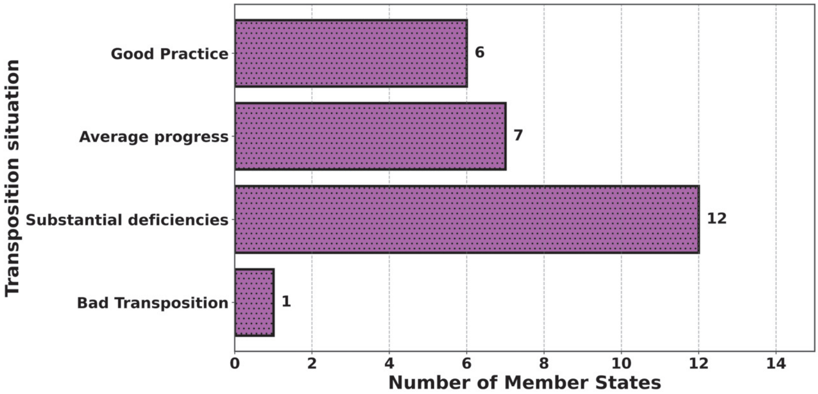

Fig. 9. Transposition situation of the EU Member States.

3 Enablers of ECs

3.1 Key Enablers of ECs in the literature

There are several types of enablers of ECs, including technical, institutional, social, and economic. A technical enabler is a technological solution, including both hardware (equipment) and software, that enhances operations and management while reducing project costs, including EC projects. A social enabler is a combination of personal behaviours (traits of EC members), policies, and awareness that promotes participation (interaction among EC members) to achieve social goals. Economic enablers are mechanisms, policies, and support systems that promote the economic growth of projects. Institutional enablers can positively influence an organization, institution, or community, helping end users (EC members) access services.

To identify the key enablers of ECs in the literature, a traditional literature review process is conducted by searching Google Scholar with two keywords, namely "energy communities" and "enabler." After analysing current literature found that economic enablers are (a) access to financial support including subsidies or grants, (b) a cooperation bank that facilitates low-interest loans, (c) crowdfunding which helps ECs by allowing members to choose and support projects that need funding from a social or local standpoint), and (d) self-ownership for locally produced energy [7]. Moreover, institutional enablers are (a) a liberalized market enables direct energy trading, encourages the involvement of prosumers, promotes the integration of RES, and developing economies of ECs with competitive markets, (b) a stable regulatory framework for ECs, (c) CO_2 taxation assist emerging economies by increasing fossil fuel prices, making RES more competitive, and enhancing the self-consumption of ECs, (d) reduced installation cost of RES than traditional energy, and (e) state financial support or debt securities. Social enablers are (a) trust, and community-based networks, (b) values including self-ownership of RES and RES-based energy production locally either onsite or through VPP, [22], and (c) social learning [25]. Technical enablers are (a) Decentralized Energy System (DES) which can work as an enabler to promote a sustainable and resilient energy future by generating energy at its point of use, reducing reliance on centralized grids, and improving grid flexibility and local energy security [26], (b) RES technology options available, (c) smart meters which are essential tools for a modern energy system, changing utilities and consumers by increasing grid efficiency and providing innovative services such as real-time consumption data, dynamic pricing, and more accurate billing, (d) net metering, and virtual net-metering, (e) blockchain which is a popular option as a security enabler [27] that can be integrated with ECs [28], (f) virtual power plants have developed into advanced facilitators of various energy assets which can be considered as enabler [29]), (g) microgrid facilitating peer-to-peer [7], and (h) EVCS where EV can play as energy storage and EVCS can sellback energy during RES generation [15]. Figure 2 illustrates the enablers of ECs.

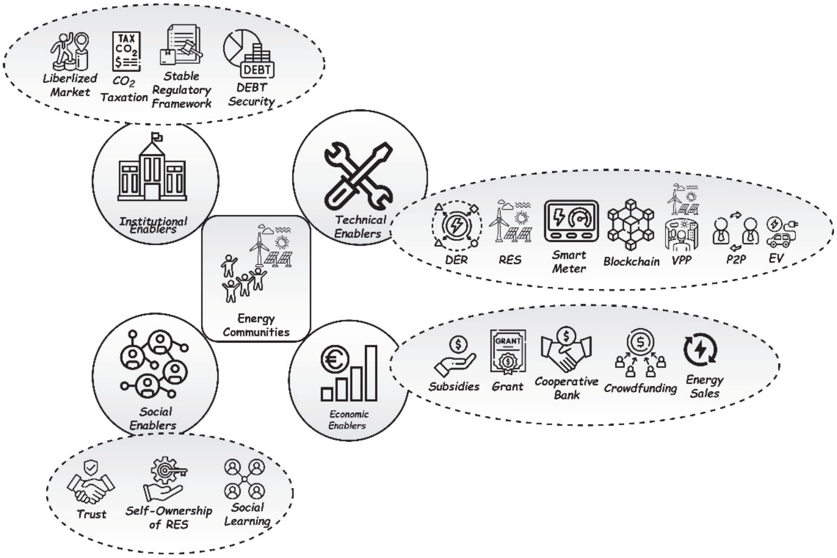

Fig. 2. Enablers of ECs.

3.2 Key Enablers considered in this study (EVCS powered by RES)

There are many enablers found in the literature but for this work RES powered EVCS is chosen as it can reduce fossil fuel consumption and promote EV in ECs. The lack of availability of EV charging infrastructure slows down interest in buying EVs in many countries [30, 31]. To increase EV adoption and fulfil the demand of EV users, adequate EVCS's are required to charge their EVs. Nevertheless, the majority of EVCSs' relies on fossil fuels, resulting in higher grid emissions as most of the EVCSs are powered by energy grids. Incorporating RES into EVCS is a crucial approach to reducing emissions associated with grid energy use, plus this incorporation can reduce emissions, and grid stress [32]. Additionally, for ECs, EVCSs can play a pivotal role in improving the operation and management of the grid. Additionally, EVCSs can also take on additional roles, such as serving as storage for the EC member, facilitating temporal optimization of consumption, and providing extra services to the outside (e.g., paid charging points for external users), which generate revenue for the EC that can then be reinvested. E-mobility and EVCS as a service is already proven in the literature, where K. Pantazis et al. make a Business Model archetype where *'Integrated Energy Services and the Electromobility Model'* offer a variety of services to members and other stakeholders [33].

As a whole RES powered EVCS contribute to reducing the use of fossil fuels, facilitating the decarbonization of the transport sector, and improving the incorporation of RES into the local energy system. This collaboration enhances individual ECs member's energy self-sufficiency and profitability by promoting e-mobility, local generation and consumption. At the community level, it improves resilience by limiting dependence on external energy suppliers, alleviating grid congestion, and increasing the adaptability of local energy systems through demand-side management and storage integration (Battery Energy Storage System (BESS) and EV as storage for EVCS).

4 Techno-economic analysis of RES-powered EVCS as enablers of ECs

The objective of this section is to look at how RES-powered EVCS can help ECs in both technical and economical ways. This section describes the results of a techno-economic assessment of RES-powered EVCS and examines their potential as a key enabler for improving the sustainability and economic viability of ECs. This section is essential to demonstrate how incorporating EVCS into ECs can aid local citizens become more energy-independent and move toward sustainable and decentralized energy systems.

In Case Study I, a university campus is considered to evaluate the technical and economic feasibility of a RES-powered EVCS. While this case study does not focus on an existing EC, a university campus is chosen because of its high energy consumption by many users and its local generation potential, which is similar to that of an EC. These similarities make university campuses ideal for testing EVCS. Furthermore, the optimisation analysis conducted for this Case Study I was conducted in a single step. In contrast, Case Study II involves integrating a building community with the university campus[4]. The main difference lies in the optimization analysis methodology and comparison with and without VPP, which now employs a two-step optimization process and incorporates VPPs to improve the technological advancement of energy integration. VPP is considered for integrating new solutions into the energy grid. VPPs

---

[4] This work has been presented and published in the IEEE EUROCON 2025 - 21st International Conference on Smart Technologies, 04-06 June 2025 [36].

coordinate distributed resources (PV, energy storage, and EVs) to optimize energy flows, offer flexibility services, and increase economic and technical feasibility, unlike Case Study I, but it can operate remotely as well. VPPs enable decentralized RES production and EV within VPP frameworks.

Techno-economic analysis of RES-powered EVCS can deliver useful results such as (a) assist ECs' managers to understand the initial investment and possible profitability, (b) optimize energy-economic parameters and see their variances before even the project is built, and (c) convince investors to invest in sustainable projects with validation of the payback period. Therefore, two techno-economic case studies have been conducted to validate the hypothesis that renewable-powered EVCS can act as key enablers of ECs.

4.1 Case Study I: RES-powered EVCS for a university

A university campus is used as a case study to evaluate the technical and economic feasibility of RES-powered EVCS. While this study does not focus on existing EC, it employs a university campus because of its energy consumption by many users and the potential for local power generation, which are similar to a EC. These similarities make university campuses ideal for testing EVCS. The aim is to validate a RES-powered EVCS as an enabler for ECs by examining performance, cost, and environmental benefits in realistic and scalable scenarios using simulation tools. In Case Study I the assessment focuses on the Caparica campus of NOVA University in Lisbon, Portugal, as a pilot site to test the feasibility of RES-powered EVCS. The main goal of case study I (RES powered EVCS for a university[5]) is to optimize the system through an integrated techno and economic feasibility analysis, evaluating its capacity to serve the university community and act as a scalable model for broader applications. Four Scenarios are considered during analysis, (a) Scenario-1 (S1) as Grid (Base Case), (b) Scenario-2 (S2) as PV-Grid, (c) Scenario-3 (S3) as Wind Turbine (WT)-Grid, and (d) Scenario-4 (S4) as PV-WT-Grid, were evaluated using Hybrid Optimization Model for Multiple Energy Resources (HOMER[6]) optimization software.

A systematic approach is utilized to achieve the main goal of this case study. (i) energy resource assessment, (ii) parking time data analysis utilizing Python, (iii) EV load profile estimate utilizing stochastic approaches, (iv) energy system sizing is optimized, and scenario analysis are evaluated, and (v) performing techno-economic analysis entering estimated load, technical, economic, and environmental data from research papers and reports into HOMER software. Techno-economic optimization is performed using HOMER software, which calculates key performance metrics such as Net Present Cost (NPC[7]), Capital Expenditure (CAPEX[8]), Operating Expenditure

---

[5] This case is selected to check EVCS feasibility after validated it in the second case study community is considered by us.

[6] HOMER is a simulation program that assists participants in performing techno-economic optimization with renewable energy sources [37].

[7] The NPC is the difference between the total cost of the project and the revenue generated by the system during the project period [38].

[8] CAPEX refers to an organization's funds to acquire, upgrade, or maintain physical assets such as property, buildings, technology, or equipment [39].

(OPEX[9]), Cost of Energy (COE[10]), and CO_2 emission reduction. Table 3 provides a summary of the economic results for Case Study I.

Table 3. Summarized Economic Analysis results of Case Study I.

Scenario	NPC (million $)	CAPEX (million $)	OPEX (million $/year)	COE ($/kWh)
S1	13.62	0.74	0.35	0.23
S2	5.66	3.67	0.023	0.027
S3	11.16	3.34	0.21	0.11
S4	5.67	5.89	-0.045	0.019

Among the four cases, S1 has the highest NPC of 13.62 million $. With a COE of 0.23 $/kWh, S1 leads in terms of achieving lowest COE among four scenarios. Additionally, S1 has the lowest CAPEX at 0.74 million $, primarily due to its allocation to energy system-related expenses. Among the four cases, S1 has the maximum OPEX. Moreover, S2's NPC is 5.66 million $, higher than S1's NPC. Hence C2's OPEX is 0.023 million $/year. Furthermore, S2 has a CAPEX of 3.67 million $.

Besides, S3 has an NPC of 11.16 million $. The OPEX of S3 is 0.21 million $/year. S3's CAPEX also comes at 3.34 million $. Among the four cases, S4 has the least NPC of 5.67 million $. On the other hand, S4 had the highest CAPEX at 5.89 million $. Nevertheless, with the highest CAPEX, S4 is regarded as the best scenario among the four cases. Furthermore, S4 has the lowest -0.045 million $/year OPEX. Conversely, S4 has the lowest energy purchase and the largest energy sales from the grid. Therefore, in the most ideal case, economic parameters are calculated in the best-case comparison to the grid scenario; so, NPC and COE in the best cases are lower than in the grid cases as base.

As observed, this case study is quite helpful for universities planning to build an EVCS and can be replicated to develop EC projects in the following case study combining university and community settings.

4.2 Case Study II: RES-powered EVCSs for a Building Community and a university

Case Study II expands on the findings of Case Study I by incorporating a building community adjacent to the university campus. Unlike the Case I, which analysed the feasibility of a RES powered EVCS, Case Study II uses a more advanced two-step optimization approach. This method incorporates the concept of VPPs, enabling the coordinated management of distributed energy resources. The use of VPPs improves system flexibility, promotes energy sharing among multiple buildings, and demonstrates the potential for scaling from a single site to a community energy system.

---

[9] OPEX or Lease Operating Expenses (LOE), lifting, or production costs, refer to items with a useful life of one year or less. Their costs are recorded as expenses in the accounts [40].

[10] The COE is defined as the annual cost ratio to the supplied electrical load [38].

Case Study II is RES-based EVCS for a building community and a university, which aimed to examine a real-world scenario involving a university and a building community[11], an energy-economic feasibility analysis of merging an EVCS and residential load with a VPP[12] or on-site RES. Data were initially gathered from NOVA University Lisbon, Caparica, Portugal, to facilitate the analysis. Later, for the residential load, a building dataset was employed from Denmark [34]. After combining the datasets, two methods, including HOMER and Genetic Algorithm (GA), were applied to perform a feasibility analysis of EVCS and building community load. HOMER performed the first-stage energy-economic optimization. Later, MATLAB employed the output of HOMER, comprising generation, grid sales, and purchasing, to complete the second stage of economic optimization by reducing EV users' energy costs. Three scenarios were considered suitable for the validation: Scenario-1 (S-1) with a G2V infrastructure; Scenario-2 (S-2) with EVCS powered by VPP; Third Scenario-3 (S-3) with EVCS powered by RES on-site incorporating BESS. Table 4 displays the summarized economic analysis of Case Study II.

Table 4 Summarized Economic Analysis results of Case Study II

Scenario	NPC (million $)	CAPEX (million $)	OPEX (million $/year)	COE ($/kWh)
S1	6.52	0.22	0.15	0.19
S2	5.38	0.51	0.112	0.13
S3	5.38	0.51	0.112	0.12

S-1 has the highest COE at 0.19 $/kWh of the three scenarios. Furthermore, it possesses the lowest CAPEX at 0.22 million $, as there is no on-site RES production. Nonetheless, it encounters the largest OPEX of 0.15 million $ per annum.

S-2 possesses the lowest NPC at 5.38 million $ among the three cases. Additionally, it possesses a COE of 0.13 $/kWh and a CAPEX of 0.51 million $. However, the OPEX of this S-2 is 0.112 million $ per year, which is a bit lower than the S-1.

In S-3, minimizing COE was the main objective using GA inside a VPP framework. The preliminary EVCS setup envisaged that EVs would charge at maximum power starting at 9 AM until completely charged. This approach enables the optimization of energy costs from an economic perspective. Also, the COE of the S-3 is 0.12 $/kWh, which is lower than the other two cases.

An analysis of the two case studies reveals significant differences. In Case Study I, the use of renewable-powered EVCSs was effective in reducing energy costs and emissions. However, the first case only utilized one-step optimization, whereas Case

---

[11] This study used a dataset of energy loads from 89 households, as reported in [34]. This dataset was chosen because of the limited building data near NOVA University Lisbon. Originating from Denmark, the dataset comprises measurements and statistical data on the annual energy load profiles of buildings, which are necessary for our case study [34].

[12] A Virtual Power Plant (VPP) is defined similarly to a standalone microgrid [41]. It can operate as a remote energy generation and storage facility. Furthermore, a centralized control system manages the functions of a set of autonomous units for the power grid [26]. These units can comprise electricity-generating systems like biogas, wind, and solar converters, as well as cogeneration hydroelectric plants, electricity consumers, and storage facilities [42].

Study II employed two-step optimization, which resulted in a lower energy bill compared to Case Study I. Additionally, Case Study II incorporates a VPP with the building community, which provides extra flexibility to ECs. The primary conclusion is that both of these case studies assist in reducing COE and energy bills, which can be replicated in ECs, particularly when combined with advanced management strategies, such as VPP, with the methodology developed during our analysis.

5 Conclusions

The research aimed to validate the role of RES-powered EVCS as enablers of ECs through techno-economic feasibility analyses. The study integrated findings from existing literature with two case analyses, using techno-economic optimization to evaluate the effectiveness of RES-powered EVCSs under various scenarios. The results indicate that incorporating EVCS powered by locally sourced renewable energy can significantly reduce energy expenditures and CO_2 emissions while improving community flexibility and resilience. In addition to quantitative findings, the study verifies that EVCS serves as a vital technological enabler for ECs. However, it is crucial to acknowledge the limitations of case studies, which are often site-specific, and to note that results may vary depending on regulatory, geographical, and socioeconomic factors. Furthermore, the methodology currently overlooks user behaviour factors, dynamic market processes, and broader grid-level interactions. Consequently, further research should broaden its focus to evaluate the scalability of these solutions by investigating their incorporation into cloud-based energy management systems. These solutions enhance stakeholder engagement, facilitate coordination among distributed assets, and expedite the transition toward sustainable and inclusive energy systems. It will not only create new opportunities for decision-makers and investors to engage in sustainable ventures, but it will also be beneficial for local people to join the new workforce required for these services.

In the future, other mathematical based optimizations, such as ant colony optimization, can be utilized to schedule the loads, make the optimization stronger, and compare with current results. One limitation of this work is not utilizing a machine learning algorithm for EV load estimation, which also can be considered for future work.

Acknowledgments. This project has received funding from the SmartGYsum project which is the European Union's Horizon 2020 research and innovation programme under the Marie Skłodowska-Curie grant agreement no. 955614. This project has received funding from the Masterpiece project which is the European Union's Horizon Europe Framework Programme for Research and Innovation under grant agreement no 101096836. Also, this research was funded (in part) by the Portuguese FCT – Fundação para a Ciência e a Tecnologia no âmbito da Unidade de Investigação CTS - Centro de Tecnologia e Sistemas/UNINOVA/FCT/NOVA, with reference CTS/00066. In addition, several icons developed by Freepik have been used, accessible at https://www.flaticon.com.

References

1. J. Zhang and M. Usman, “Redefining energy policy for sustainable growth: The interplay of fossil fuel subsidies, energy security risks, and energy balances in shaping geopolitical stability,” Energy, vol. 322, p. 135620, May 2025, doi: 10.1016/j.energy.2025.135620.
2. M. M. Sokołowski, “Renewable and citizen energy communities in the European Union: how (not) to regulate community energy in national laws and policies,” Journal of Energy and Natural Resources Law, vol. 38, no. 3, pp. 289–304, Jul. 2020, doi: 10.1080/02646811.2020.1759247.
3. J. Lowitzsch, C. E. Hoicka, and F. J. van Tulder, “Renewable energy communities under the 2019 European Clean Energy Package – Governance model for the energy clusters of the future?,” Renewable and Sustainable Energy Reviews, vol. 122, p. 109489, Apr. 2020, doi: 10.1016/j.rser.2019.109489.
4. I. Campos and E. Marín-González, “People in transitions: Energy citizenship, prosumerism and social movements in Europe,” Energy Res Soc Sci, vol. 69, p. 101718, Nov. 2020, doi: 10.1016/j.erss.2020.101718.
5. European Commission, “More than 9000 energy communities in Europe.” Accessed: Jun. 09, 2025. [Online]. Available: https://build-up.ec.europa.eu/en/news-and-events/news/more-9000-energy-communities-europe
6. M. Blohm, “An Enabling Framework to Support the Sustainable Energy Transition at the National Level,” Sustainability, vol. 13, no. 7, p. 3834, Mar. 2021, doi: 10.3390/su13073834.
7. J. Palm, “Energy communities in different national settings – barriers, enablers and best practices. (NEWCOMERS),” 2021. [Online]. Available: https://www.newcomersh2020.eu/
8. D. Adebanjo, T. Laosirihongthong, P. Samaranayake, and P.-L. Teh, “Key Enablers of Industry 4.0 Development at Firm Level: Findings From an Emerging Economy,” IEEE Trans Eng Manag, vol. 70, no. 2, pp. 400–416, Feb. 2023, doi: 10.1109/TEM.2020.3046764.
9. A. AlJaber, P. Martinez-Vazquez, and C. Baniotopoulos, “Barriers and Enablers to the Adoption of Circular Economy Concept in the Building Sector: A Systematic Literature Review,” Buildings, vol. 13, no. 11, p. 2778, Nov. 2023, doi: 10.3390/buildings13112778.
10. P. Casati, M. Moner-Girona, S. I. Khaleel, S. Szabo, and G. Nhamo, “Clean energy access as an enabler for social development: A multidimensional analysis for Sub-Saharan Africa,” Energy for Sustainable Development, vol. 72, pp. 114–126, Feb. 2023, doi: 10.1016/j.esd.2022.12.003.
11. S. Kaufman and A. Boxshall, “Eleven enablers of science thought leadership to facilitate knowledge exchange in environmental regulation,” Environ Sci Policy, vol. 147, pp. 336–348, Sep. 2023, doi: 10.1016/j.envsci.2023.06.018.
12. Y. Yeh, S. Lai, and C. Ho, “Knowledge management enablers: a case study,” Industrial Management & Data Systems, vol. 106, no. 6, pp. 793–810, Jul. 2006, doi: 10.1108/02635570610671489.
13. “What is Enabling Technology?,” University of Birmingham. Accessed: Aug. 27, 2025. [Online]. Available: https://www.birmingham.ac.uk/research/facilities/enabling-technologies/et-definition
14. M. R. Almassalkhi and S. Kundu, “Intelligent Electrification as an Enabler of Clean Energy and Decarbonization,” Current Sustainable/Renewable Energy Reports, vol. 10, no. 4, pp. 183–196, Sep. 2023, doi: 10.1007/s40518-023-00228-z.
15. N. Baumgartner, D. Sloot, and W. Fichtner, “ENERGY COMMUNITIES AS ENABLERS FOR INNOVATIVE TECHNOLOGIES? The Case of Vehicle-to-Grid in Three European Countries,” in BEHAVE 2023 the 7th European Conference on Behaviour Change for Energy Efficiency, 2023, pp. 216–227.
16. European Commission, “Directive (EU) 2018/2001 of the European Parliament and of the Council of 11 December 2018 on the promotion of the use of energy from renewable sources

(recast)," Dec. 2018. Accessed: May 15, 2025. [Online]. Available: HTTP://DATA.EUROPA.EU/ELI/DIR/2018/2001/OJ

17. European Commission, "Regulation (EU) 2019/942 of the European Parliament and of the Council of 5 June 2019 establishing a European Union Agency for the Cooperation of Energy Regulators (recast)."
18. J. Lowitzsch, C. E. Hoicka, and F. J. van Tulder, "Renewable energy communities under the 2019 European Clean Energy Package – Governance model for the energy clusters of the future?," Renewable and Sustainable Energy Reviews, vol. 122, p. 109489, Apr. 2020, doi: 10.1016/j.rser.2019.109489.
19. Nicolas Peraudeau, Achille Hannoset, Nicolas Peraudeau, and et al., "Energy Communities in the EU - Task Force Energy Communities," Dec. 2019.
20. EUR-Lex, "Directive (EU) 2023/2413 of the European Parliament and of the Council of 18 October 2023 amending Directive (EU) 2018/2001, Regulation (EU) 2018/1999 and Directive 98/70/EC as regards the promotion of energy from renewable sources, and repealing Council Directive (EU) 2015/652," Oct. 2023. Accessed: Jun. 09, 2025. [Online]. Available: https://eur-lex.europa.eu/eli/dir/2023/2413/oj/eng
21. REScoop.eu, "Transposition tracker - Definitions." Accessed: Jun. 09, 2025. [Online]. Available: https://www.rescoop.eu/policy/transposition-tracker/rec-cec-definitions
22. A. Dioba, A. Giannakopoulou, D. Struthers, A. Stamos, S. Dewitte, and I. Fróes, "Identifying key barriers to joining an energy community using AHP," Energy, vol. 299, p. 131478, Jul. 2024, doi: 10.1016/j.energy.2024.131478.
23. J. Young and S. M. Halleck Vega, "What is the role of energy communities in tackling energy poverty? Measures, barriers and potential in the Netherlands," Energy Res Soc Sci, vol. 116, p. 103693, Oct. 2024, doi: 10.1016/j.erss.2024.103693.
24. V. Brummer, "Community energy – benefits and barriers: A comparative literature review of Community Energy in the UK, Germany and the USA, the benefits it provides for society and the barriers it faces," Renewable and Sustainable Energy Reviews, vol. 94, pp. 187–196, Oct. 2018, doi: 10.1016/j.rser.2018.06.013.
25. D. Coy, S. Malekpour, A. K. Saeri, and R. Dargaville, "Rethinking community empowerment in the energy transformation: A critical review of the definitions, drivers and outcomes," Energy Res Soc Sci, vol. 72, p. 101871, Feb. 2021, doi: 10.1016/j.erss.2020.101871.
26. E. M. Gui and I. MacGill, "Typology of future clean energy communities: An exploratory structure, opportunities, and challenges," Energy Res Soc Sci, vol. 35, pp. 94–107, Jan. 2018, doi: 10.1016/j.erss.2017.10.019.
27. A. Verma et al., "Blockchain for Industry 5.0: Vision, Opportunities, Key Enablers, and Future Directions," IEEE Access, vol. 10, pp. 69160–69199, 2022, doi: 10.1109/ACCESS.2022.3186892.
28. K. Kotilainen, J. Valta, K. Systa, S. J. Makinen, P. Jarventausta, and T. Bjorkqvist, "Exploring the Potential of Blockchain as an Enabler for Three Types of Energy Communities," in 2019 16th International Conference on the European Energy Market (EEM), IEEE, Sep. 2019, pp. 1–6. doi: 10.1109/EEM.2019.8916261.
29. S. Abdelkader, J. Amissah, and O. Abdel-Rahim, "Virtual power plants: an in-depth analysis of their advancements and importance as crucial players in modern power systems," Energy Sustain Soc, vol. 14, no. 1, p. 52, Aug. 2024, doi: 10.1186/s13705-024-00483-y.
30. S. Sachan and P. P. Singh, "Charging infrastructure planning for electric vehicle in India: Present status and future challenges," Regional Sustainability, vol. 3, no. 4, pp. 335–345, Dec. 2022, doi: 10.1016/j.regsus.2022.11.008.
31. G. J. Osório et al., "Rooftop photovoltaic parking lots to support electric vehicles charging: A comprehensive survey," International Journal of Electrical Power & Energy Systems, vol. 133, p. 107274, Dec. 2021, doi: 10.1016/j.ijepes.2021.107274.
32. A. Khan, S. Memon, and T. P. Sattar, "Analyzing Integrated Renewable Energy and Smart-Grid Systems to Improve Voltage Quality and Harmonic Distortion Losses at Electric-Vehicle

Charging Stations," IEEE Access, vol. 6, pp. 26404–26415, 2018, doi: 10.1109/ACCESS.2018.2830187.

33. K. Pantazis, A. Bagaini, S. M. M. Ahmed, and E. Croci, "Energy Community Business Models Archetypes," in 2025 IEEE 19th International Conference on Compatibility, Power Electronics and Power Engineering (CPE-POWERENG), IEEE, May 2025, pp. 1–7. doi: 10.1109/CPE-POWERENG63314.2025.11027308.
34. A. Marszal-Pomianowska, P. Heiselberg, and O. Kalyanova Larsen, "Household electricity demand profiles – A high-resolution load model to facilitate modelling of energy flexible buildings," Energy, vol. 103, pp. 487–501, May 2016, doi: 10.1016/j.energy.2016.02.159.
35. European Commission, "Energy communities." Accessed: Jun. 09, 2025. [Online]. Available: https://energy.ec.europa.eu/topics/markets-and-consumers/energy-consumers-and-prosumers/energy-communities_en
36. D. M. Mahmud, S. M. M. Ahmed, S. Hasan, and M. Zeyad, "Grid-connected microgrid: design and feasibility analysis for a local community in Bangladesh," Clean Energy, vol. 6, no. 3, pp. 447–459, Jun. 2022, doi: 10.1093/ce/zkac022.
37. M. Zeyad, S. M. M. Ahmed, S. Hasan, and D. M. Mahmud, "Community microgrid: an approach towards positive energy community in an urban area of Dhaka, Bangladesh," Clean Energy, vol. 7, no. 4, pp. 926–939, Aug. 2023, doi: 10.1093/ce/zkad027.
38. M. J. Turner and J. W. Hesford, "The Impact of Renovation Capital Expenditure on Hotel Property Performance," Cornell Hospitality Quarterly, vol. 60, no. 1, pp. 25–39, Feb. 2019, doi: 10.1177/1938965518779538.
39. M. J. Kaiser, "The role of factor and activity-based models in offshore operating cost estimation," J Pet Sci Eng, vol. 174, pp. 1062–1092, Mar. 2019, doi: 10.1016/j.petrol.2018.10.093.
40. H. Saboori, M. Mohammadi, and R. Taghe, "Virtual Power Plant (VPP), Definition, Concept, Components and Types," in 2011 Asia-Pacific Power and Energy Engineering Conference, IEEE, Mar. 2011, pp. 1–4. doi: 10.1109/APPEEC.2011.5749026.
41. T. Popławski, S. Dudzik, P. Szeląg, and J. Baran, "A Case Study of a Virtual Power Plant (VPP) as a Data Acquisition Tool for PV Energy Forecasting," Energies (Basel), vol. 14, no. 19, p. 6200, Sep. 2021, doi: 10.3390/en14196200.

Energy Communities in the EU: An analysis of Ownership, Funding Mechanisms, and Business Models

Konstantinos Pantazis[1,2], Tania Molteni[1], Annamaria Bagaini[1], Edoardo Croci[1],

[1] Centre for Research in Geography, Resources, Environment, Energy and Networks (GREEN), Bocconi University, Via Guglielmo Roentgen, 1, 20136 Milan, Italy
{konstantinos.pantazis, annamaria.bagaini, tania.molteni, edoardo.croci}@unibocconi.it
[2] Department of Electrical, Electronic and Control Engineering, School of Industrial Engineering, University of Extremadura, Campus Universitario, Av. de Elvas, s/n, 06006 Badajoz, Spain
kpantazi@alumnos.unex.es

Abstract: The current book chapter is related to the research conducted within the context of the SmartGySum project. The study presented here was carried out during the collaboration of the early-stage researcher 15 (ESR15) with the research team of Bocconi University, which is the lead partner in work package 5 (WP5) of the SmartGySum project focusing on green economy management models and systems. ESR15's primary objective is to identify the enablers and barriers that can enhance the replicability of business models for green energy systems. In this context, ESR15 specifically investigates Energy Communities (ECs), with the aim of identifying and assessing the key barriers that affect the establishment, development, and expansion of ECs within the EU. Additionally, ESR15 aimed to explore the different business models (BMs) that ECs can develop. The results provided below focus on how the ownership models of ECs affect the funding mechanisms they utilize to support their projects, as well as the financial barriers these ECs encounter[13] (see section 3). Moreover, an analysis of the ECs BMs is presented[14]. In particular, an analytical framework was developed for the evaluation of the EC's BMs. This framework was subsequently applied, resulting in the creation of distinct categories of EC BMs that explain how these communities create, deliver, and capture value (section 4).

Keywords: Energy Community · Business Models · Ownership Models · Funding Mechanisms · Barriers

1 Introduction

---

[13] This work has been presented and published in the 16th international scientific conference on energy and climate change, 11-13 October 2023 [59].

[14] This work has been presented and published in the 19th international conference on compatibility, power electronics and power engineering (CPE-POWERENG), 20-22 May 2025 [72].

Reaching 3,870 GW, global renewable power capacity [1] provides around 13% of world’s final energy consumption in 2023 [2]. The transition from fossil fuels to renewable energy is particularly advanced in the European Union (EU) compared to other countries. In 2023, renewable sources, which include various types, such as wind, biomass, and geothermal energy, accounted for around 25% of the EU’s final energy consumption. In the same year the electricity generated by renewables, in the EU, accounted for over 45% of final electricity consumption [3]. However, many studies have pointed out that this change is not merely technological but instead socio-technical [4], [5], [6]. This socio-technical shift, from fossil fuels to renewable energy, is leading to the transformation of the energy system from a centralized, vertically integrated model to a liberalized and decentralized system. This change empowers citizens, municipalities or small and medium-sized enterprises (SMEs) to produce and consume their own energy, transforming them from passive consumers into prosumers [7]. This transformation has also sparked researchers' interest in analyzing how these new actors can influence and drive the transition towards a sustainable energy system. Special attention is given to Energy Communities (ECs). Although it lacks a generally accepted definition in academic literature, ECs can be described as collective initiatives that can develop activities across the energy value chain. These activities aim for environmental and social benefits rather than economic profit in the area where they operate [8].

Although EC initiatives have recently gained prominence in academic and policy discourse, citizen engagement in energy-related initiatives, ranging from small-scale groups to entire local communities, has a long tradition within the EU. Citizen participation and community ownership over energy sources can be traced back to 1970 and 1980 in countries like the Netherlands and Belgium [9], or even earlier at the end of the 19th century in the Alpine region in Italy [10]. However, ECs rose in relevance after the publication of the two EU directives, namely, the Renewable Energy Directive 2018/2001/EU (REDII) that defines Renewable Energy Communities (REC) and the Internal Market Energy Directive 2019/994/EU (IEMD) that defines Citizen Energy Communities (CEC)[15]. While RECs and CECs allow different types of membership, technologies, and activities and have different geographical restrictions, both are legally recognized entities that operate on the basis of free and voluntary participation, are controlled by shareholders or members, and focus on social, economic, and environmental benefits rather than financial gains [11].

The EU policy framework related to ECs has further evolved with the introduction of the Fit for 55 package and the REPowerEU plan (EU Regulation 2023/435). These initiatives reinforce the EU’s climate and energy strategy and, among other things, set targets to create at least one EC in every municipality with more than 10,000 inhabitants by the end of 2025 [12]. Additionally, the updated RED III (EU Directive 2023/2413) sets a target of 43.5% renewables in the final energy consumption by 2030 and encourages EU countries to make it easier to set up renewable energy systems, especially for small solar panel installations, to support ECs and self-consumption [13]. Finally, the revised Energy Efficiency Directive (EU Directive 2023/179) underlines the importance of ECs in fighting energy poverty and strengthening energy-saving targets [14].

---

[15] See chapter 13.

The favorable EU policy framework has enhanced the growth of ECs and enabled their participation in the energy system. As a result, there are more than 10,000 ECs in the EU that have developed more than 22,000 projects [15]. However, regardless of common EU framework, the current landscape of EC development is quite diverse, with some countries being more developed than others [15], [16]. The variation regarding the development of ECs in the EU is characterized not only by quantitative but also by qualitative differences, as Western countries host more EC initiatives and engage in a greater variety of activities than Eastern European countries [17].

The activities carried out by various ECs extend beyond mere energy production and self-consumption. They encompass energy storage, flexibility services for the grid, e-vehicle charging stations, and initiatives related to energy saving and sharing. Additionally, many ECs have been established by a diverse range of actors, both public and private, benefiting from this collaboration. Consequently, it is evident that ECs can vary internally, as they operate in different ways, engage in various activities, offer unique services, and involve a wide array of participants. As a result, numerous scholars from different scientific backgrounds are trying to analyze this complex topic [16], [17], [18].

Walker & Devine-Wright [19] examine the full range of social arrangements of ECs based on two dimensions, namely the process dimension, that focuses on explaining who "participates," "manages," and has "influence" in ECs, and the outcome dimension, which refers to "who the project is for" and who "benefits" socially and economically [19]. Gui et al. [20] explores the different configurations that ECs can take in the transition from the current centralized to a decentralized energy system. The authors defined three different typologies of ECs, namely the centralized, the distributed, and the decentralized ECs. More recent studies have explored ECs from various perspectives. Dudka et al., [21] drawing from institutional logic, aim to categorize ECs by developing typologies of energy citizenship while other studies investigate the topic of ECs through a Business Model (BM) lens [22], [23], [24], [25], [26], [27]. Furthermore, other researchers consider the various financing methods that ECs can adopt for their project development [28], [29], [30].

Nevertheless, the results of this research demonstrate that while there has been a growing number of scientific publications on ECs, several areas remain relatively unexplored, or there has not been a consensus between academics on how to approach and analyze ECs. It is observed that although there are studies that examine ECs from a BM perspective, scholars haven't defined a generally accepted way to analyze and categorize EC BMs. Moreover, there are studies that have analyzed the different ownership models or the funding mechanisms that ECs can use; however, there is a lack of scientific studies that examine how the ownership model affects the funding mechanisms. In addition, there is a lack of literature examining the financial barriers faced by ECs with different ownership models. Therefore, the present study seeks to address the above-mentioned gaps in literature by utilizing various approaches and methodologies. Thus, this chapter pursues three main objectives. First, it aims to examine the academic literature on ECs; second, to identify the different EC ownership models and the financial barriers they encounter; and third it seeks to systematize and categorize the various types of EC BMs.

To that end, a literature review was conducted, aiming to examine the academic literature on the topic and identify the different research areas that have emerged concerning the ECs as well as identified research gaps. Second, a survey was conducted, gathering information from different EU countries through a questionnaire on how the ownership model of ECs affects the funding mechanism used to finance their generation plants as well as the financial barriers ECs face. Finally, the research examines the literature of EC BMs and provides a tailor-made analytical framework that allows the analysis and categorization of different EC BMs.

The next sections summarize the results of this study. Section 2 presents the current academic literature on the topic of ECs. Section 3 outlines the findings related to the ownership models of ECs, the funding mechanisms they utilize, and the financial barriers they face. Section 4 introduces a customized analytical framework for EC BM analysis based on literature review. This framework allows for the analysis and categorization of different EC BMs. Furthermore, by applying this framework four EC BM archetypes were identified and presented in the same section. Finally, Section 5 presents the conclusions of current research.

2 Literature review on ECs

As already mentioned, the topic of ECs has attracted a lot of attention in academia, with many studies analyzing it from different disciplinary backgrounds [31], [32]. In the first stage of this research, the existing body of literature was reviewed to provide a clear map of the current academic landscape on the topic. Hence, a literature review and desk research were conducted by retrieving papers and reports from the Web of Science, Scopus and Google Scholar. This approach enables a preliminary but comprehensive understanding of the topic of ECs, allowing for the retrieval of information on how the topic of EC has been addressed. Thus, a wide range of academic papers and reports has been compiled to establish a solid knowledge base for analyzing the current state and evolution of the EC. This process included reviewing key policy documents, such as EU EC directives, and examining statistical databases that illuminate current trends in EC development. The analysis indicates that the numbers of EC has recently increased in the EU [33]. However, western European countries have a more developed network of ECs than the southeastern European countries [15]. Moreover, the adoption and implementation of EU directives vary significantly among EU member states, with some possessing more comprehensive legal provisions regarding ECs than others [34].

Furthermore, the literature review reveals an exponential increase in academic studies since 2017 concerning the topic of ECs [35], [36], [37]. However, some countries have focused on this topic more than others. It appears an uneven geographical distribution of publications, with the United Kingdom (UK), Germany, the Netherlands, and Spain have the most published papers [38]. However, a study conducted by Giannarelli et al. (2024) concludes that Italy, Germany, Austria and Spain as the country's most frequently appeared in the literature [39]. This may be attributed to the longer tradition of citizen participation in the energy system in these countries [9], [10]. Additionally, as previously mentioned, these countries have stronger policy frameworks that support the establishment and development of ECs [9], [40]. Despite the differences in the studies, which may be due to the time period in which they were carried out or their focus, both show that Europe is at the forefront of EC research, with 77% of scientific articles derived from European countries [38].

However, the diversity of the topic of ECs is not only related to the geographical distribution of the published scientific work but also to the research areas that have been explored. The analysis of the literature revealed that research on the topic revolved around different areas [31], [32]. Some studies concentrate on the role ECs have in energy transition, and the scholars who belong to this research area analyze, among other things, the various definitions that exist about ECs [35], [37], [41], the benefits they provide to the environment and society, the drivers for the development of ECs, etc. [22], [42], [43]. Some other studies focus on the different technologies that have been or can be utilized by ECs and evaluate them from a technoeconomic perspective [44], [45], [46]. Finally, some scholars center on the different models that ECs can develop within the energy market, such as Peer-to-Peer (P2P), aggregators, and prosumers [47], [48], [49]. In addition, scholars in this research area investigate how these EC arrangements can influence and be influenced by the energy market [49], [50].

Nonetheless, it was found that there are areas of research that have not been sufficiently explored. For instance, studies related to EC BMs and the barriers faced by ECs have been studied less. In addition, it was found that although there are studies that illustrate the barriers that ECs face, it appears that there is a lack of a systematic categorization of these barriers. The identification of these research gaps facilitated the development of research questions that determined the next research steps presented in the following sections.

3 Energy Communities: Analysis of ownership models and funding mechanisms

As previously mentioned, ECs comprise diverse actors and can adopt various ownership models and legal structures. Some ECs, for instance, are limited liability companies, cooperatives, or non-profit organizations. Furthermore, ECs may not be initiated and managed exclusively by citizens, since other types of actors may set up the initiatives. According to Krug M. et al. [51] many EC projects in Italy have been initiated by companies or governmental bodies, including SMEs and municipalities, while a significantly smaller proportion has been initiated by citizens.

Both the ownership model and the initiators of the ECs impact how a community can raise capital and fund its projects. For example, the literature shows that private investors, such as private banks, often do not trust ECs due to the absence of liability in the case of a project failure [52], [53] or because they view these businesses as unprofitable [54], [55]. In addition, the launching of ECs by different actors, either public or private, is probably linked to the fact that the initial phase of establishing an EC is considered the most difficult [29], [42]. Moreover, the understanding of the energy market and the financial capacity and commitment of the members to establish an EC are considered essential [29]. De Bakker et al. [56] argue that ECs often face internal shortcomings, such as insufficient knowledge and money, as well as external constraints, such as legal barriers; therefore, they are obliged to develop synergies with various partners. Consequently, ECs often depend on external support from organizations such as local businesses, NGOs, or public authorities for money and guidance [57].

However, there is a lack of academic literature that examines how different types of EC ownership models and initiators affect funding mechanisms that ECs can use. With funding mechanisms, we refer to the "ways by which a supplier makes financial resources available to the organizations that require them. These methods can have a variety of implications for capital recovery, expected returns, ownership rights, and other factors." [58]. Therefore, this research aims first to identify and categorize the EC based on the ownership models and types of initiators of ECs and second to investigate the funding mechanisms that these ECs use and the barriers they encounter in order to raise capital [59].

To define the various ownership models of ECs, this study utilizes four dimensions identified by the International Renewable Energy Agency (IRENA) [60]: (i) membership, (ii) the level of democratic governance, (iii) the local distribution of benefits, and (iv) the main purpose of the organization. Membership refers to the various types of actors who participate in and hold shares in the ECs. The level of democratic governance pertains to how decisions are made within the community. For instance, many ECs operate under the one-member, one-vote principle, which means that each member has one vote, regardless of the number of shares they hold. The local distribution of benefits indicates the extent to which the EC generates social, environmental, and economic benefits at the local level. The purpose of the organization relates to the primary goals of the ECs, which may include economic, environmental, or social objectives, such as distributing profits among participants or addressing energy poverty. In addition, this study defines the initiators of the EC as any public or private actor, including SMEs, local authorities, or citizens involved in the establishment and setup of the EC.

Among the various funding mechanisms that exist [58], four different types have been highlighted in the literature in relation to ECs: i) Equity finance consists of shares that a community offers in exchange for ownership rights to the community or a project [61], ii) debt finance refers to the money that an EC borrows in the form of a loan from another entity and must repay over a certain period of time at an interest rate, iii) grants refer to capital that ECs can get without having the obligation to pay it back and can be provided either nationally, regionally, or even by the EU, and iv) alternative finance, which is associated with crowdfunding and crowd-investment platforms that have developed from ECs [62].

To investigate how the ownership model of ECs influences the funding mechanisms utilized to support their energy generation plants, a survey was conducted using a self-completion questionnaire, and 25 responses from different ECs were collected from seven EU countries16. The questionnaire aimed to analyze the characteristics of ECs and their ownership models, the funding mechanisms utilized, as well as the financial barriers encountered by different ECs. The analysis focuses on ECs that have developed

---

[16] The seven EU countries that participated in the survey are Greece, Spain, France, Austria, Belgium, Sweden, and the Netherlands.

energy generation plants and does not consider other types of activities or services, such as e-mobility or flexibility services. Therefore, the questionnaire was divided into three sections: (i) general characteristics of ECs, such as the year of establishment, stage of development, and characteristics related to the ownership model; (ii) characteristics of the power plants developed by ECs, such as the type of technology used, the number of end-users; and (iii) economic characteristics, including funding mechanisms, investment size, and the main barriers ECs face.

Regarding the general characteristics of the ECs and the main technology used, the results revealed that the vast majority of the ECs are small, in terms of number of members and mostly utilize PV panels as energy generation units. Specifically, only three communities reported it as large (500-2000 members), or very large (more than 2000 members) while the rest have less than 500 members. In relation to the year of establishment, most ECs, 20 out of 25 ECs, were initiated from 2017 onwards. Furthermore, the majority of the ECs in the sample are non-profit, 16 ECs, and only 6 ECs were described as for-profit ECs, while 3 ECs declared that their main goals were not financial.

The analysis of the ownership models of the ECs revealed that the only reported differences were related to the type of membership. There were no significant variations in governance, local profit distribution, or the purpose of the organization. Additionally, differences concerning the initiators were noted. Consequently, this study categorizes the ECs based on the different types of members involved and the various actors who initiate the ECs. A total of eight distinct categories of ECs were defined (see Tab. 1).

Table 1. ECs in the sample categorized by initiators and membership.

Categories	Initiators	Membership	Number of EC in the sample
1	Citizens	Citizen	4
2	Citizens	Citizens + Private	6
3	Citizens	Citizens + Public	1
4	Citizens	Citizens + Public + Private	7
5	Public	Public	1
6	Public	Public + Citizens	1
7	Private	Citizens	2
8	Citizens + Public + Private	Citizens + Public + Private	3
Total			25

Most ECs employed a combination of funding mechanisms. Debt capital was utilized by nearly 70% of ECs, while approximately 60% relied on equity capital. Additionally, around 40% of the ECs in the sample used grants or crowdfunding. Regarding the relationship between the eight categories found in this study (see Tab. 1) and the funding mechanism they used, it is observed that the ECs initiated by citizens having public and/or private actors as members (Tab. 1, categories, 2,3 and 4) can more easily raise capital using equity or other internal resources than the ECs having only citizens as members (Tab 1. Category 1). Furthermore, this study, like other studies [63], shows that the size of the community in terms of the number of members as well as the total capital required to fund the project could affect the choice regarding the funding mechanisms. Specifically, ECs, with investments of more than 200,000 euros in energy generation plants, tend to use debt capital. However, large ECs (more than 2000 members) can use different funding mechanisms such as green bonds provided to their members, thus reducing the financial risk by depending on debt capital.

Regarding the financial barriers that ECs encounter, it is observed that ECs in the sample face problems raising capital both from private and public actors. Table 2 summarizes the main barriers that ECs encounter in order to raise capital and fund their generation plants. The barriers that are reported more frequently are the lack of grants or subsidies at the national level (barriers 1-3), followed by barriers related to private funding (Tab. 2, barriers 4-6), while barriers in relation to crowdfunding and citizen participation are reported less (Tab 2, barriers 7 and 8).

Table 2. EC barriers regarding the funding mechanism of energy generation plants.

N.	Barriers	Number of ECs reporting impact
1	No subsidies or grants for EC provided at a national level	14
2	Public grants or prizes are not tailored-made for your EC	14
3	Complex bureaucratic processes make it difficult to access public finance	14
4	Private financial institutions or banks do not fund your generation plant because they consider it non-profitable.	11
5	No access to favorable loans, such as soft loans, green loans, etc.	12
6	Unattractive environment for private investors because of the absence of feed in tariff (FiT) or other pricing mechanisms	8
7	Absence of a legislative framework for the proper functioning of crowdfunding or crowd-investment platforms	7
8	Low participation of people in funding energy generation plants; thus, it isn't easy to raise capital from equity shares	11

However, the present analysis reveals differences between EC categories in terms of the barriers they face. The lack of citizen participation is identified as a barrier by communities initiated by citizens (Tab.1, categories 1, 2, 3 and 4) but not by those initiated by public or commercial actors. Furthermore, it appears that citizen-initiated ECs, which also include public and private actors as members (Tab. 1, categories 2, 3, and 4), can more easily raise funds internally through equity compared to those ECs whose members consist solely of citizens (Tab. 1, category 1). Lastly, regarding access to public funding mechanisms, it appears that all ECs encounter barriers, regardless of the category they belong to. However, due to the limited sample size of this study, additional research is needed to validate this trend.

4 Energy Communities Business Models

The differences between ECs extend beyond just the initiators and the types of members involved. Numerous other factors have been reported in academic literature regarding the categorization and analysis of ECs. Scholars have focused on examining the motivations and roles of actors within ECs, in addition to the types of actors involved. While some actors may only act as consumers, others may also act as prosumers or producers [16], [18], [64]. In addition, ECs can develop different revenue-sharing mechanisms among EC members. As a result, ECs can adopt various BMs based on their objectives, structure, technology preferences, and revenue sharing mechanism [24]. Hence it was aimed to expand the research focus on the topic by examining the literature related to the EC and BMs.

According to Shafer et al. [65], a BM is "a representation of a firm's underlying core logic and strategic choices for creating and capturing value within a value network" [65]. With the increased focus on sustainability-related issues, new approaches have emerged in BM studies. Porter & Kramer [66] criticize the neoclassical thinking that sets the goal of profit maximization without considering environmental and social factors. Thus, the authors suggest the concept of "shared value", arguing that environmental and social challenges should not be seen as obstacles to business activities but rather as opportunities for innovation, technological or organizational, that can expand or create markets [66].

The above-mentioned discussion is essential for ECs, as they are entities that aim for environmental and social benefits rather than economic gains. Therefore, the value that ECs aim to bring to society is related to issues such as tackling energy poverty, raising awareness about environmental issues, promoting renewable energy sources, and combating climate change.

However, based on the complexity of the EC configurations and the different approaches to analyze BMs, there are a variety of perspectives and analytical frameworks in the literature concerning EC BMs [24], [67], [68], [69]. For instance, some studies have used the Business Model Canvas (BMC), which is the most widely used analytical framework to analyze and categorize different BMs [70], [24], [28]. Nevertheless, other studies have employed the four macro categories of BM analysis: value proposition, value creation, value delivery, and value capture [22], [71]. Additionally, some researchers have examined the unique features of ECs, such as membership types or governance structures, to develop categories that better organize and differentiate the various EC BMs [26]. The studies mentioned aim to analyze ECs from a BM perspective and categorize them in different BM archetypes, which is intended to provide an abstract theoretical framework that illustrates a set of mechanisms that help explain how various EC initiatives differ in terms of their operations, value creation, and value capture.

However, the different dimensions and frameworks used by scholars to analyze and categorize EC BM led to confusion due to divergent results. Hence, this study aims to analyze the literature in order to identify and categorize the key dimensions that have been used and to develop a customized analytical framework for the analysis of EC BM [72]. This framework facilitates the analysis of ECs from the BM perspective, incorporating both established dimensions from the business literature, such as the value proposition, and the unique characteristics of ECs, such as governance. Furthermore, the use of this framework allows the categorization of different ECs BM.

5 Energy community business model framework

By conducting a semi-structured literature review, 30 papers discussing EC from a BM perspective were identified. Later, through content analysis, 30 dimensions emerged as unique characteristics of a EC BM. However, the strong thematic relationships among these 30 dimensions led to their merging, resulting in the identification of 13 unique dimensions. In the final stage of this research, only the most frequently occurring dimensions with high relevance to BM analysis were retained to develop the analytical framework of EC BM, which consists of 5 dimensions (see Tab.3). Specifically, the five dimensions identified are the “value proposition”, “value capture”, “main functions”, “governance”, and “membership”.

Table 3. The Five Dimensions of the Tailor-made BM Framework for ECs.

Dimensions	Description	Occurrences
Value Proposition	Refers to EC’s main objective and the benefits provided to its members and society	21
Value Capture	Refers to revenue stream and cost structure of the EC.	9
Main Function	Refers to the main activities, technologies and services of the EC.	12
Governance	Refers to the management, decision-making and control of the EC.	9
Membership	Refers to the different types of actors who participate in the EC as members.	16

The value proposition is the cornerstone of BM analysis and describes the EC's main objectives. As Osterwalder [73] states, the value proposition explains why a customer chooses one business over another, since it solves their needs or solves a specific problem. However, in literature related to the topic of EC, different terms appear that describe the same concept, such as goals [69], unique value proposition [24], and generated benefits [74], etc. Hence, the first dimension that appears to be strongly related to EC BM analysis is the value proposition that was defined in this study as the main benefits that ECs provide to their members and to society.

Similarly to value proposition, the dimension of value capture appears many times in literature, albeit in different terms. Many scholars use terms such as financial model [22], financial characteristics [69], value-sharing mechanisms [75], or energy value capture [26]. Nevertheless, all these terms refer to the revenue stream and cost structure of an EC, which explain the respective returns in relation to the value the EC provides to its members and society, as well as the costs associated with building and maintaining the community.

The main function dimension incorporates characteristics of value creation and value delivery, as it refers to activities, technologies, and services provided by the EC to create and deliver value to its members and society. Furthermore, studies that concentrate on technologies employed by ECs fall under this dimension since these technologies are crucial for creating and delivering value and achieving EC's objectives. However, the terminology used by academic scholars varies; for instance, [16], [26] use the term key function. Nevertheless, the meaning stays the same as it elucidates the various energy services and activities that ECs engage in, including self-production, energy sharing, supply, etc.

Governance structure and membership are the last two dimensions identified in the literature as key dimensions influencing how ECs can implement different BMs. The former pertains to the internal governance of the EC, specifically the decision-making process and community control exercised by its members [76]. Many scholars used the terminology defined by EU directives: autonomy and effective control [11], while others used terms such as recruitment and participation processes [77] or the legal forms of ECs [11], [18]. All terms similar to governance were considered since they discuss how the EC makes the decisions. For example, the legal form of an EC is highly related to the governance structure since it implies the way in which the community is governed. The cooperative legal framework, for example, imposes the “one member, one vote principle”, which means that each member has one vote in the community assembly regardless of the shares held in the community by this member, while partnerships operate under quotas/shares and employ an entirely different decision-making process.

On the other hand, membership is related to the type of actors that participate in the EC, such as citizens/natural persons, SMEs or large enterprises, local authorities, and public actors. Membership has been discussed frequently in literature as a dimension that highly affects the EC function from many aspects [67]. However, scholars use varying terms, such as participants [11] or energy community members [26]. Moreover, many studies focus on the role of the members and differentiate them as prosumers, consumers, or storage operators [21]. Therefore, the membership dimension not only discusses the type of actors who participate in the EC but also their role within the community.

5.1 Energy Community Business Model Archetypes

The five dimensions described above can be used as a conceptual framework to examine, analyze, and categorize ECs into different BMs. Thus, by utilizing this framework, four different EC BM archetypes were identified and presented below, namely the self-consumption model, the third-party model, the aggregator model, and the integrated energy services and e-mobility model.

5.1.1 Self-consumption model

The value proposition of this archetype is based on reducing the energy bill for community members through the construction of collective power plants that operate with the aim of self-consuming energy, instead of selling it to the grid. The self-consumption model protects members from energy price fluctuations since they produce the energy they consume. Vulnerable households can benefit, as the self-consumption model often aims to combat energy poverty.

The main benefits for members in this model, which does not aim to sell energy, is to reduce the energy bill. However, opt-in and opt-out fees could cover the costs associated with the EC, including installation and maintenance of power plants, as well as other costs related to establishing and operating the community. A member of the EC buys at least one share of the EC, thereby increasing the share capital of the community. Additionally, the community can use the annual fees for EC members to cover labor costs and other expenses. However, this type of EC usually relies on voluntary work and does not incur high maintenance expenses. In addition, the installation of the power plant is the largest cost for this type of community, as the maintenance expenses are very low. Therefore, it is often possible to raise the initial capital through public funding or crowdfunding campaigns.

The main function of this archetype is related to the creation and supply of energy through an energy production system, usually photovoltaic (PV), which is owned by the community and supplies energy to the energy grid. A licensed supplier is required to calculate the community's output from the energy plant and subtract it from the amount of energy consumed by the community. By offsetting the energy produced and consumed, community members do not pay for electricity, as the electricity they have consumed has been produced by their power plant.

This EC BM archetype usually is citizen-driven, although the membership can vary, and different types of members, such as SMEs or local authorities, can participate. However, all of them can be considered as collective prosumers, with no distinct roles within the community, since they collectively produce and consume energy. To enhance the community's performance, the EC operation may assign specific responsibilities to certain members. Finally, the governance structure of this archetype is usually based on the cooperative model, applying the one-member-one-vote principle described earlier.

5.1.2 Third Party model

The value proposition of this archetype is based on reducing energy costs for members of the EC through the collective purchase of renewable energy at a lower price or through the rental of energy production assets provided by third parties. Therefore, the third party plays a crucial role in this EC BM, functioning as an external stakeholder who can aid in the establishment and operation of the EC by offering energy services, providing technical and management support, or even financing the entire project.

The value capture mechanisms are different for the third party and the EC members. The third-party benefits by securing a long-term revenue stream from the EC members either by selling energy or services at a fixed price through long-term agreements or by lending energy production assets to the EC. On the other hand, the EC members benefit from the reduction of electricity costs and from not assuming any financial risk or obligation to maintain energy assets.

The main function of this model is to purchase energy by supporting the creation of an EC that acts as an energy buyer. In this model, a third party undertakes the installation and maintenance of the project. Therefore, the third party manages and governs the project. Due to their dependence on the third party to provide specialized services that meet the requirements of the community, the EC members are thus excluded from decision-making and control of the energy production assets. This EC model usually includes residents or SMEs living close to each other, such as households in large building complexes, social housing, small towns, etc. All members of the EC are consumers who own the properties where the power plants are located.

5.1.3 Aggregator model

The value proposition of an EC aggregator is that it can manage energy production and demand better than a single prosumer or EC, thanks to economies of scale, and it facilitates the sharing of self-generated energy while offering flexibility and balancing services to the grid. Value capture mechanisms vary by community member's role since some are prosumers, other producers, or simple consumers. However, all EC members shall own, finance, and install the storage system and the necessary technologies to monitor and optimize the services. Thus, the community can save energy, and prosumers can earn money from the energy they provide to consumers or the grid. Moreover, the EC can generate revenue from opt-in and opt-out fees and from the fees for services provided to external actors. Nevertheless, the revenue distribution is based on the role of members and the service they provide.

The main function of this archetype is to concentrate the total supply and demand within a community. Prosumers in the community provide energy both to consumers and also provide services to external stakeholders, like the grid operators. Specifically, the aggregator can provide energy, flexibility, and auxiliary services on both the supply and demand sides since it can store the excess energy from the system or can transmit the excess energy produced by the community to the system. An aggregator uses a platform for daily operations to coordinate the different members of the EC. Although the implementation of this model can take different forms, the general function involves the use of the platform by the aggregator to manage energy sharing and optimize demand-side management on the community side, as well as to support the interactions of the members with external actors.

It becomes obvious that different types of members can be involved in this type of EC model, SMEs, citizens, and local authorities, albeit with different roles, since, as highlighted earlier, some can be prosumers or simple consumers. Despite the different roles of the members, they all share a common interest in sharing energy with each other, participating in the energy market, and being managed by an aggregator. In terms of governance, all members participate in decision-making, and the energy assets can be owned and controlled either individually or collectively; however, the interaction with suppliers and network operators is controlled, managed, and promoted by the aggregator.

5.1.4 Integrated energy services and e-mobility model

The value proposition of this model includes providing low-carbon solutions through integrated services and facilitating various actors; hence, this EC BM archetype is characterized by the fact that it provides a wide range of energy-related services to both EC members and external stakeholders. The types of actors participating in this EC BM and their roles vary; therefore, different value capture mechanisms exist depending on the actors, their roles, and the services provided. For instance, the e-vehicle services, energy savings, or opt-in and opt-out membership fees can serve as revenue streams.

The function of this EC resembles the aggregator archetype presented earlier, with EC members having distinct roles and services provided both internally and externally to the community. However, this model also includes activities that go beyond energy generation and flexibility provision, as it also offers other services, such as electric vehicle charging stations, car sharing, etc.

The EC members, who participate in decision-making based on their quotas, can collectively or individually own the EC's assets. The EC in this BM provides management services and interacts with suppliers and network operators by offering them solutions and thus securing long-term contracts. However, this model tailors its services to meet the needs of its members.

6 Conclusion

ECs represent an innovative and multifaceted topic that has acquired increasing attention in the last years, especially after the publication of two EU directives. Many studies have analyzed ECs from different angles, including its configurations, the different types of members that participate and their motives, the various technologies and activities performed by ECs as well as the benefits provided to members and society. The present study aimed to analyze academic literature and identify the current research areas related to the topic of ECs. A literature review and desk research were conducted, and it was found that, although the scholars' focus on the topic has increased remarkably in the last few years, there are still gaps that this research aimed to address.

Two important gaps were found in the literature. First, it appeared that there are no scientific studies that analyze how the ownership model influences the funding mechanisms that ECs use to finance their energy generation plants. Thus, in this research, a survey was conducted to gather primary data from ECs. It aimed to analyze the preferred funding mechanisms that ECs used based on their ownership models, as well as the main financial barriers they encounter. The second research gap is associated with the different BMs that ECs can develop, since there is no generally accepted analytical framework to analyze and categorize EC BMs. This study analyzed the literature, and a tailor-made analytical framework was created that incorporates all unique characteristics of ECs and can facilitate the analysis and categorization of different EC BMs. Moreover, 4 EC BM archetypes were defined that explain the different mechanisms in which different ECs can create, deliver, and capture value.

The results of the current study consolidate existing knowledge on ECs and extend it to new areas. The results from the literature review and desk research served as the preliminary step in this study and guided the subsequent phases. Consequently, this review primarily serves academic purposes, providing an overview of how various studies have approached the topic of ECs, highlighted different research areas, and identified existing research gaps.

The analysis of the ownership model and funding mechanisms of ECs provides useful information for both EC members and policymakers, as it highlights the financial barriers related to the development of ECs. In addition, it can facilitate the decision-making for ECs regarding the best funding mechanisms based on EC's ownership model and the size of the community. For policymakers, this research can enhance their understanding of how different ownership models affect funding mechanisms. Consequently, the development of new funding mechanisms tailored to specific types of EC ownership can help to promote specific policy objectives. For example, ECs established through citizen-led initiatives could benefit from innovative financing instruments. These instruments can support ownership models that face challenges in raising capital and financing their energy generation plants while promoting equity and citizen participation in the energy transition. In addition, new funding mechanisms, such as public guarantees, that mitigate the financial risk associated with some EC ownership models can enhance the confidence of private investors in supporting ECs. However, the benefits of this research could also be academically significant, as it can support cross-disciplinary studies that focus on both finance and governance, thereby promoting an interdisciplinary approach to the topic of ECs. Therefore, future research can focus on the analysis of real case studies aimed at collecting primary data on how the different ownership models of ECs affect funding mechanisms.

Finally, the study on EC BMs attempts to explain the mechanisms through which ECs operate from BM's perspective and provide an analytical framework tailored to ECs' unique characteristics. This study goes beyond the analysis of different ownership models of EC, since it aims to analyze the way in which ECs create, deliver, and capture value, economic, social, or environmental. Policymakers can benefit from this study by understanding how various EC BMs can advance policy objectives. For instance, the self-consumption model may be an ideal way to combat energy poverty since it aims to reduce energy bills. Meanwhile, the aggregator model defined in this study could help address grid imbalances that arise from the intermittent nature of renewables by providing flexibility services to the grid. Additionally, EC BMs can support initiatives like car-sharing and e-mobility services that encourage sustainable commuting. Moreover, the customized analytical framework for analyzing EC BMs can aid in the creation of new models, enable ECs to redefine their value propositions, and help examine the mechanisms through which they can achieve their goals. Furthermore, the findings of the current study hold academic significance as they offer an analytical framework specifically designed for analyzing EC BMs. Researchers can also use this framework to find different EC BMs from those shown here by applying it to real-world case studies.

Acknowledgments This work has received funding from the SmartGYsum project which is the European Union's Horizon 2020 research and innovation programme under the Marie Skłodowska-Curie grant agreement no. 955614. This project has received funding from the Masterpiece project which is the European Union's Horizon Europe Framework Programme for Research and Innovation under grant agreement no 101096836.

References

1. International Renewable Energy Agency, "Renewable Capacity Highlights," Mar. 2024. [Online]. Available: www.irena.org/Data/Statistical-
2. International Energy Agency, "Renewables 2024," 2024. [Online]. Available: www.iea.org
3. Eurostat, "Renewable Energy Statistics." Accessed: May 07, 2025. [Online]. Available: https://ec.europa.eu/eurostat/statistics-explained/index.php?title=Renewable_energy_statistics#:~:text=The%20EU%20reached%20a%2024.5,than%20in%202004%20(9.6%25).
4. M. Leach, I. Scoones, and A. Stirling, Dynamic Sustainabilities-Technology, Environment, Social Justice. 2010.
5. D. Loorback, N. Frantzeskaki, and F. Avelino, "Sustainability Transitions Research-Transforming Science and Practice for Societal Change," vol. 42, pp. 599–626, 2017.
6. J. Markard, R. Raven, and B. Truffer, "Sustainability transitions: An emerging field of research and its prospects," Res Policy, vol. 41, no. 6, pp. 955–967, Jul. 2012, doi: 10.1016/j.respol.2012.02.013.
7. D. Scholten, M. Bazilian, I. Overland, and K. Westphal, "The geopolitics of renewables: New board, new game," Energy Policy, vol. 138, Mar. 2020, doi: 10.1016/j.enpol.2019.111059.
8. A.-R. Kojonsaari and J. Palm, "Distributed Energy Systems and Energy Communities Under Negotiation," Technology and Economics of Smart Grids and Sustainable Energy, vol. 6, 2021, doi: 10.1007/s40866-021-00116-9/Published.
9. F. Coenen and T. Hoppe, Renewable Energy Communities and the Low Carbon Energy Transition in Europe. Springer International Publishing, 2021. doi: 10.1007/978-3-030-84440-0.
10. C. Candelise and G. Ruggieri, "The Community Energy Sector in Italy: Historical Perspective and Recent Evolution," in Renewable Energy Communities and the Low Carbon Energy Transition in Europe, Cham: Springer International Publishing, 2021, pp. 97–118. doi: 10.1007/978-3-030-84440-0_5.
11. Caramizaru and A. Uihlein, "Energy communities: an overview of energy and social innovation," 2020. doi: 10.2760/180576.
12. European Commission, "Energy Communities." Accessed: May 07, 2025. [Online]. Available: https://energy.ec.europa.eu/topics/markets-and-consumers/energy-consumers-and-prosumers/energy-communities_en

13. European Union, Directive 2023/2413 of the European Parliament and of the Council. 2023. Accessed: May 07, 2025. [Online]. Available: https://eur-lex.europa.eu/eli/dir/2023/2413/oj/eng
14. European Union, "Directive 2023/1791 of the European Parliament and of the Council," Sep. 2023. Accessed: May 07, 2025. [Online]. Available: https://eur-lex.europa.eu/legal-content/EN/TXT/?uri=CELEX%3A32023L1791
15. V. J. Schwanitz et al., "Statistical evidence for the contribution of citizen-led initiatives and projects to the energy transition in Europe," Sci Rep, vol. 13, no. 1, Dec. 2023, doi: 10.1038/s41598-023-28504-4.
16. R. Roberto, G. Ferruzzi, V. Negro, and M. Noussan, "Mapping of Energy Community Development in Europe: State of the Art and Research Directions," Energies (Basel), vol. 16, no. 18, p. 6554, Sep. 2023, doi: 10.3390/en16186554.
17. S. Ahmed, A. Ali, and A. D'Angola, "A Review of Renewable Energy Communities: Concepts, Scope, Progress, Challenges, and Recommendations," Sustainability, vol. 16, no. 5, p. 1749, Feb. 2024, doi: 10.3390/su16051749.
18. M. Koltunov et al., "Mapping of Energy Communities in Europe: Status Quo and Review of Existing Classifications," Sustainability, vol. 15, no. 10, p. 8201, May 2023, doi: 10.3390/su15108201.
19. G. Walker and P. Devine-Wright, "Community renewable energy: What should it mean?," Energy Policy, vol. 36, no. 2, pp. 497–500, Feb. 2008, doi: 10.1016/j.enpol.2007.10.019.
20. E. M. Gui and I. MacGill, "Typology of future clean energy communities: An exploratory structure, opportunities, and challenges," Energy Res Soc Sci, vol. 35, pp. 94–107, Jan. 2018, doi: 10.1016/j.erss.2017.10.019.
21. Dudka, N. Moratal, and T. Bauwens, "A typology of community-based energy citizenship: An analysis of the ownership structure and institutional logics of 164 energy communities in France," Energy Policy, vol. 178, p. 113588, Jul. 2023, doi: 10.1016/j.enpol.2023.113588.
22. D. Brown, S. Hall, and M. E. Davis, "Prosumers in the post subsidy era: an exploration of new prosumer business models in the UK," Energy Policy, vol. 135, Dec. 2019, doi: 10.1016/j.enpol.2019.110984.
23. S. T. Bryant, K. Straker, and C. Wrigley, "The typologies of power: Energy utility business models in an increasingly renewable sector," J Clean Prod, vol. 195, pp. 1032–1046, Sep. 2018, doi: 10.1016/j.jclepro.2018.05.233.
24. F.G. Reis, I. Gonçalves, M. A.R. Lopes, and C. Henggeler Antunes, "Business models for energy communities: A review of key issues and trends," Renewable and Sustainable Energy Reviews, vol. 144, Jul. 2021, doi: 10.1016/j.rser.2021.111013.
25. S. Hall and K. Roelich, "Business model innovation in electricity supply markets: The role of complex value in the United Kingdom," Energy Policy, vol. 92, pp. 286–298, May 2016, doi: 10.1016/j.enpol.2016.02.019.
26. M. Kubli and S. Puranik, "A typology of business models for energy communities: Current and emerging design options," Renewable and Sustainable Energy Reviews, vol. 176, Apr. 2023, doi: 10.1016/j.rser.2023.113165.
27. C. Nolden, J. Barnes, and J. Nicholls, "Community energy business model evolution: A review of solar photovoltaic developments in England," Renewable and Sustainable Energy Reviews, vol. 122, Apr. 2020, doi: 10.1016/j.rser.2020.109722.

28. T. Braunholtz-Speight et al., “The Evolution of Community Energy in the UK,” 2018. Accessed: Apr. 22, 2025. [Online]. Available: https://ukerc.ac.uk/publications/evolution-of-community-energy-in-the-uk/
29. P. Mirzania, A. Ford, D. Andrews, G. Ofori, and G. Maidment, “The impact of policy changes: The opportunities of Community Renewable Energy projects in the UK and the barriers they face,” Energy Policy, vol. 129, pp. 1282–1296, Jun. 2019, doi: 10.1016/j.enpol.2019.02.066.
30. C. Nolden, “Governing community energy-Feed-in tariffs and the development of community wind energy schemes in the United Kingdom and Germany,” Energy Policy, vol. 63, pp. 543–552, Dec. 2013, doi: 10.1016/j.enpol.2013.08.050.
31. T. van der Schoor and B. Scholtens, “The power of friends and neighbors: a review of community energy research,” Aug. 01, 2019, Elsevier B.V. doi: 10.1016/j.cosust.2019.08.004.
32. M. L. Lode, G. te Boveldt, T. Coosemans, and L. Ramirez Camargo, “A transition perspective on Energy Communities: A systematic literature review and research agenda,” Renewable and Sustainable Energy Reviews, vol. 163, Jul. 2022, doi: 10.1016/j.rser.2022.112479.
33. European Commission, “European Energy Communities: Sector Coupling, Flexibility, and Operational Perspectives.” Accessed: Jul. 10, 2025. [Online]. Available: https://build-up.ec.europa.eu/en/resources-and-tools/articles/european-energy-communities-sector-coupling-flexibility-and?
34. REScoop, “Transposition tracker.” Accessed: May 07, 2025. [Online]. Available: https://www.rescoop.eu/policy/transposition-tracker
35. L. Gruber, U. Bachhiesl, and S. Wogrin, “The current state of research on energy communities,” Elektrotechnik und Informationstechnik, vol. 138, no. 8, pp. 515–524, Dec. 2021, doi: 10.1007/s00502-021-00943-9.
36. H. Busch, S. Ruggiero, A. Isakovic, and T. Hansen, “Policy challenges to community energy in the EU: A systematic review of the scientific literature,” Nov. 01, 2021, Elsevier Ltd. doi: 10.1016/j.rser.2021.111535.
37. T. Bauwens et al., “Conceptualizing community in energy systems: A systematic review of 183 definitions,” Renewable and Sustainable Energy Reviews, vol. 156, Mar. 2022, doi: 10.1016/j.rser.2021.111999.
38. Dall-Orsoletta, J. Cunha, M. Araújo, and P. Ferreira, “A systematic review of social innovation and community energy transitions,” Jun. 01, 2022, Elsevier Ltd. doi: 10.1016/j.erss.2022.102625.
39. F. Gianaroli, M. Preziosi, M. Ricci, P. Sdringola, M. A. Ancona, and F. Melino, “Exploring the academic landscape of energy communities in Europe: A systematic literature review,” 2024, doi: doi.org/10.1016/j.jclepro.2024.141932.
40. L. Neij et al., “Energy communities—lessons learnt, challenges, and policy recommendations,” Oxford Open Energy, vol. 4, 2025, doi: 10.1093/ooenergy/oiaf002.
41. H. Busch, S. Ruggiero, A. Isakovic, F. Faller, and T. Hansen, “Co2mmunity Co-producing and co-financing renewable community energy projects,” 2019. Accessed: Apr. 08, 2024. [Online]. Available: https://www.researchgate.net/publication/330753683_Co2mmunity_Co-producing_and_co-financing_renewable_community_energy_projects

42. V. Brummer, "Community energy – benefits and barriers: A comparative literature review of Community Energy in the UK, Germany and the USA, the benefits it provides for society and the barriers it faces," Renewable and Sustainable Energy Reviews, vol. 94, pp. 187–196, Oct. 2018, doi: 10.1016/j.rser.2018.06.013.
43. T. Bauwens, "Explaining the diversity of motivations behind community renewable energy," Energy Policy, vol. 93, pp. 278–290, Jun. 2016, doi: 10.1016/j.enpol.2016.03.017.
44. T. Terlouw, T. AlSkaif, C. Bauer, and W. van Sark, "Multi-objective optimization of energy arbitrage in community energy storage systems using different battery technologies," Appl Energy, vol. 239, pp. 356–372, Apr. 2019, doi: 10.1016/j.apenergy.2019.01.227.
45. Liu, H. Yang, and Y. Zhou, "Peer-to-peer trading optimizations on net-zero energy communities with energy storage of hydrogen and battery vehicles," Appl Energy, vol. 302, Nov. 2021, doi: 10.1016/j.apenergy.2021.117578.
46. N. Good and P. Mancarella, "Flexibility in Multi-Energy Communities with Electrical and Thermal Storage: A Stochastic, Robust Approach for Multi-Service Demand Response," IEEE Trans Smart Grid, vol. 10, no. 1, pp. 503–513, Jan. 2019, doi: 10.1109/TSG.2017.2745559.
47. Koskela, A. Rautiainen, and P. Järventausta, "Using electrical energy storage in residential buildings – Sizing of battery and photovoltaic panels based on electricity cost optimization," Appl Energy, vol. 239, pp. 1175–1189, Apr. 2019, doi: 10.1016/j.apenergy.2019.02.021.
48. P. Olivella-Rosell et al., "Local flexibility market design for aggregators providing multiple flexibility services at distribution network level," Energies (Basel), vol. 11, no. 4, Apr. 2018, doi: 10.3390/en11040822.
49. T. Sousa, T. Soares, P. Pinson, F. Moret, T. Baroche, and E. Sorin, "Peer-to-peer and community-based markets: A comprehensive review," Renewable and Sustainable Energy Reviews, vol. 104, pp. 367–378, Apr. 2019, doi: 10.1016/j.rser.2019.01.036.
50. Lage, R. Castro, G. Manzolini, V. Casalicchio, and T. Sousa, "Techno-economic analysis of self-consumption schemes and energy communities in Italy and Portugal," Solar Energy, vol. 270, Mar. 2024, doi: 10.1016/j.solener.2024.112407.
51. Krug, M. R. Di Nucci, M. Caldera, and E. De Luca, "Mainstreaming Community Energy: Is the Renewable Energy Directive a Driver for Renewable Energy Communities in Germany and Italy?," Sustainability (Switzerland), vol. 14, no. 12, Jun. 2022, doi: 10.3390/su14127181.
52. European Commission, "Barriers and action drivers for the development of different activities by renewable and citizen energy communities.," 2024. [Online]. Available: www.canopee.studio
53. Friends of the Earth, "Barriers and threats to the people-owned energy revolution," 2021.
54. P. A. Strachan, R. Cowell, G. Ellis, F. Sherry-Brennan, and D. Toke, "Promoting Community Renewable Energy in a Corporate Energy World," Sustainable Development, vol. 23, no. 2, pp. 96–109, 2015, doi: 10.1002/sd.1576.
55. P. Bertheau, J. Dionisio, C. Jütte, and C. Aquino, "Challenges for implementing renewable energy in a cooperative-driven off-grid system in the Philippines," Environ Innov Soc Transit, vol. 35, pp. 333–345, Jun. 2020, doi: 10.1016/j.eist.2019.03.002.

56. de Bakker, A. Lagendijk, and M. Wiering, “Cooperatives, incumbency, or market hybridity: New alliances in the Dutch energy provision,” Energy Res Soc Sci, vol. 61, Mar. 2020, doi: 10.1016/j.erss.2019.101345.
57. M. Martiskainen, “The role of community leadership in the development of grassroots innovations,” Environ Innov Soc Transit, vol. 22, pp. 78–89, Mar. 2017, doi: 10.1016/j.eist.2016.05.002.
58. S. B. Serrano, R. Bodini, M. Roy, and G. Salvatori, Financial Mechanisms for Innovative Social and Solidarity Economy Ecosystems Co-founder and CEO, SOKIO Cooperative. 2019. [Online]. Available: www.ilo.org/publns
59. K. Pantazis, C. Edoardo, and T. Molteni, “Energy Communities in the EU: Analysis of ownership models and funding mechanisms,” in 16th International Conference on Energy and Climate Change, 2023, pp. 115–134.
60. International Renewable Energy Agency, Community-ownership models: Innovation Landscape Brief. 2020. Accessed: Apr. 08, 2024. [Online]. Available: https://www.irena.org/-/media/Files/IRENA/Agency/Publication/2020/Jul/IRENA_Community_ownership_2020
61. J. Arnould and D. Quiroz, “Energy communities in the EU Opportunities and barriers to financing,” 2022. [Online]. Available: www.profundo.nl.
62. Rescoop.eu, “Compile,” 2021. Accessed: Apr. 08, 2024. [Online]. Available: https://www.rescoop.eu/toolbox/compile-toolkit-financing-guide
63. T. Braunholtz-Speight et al., “Business models and financial characteristics of community energy in the UK,” Nat Energy, vol. 5, no. 2, pp. 169–177, Feb. 2020, doi: 10.1038/s41560-019-0546-4.
64. C. E. Hoicka and J. L. MacArthur, “From tip to toes: Mapping community energy models in Canada and New Zealand,” Energy Policy, vol. 121, pp. 162–174, Oct. 2018, doi: 10.1016/j.enpol.2018.06.002.
65. S. M. Shafer, H. J. Smith, and J. C. Linder, “The power of business models,” Bus Horiz, vol. 48, no. 3, pp. 199–207, 2005, doi: 10.1016/j.bushor.2004.10.014.
66. M. E. Porter and M. R. Kramer, “Creating Shared Value: How to reinvent capitalism-and unleash a wave of innovation and growth,” Harvard Business Review, Jan. 2011. Accessed: Feb. 10, 2025. [Online]. Available: https://hbr.org/2011/01/the-big-idea-creating-shared-value
67. Mohammadi, “Investigation of Community Energy Business Models from an Institutional Perspective: Intermediaries and Policy Instruments in Selected Cases of Developing and Developed Countries,” Sustainability (Switzerland), vol. 15, no. 10, May 2023, doi: 10.3390/su15108423.
68. López et al., “European energy communities: Characteristics, trends, business models and legal framework,” Renewable and Sustainable Energy Reviews, vol. 197, Jun. 2024, doi: 10.1016/j.rser.2024.114403.
69. M. Bertolini and G. Morosinotto, “Business Models for Energy Community in the Aggregator Perspective: State of the Art and Research Gaps,” Energies (Basel), vol. 16, no. 11, Jun. 2023, doi: 10.3390/en16114487.
70. Osterwalder and Y. Pigneur, Business Model Generation. A Handbook for Visionaries, Game Changers, and Challengers. John Wiley & Sons, 2010.

71. M. Mlinarič, N. Kovač, J. Barnes, and N. Bocken, “New Clean Energy Communities in a Changing European Energy System (NEWCOMERS) Typology of new clean energy communities,” 2019.
72. Pantazis, A. Bagaini, S. M. M. Ahmed, and E. Croci, “Energy Community Business Models Archetypes,” in 2025 IEEE 19th International Conference on Compatibility, Power Electronics and Power Engineering (CPE-POWERENG), IEEE, May 2025, pp. 1–7. doi: 10.1109/CPE-POWERENG63314.2025.11027308.
73. Osterwalder, Y. Pigneur, and C. L. Tucci, “Clarifying Business Models: Origins, Present, and Future of the Concept,” Communications of the Association for Information Systems, vol. 16, 2005, doi: 10.17705/1cais.01601.
74. De Vidovich, L. Tricarico, and M. Zulianello, “How Can We Frame Energy Communities’ Organisational Models? Insights from the Research ‘Community Energy Map’ in the Italian Context,” Sustainability (Switzerland), vol. 15, no. 3, Feb. 2023, doi: 10.3390/su15031997.
75. J. M. Schwidtal et al., “Emerging business models in local energy markets: A systematic review of peer-to-peer, community self-consumption, and transactive energy models,” vol. 179, 2023, doi: 10.48420/169307.
76. F. D. Minuto and A. Lanzini, “Energy-sharing mechanisms for energy community members under different asset ownership schemes and user demand profiles,” Renewable and Sustainable Energy Reviews, vol. 168, Oct. 2022, doi: 10.1016/j.rser.2022.112859.
77. A. Ghorbani, L. Nascimento, and T. Filatova, “Growing community energy initiatives from the bottom up: Simulating the role of behavioural attitudes and leadership in the Netherlands,” Energy Res Soc Sci, vol. 70, Dec. 2020, doi: 10.1016/j.erss.2020.101782.

ISBN

9 788409 810192

SMARTGYsum project has received funding from the European Union’s Horizon 2020 research and innovation programme under the Marie Skłodowska-Curie grant agreement No 955614.